Unusual Astrophysical Objects: Blank Field Sources and Gravitational Lenses

---

Dissertation

zur

Erlangung der naturwissenschaftlichen Doktorwürde
(Dr. sc. nat.)

vorgelegt der

Mathematisch-naturwissenschaftlichen Fakultät

der

Universität Zürich

von

Matteo Chieregato

aus

Italien

Promotionskomitee
Prof. Dr. Daniel Wyler (Vorsitz)
Prof. Dr. Philippe Jetzer (Leitung der Dissertation)
Prof. Dr. Aldo Treves

Zürich 2007

Die vorliegende Arbeit wurde von der Mathematisch-naturwissenschaftlichen Fakultät der Universität Zürich auf Antrag von Prof. Dr. Ben Moore und Prof. Dr. Daniel Wyler als Dissertation angenommen.

The International Ph. D. programme is a joint Ph. D. of Università dell'Insubria and Universität Zürich. The programme has been carried out partly at the Dipartimento di Fisica e Matematica of Università dell'Insubria - sede di Como and partly at the Institut für Theoretische Physik at the Universität Zürich. This thesis is intended to be discussed both at the Università dell'Insubria - Como and at the Universität Zürich, according to the agreement between the two universities.

A mio padre

Contents

List of Figures

List of Tables

Summary

This thesis treats of observational astrophysics. In particular, the first part concerns X-ray sources without optical counterparts (Blank Field Sources, BFS). The search for BFS paves the way to the identification of unusual objects in the X-ray sky, hidden in the bulk of X-ray catalog entries. This is especially true for sources powered by compact objects, either neutron stars or black holes. After a BFS is sought, detailed X-ray and optical studies have to be pursued; two examples are the cases here described of the Ultra-Luminous X-ray Source NGC 1313 X-2, and of the ROSAT Isolated Neutron Star RBS 1774.

The second part of the thesis focuses on gravitational lensing. The peculiarity of the gravitational lensing technique is that it directly probes the mass of the lens, not its light emission as usual. This makes it well suited to gather information hardly obtainable in any other way. Specifically, microlensing toward the Galactic Bulge can be utilized to track Galactic compact objects. That is, galactic neutron stars and black holes are suited to be discovered and studied both with microlensing and with BFS searches, therefore linking the two parts of the thesis. Here we expose some preliminary results on this line of research. Strong gravitational lensing is instead the weapon of choice to probe distant galaxies mass distributions. It is discussed in some detail the case of Q0045-337, in which we face the possibility of the discovery of a new rare spiral galaxy lens.

In Chapter 1 we present a sample of BFS detected in the Brera Multiscale Wavelet catalog of ROSAT HRI observations (HRI-BMW). We filtered the initial $\sim$ 29000 catalog entries on the basis of of source brightness, distance from possible counterparts at other wavelengths, point-like shape and a good estimate of the X-ray flux (f_X). We reconstructed an X-ray position corrected from systematic boresight errors for the subset of filtered sources and then checked again the new positions against possible counterparts at other wavelengths in a 4 σ radius. Our final sample consists of three BFS, among which two objects show also evidence of a transient behaviour. The observed f_X and the limiting magnitude of the optical catalogs fix a lower limit on $f_X/f_{opt} \sim 40$ for the selected BFS. This value puts them well beyond 90% threshold for usual source classes, once HRI energy band and proper spectral shape are taken into account, leaving room for speculation on their nature. At the end of the Chapter some preliminary result of the observational follow-up campaign we are conducting is reported.

The sieving of the HRI-BMW catalog allowed us to individuate, besides the

final BFS sample, quite a number of other peculiar objects, that at some point were considered BFS candidates, but did not made it through the whole selection procedure. We dubbed these objects Failed Blank Field Sources (FBFS), and we present them in Chapter 2. Some of them are truly failed BFS, since they have a possible counterpart at other wavelengths at a distance between 4 and 2 error radii, while for some other we propose an optical or radio identification.

In Chapter 3 we expose new optical and *Chandra* observations of the field containing the ultraluminous X-ray source NGC 1313 X-2. On an ESO 3.6 m image, the *Chandra* error box embraces a $R = 21.6$ point-like object and excludes a previously proposed optical counterpart. The resulting X-ray/optical flux ratio of NGC 1313 X-2 is ~ 500. The value of f_X/f_{opt}, the X-ray variability history and the spectral distribution derived from a re-analysis of the *ROSAT*, *ASCA* and *XMM* data indicate a luminous X-ray binary in NGC 1313 as a likely explanation for NGC 1313 X-2. If the X-ray soft component observed in the *XMM* EPIC spectrum originates from an accretion disk, the inferred mass of the compact remnant is $\approx 100 M_\odot$, making it an intermediate mass black hole. The derived optical luminosity ($L \approx 10^5 L_\odot$) is consistent with that of a $\approx 15 - 20 M_\odot$ companion. The properties of the environment of NGC 1313 X-2 are briefly discussed

In Chapter 4 we report on the results of a deep *XMM-Newton* observation of RBS 1774, the last dim isolated neutron star candidate found in the *ROSAT* archive data. Spectral and timing analysis of the high-quality PN and MOS data confirm the association of this source with an isolated neutron star. The spectrum is thermal and blackbody-like, and there is evidence at a significance level $> 4\sigma$ that the source is an X-ray pulsar, with spin period of 9.437 s. Spectral fitting reveals the presence of an absorption feature at ~ 0.7 keV, but at this level data do not have enough resolution to allow us to discriminate between an absorption line or an edge. We compare the newly measured properties of RBS 1774 with those of other known dim isolated neutron stars, and discuss possible interpretations for the absorption feature.

Chapter 5 is a short introduction to the phenomenon of gravitational lensing and on its astrophysical application. The aim is to make this thesis self-contained, avoiding to load the following Chapters with excess of theoretical notions. Gravitational lensing conjugates in three forms, strong, weak and micro. Here we concentrate only on strong lensing and microlensing, since these are the lines of research that we carry on in the rest of the thesis, and in general we favour the exposition of the concepts actually needed further on.

Chapter 6 reports on the status of a work-in-progress on microlensing that we are conducting. In particular, we discuss the status of available databases of microlensing events in light of the recent releases of MACHO, OGLE and EROS collaborations. We then analyze the statistical significance of the anomalous event distribution in one of the MACHO fields, field 104, and we examine some hypotheses on the origin of the anomaly.

Late-type strong lensing galaxies known so far are rare. They are precious to study the mass distribution of a spiral galaxy and its image-splitting cross section. Recently, an observational campaign based on ESO VLT adaptive optics, aimed to observe distant quasars host galaxies, discovered a disk-like galaxy at ~ 1.2 arcsec from the QSO Q0045-3337 (Falomo et al. 2005). In Chapter 7 we discuss the possible lensing effect of the galaxy. We performed two dimensional surface photometry on the VLT image of the galaxy, confirming its spiral nature. We then verified if simple mass models, partially constrained by observational data, require unrealistic parameters to produce a still hidden second quasar image. We also evaluated the respective viability of an instrumental or a lensing origin of the observed QSO deformation. We found a residual image after galaxy model subtraction, likely not related to gravitational lensing. Existing data are not sufficient to assess the presence of image splitting, nor to constrain the number of images or discriminate between galaxy mass models. Further observations are mandatory to progress in the study of this remarkable system, that could shed more light on the lensing behaviour of spiral galaxies.

The material of Chapters 1 (except partly for Section 1.6), 2, 6 and 7 and of Appendix A is either published with me as first author or original, but in any case carried out mainly by me. Chapters 3, 4 and Appendixes B and C are based on publications to which I contributed but in which I am not the first author. Section 1.6 is based on Appendix B but it has been elaborated by me to be included in this Thesis. Chapter 5 is a synthesis, written by me, of existing works on gravitational lensing, in particular of the one by Jetzer (2002), integrated by some more details on mass models relevant for strong lensing and by some up-to-date results in the rapidly evolving field of bulge microlensing.

Zusammenfassung

Die vorliegende Doktorarbeit befasst sich mit beobachtender Astrophysik. Der erste Teil der Arbeit beinhaltet die Untersuchung von Röntgenquellen ohne optischen Spektralanteil ("Quellen im freien Feld", auf Englisch "Blank Field Sources", kurz BFS). Die Suche nach BFS ermöglicht die Identifikation von ungewöhnlichen Objekten am Röntgenhimmel, die in der Fülle von Einträgen im Katalog der Röntgenquellen versteckt sind. Dies gilt insbesondere für Quellen, die auf kompakten Objekten wie Neutronensternen oder schwarzen Löchern beruhen. Nachdem eine Röntgenquelle als BFS identifiziert wurde, müssen detaillierte Untersuchungen ihres optischen sowie ihres Röntgenspektrums vorgenommen werden; zwei Beispiele sind die hier beschriebenen Fälle der ultraintensiven Röntgenquelle NGC 1313 X-2 und des isolierten Neutronensterns ROSAT RBS 1774.

Der zweite Teil der Arbeit befasst sich mit Gravitationslinsen. Die Untersuchung von Gravitationslinsen hat insbesondere den Vorteil, dass sie erlaubt, die Masse einer Linse direkt zu untersuchen, d. h. ohne den Umweg über deren Lichtemission. Diese Technik eignet sich daher gut, um Informationen zu erheben, die auf anderem Wege kaum erhältlich wären. Im Besonderen können sehr geringe Linseneffekte (sogenanntes "Microlensing") in Richtung des Zentrums der Milchstrasse dazu verwendet werden, galaktische kompakte Objekte ausfindig zu machen. Galaktische Neutronensterne und schwarze Löcher können daher sowohl mittels Microlensing, als auch mithilfe von BFS entdeckt und erforscht werden, und dies verbindet die beiden Teile der vorliegenden Arbeit. Im folgenden werden einige vorläufige Ergebnisse dieser Forschungsrichtung dargestellt.

Starke Gravitationslinsen hingegen eignen sich gut, die Massenverteilungen entfernter Galaxien zu untersuchen. Hier wird der Fall der Quasar Q0045-337 diskutiert, bei der es sich möglicherweise um ein neues Exemplar der seltenen auf Spiralgalaxien beruhenden Linsen handelt.

In Kapitel 1 wird eine BSF-Probe präsentiert, die im Brera Multiscale Wavelet Katalog verzeichnet ist und mit ROSAT HRI Beobachtungen (HRI-BMW) detektiert wurde. Die anfänglich $\sim$ 29000 Katalogeinträge wurden anhand folgender Kriterien gefiltert: Intensität der Quellen, Distanz zu möglichen Spektralanteilen anderer Wellenlängen, punktartige Form sowie gute Abschätzung des Röntgenflusses (f_X). Wir rekonstruierten für die so erhaltene Teilmenge von Quellen von systematischen Peilrichtungsfehlern bereinigte Positionen, welche anschliessend erneut auf mögliche Spektralanteile anderer Wellenlängen im Radius von 4σ untersucht wurden. Der endgültige Probensatz besteht aus drei BFS,

von denen zwei zusätzlich Anzeichen eines Übergangsverhaltens aufweisen. Der beobachtete Röntgenfluss f_X und die maximale Magnitude der optischen Kataloge ergeben eine untere Schranke von $f_X/f_{opt} \sim 40$ für die ausgewählten BSF. Dieser Wert identifiziert sie, unter Berücksichtigung des HRI Energiebandes und der spektralen Form, als weit entfernt von der 90% Schwelle für gewöhnliche Quellenklassen, was Raum für Spekulationen über ihre Beschaffenheit offen lässt. Am Ende des Kapitels werden einige vorläufige Ergebnisse der anschliessenden Beobachtungskampagne, die wir durchführen, präsentiert.

Durch das Filtern des HRI-BMW Kataloges konnten wir neben dem endgültigen BFS Probensatz auch einige weitere bemerkenswerte Objekte identifizieren, die zunächst als Kandidaten für BSF gegolten haben, im weiteren Verlauf des Selektionsprozesses jedoch ausgesiebt wurden. Diese Objekte, die wir mit "Failed Blank Field Sources" (FBFS) bezeichnet haben, werden in Kapitel 2 vorgestellt. Bei einigen von ihnen handelt es sich um FBFS im eigentlichen Sinne, da sie einen möglichen Spektralanteil bei anderen Wellenlängen bei einer Distanz zwischen 4 und 2 Fehlerradien haben. Für gewisse andere Objekte schlagen wir eine Identifikation im optischen oder im Radiobereich vor.

In Kapitel 3 stellen wir neue optische und *Chandra*-Beobachtungen des Bereichs vor, in welchem die ultraluminöse Röntgenquelle NGC 1313 X-2 liegt. Auf einem ESO 3.6 m Bild umfasst die *Chandra*-Fehlerbox ein punktförmiges Objekt mit R = 21.6 und schliesst einen zuvor vorgeschlagenen optischen Spektralanteil aus. Das resultierende Verhältnis des Röntgenflusses zum optischen Fluss von NGC 1313 X-2 liegt bei ~ 500. Der Wert von f_X/f_{opt}, die Entwicklung der Intensitätsschwankungen im Röntgenbereich und die spektrale Verteilung, die aus einer erneuten Analyse der *ROSAT*, *ASCA* und *XMM* Daten abgeleitet wurden, deuten auf einen hellen Röntgendoppelstern in NGC 1313 als wahrscheinliche Erklärung für NGC 1313 X-2 hin. Wenn die weiche Komponente der Röntgenstrahlung, die im *XMM* EPIC-Spektrum beobachtet wird, von einer Akkretionsscheibe stammt, so ist die Masse des kompakten Partners $\approx 100 M_\odot$, was einem schwarzen Loch mittlerer Masse entspricht. Die hergeleitete optische Luminosität ($L \approx 10^5 L_\odot$) ist mit jener eines $\approx 15 - 20 M_\odot$ Partners konsistent. Die Eigenschaften der Umgebebung von NGC 1313 X-2 werden kurz diskutiert.

In Kapitel 4 stellen wir Ergebnisse einer tiefen *XMM-Newton*-Beobachtung von RBS 1774 vor, des letzten Kandidaten für einen schwach leuchtenden isolierten Neutronenstern, der in den Daten des *ROSAT*-Archivs gefunden wurde. Spektrale und zeitliche Analysen der qualitativ hoch stehenden PN und MOS Daten bestätigen, dass diese Quelle einem isolierten Neutronenstern zugeordnet werden kann. Das Spektrum ist thermisch und entspricht der Schwarzkörperstrahlung, und es bestehen Hinweise auf einem Signifikanzniveau von $> 4\sigma$ dafür, dass es sich bei der Quelle um einen Röntgenpulsar mit einer Rotationsdauer von $9.437s$ handelt. Das Spektrum weist ein Absorptionsphänomen bei einer Energie um $\sim 0.7keV$ auf. Die Auflösung der Daten in diesem Bereich ist jedoch nicht hoch genug, um zwischen einer Absorptionslinie und einer

Absorptionsbande unterscheiden zu können. Wir vergleichen die kürzlich gemessenen Eigenschaften von RBS 1774 mit denen von anderen bekannten dunklen isolierten Neutronensternen und diskutieren mögliche Interpretationen des oben erwähnten Absorptionsphänomens.

Kapitel 5 ist eine kurze Einführung in das Phänomen der Gravitationslinsen und dessen Anwendungen in der Astrophysik und dient dazu, die vorliegende Arbeit selbsterklärend zu halten, ohne die folgenden Kapitel mit theoretischen Begriffserklärungen zu beladen. Die Gravitationslinseneffekte werden eingeteilt in drei Intensitätsstufen: stark, schwach und sehr schwach (letzteres wird im Englischen als "Microlensing" bezeichnet). Wir legen hier den Schwerpunkt auf starke Gravitationslinsen und Microlensing, da diese Effekte für unsere Forschungsarbeit relevant sind. Die Darstellung ist vor allem auf die Anwendungen in den folgenden Kapiteln ausgerichtet.

Kapitel 6 ist ein Zwischenbericht über die laufende Arbeit zum Microlensing, die wir durchführen. Wir diskutieren den momentanen Stand der Datensätze zu Microlensing-Ereignissen, die aus den aktuellen Projekten MACHO, OGLE und EROS hervorgehen. Wir analysieren sodann die statistische Signifikanz der anomalen Ereignisverteilung in einem der MACHO-Bereiche, dem Bereich 104, und untersuchen einige Hypothesen zum Ursprung dieser Anomalität.

Bis heute sind nur sehr wenige starke Gravitationslinsen, die auf "späten" (engl. "late-type") Galaxien beruhen, bekannt. Es ist kostspielig, für Spiralgalaxien die Massenverteilung und den Wirkungsquerschnitt für eine Bildaufspaltung durch Linseneffekte zu studieren. Kürzlich wurde im Rahmen einer auf ESO VLT adaptiver Optik basierenden Kampagne zur Beobachtung von Galaxien, die Quasare beherbergen, eine scheibenartige Galaxie entdeckt, die $\sim 1.2 arcsec$ von QSO Q0045-3337 entfernt ist (Falomo et al. 2005). In Kapitel 7 untersuchen wir den möglichen Linseneffekt dieser Galaxie. Wir führten eine zweidimensionale Oberflächen-Photometrie mit dem VLT-Bild der Galaxie durch, welche eine Spiralform bestätigte. Anschliessend überprüften wir, ob einfache Massenverteilungsmodelle, die teilweise durch Beobachtungsdaten bedingt sind, unrealistische Parameterwerte erfordern, um ein nach wie vor verborgenes Bild eines Quasars hervorzurufen. Zudem untersuchten wir, ob die beobachtete QSO-Deformation ihren Ursprung in den Messinstrumenten oder in Linseneffekten haben könnte. Nach Subtraktion des dem Galaxiemodell entsprechenden Bildes blieb ein Restbild zurück, welches wahrscheinlich nicht mit Linseneffekten zusammenhängt. Die vorhandenen Daten reichen weder aus, zu entscheiden, ob Bildaufspaltung vorliegt, noch die mögliche Anzahl der Bilder einzuschränken oder zwischen verschiedenen Massenverteilungsmodellen von Galaxien zu unterscheiden. Es sind zwangsläufig weitere Beobachtungen notwendig, um Fortschritte im Studium dieses bemerkenswerten Systems zu erzielen, welches die Eigenschaften von Spiralgalaxien als Gravitationslinsen erhellen könnte.

Der Stoff der Kapitel 1 (ausser teilweise des Abschnitts 1.6), 2, 6 und 7 und des Anhangs A wurde entweder von mir als Erstautor publiziert oder ist

original, aber jedenfalls hauptsächlich von mir erarbeitet. Kapitel 3, 4 und die Anhänge B und C basieren auf Publikationen, zu denen ich beigetragen habe, bei denen ich jedoch nicht als Erstautor aufgeführt bin. Der auf Anhang B basierende Abschnitt 1.6 wurde von mir ausgearbeitet und dem Rahmen der Arbeit angepasst. Kapitel 5 ist eine von mir erstellte Synthese aus existierenden Arbeiten über Gravitationslinsen, speziell aus derjenigen von Jetzer (2002), vervollständigt durch einige Details zu Massenverteilungsmodellen, die für starke Gravitationslinsen relevant sind, und durch einige aktuelle Resultate im sich schnell entwickelnden Gebiet des "Bulge Microlensings".

Sommario

Questa tesi tratta di astrofisica osservativa. In particolare, la prima parte riguarda sorgenti di raggi X senza controparti ottiche ("sorgenti di campo vuoto", in inglese Blank Field Sources, BFS). La ricerca di BFS apre la strada all'identificazione di oggetti insoliti nel cielo X, nascosti nella massa delle voci dei cataloghi X. Ciò è in special modo vero per sorgenti la cui energia è fornita da oggetti compatti, siano stelle di neutroni o buchi neri. Una volta che individuata una BFS, deve essere studiata in dettaglio nelle bande X e ottica; due esempi sono i casi qui descritti, la sorgente X ultra luminosa (Ultra-Luminous X-ray Source) NGC 1313 X-2 e la stella di neutroni isolata di ROSAT (ROSAT Isolated Neutron Star) RBS 1774.

La seconda parte della tesi è focalizzata sulle lenti gravitazionali. La peculiarità della tecnica basata sull'uso di lenti gravitazionali è che sonda direttamente la massa della lente, non la sua emissione luminosa come di consueto. Ciò la rende adatta a raccogliere informazioni difficilmente ottenibili in qualunque altro modo. Specificatamente, il microlensing verso lo Sferoide Galattico pu essere utilizzato per individuare le tracce di oggetti compatti galattici. In altre parole, stelle di neutroni e buchi neri galattici sono adatti ad essere scoperti e studiati sia tramite il microlensing sia tramite ricerche di BFS, fornendo quindi il legame tra le due parti della tesi. Qui esponiamo alcuni risultati preliminari in questa linea di ricerca. Lo studio delle lenti gravitazional forti è invece la prima scelta per sondare distribuzioni di massa di galassie distanti. È discusso in dettaglio il caso di Q0045-337, in cui ci confrontiamo con la possibilità della scoperta di una nuova, rara, lente del tipo galassia a spirale.

Nel capitolo 1 presentiamo un campione di BFS trovate nel catalogo Brera Multiscale Wavelet di osservazioni di ROSAT HRI (HRI-BMW). Abbiamo filtrato le $\sim$ 29000 voci del catalogo di partenza sulla base di luminosità della sorgente, distanza dalle possibili controparti in altre lunghezze d'onda, aspetto puntiforme e buona stima del flusso X (f_X). Abbiamo ricostruito una posizione X libera da errori sistematici di boresight per il sottoinsieme delle sorgenti filtrate e poi ricontrollato le nuove posizioni contro possibili controparti ad altre lunghezze d'onda in un raggio di 4 σ. Il nostro campione finale consiste di tre BFS, tra cui due oggetti mostrano un comportamento transiente. Gli f_X osservati e la magnitudine limite dei cataloghi ottici fissano un limite inferiore per le nostre BFS $f_X/f_{opt} \sim 40$. Questo valore li pone ben oltre la soglia del 90% per le classi di sorgenti usuali, una volta che siano considerate la banda di energia dell'HRI e la forma spettrale, lasciando spazio alle speculazioni sulla loro natura.

Alla fine del Capitolo sono riportati alcuni risultati preliminari della campagna osservativa di follow-up che stiamo conducendo.

Il setaccio del catalogo HRI-BMW ci ha permesso di individuare, oltre al campione finale delle BFS, un certo numero di altri oggetti singolari, che a un certo punto erano stati considerati candidate BFS, ma non sono riuscite a superare l'intera procedura di selezione. Abbiamo chiamato questi oggetti sorgenti di campo bianco fallite (Failed Blank Field Sources, FBFS), e le presentiamo nel Capitolo 2. Alcune di queste sono realmente BFS fallite, dato che hanno possibili controparti ad altre lunghezze d'onda a una distanza tra 4 e 2 raggi d'errore, mentre per altre proponiamo un'identificazione ottica o radio.

Nel Capitolo 3 esponiamo nuove osservazioni, ottiche e con il satellite Chandra, del campo che contiene la sorgente X ultra luminosa NGC 1313 X-2. In un immagine con il 3.6 m dell'ESO, il circolo d'errore di Chandra comprende un oggetto puntiforme di $R = 21.6$ ed esclude una controparte ottica precedentemente proposta. Il valore del rapporto tra i flussi nelle bande X e ottica è ~ 500. Il valore di f_X/f_{opt}, la storia della variabilità X e la distribuzione spettrale derivata da una rianalisi dei dati*ROSAT*, *ASCA* and *XMM* indicano una binaria X luminosa in NGC 1313 come probabile spiegazione per NGC 1313 X-2. Se la componente soft X osservata nello spettro dell'EPIC di XMM ha origine da un disco di accrescimento, la massa dell'oggetto compatto è $\approx 100 M_\odot$, rendendolo un buco nero di massa intermedia. La luminosità ottica derivata ($L \approx 10^5 L_\odot$) è consistente con quella di una compagna di $\approx 15 - 20 M_\odot$. Le proprietà dell'ambiente circostante NGC 1313 X-2 sono brevemente discusse.

Nel capitolo 4 riportiamo i risultati di un'osservazione profonda con XMM di RBS 1774, l'ultima candidata "stella di neutroni isolata fioca" trovata nei dati d'archivio di *ROSAT*. L'analisi spettrale e temporale dei dati di alta qualità del MOS e del PN confermano l'associazione di questa sorgente con una stella di neutroni isolata. Lo spettro è termico e simil-corpo nero, ed è provato ad un livello di significatività di $> 4\sigma$ che la sorgente sia una pulsar X, con periodo di rotazione di 9.437 s. Il fit spettrale rivela la presenza di una feature di assorbimento a ~ 0.7 keV, ma a questo livello i dati non hanno sufficiente risoluzione da permetterci di discriminare tra una linea in assorbimento o un edge. Paragoniamo le proprietà nuovamente misurate di RBS 1774 con quelle delle altre stelle di neutroni isolate fioche, e discutiamo delle possibili interpretazioni della feature di assorbimento.

Il capitolo 5 è una breve introduzione al fenomeno delle lenti gravitazionali (Gravitational Lensing) e alle sue applicazioni astrofisiche. Lo scopo è di rendere questa tesi autonoma, evitando di caricare i capitoli successivi con un eccesso di nozioni teoriche. Le lenti gravitazionali si dividono in forti, deboli e micro. Qui ci concentriamo solo sulle lenti forti e sul microlensing, dato che queste sono le linee di ricerca portate avanti nel resto della tesi, e in generale è favorita l'esposizione dei concetti di cui ci sia un reale bisogno in seguito.

Il capitolo 6 riferisce sullo stato di un lavoro *in fieri* sul microlensing che

stiamo svolgendo. In particolare, discutiamo lo stato dei database di eventi di microlensing ottenibili, alla luce delle release recenti delle collaborazioni MACHO, OGLE and EROS. Quindi analizziamo la significatività della distribuzione anomala di eventi in uno dei campi di MACHO, il campo 104, ed esaminiamo alcune ipotesi sull'origine dell'anomalia.

Fino ad ora sono noti rari esempi di galassia late-type che siano lenti forti. Essi sono preziosi per studiare tanto la distribuzione di massa di una galassia a spirale quanto la sua sezione trasversa per la divisione dell'immagine. Recentemente, una campagna osservativa basata sull'ottica adattiva del VLT dell'ESO, mirata all'osservazione delle galassie ospite di quasars distanti, ha scoperto una galassia a disco a $\sim$ 1.2 arcsec dal QSO Q0045-3337 (Falomo et al. 2005). Nel capitolo 7 discutiamo il possibile effetto della galassia come lente. Abbiamo eseguito la fotometria di superficie in due dimensioni sull'immagine VLT della galassia, confermandone la natura di spirale. Abbiamo quindi verficato se semplici modelli di massa, parzialmente vincolati dai dati osservati, richiedano parametri non realistici per produrre una seconda immagine del quasar, ancora nascosta. Abbiamo anche valutato la rispettiva probabilità di un'origine strumentale o dovuta a un effetto di lente per la deformazione del QSO osservata. Abbiamo trovato un'immagine residua dopo la sottrazione del modello di galassia, probabilmente non correlata con l'effetto di lente gravitazionale. I dati esistenti sono insufficienti sia per affermare la presenza di immagini multiple, sia per vincolare il numero delle immagini o per discriminare tra i modelli di massa della galassia. Ulteriori osservazioni sono d'obbligo per progredire nello studio di questo notevole sistema, che potrebbe fare un po' più di luce sul comportamento delle galassie a spirale come lenti.

Il materiale dei Capitoli 1 (eccetto che parzialmente per la Sezione 1.6), 2, 6 e 7 e dell'Appendice A è o pubblicato con me come primo autore, o originale, ma in ogni caso condotto principalmente da me. I Capitoli 3, 4 e le Appendici B e C sono basati su pubblicazioni a cui ho contribuito ma in cui non sono il primo autore. La Sezione 1.6 è basata sull'Appendice B ma è stata rielaborata da me per essere inclusa in questa Tesi. Il Capitolo 5 è una sintesi, scritta da me, di lavori esistenti sulle lenti gravitazionali, in particolare di quello di Jetzer (2002), integrata da qualche ulteriore dettaglio su modelli di massa rilevanti per le lenti forti e da qualche risultato aggiornato nel campo in rapida evoluzione del microlensing verso lo Sferoide Galattico.

Chapter 1

Blank Field Sources in the ROSAT HRI Brera Multiscale Wavelet Catalog [1]

1.1 Introduction

It is well known that one can discriminate among classes of X-ray sources evaluating the ratio between their fluxes in X-ray and optical bands (e.g. Maccacaro et al. [133]; Motch et al. [162]; Zickgraf et al. [262]), especially if some spectral information is supplemented. Blank Field Sources (BFS), i.e. X-ray sources with no optical counterparts, stand somehow apart from the bulk of X-ray zoology in that they represent rarer, less studied objects (e.g. Cagnoni et al. [35]). In particular, known X-ray sources concentrate at not too high values of f_X/f_{opt}, e.g., stars have $f_X/f_{opt} \lesssim 1$, galaxies and AGN reach f_X/f_{opt} of a few tens. At larger values of f_X/f_{opt}, peculiar populations start to show up: some examples are isolated neutron stars, type 2 quasars, extreme BL Lacs or high-redshift clusters of galaxies.

The search of BFS aims at objects with high f_X/f_{opt}: the observed X-ray flux and the upper limit from the absence of an optical detection establish a lower limit on the f_X/f_{opt}. A careful selection of bright BFS is therefore a powerful tool for finding population leftovers from usual source classes. The status of BFS is somehow a transitory condition that expresses our lack of knowledge on

[1] This chapter is an updated version of Chieregato, M., Campana, S., Treves, A., Moretti, A., Mignani, R. P. & Tagliaferri, G.: "Blank Field Sources in the ROSAT HRI Brera Multiscale Wavelet Catalog", 2005, A&A 444, 69. The changes made are the elimination of 1BMW043306.8+155307, now recognized as spurious, a slight enlargement of the discussion on transient BFS at the end of Section 1.5.1, and the addiction of the final paragraph 1.6. These improvements have been discussed in Treves, A., Campana, S., Chieregato, M., Moretti, A., Nelson, T. & Orio, M.: "Persistent and Transient Blank Field Sources", 2006, to appear in Ap&SS, in the proceedings of "Isolated Neutron Stars: from the Interior to the Surface", edited by D. Page, R. Turolla and S. Zane, astro-ph/0609194, reported as Appendix B.

the real nature of these sources. New X-ray observations can provide temporal and spectral information on BFS, while deeper optical/near IR pointings can either reveal the counterpart or establish a much stronger lower limit on the f_X/f_{opt}. With the aid of these information, BFS can be identified and classified properly.

In this paper we present a sample of luminous BFS from the ROSAT HRI Brera Multiscale Wavelet catalog (BMW-HRI: Panzera et al. [179]; Campana et al. [39]; Lazzati et al. [129]), with $f_X/f_{opt} \gtrsim 40$[2], along with archival X-ray spectral data from other observations (when available). This is the first study to exploit all ROSAT HRI data for BFS search (see Musso et al. [167] for the first search on a much smaller dataset). A key factor in the identification process is the uncertainty of the X-ray position (see Cagnoni et al. [35]; Rutledge et al. [207]); on this respect, the use of HRI rather than ROSAT PSPC images for searching BFS is much superior.

The paper is organized as follows: in Section 1.2 we briefly describe the BMW-HRI catalog and its cross-identification program with optical, infrared and radio catalogs, in Section 1.3 we introduce the method of sample selection, while the final sample of BFS is presented in Section 1.4. In Section 1.5 we discuss the possible nature of BFS. New observations and future search plans are mentioned in Section 1.6.

1.2 The BMW-HRI catalog

1.2.1 Catalog description

The BMW-HRI catalog (Panzera et al. [179]) is derived from an analysis of the ROSAT HRI data set with a source detection algorithm based on the wavelet transform (Lazzati et al. [129]; Campana et al. [39]).

The up-to-date version of the catalog contains 28998 entries, down to a count rate of $\sim 10^{-4}$ cts s^{-1}. The total sky coverage is 732 deg^2 ($\sim 1.8\%$ of the sky). For each entry name, position, count rate, extension and relative errors are provided, along with derived parameters like flux and Galactic column density and ancillary information about the pointing. Furthermore, results of cross-correlations with GSC2, 2MASS, IRAS, and FIRST catalogs are reported (see Section 1.2.2 and Table 1.1). In the following, some of the basic characteristics of the catalog are discussed in order to permit an understanding of the BFS selection method. Further details can be found in Panzera et al. ([179]).

Extension. The wavelet transform is particularly powerful in dealing with extended sources. In practice, each detected source is characterized by its extension, alongside with the more usual parameters (count rate and position). Extended sources, especially when observed at large off-axis angles, are often broken in various point-like sources by other detection algorithms. This risk is

[2] Actually this value is $f_{0.5-2keV}/f_{BJ}$, see Section 1.2.1

minimized by the wavelet transform.

Detection threshold and spurious sources. Each BMW-HRI source is characterized also by a detection probability value (peak significance). This value is the probability, in units of Gaussian σ, that the source is not spurious (i.e. a background fluctuation). This probability is the result of numerical simulations of random fields (without sources), repeated for different wavelet transform scales; it takes into account the number of background peaks mismatched as sources by the detection algorithm, for a given signal to noise ratio threshold in wavelet space. The mean number of spurious sources expected over an image is kept constant (0.4 spurious detections per field), varying the detection threshold. That is, the detection threshold depends on the mean background counts value on the image and on the scale at which the search is performed (see Lazzati et al. [129]). The mean threshold value in the overall catalog is $\sim 4.2\sigma$.

Errors. In principle, the error for each parameter found with the wavelet transform algorithm can be estimated from the covariance matrix. In practice, such errors are reliable only when the number of source and background counts are sufficiently high ($\gtrsim 2 \times 10^{-2}$ counts per pixel). Otherwise, the distribution of the wavelet transform coefficients becomes Poissonian rather than Gaussian (in the lowest scales). If this is the case, a better estimate of the errors can be given by means of basic statistics (such as the error on the number of counts N is $\sqrt{N}$, for more details see Lazzati et al. [129]). The errors reported here and in the catalog are the maximum between the covariance matrix and the statistical estimates by Lazzati et al. ([129]).

Boresight correction uncertainty. There is an additional source of errors on the absolute position determination of HRI sources, the uncertainty on the boresight correction. If the alignment between the node and the telescope optical axis is perfect, on-axis images are exactly in the center of the instrument. However, in the real situation there is always a finite misalignment that needs to be corrected. Unfortunately, uncertainties in the aspect solution (that describes the orientation of the telescope as a function of time) and errors in the alignment between the star trackers and the ROSAT X-ray Telescope introduce uncertainties in the boresight correction, of variable size for each observation. In practice, the systematic offset between accurately known optical positions and X-ray positions can be used to evaluate the extent of boresight correction uncertainties. For the ROSAT HRI, the offset can be as large as $10''$, even if in most cases it will be much less (David et al. [55]). The $10''$ value is conservatively assumed as a fiducial value for the boresight offset. Usually, the statistical errors on the position from the detection algorithm, calculated as in the previous section, are much less than $10''$ and therefore can be neglected in a first approximation.

Multiple detections. As each pointing is treated separately, not all of the catalog entries correspond to independent sources. An estimate of the overall number of independent sources can be given compressing the catalog in a $10''$

radius (again, the fiducial error value indicated by the boresight uncertainty). This procedure selects only a source for each $10''$ cone radius, on the basis of an autocorrelation of the position. With this procedure, 20433 sources are left. Obviously, the compression brings to the loss of sources truly close to each other.

1.2.2 Multiwavelength catalog cross correlations

In the following, we will largely use the term *off-band* to indicate a wavelength passband different from X-rays. The limiting flux of a given catalog in a given band will be generically denominated $f_{\rm offband}$. For each of the BMW-HRI entries, cross correlations with GSC2 (McLean et al. [143]), 2MASS Second Data Release (Kleinmann et al. [124]), IRAS Point Source Catalog (Beichman et al. [14]) and FIRST Survey Catalog (White et al. [242]) were performed by Panzera et al. ([179]). Off-band catalog properties are summarized in Table 1.1. The adopted radius for the cross-correlation is $10''$ (see Section 1.2.1), assumed as positional X-ray uncertainty. In fact, the positional uncertainties for GSC2, 2MASS SDR and FIRST catalogs are $< 0.5''$ (3σ, McLean et al. [143]), $< 0.5''$ (1σ, see the 2MASS documentation for an extensive discussion), $< 0.5''$ (90%, McMahon et al. [145]) respectively, so that they can be safely neglected for cross-identification purposes. An exception is the case of IRAS PSC, for which the positional accuracy varies with source size, brightness and spectral shape and it is different in different directions, but it is usually better than $20''$ (see Beichman et al. [14]), so this last value has been used as cross-correlation radius with this catalog. Note that: a) when two or more entries in the correlating catalog are found, only the brightest source parameters are reported (but in any case the number of found sources is given), b) the sky coverage of the off-band catalogs is usually not complete (see again Table 1.1). In particular, the preliminary, unpublished version of the GSC2 (GSC2.3) catalog used in Panzera et al. ([179]) lacks coverage of the zones where a bright source caused an overexposure of the Schmidt plates. For the 2MASS and FIRST, more complete catalogs are now available (2MASS All Sky Data Release, FIRST Survey Catalog 03Apr11 Version). Our final list has been checked with them.

1.3 Sample selection

1.3.1 Catalog mask

The first sample selection was made on the basis of the following criteria:

a. blank field sources, i.e. without any cross identification in the other databases (see Section 1.2.2 and Table 1.1): 6061 catalog entries;

b. point-like sources (significance of the extension=0): 4955 catalog entries;

c. bright sources, i.e. with $f_X \geq 2.7 \times 10^{-13}$ erg s^{-1} cm^{-2}: 275 catalog entries.

Table 1.1 BMW-HRI cross-identifications.

Catalog	Survey	Band	Coverage	Depth
GSC2	POSSII	BJ	Dec: > 0	22.5
(prel.)	"	R	Dec: > 0	20.8
	"	I	Dec: $> 0^*$	19.5
	SERC	BJ	Dec: < 0	23
	" +AAO	R	Dec: < 0	22
	"	I	Dec: $< 0^*$	19.5
2MASS SDR	2MASS	J	50% sky	15.8
(2000)		H	50% sky	15.1
		K	50% sky	14.3
IRAS PSC	IRAS	12 μm	98% sky	0.4 Jy
(1989)		25 μm	98% sky	0.5 Jy
		60 μm	98% sky	0.6 Jy
		100 μm	98% sky	1.0 Jy
FIRST SC	FIRST	1.4 GHz	20% sky	$\sim$ 1 mJy
(2001)				

* work in progress.

The reported numbers are catalog entries, i.e. no compression was applied to eliminate multiple detections (see Section 1.3.2 below). The f_X we used is computed from the observed source counts, in the 0.5-2 keV range, considering only channels 2-9 (e.g. David et al. [55]). The assumed spectral shape is a power law with photon index Γ=2 (i.e. the same of the Crab pulsar and nebula) and column density 5×10^{19} atoms cm^{-2} (parameter # 48 in the BMW-HRI catalog). The chosen model for the count rate-flux conversion uses constant negligible column density, instead of the integrated Galactic one in the source direction. While the latter is commonly adopted in extragalactic surveys, it would introduce a larger error on low-latitude galactic BFS, which are expected to be low-luminosity, nearby objects (see Section 1.5). Furthermore, the chosen f_X derived with this choice is lower than the one with Galactic N_H, so the obtained $f_X/f_{offband}$ limit is lower. We chose to select sources on the basis of f_X and not of, for example, f_X/f_{BJ}. This brings naturally to different $f_X/f_{offband}$ ratios for sources in different parts of the sky, due to the variable depths of the surveys available to us. However, in such a way the selection is based on a directly observed quantity, the number of counts, not on the basis of a non-detection, and it provides a more homogeneous sample for future observations. We carefully evaluated the $f_X/f_{offband}$ keeping into account the different depths and photometric band used in the different catalogs. The obtained lower limit for the f_X/f_{opt} from the GSC2 catalog are $f_X/f_{BJ} > 37$ (Northern sky), $f_X/f_{BJ} > 59$ (Southern sky), $f_X/f_{RF} > 43$ (Northern sky), $f_X/f_{RF} > 129$ (Southern sky). A detailed description of method and used values can be found in Appendix A.

In conclusion, at odds with the majority of similar studies, our sources are blank at various wavelengths (see again Table 1.1). We note also that, although we selected point-like sources, we cannot exclude that the real nature of some

source is extended (i.e. only the brightest peak has been detected with HRI).

1.3.2 Multiple detections removal

The removal of multiple detections from the sample could be done, in principle, using automatic compression criteria (position based), like in Section 1.2.1. However, given the limited size of our sample of BFS candidates (275 elements), we preferred to remove multiple detections by hand to avoid, when possible, the loss of sources truly close to each other.

We used positional coincidence as the main criterion for identifying multiple detections. Another useful piece of information was the flux level. Unfortunately, positional coincidence can be weakened by the boresight uncertainty, while obviously the flux criterion is not fulfilled for highly variable sources. In practice multiple detections were reasonably identified in most of the cases. After multiple detections removal, we are left with 226 catalog entries.

1.3.3 Total counts cut

We made a further screening on the number of total counts, rejecting sources with less than 25 photons (on the original detection, i.e. before applying vignetting and Point Spread Function loss corrections). This has been done in order to strengthen the derived source parameters (obviously, due to the statistics increase). After the total counts cut, we are left with 201 sources.

1.3.4 Are the BFS sources real?

We re-evaluated the number of spurious sources expected in this 201 subsample, again on the basis of simulations of random fields with the above masks. In particular, the flux cut is very effective in the removal of spurious sources. In fact, the expected number of spurious source is ~ 2 in the 201 subsample (see Moretti et al. [157]). Our BFS are therefore likely not to be fake detections.

1.3.5 Visual inspection: when a blank is not a blank

We inspected Digitized Sky Survey 2 (DSS2; McLean et al. [142]), Super Cosmos Sky Survey (SSS; Hambly, Irwin & MacGillivray [97]), 2MASS, FIRST, Sydney University Molonglo Sky Survey (SUMSS; Bock, Large & Sadler [25]), NRAO VLA Sky Survey (NVSS; Condon et al. [51]) and Westerbork Northern Sky Survey (WENSS; Rengelink et al. [203]) images for each of the 201 sources left. Furthermore, we cross-checked source positions with Simbad, NED and with the VIZIER catalogs (in particular the USNO-B1.0 catalog, Monet et al. [154]). We excluded from the sample sources and fields already known and well studied or too complex (e.g. Magellanic Clouds, M31, Orion Nebula). We excluded also sources positionally coincident with bright stars (holes in the GSC2 coverage), or at the periphery of optically extended emission (more than $10''$ from the centroid

and so escaped the automatic cross-identification). We found, and excluded, some cases in which our X-ray sources coincided with reliable USNOB1.0 entries (the criteria for the GSC2 detection are somewhat more conservative), or with counterparts at other wavelengths (IRAS Faint Sources Catalog, Moshir et al. [161]). We prefer not to be too severe at this stage, deferring strict cuts after the boresight correction. 72 sources survived this phase.

1.3.6 Cheshire cat: elimination of fluctuations

We put aside from the primary sample sources which have not been detected in a longer HRI or ROSAT PSPC pointing (the PSPC had the same passband but a substantially larger effective area than the HRI). These could be variable sources detected at peak flux, but they are also candidates for false detections. No source has been inserted in this subclass on a non-detection basis with other instruments, because of the different passband, i.e., given the absence of spectral information on our sources, the non-detection could be ought to a peculiar spectral shape. For some sources the suspicion of a false detection is strengthened by the number of non-detections or by the respective length of the pointings. However, there are cases for which source parameters like detection probability and number of counts seem to indicate a real source. Furthermore, as discussed in Section 1.3.4, we expected only ~ 2 spurious detection in 201 sources. Of the 72 sources, 16 were placed in this transient candidate sub-sample, while for the other 56 there was no evidence of a transient nature.

1.3.7 Pin-pointing the sources to the sky: boresight correction

We performed some astrometry on the remaining fields (including those of transient candidates), in order to get rid of the $10''$ fiducial boresight uncertainty and therefore to fully exploit the HRI angular resolution capability. Furthermore, the error given by the detection algorithm (see Section 1.2.1), while not being entirely statistical, can be as a first approximation treated as random, so that the usual Gaussian relations can be used. In contrast, the offset given by the boresight uncertainty varies in a random way in the ensemble of all the pointings, but is systematic in nature for all the sources in the single pointing, weakening the rejection of distant optical associations to BFS.

For each pointing, we matched X-ray sources to optical counterparts (optical positions of known X-ray emitters), if any, or to optical catalog sources distant less than $10''$. We excluded X-ray extended sources and sources with no optical catalog entry in $10''$. Ambiguous cases, i.e. with two or more optical sources present, were treated individually using the distance and the optical luminosity as criteria for the identification and then checked a posteriori. Even if only another X-ray source was present, the shift for this source has been applied to the pointing, although obviously in these cases the corrected positions and uncertainties have to be taken *cum grano salis*. Generally, the new error is less

than $10''$; even if it remains around $10''$, the new position should be free from systematic boresight uncertainty. Note that performing the boresight correction only after the selection of Section 1.3.1 can bring to the loss of BFS. However, this allows us to deal with a limited number of sources and boresight corrections.

1.4 The data

The elimination of sources with an off-band counterpart in a 4σ radius from the boresight corrected position left us with our final sample of three sources (two of them transient candidates)[3]. This 4σ limit assures us that starting with 1340 sources (i.e. sources outside the inner $3'$ in the BMW-HRI catalog and obeying to the cuts above unless the lack of counterparts), only 0.08 of them would lie outside the error region by chance.

In summary, our final BMW-HRI Blank Fields Sources are:

- Blank: no counterpart at other wavelengths in a 4σ radius from the boresight corrected position.
- Bright: $f_X \geq 2.7 \times 10^{-13}$ erg s^{-1} cm^{-2}. Note that from the GSC2 magnitude limit, this is equivalent to f_X/f_{BJ} respectively ≥ 37 and ≥ 59 for Northern and Southern sources.
- Point-like: extension significance is 0.
- Well detected: total (uncorrected) counts ≥ 25.

After this selection we end up with one persistent BFS plus two transient BFS[4]. We report the new positions and error radii (as obtained from the boresight correction procedure), the flux, the detection probability (i.e. the probability to detect a background fluctuation as a source), the total number of counts, the Galactic coordinates, the integrated Galactic column density, the distance from the nearest off-band association (in terms of error radii), the lower limit on the f_X/f_{BJ} and the upper limit on the radio emission (see Table 1.2). Note that, though with different depth, all but one (1BMW200739.8-484819) of the sources have a radio flux upper limit.

[3] A third transient, 1BMW043306.8+155307, was eliminated after the publication of the paper, because a careful further analysis showed that its detection was due to an instrumental defect in the HRI

[4] see the above note

Table 1.2 BFS parameters.

Name	R.A.	Dec	bII	Err. rad.	Flux	Prob.	Cts	N_H	f_x/f_{BJ}	Close ass.
	J2000	J2000		$''$	erg cm^{-2} s^{-1}	σ		10^{20} cm^{-2}		(sigma)
1BMW042142.4-571541	04 21 42.6	-57 15 39	-42.54	2.9	6.5×10^{-13}	14.0	742	1.8	>141	5.3
1BMW135703.0+181122	13 57 02.7	+18 11 22	72.45	7.1	3.5×10^{-13}	4.2	112	2.1	>47	6.3
1BMW200739.8-484819	20 07 39.9	-48 48 19	-32.31	5.8	3.0×10^{-13}	4.3	55	5.1	>65	5.2

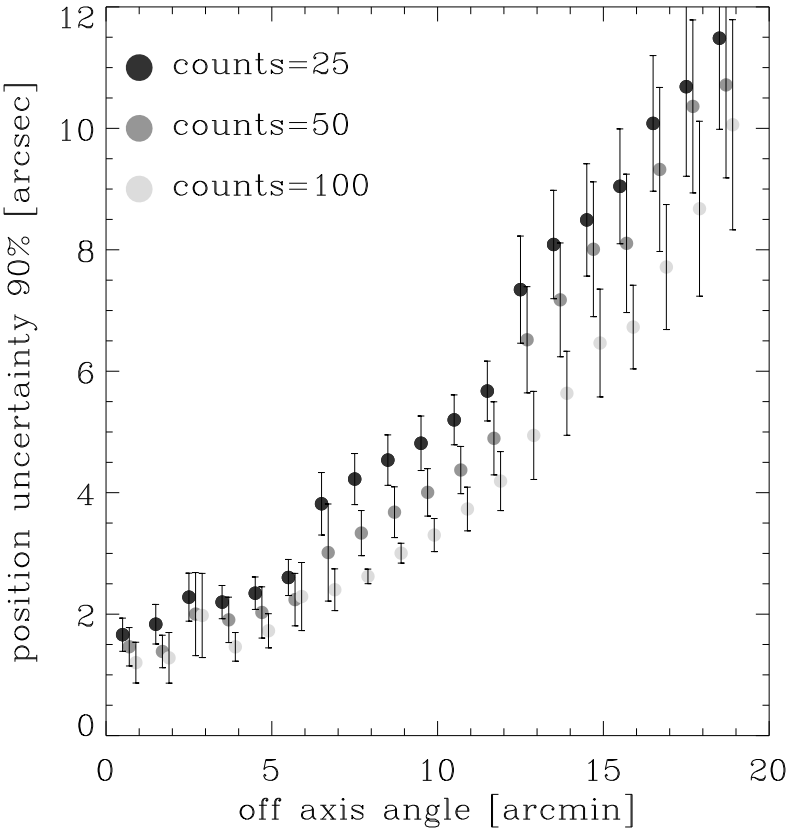

Figure 1.1 BMW-HRI position error: the statistical errors on position of BMW-HRI sources for different number of counts as a function of the off-axis angle. Error bars are at 2σ. The change in the slope of the curves corresponds to angular resolution loss at the change of image rebinning. An offset of $0.2'$ and $0.4'$ has been applied to points in the 50 counts bin and 100 counts bin, respectively, for visualization purposes.

1.4.1 Properties of BFS

The final error radius estimate for our sources is quite different from case to case, ranging from $\sim 3''$ to $\sim 7''$; the latter large error is due to the large off-axis angle and to the low number of counts (see Figure 1.1). In fact, all our sources are quite offset from the center of the pointing ($> 15'$). This depends from the used selection procedure and needs some comments. First, we concentrate on the consequences of the requirement of absence of offband counterparts in a $10''$ radius. This affects strongly the overall distribution in detector coordinates. In fact, the fiducial $10''$ radius for the initial correlation, chosen to match the worst

case boresight error, is huge in comparison to the statistical positional error for the innermost sources, but it corresponds to the intrinsic error for the outermost sources (see Figure 1.1). Sources in the innermost part are preferentially associated with optical counterparts which may not be the true ones, since they have been searched for over a region much larger than their error boxes. The overall effect is to deplete the distribution from inner sources, enhancing the proportion of outer sources. This bias is present independently of the real size of the boresight correction error. Second, there is a trend in overestimating outer source counts (especially at low values), since it is favorable to detect them on top of a positive background fluctuation (an effect known as Eddington bias, see Hasinger et al. [100]; Moretti et al. [155]). This again adds on the enhancement of outer sources. The first bias leads to the loss of BFS, but it does not affect our selected sources. The effect of the second bias on the estimated flux can be evaluated a posteriori from the duration of the pointings and the number of counts. Very conservative assumptions give a factor of ~ 2 as the maximum overestimate.

1.4.2 1BMW042142.4-571541

This source is the brightest of our sample and the one with the highest number of detected photons. The good statistics involves a small detection algorithm error radius, so the position determination is quite accurate (see Figure 1.2). The boresight correction was performed with the known position of the quasar HE 0419-5657 and the nucleus of NGC 1547 as well as with other eleven sources matched to optical catalogs. The source is close ($\sim 15''$ but actually more than 5 σ) to a bright star (BJ=13.31, F=11.61 in the GSC2.2); this makes less reliable the lower limit on the f_X/f_{opt}, in particular in the red band. There are two fake USNO B1.0 sources along the saturation spikes of the bright star (see Figure 1.2). The source was observed with Einstein (1E 0420.7-5723) and with the ROSAT PSPC (1WGAJ0421.7-5716) and was also detected as a RASS Bright Source (1RXS J042144.0-571601). The WGA computed flux is 8.8×10^{-13} erg cm^{-2} s^{-1}, consistent with the RASS count rate. Taking into account the caveats on the count rate to flux conversion, this could mean that there is no evidence for long term flux variations.

We re-extracted the archival PSPC observation of this source (sequence rp700034n00). The source was very close to the PSPC rib; despite this, we attempted a rough spectral analysis. We extracted source photons from a circle of radius $200''$ centered on source position. We used as background region a circle of radius $240''$, centered in an empty region south of the source. The collected counts were 321. We rebinned channels by a variable factor in order to have at least 20 photons in each bin. Channels 1-11 and 136-256 were ignored. Figure 1.3 shows the resulting spectrum, which we then fitted with XSPEC (v.11.2). Due to the poor statistics, we considered a limited number of models, as shown in Table 1.3. The spectrum is definitely soft, without evidence of absorption

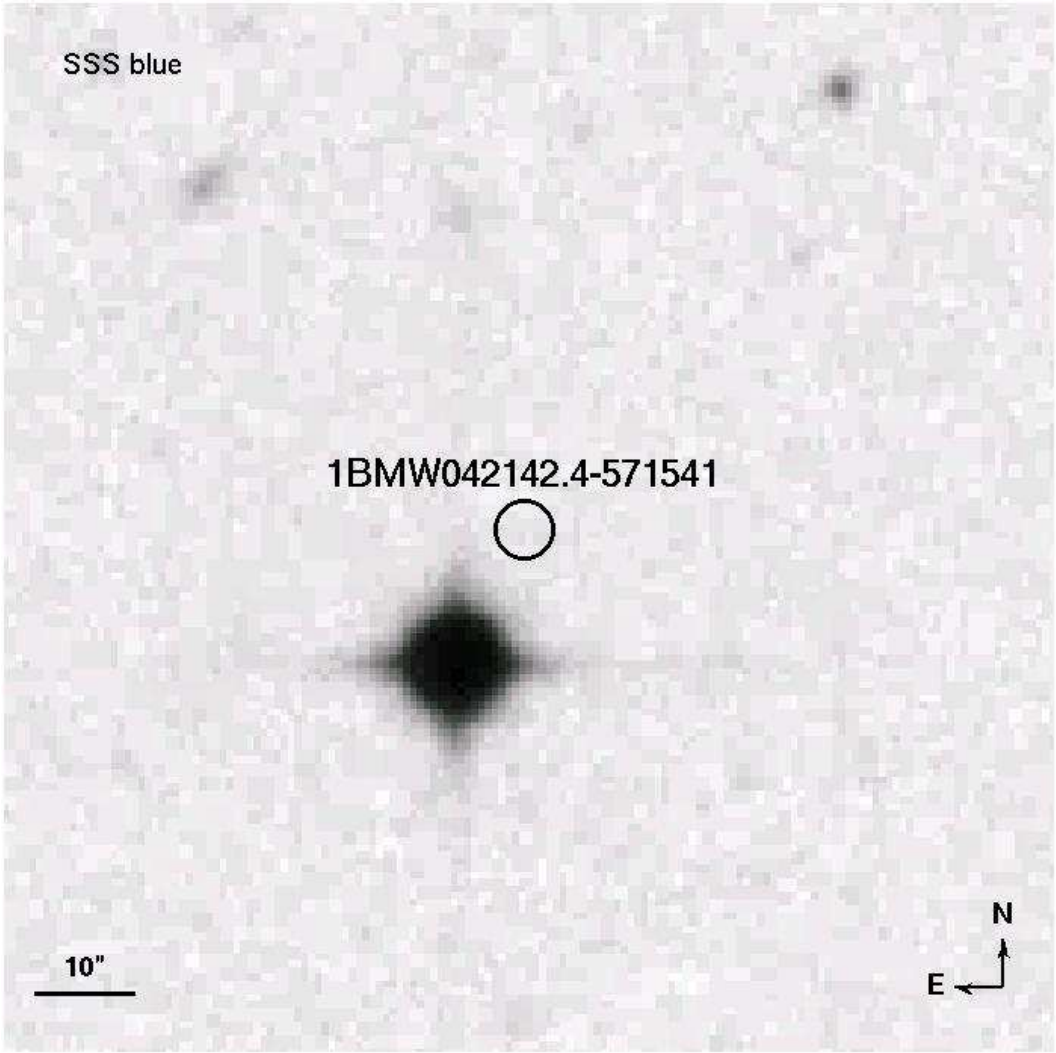

Figure 1.2 The X-ray position of 1BMW042142.4-571541 superimposed to the corresponding blue image along with its 1σ error circle.

excess. The best fit absorbed blackbody model tends to null absorption, with a 90% upper limit on column density of $\sim 3 \times 10^{19}$ atoms cm^{-2}. The power law fit gives a relatively better reduced χ^2 (1.3 versus 1.4). Furthermore, the best column density value is quite close to the integrated Galactic value of 1.2×10^{20} atoms cm^{-2} (see Figure 1.3). Freezing absorption at the Galactic value, the reduced χ^2 does not change appreciably. The bremsstrahlung fit gives the best reduced χ^2 (1.3) and the column density is $\sim 1.3 \times 10^{20}$ atoms cm^{-2}.

Table 1.3 Spectral fits for PSPC observation of 1BMW042142.4-571541.

Model	N_H	kT /Γ	Flux(0.1-2 keV)	$\chi^2_{\rm red}$
	10^{20} cm^{-2}	keV	10^{-13} cgs	
B.body	$0^{+0.3}$	$0.19^{+0.02}_{-0.02}$	5.6	1.4
B.body	1.8(frozen)	$0.15^{+0.02}_{-0.01}$	6.9	1.9
Pow.-law	$1.8^{+1.8}_{-1.4}$	$1.8^{+0.7}_{-0.6}$	6.5	1.3
Pow.-law	1.8(frozen)	$1.8^{+0.2}_{-0.2}$	6.5	1.2
Bremss.	$1.3^{+1.0}_{-0.9}$	$1.46^{+14}_{-0.77}$	6.2	1.3
Bremms.	1.8(frozen)	$1.03^{+0.49}_{-0.25}$	6.2	1.2

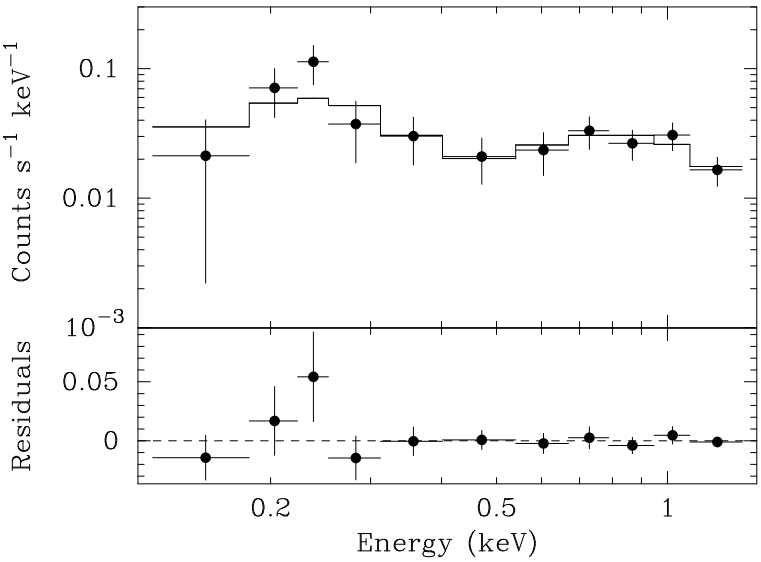

Figure 1.3 Power law spectral fit of the PSPC observation of 1BMW0421.4-571541.

1.4.3 Transient BFS

In this section are presented two sources (see Table 1.2) that, while fulfilling all the others criteria for BFS, show additional strong evidence of a transient behaviour. In fact, despite their brightness in the BMW-HRI catalog ($f_X \geq 2.7 \times 10^{-13}$ erg s^{-1} cm^{-2}), for each of them there is at least another ROSAT

HRI or PSPC pointing where they have not been detected (deeper than the HRI exposure that revealed them).

1BMW135703.0+181121. 1BMW135703.0+181121 has been detected in a $\sim$ 5.5 ks HRI pointing in Jan. 1998; we included it in the possible transient sub-sample since it has not been detected in three longer PSPC pointings ($\sim$11.4 ks, Jan. 1992; $\sim$8 ks, Jul. 1990; $\sim$5.6 ks, Jul. 1992; also it was not seen in a shorter $\sim$1.1 ks HRI pointing in Jan. 1992). The high number of counts detected points toward a real, transient source. The boresight corrected position has been obtained with three sources. There are no counterpart at other wavelength in a $45''$ radius ($\sim 6.3\sigma$, see Fig. 1.4).

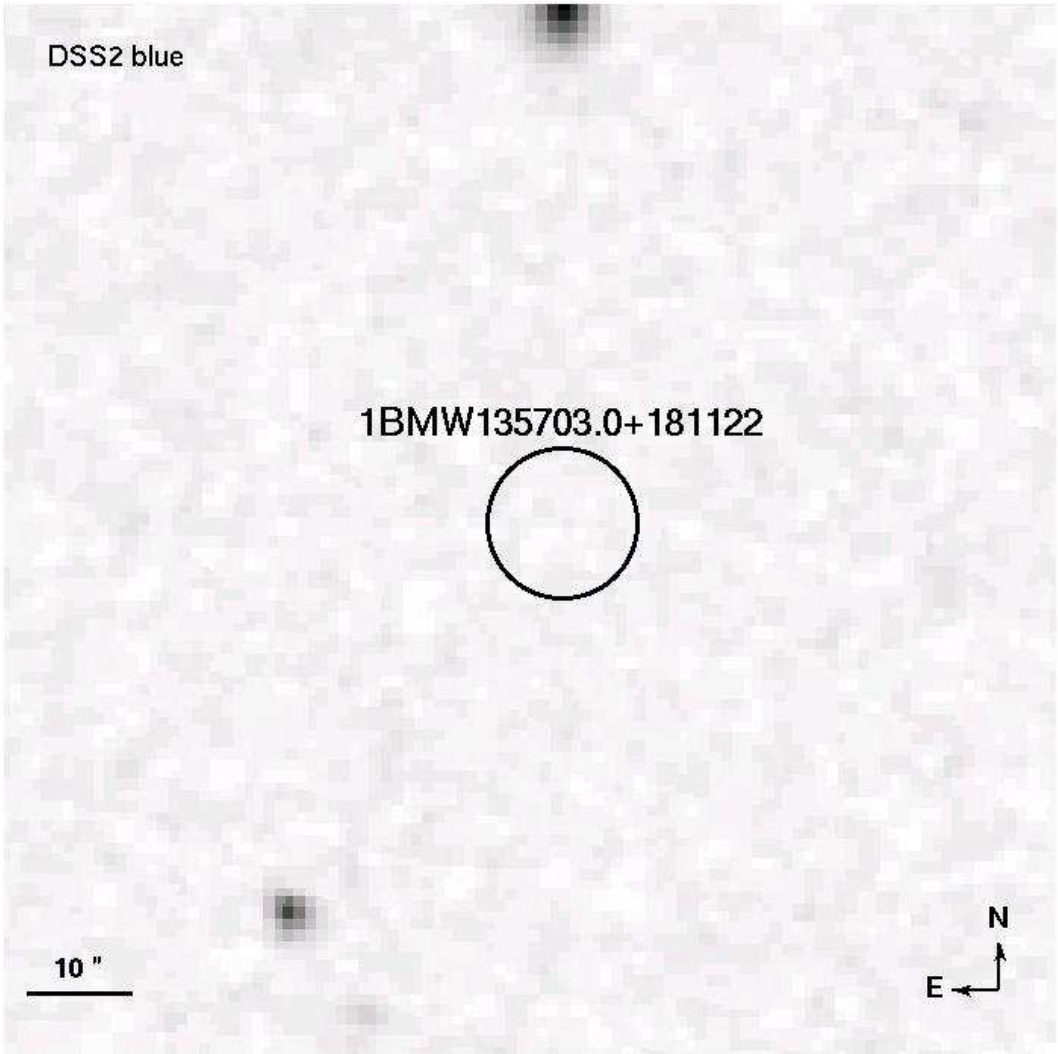

Figure 1.4 The X-ray position of 1BMW135703.0+181121 superimposed to the corresponding blue image along with its 1σ error circle.

1BMW200739.8-484819. This source has been detected in a $\sim$ 3.2 ks pointing in Oct. 1996, while no corresponding source was observed in four other pointings of comparable length (2.6-3.6 ks) at distance of $\sim$ days, nor in two $\sim$ 11 ks ROSAT PSPC pointings in Nov. and Apr. 1992. The closest optical catalog source is at more than $30''$ (see Figure 1.5) from the boresight corrected X-ray position (the boresight correction has been performed with the other two X-ray sources detected in the Oct. 1996 HRI pointing). Two objects, A and B in Figure 1.5, are clearly visible in the blue SSS image, respectively at $\sim 16''$ ($\sim 2.7\sigma$) and $\sim 13''$ ($\sim 2.3\sigma$). Object B (BJ=22) is reported to be extended, object A (BJ=22.3) is possibly extended too. Oddly, while nothing is apparent at that position in the red SSS image, a source can be seen both in the shallower ESOI RED image and in the SSS I image, at a position almost coincident with object B, with RF=20.2 (more than 2 mag brighter than in the Schmidt plate limit) and IN=19.0. An obvious hypothesis could be the presence of an optically variable source, that perhaps could be identified with 1BMW200739.8-484819.

1.5 Discussion: nature of the blank fields

In order to proceed further with hypotheses on BFS nature we need to compare the f_X/f_{BJ} limits of BFS with existing classification schemes. We chose as a reference scheme the one of the RASS-Hamburg optical identification program (Zickgraf et al. [262]), which uses similar X-ray (0.1-2.4 keV) and optical (Johnson B) bands. We converted the RASS-Hamburg limits (see Table 6 of Zickgraf et al. [262]) to BMW-HRI and GSC2 f_X/f_{BJ} (the deepest GSC2 band), keeping into account the different X-ray energy band and spectral shape used for flux evaluation, and the different optical band. The resulting classification scheme is shown in Table 1.4 (see Appendix A for details about the conversion). The f_X/f_{BJ} lower limits of BFS, $\simeq 37$ in the Northern sky and $\simeq 59$ and in the Southern sky (due to different GSC2 depth, see Table 1.1), are a factor of ~ 2 and ~ 3 beyond the limits of our reference values for different classes, respectively. This points out the possibility that BFS are unusual objects, left outside from classifications, or at least very peculiar members of the more ordinary categories.

Table 1.4 f_X/f_{BJ} for various classes of sources, adapted to BMW-HRI fluxes and GSC2 BJ band.

Class	Lower limit	Upper limit	B-V
Stars	1.3×10^{-5}	0.6	-0.5÷2
White Dwarfs	1.2×10^{-5}	9.3×10^{-4}	-0.3÷1.5
Cat. var.	1.8×10^{-2}	4.7	-0.1÷1
Galaxies	3.1×10^{-2}	11.1	0.4÷1.5
Gal. clusters	0.2	16.9	1.0÷1.5
AGN (w. BLLacs)	0.2	12.0	-0.5÷1.5

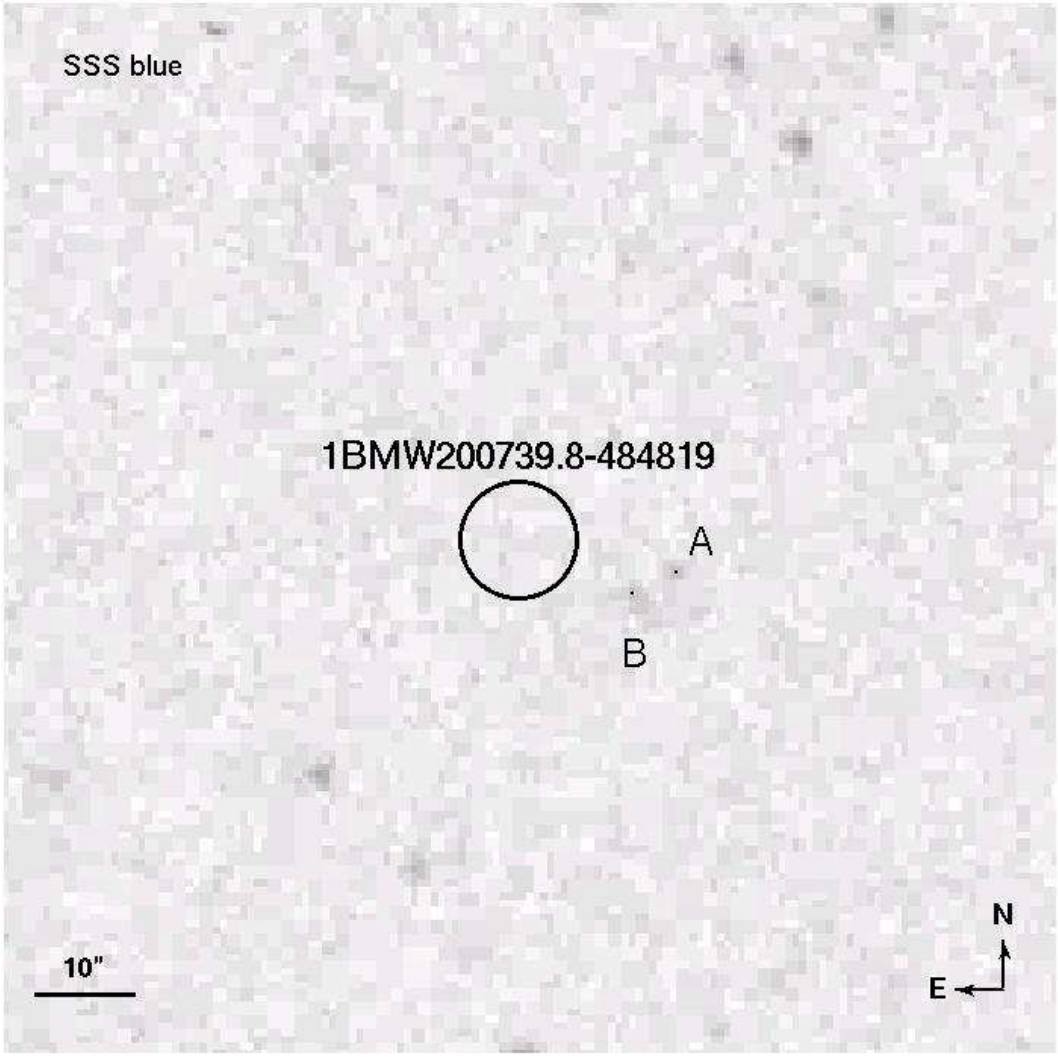

Figure 1.5 The X-ray position of 1BMW200739.8-484819 superimposed to the corresponding blue image along with its 1σ error circle.

1.5.1 BFS as unusual sources

It is well known that some rare class of sources can reach extreme values of f_X/f_{opt} (see Cagnoni et al. [35]). Here we will focus on our specific sample and discuss the possibility that our BFS belong to the following categories:

a. Isolated Neutron Stars (INS).

b. X-ray binaries.

c. High Redshift or Dark Clusters of Galaxies.

d. Type 2 Quasars.

e. Extreme BL Lac.

Isolated Neutron Stars. Isolated Neutron Stars (INS; see Treves et al. [226], Haberl [88], Haberl [89]) are extreme BFS. The bona-fide f_X/f_{opt} lower limit used to assess their nature is 1000, but for optically identified objects the real value can be as high as 10^5. The X-ray spectrum is optimally fitted by a black body with kT$\sim$60-100 eV. The optical emission lies a factor of a few over the Rayleigh-Jeans tail of the blackbody and no emission outside the optical/soft X-ray range has been found. The low column densities from the X-ray spectra and the parallax measured distance for RXJ1856.5-3754 (Walter & Lattimer [240]) makes this source an intrinsecally faint and closeby object, probably emitting from the neutron star surface.
Different kind of isolated neutron stars can also reach high f_X/f_{opt} values: Anomalous X-ray Pulsars (AXP; Israel, Mereghetti & Stella [107]), close-by radio pulsars with substantial cooling X-ray thermal emission (e.g. PSR 0656+14) and Geminga-like objects (Bignami & Caraveo [18]). AXPs are young, luminous and distant objects and should be much closer to the Galactic plane than our BFS. The radio limit, though not strong, argue against close-by cooling radio pulsars. This does not apply to Geminga-like neutron stars for which the radio emission is only marginal. Converting the X-ray flux of Geminga to the HRI pass-band and using V=25.6, yields $f_X/f_V \sim 67$, making it consistent with our BFS candidates. In the cooling framework, the same physical mechanism is at the basis of INS emission and of the soft thermal component of young radio pulsars and Geminga-like objects. Basing on this scenario, Popov et al. ([192], [193]) produced the log N-log S of cooling neutron stars (all the three categories), allowing us to estimate that only ~ 1 unidentified INS is expected for our flux and sky coverage. If our steady BFS (1BMW042142.4-571541)) is an INS, no optical counterpart could be revealed up to the $\sim$ 28 mag; therefore, this possibility could be strengthened by the absence of optical sources in deeper observations, reaching the critical f_X/f_{opt} lower limit of 1000, corresponding to magnitude $\sim$ 25-26, together with a better position from Chandra. At the same time the well-defined properties of the X-ray emission could be tested by observations

with an instrument with sufficient soft response, like the XMM-Newton EPIC pn camera.

X-ray binaries. Some kind of X-ray binaries can reach high values of f_X/f_{opt}. In particular, BFS searches have already discovered Ultraluminous X-ray Sources (ULX; e.g. Cagnoni et al. [36]). However, the observed flux level of BFS is too low for a Galactic object and none of our BFS can belong to nearby galaxies, excluding ULXs, supersoft sources and bursting LMXBs. Therefore, we consider unlikely known classes of X-ray binaries (see however the discussion on possible transients).

Clusters of Galaxies. BFS research has already been effective for the discovery of clusters of galaxies since Cagnoni et al. ([34]). Furthermore, several distant clusters have already been discovered in the BMW-HRI catalog as extended objects (Moretti et al. [157]). Distant clusters may escape this selection if only the X-ray peak is bright enough to be detected, resulting in a point source, while the rest is concealed in the background. This effect is strongly favoured at large off-axis angle (and consequent PSF degradation) like those at which BFS are detected. Therefore, if some BFSs are galaxy clusters, we expect them to be at quite high redshift. The f_X/f_{opt} of clusters of galaxies is the highest among the X-ray emitting classes of Table 1.4. For normal galaxy clusters, the values reached are usually lower than those of BFS (and if only the peak of the X-ray emission is computed, the resulting f_X/f_{opt} is further lowered). Despite this, there are two effects that could boost the f_X/f_{opt}. The first, and more effective, is the redshift of the optical emission. In fact, for a redshift of 0.75, the 4000 Å break of the cD galaxy (or of any early type galaxy of the cluster) would be redder than the GSC2 F band. Even a lower redshift could result in a sufficient enhancement of the f_X/f_{opt}. Second, the X-ray peak could be not coincident with the optical one (if the cluster is not virialized, or if there is no cD galaxy, like in Bautz-Morgan type III clusters, or if there is a central cooling flow). Optical-near IR deeper observations should reveal a substantial increase of galaxy counts in proximity of BFS and, if there is any, the cD galaxy of the cluster. An even more strong test would be X-ray observations with Chandra or XMM-Newton, that should reveal an extended source.

BL Lacs. BL Lacs stand somehow apart from the bulk of AGNs in that they can reach high f_X/f_{opt} values. The unified spectral energy distribution of BL Lacs (Fossati et al. [74]; Ghisellini et al. [77]) can be described by a two peak emission, in which the lower energy peak (radio to X-ray) is commonly ascribed to synchrotron emission, while the high energy peak (X-ray to γ-ray) is probably due to inverse Compton emission. In this scenario, different BL Lacs are distinguishables on the basis of the shifts of the peaks, creating the so-called blazar sequence. By tuning the position of the peaks, it is possible to produce the old categories of X-ray selected and radio selected BL Lacs, the former being those capable of high f_X/f_{opt} values.

In order to check the viability of BL Lacs hypothesis for BFS we consider the different α_{xo} (the power law index connecting the X-ray flux to the optical flux) and α_{xr} (the power law index connecting the X-ray flux to the radio flux) for Einstein Slew Survey BL Lacs (Perlman et al. [184]) and the upper limit for BFS. Despite the poor radio limits, the locus occupied by BFS is partially superimposed to the most extreme Slew BL Lacs, with the brightest BFS, 1BMW042142.4-571541, exhibiting an α_{xo} limit substantially lower. If these objects were indeed BL Lacs, they would probably stretch the sequence in the α_{xo}-α_{xr} plane, representing a still undiscovered extreme population. The identification of the optical and possibly of the radio counterpart would be very important for testing the BL Lac hypothesis. In this case, further X-ray observations should show a power law spectrum without evidence of absorption excess.

Type 2 Quasars. Evidences for a substantial population of type 2 Quasars, as requested by unification models (Urry & Padovani [234]; Comastri et al. [50]), has been continuously increasing in the recent past. In particular, the resolution of the largest fraction of the cosmic X-ray background in discrete sources (Hasinger et al. [101]; Mushotzky et al. [166]; Campana et al. [40], Giacconi et al. [78], Moretti et al. [156], Brandt & Hasinger [30]) has brought to infer the existence of an adequate number of highly absorbed and luminous AGNs, responsible for the hard part of the background. Up to now, while only a few type 2 quasars have been firmly identified (e.g. Stern et al. [217]; Norman et al. [173]), many candidates are being produced either by deep fields, pencil beam searches (Chandra Deep Field North, Barger et al. [13]; Chandra Deep Field South, Szokoly et al. [223]; Lockman Hole, Mainieri et al. [134]), or by dedicated shallower surveys, with a substantial sky coverage (Hellas2XMM, Baldi et al. [10]; ChaMP, Green et al.[83]; SEXSI, Harrison et al. [99]; BMW-Chandra, Romano et al. [206]). The most striking characteristic of type 2 quasars is the severe absorption excess. In particular, this makes them Extremely Red Objects, with R-K$>$ 5. Therefore, if some BFS are type 2 quasar, we expect them to have a relatively bright near-IR counterpart. Unfortunately, the near-IR limit of the 2MASS (Table 1.1) is not sufficient to confirm or rule out this possibility. Deeper near-IR observations are therefore mandatory to test the viability of this scenario. Future X-ray spectral information could also be extremely useful, confirming or excluding the need of absorption excess to fit the spectra. A number of sources capable of very high f_X/f_{opt} ratios was recently discovered in Chandra Deep Fields, the so-called Extreme X-ray Objects (EXO; Koekemoer et al. [126]). The nature of these sources is still not clear, but they share with type 2 quasars the extremely red color. However, these sources have X-ray fluxes much fainter than BFS ($\leq 4 \times 10^{-15}$ erg cm^{-2} s^{-1}), so they are likely to belong to different populations.

The nature of BFS reported here is probably non-unique. In order to accomodate the possible transients in one of the above classes, a key factor is

variability. The most variable candidates, BL Lacs, can vary up to a factor of ~ 100 (e.g. Mkn 501; Pian et al. [188]), enough to explain the non-detections. This makes BL Lacs appealing candidates for possible transients. The variability of type 2 quasars, instead, seems not sufficient. Other known transient source classes usually can not produce such high f_X/f_{opt} values. An alternative explanation could be that of a new kind of transient, capable of great flux variability but reaching much lower peak maximum luminosity. According to this idea, the f_X/f_{opt} would be greatly boosted by the non-simultaneity of X-ray and optical observations. If we suppose that the transient BFS belong to an homogeneous class, they could represent a numerically consistent population. In fact, if the distribution of sources were isotropic this would translate in a rate of 10^5 transient BFS per year, otherwise the number should be scaled with the solid angle. Such a large parent population could point to isolated neutron stars or white dwarfs. In particular one may wonder if transient BFS are related to a sudden release of the internal energy of a neutron star, a process which may be at work in the recently discovered Rotating Radio Transients (RRATs, McLaughlin et al. [141]).

1.6 New observations

The interpretation of BFS requires further multi-wavelength data. We started an X-ray and optical follow-up program on BFS. In particular, the three BFS have been observed with the Swift XRT (P.I. Moretti). The two transient BFS, 1BMW135703.0+181121 and 1BMW200739.8-484819 were not detected in observations of respectively 9 ks and 8 ks, resulting in $0.3-10$ keV 3σ upper limits of 1.8×10^{-3} counts s^{-1} and 2.2×10^{-3} counts s^{-1}. Assuming a power law spectrum with photon index 2 and a Galactic column density (see Table 1.2) the obtained upper limits on the unabsorbed 0.3-10 keV fluxes are respectively 5×10^{-14} and 8×10^{-14} erg cm−2 s−1. 1BMW042142.4-571541 was observed for 11 ks; it was detected at a rate of $(2.2\pm 0.2) \times 10^{-2}$ counts s^{-1} (~ 200 counts), but there is a possible contamination from a bright star closeby. The spectrum is very soft and consistent either with a black body (250±30 eV) or a double Raymond-Smith model.

Optical observations of BFS are in progress. In particular, 1BMW135703.0 +181121 was observed with the I and R filters and the MiniMo camera with the 3.5 WIYN telescope in 10 minutes exposures on 2004 June (P.I. M. Orio). The absence of optical counterparts in the 3σ spatial error circle allowed us to infer a 5σ upper limit of $R = 23.4$. VLT ESO observations of 2007–48 were performed in May 2006 (P.I. R. Mignani), but they have not yet been analyzed.

In the future, more will be known on these mysterious and fascinating lacunae in the X-ray/optical sky.

Chapter 2

Failed Blank Field Sources: other objects in the ROSAT HRI Brera Multiscale Wavelet Catalog

2.1 Introduction

The sieving of the HRI-BMW catalog described in Chapter 1 allowed us to individuate, besides the final BFS sample, quite a number of other peculiar objects which, we believe, deserve further discussion. We dubbed these sources Failed Blank Field Sources (FBFS), since while at some point of the selection procedure they have been considered possible BFS, finally they failed to satisfy one or more necessary criteria. This chapter presents a selection of the FBFS we found. In the next three sections are shown sources for which the nearest off-band counterpart is too close to allow an inclusion in the BFS sample, but not so close to propose an identification. Six of them have no off-band source in a three sigma radius. We parted the three sources of Section 2.3 from the three sources of Section 2.2 on the basis of a transient/persistent criterion like in Chapter 1. Other five objects have off-band sources between two and three sigma, and are displayed in Section 2.4.

Section 2.5 is dedicated to some source for which instead a radio identification (and sometimes also an optical one) is proposed. Finally, a bunch of sources with a possible new optical identification is shown in Sections 2.6 and 2.7.

2.2 Three σ Failed Blank Field Sources

The three sources in this Section fulfilled almost all the criteria of Section 1.4. The two exceptions are the distance from the nearest off-band counterpart, that

for these FBFS is between 3σ and 4σ, and the detection significance (that is in any case more than 3σ). Using two dimensional circular Gaussian statistical properties, the probability that a source is displaced more than 3σ from its real counterpart is $\sim 1\%$.

Since we dealt with 1340 sources (see 1.4), we expect 13 such cases. However, especially for large positional errors and crowded fields, by-chance unrelated off-band sources that happen to fall in the three sigma error circle are likely to outnumber true associations (Rutledge et al. [207]), so it is not possible to conclude that all these objects have simply a large displacement between the observed position and the true one.

Table 2.1 Three σ FBFS

Name	R.A.	Dec	Err. rad.	Flux	Cts
	bII	N_H	Close ass.	f_X/f_{BJ}	Prob.
	J2000	J2000	$''$	erg cm^{-2} s^{-1}	
		10^{20} cm^{-2}	(sigma)		σ
1BMW160956.7-385936	16 09 56.40	-38 59 37.5	4.11	6.04×10^{-13}	46
	9.27	20.5	3	>131	5.9
1BMW121639.7+452307	12 16 39.55	+45 23 04.6	9.98	3.10×10^{-13}	44
	70.47	1.19	3.3	>42	3.6
1BMW074537.2+414210	07 45 37.13	+41 42 07.0	9.82	2.86×10^{-13}	97
	27.32	5.44	3.2	>39	3.8

1BMW160956.7-385936. This bright source has the lowest Galactic latitude (bII=9.27) in our sample. It apparently coincides with a hole in the periphery of the dense Lupus III molecular cloud, so the large column density could actually be an overestimate. The boresight correction was performed with eleven sources. Of these, seven are known X-ray emitters. The error radius on the position is quite small and there are no optical counterparts up to a distance of 3 σ radius (object A in Figure 2.1, with BJ=15.2, RF=13, IN=11.4, J=10.4, H=9.7, K=9.4). Object A appears actually a blend of two stars in digitized images; it seems to saturate slightly the images, in particular in the red band. There are various PSPC pointings of this region. This source has been detected only in three pointings (1WGA J1609.9-3859, 1WGA J1609.9-3858, 1WGA J1610.0-3859), hinting for substantial long term flux variation. An indication of variation is given also by the fluxes reported in the WGA, that range from 8.8×10^{-14} erg cm^{-2} s^{-1} to 3.6×10^{-13} erg cm^{-2} s^{-1}. This source is identified in the WGA catalog with the optical object A (see Figure 2.1) and classified as an M5 star. Our position determination, with object A at $\sim 3\sigma$, makes this identification unlikely, though not completely rejectable. The number of photons detected by the PSPC is low (from 33 to 52), so the spectral information is very rough. The photons detected are distributed as follows: 17 low band counts, 24 mid band counts, 11 high band counts for 1WGA1610.0-3859, 8 low band counts, 19 mid band counts, 18 high band counts for 1WGA1609.9-3859,

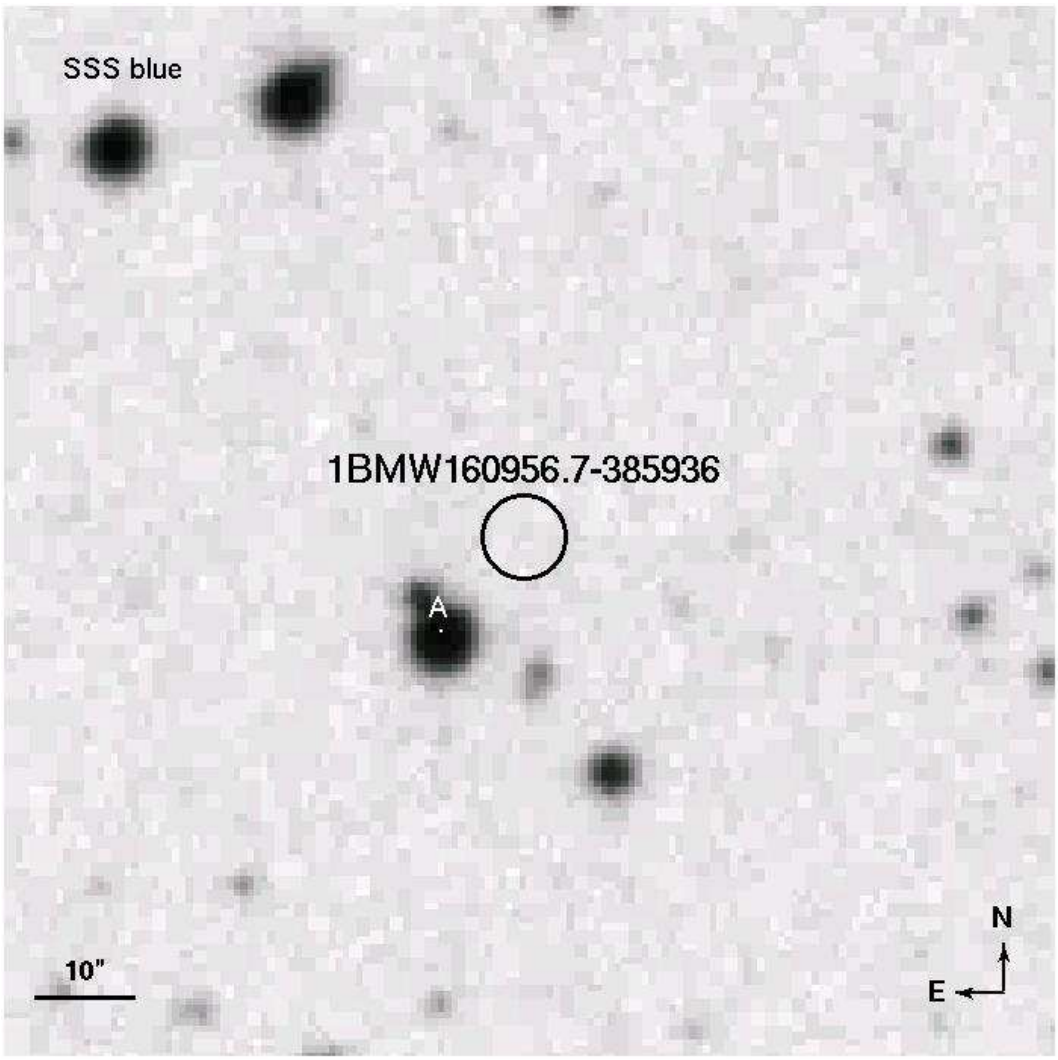

Figure 2.1 The X-ray position of 1BMW160956.7-385936 superimposed to the corresponding blue image along with its 1σ error circle.

1 low band count, 13 mid band counts, 19 high band counts for 1WGA1609.9-3858 (using WGA bands, i.e. low band from 0.1 to 0.4 keV, mid band from 0.4 to 0.9 keV and high band from 0.9 to 2.4 keV). With the caution due to such low counting statistics, the numbers above suggest a possible spectral variation, which would agree with the different flux values.

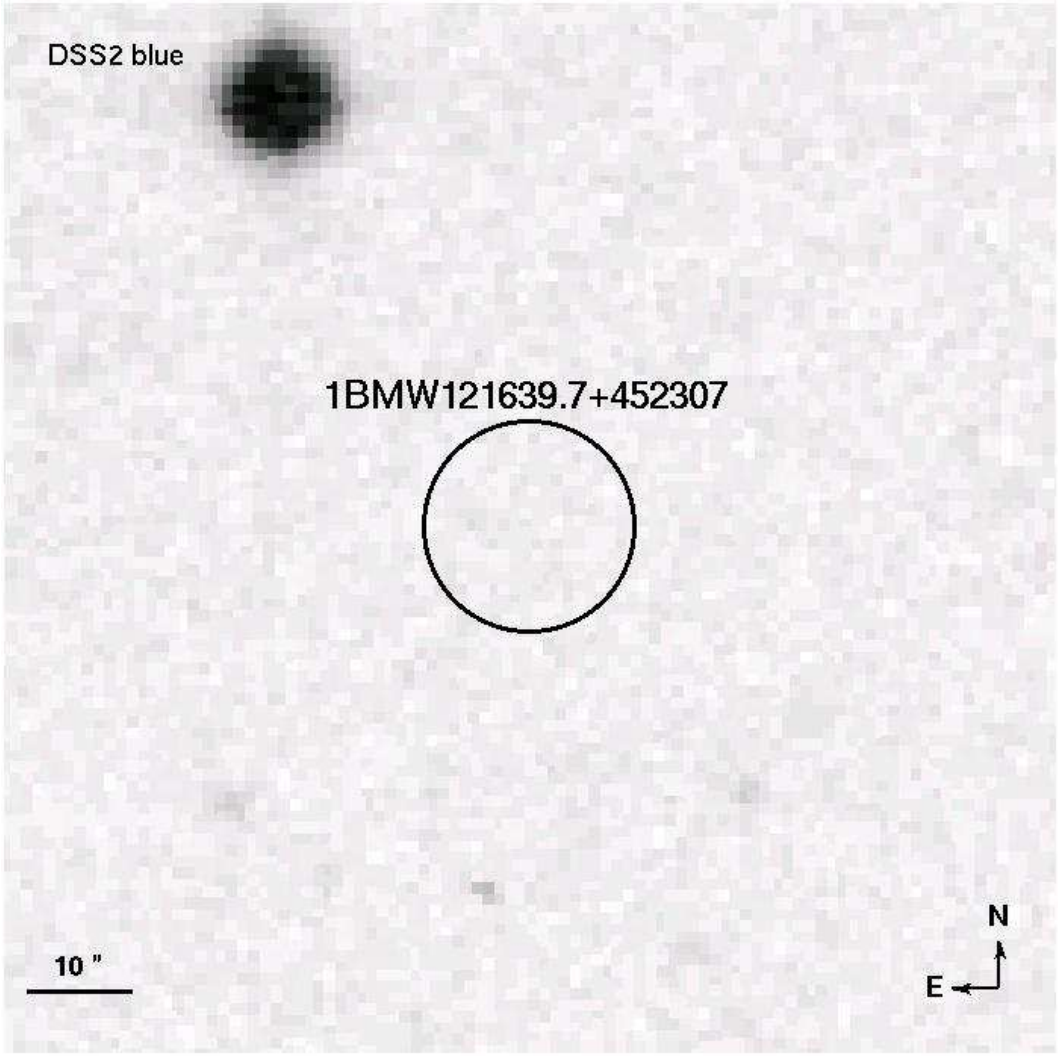

Figure 2.2 The X-ray position of 1BMW121639.7+452307 superimposed to the corresponding blue image along with its 1σ error circle.

1BMW121639.7+452307. The error circle for this source is still $\sim 10''$, even after the boresight correction (accomplished with the aid of four matches with optical catalogs). Nevertheless, the nearest optical source is at more than 3 σ (see Figure 2.2). The non-detection in the FIRST provide a significant radio upper limit. The source is at very high galactic latitude (bII=70.4), possibly

indicating an extragalactic nature.

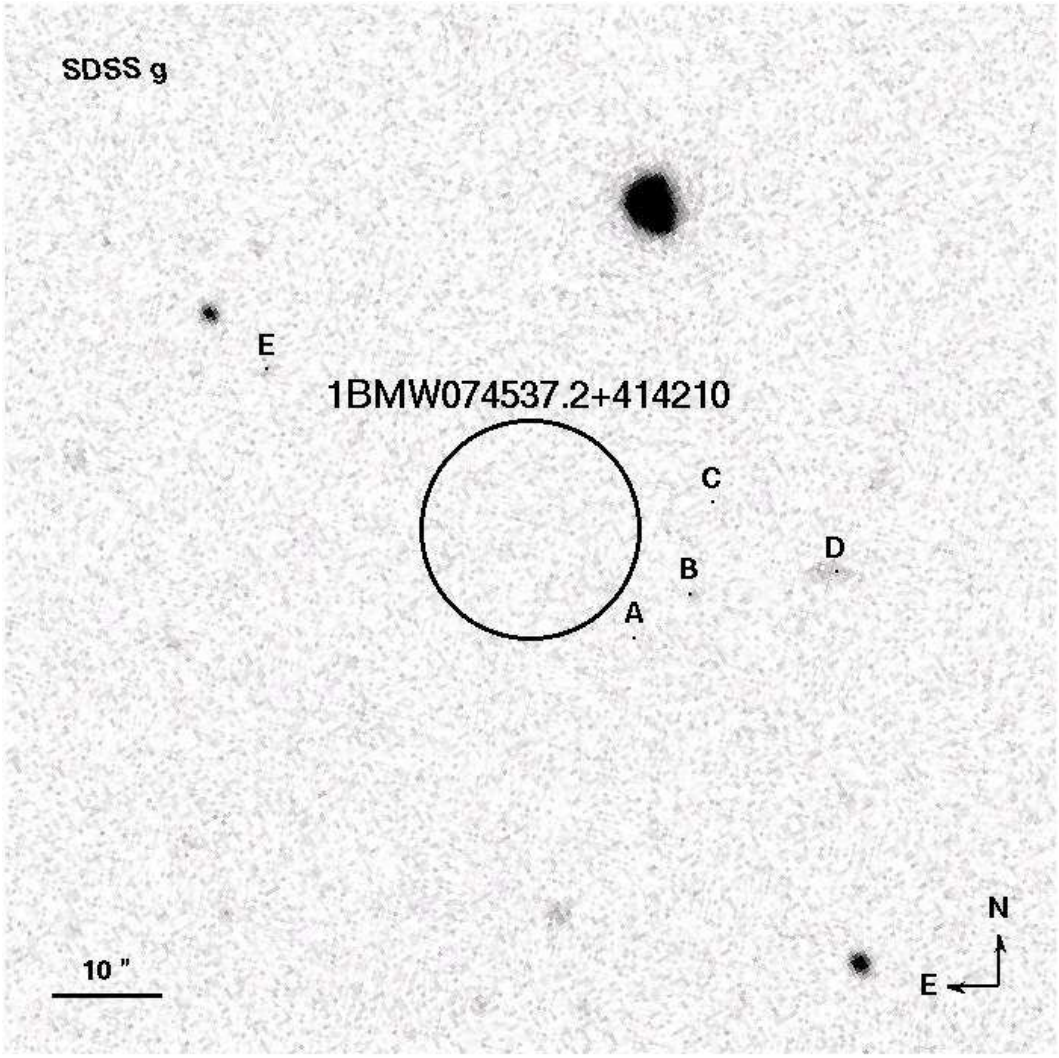

Figure 2.3 The X-ray position of 1BMW074537.2+414210 superimposed to the corresponding blue image (SDSS g) along with its 1σ error circle.

1BMW074537.2+414210. We carried out the boresight correction for 1BMW074537.2+414210 with the optical catalog positions of four sources. The obtained position determination is rather poor (9.8 $''$ error radius). This is the only source of our sample included in the sky coverage of the Sloan Digitized Sky Survey (SDSS; York et al. [249]). There are three SDSS sources in a 2 σ radius (A, B and C; see Table 2.2 and Figure 2.3). Therefore, it is not strictly speaking a three σ FBFS. However, this is due only to the much deeper optical images (all these three sources have g>23), so we decided to keep it in this subsample. There are no sources in a 3 σ radius in other catalogs. The non-detection in the

FIRST provides a significant radio upper limit.

Table 2.2 SDSS sources near to 1BMW074537.2+414210.

Label	R.A.	Dec	u	g	r	i	z	Distance
	J2000	J2000						$''$
A	07 45 36.29	+41 41 57.2	23	23.2	22.3	21.5	21.3	13.6
B	07 45 35.85	+41 42 01.2	23.6	23.1	22	21.6	21.4	15.5
C	07 45 35.66	+41 42 09.4	24.6	23.6	22.6	21.5	20.8	16.7
D	07 45 34.66	+41 42 03.1	21.9	21.5	20.8	20.7	21.2	28
E	07 45 39.25	+41 42 21.5	24.2	23	21.6	20.7	20.1	27.8

2.3 Failed Blank Field Sources: three σ transient candidates

The three sources of this section are characterized by a possible transient behaviour, i.e. they have been observed in some HRI pointing, but not observed in some other longer HRI or PSPC pointing, like the sources of Section 2.3. At odds with the BFS of Section 2.3, however, these sources, after the boresight correction, have a possible optical counterpart at a distance between three and four σ.

Table 2.3 Three σ transient FBFS parameters.

Name	R.A.	Dec	Err. rad.	Flux	Cts
	bII	N_H	Close ass.	f_X/f_{BJ}	Prob.
	J2000	J2000	$''$	erg cm^{-2} s^{-1}	
		10^{20} cm^{-2}	(sigma)		σ
1BMW020448.1+301113	02 04 48.00	+30 11 13.8	5.73	3.60×10^{-13}	30
	-30.06	5.70	3.7	> 50	5.2
1BMW095910.1+690514	09 59 09.57	+69 05 17.6	9.19	3.24×10^{-13}	374
	41.15	4.03	3.4	>45	3.9
1BMW042138.3-550348	04 21 38.69	-55 03 48.2	9.23	3.02×10^{-13}	39
	-43.13	1.30	3.1	>66	3.7

1BMW020448.1+301113. This source has been detected in a Feb. 1998 HRI pointing of $\sim$ 1.4 ks, while it has not been detected in another $\sim$ 36.5 ks HRI pointing in Feb. 1998 and in two PSPC pointings ($\sim$ 12 ks, Aug. 1993; $\sim$ 10.8 ks, Aug. 1995). The detection probability of 5.22 σ is fairly stringent (the highest among the transient candidates considered here). The boresight correction for the Feb. 1998 HRI pointing was performed with the other two sources detected in the same observation. The nearest optical source in the USNO-B1.0 catalog is at $\sim 37''$ ($\sim 6.4\sigma$; see Figure 2.4). There are a handful of APM detections either only in the blue or only in the red colors, the nearest

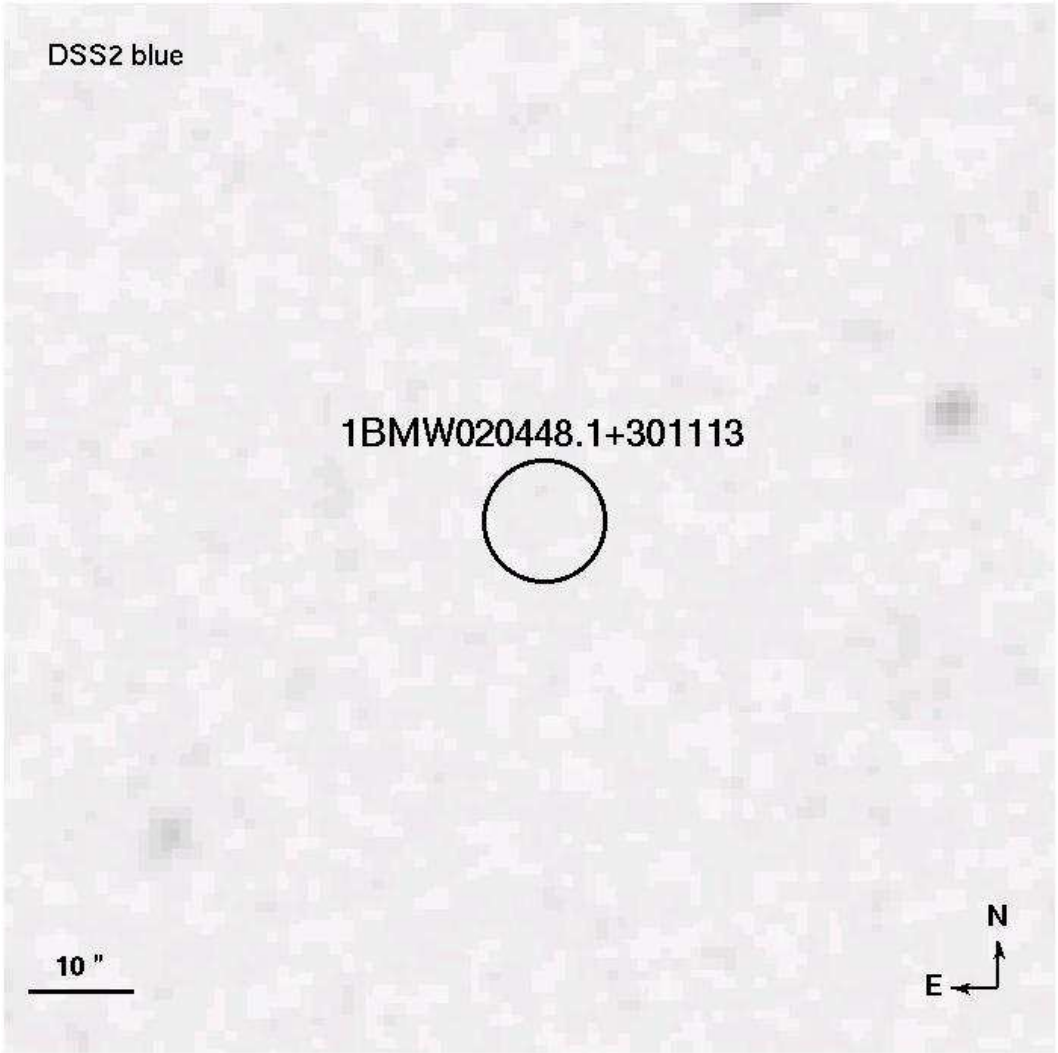

Figure 2.4 The X-ray position of 1BMW020448.1+301113 superimposed to the corresponding blue image along with its 1σ error circle.

at $\sim 21''$ ($\sim 3.7\sigma$). However, inspection of DSS2 images is not able to confirm any of these detections. If we would consider as fake the APM countert.cparts, 1BMW020448.1+301113 should be re-classified as a transient BFS like those of Section 1.4.3.

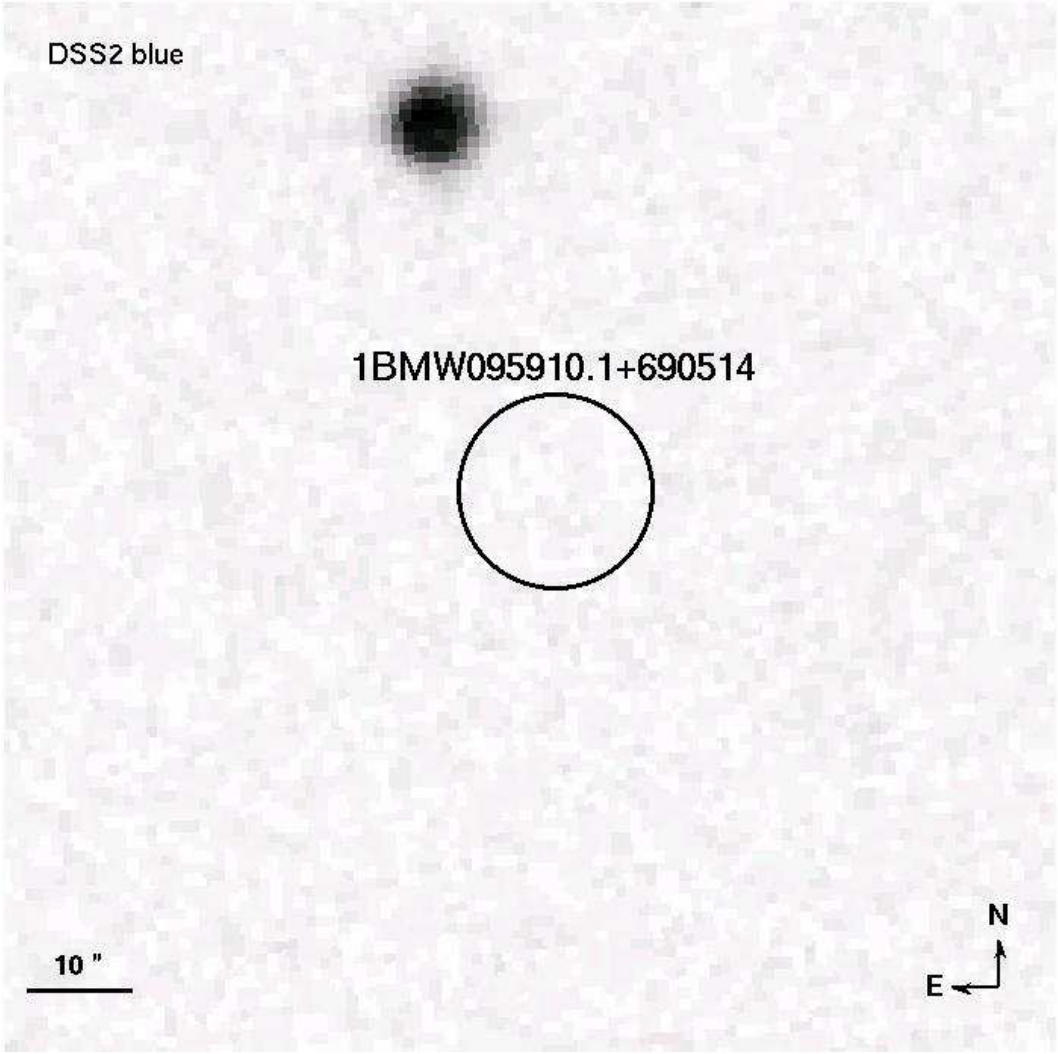

Figure 2.5 The X-ray position of 1BMW095910.1+690514 superimposed to the corresponding blue image along with its 1σ error circle.

1BMW095910.1+690514. This source has been detected in a $\sim$ 19.8 ks pointing of SN1993J in M81, in Sep. 1997 and has never been spotted in any other of the numerous pointings of the same field. Nevertheless, the high number of collected photons and the good SNR point towards a real, transient, not spurious source. The projected distance from the center of M81 is $\sim$ 20 kpc, so the source could either be located in the halo of M81 or be unassociated.

The boresight correction for this source has been performed with the known, accurate positions of M81 nucleus, of SN1993J and with the aid of a cross-correlation with Chandra detected sources (Swartz et al. [222]). The nearest catalog optical source is at $\sim 31''$ ($\sim 3.4\sigma$), detected only in the blue both in POSS I and II by the USNOB1.0 and possibly extended or a blend, but it is not visible in the digitized images. The nearest visible source is at $\sim 37''$, i.e. at $\sim 4\sigma$ (see Figure 2.5). From inspection of the X-ray image, it seems that this source is only a part of a more extended emission broken by the detection algorithm in two different sources. Posing this object at the distance of M81, ~ 3.6 Mpc, and taking in account Galactic absorption, the obtained 0.5-2 keV luminosity is $\sim 8 \times 10^{38}$ erg cm^{-2} s^{-1}, compatible with an ULX in the halo of M81.

1BMW042138.3-550348. 1BMW042138.3-550348 has been detected in a ~ 2.2 ks pointing in Sep. 1995, while it has not been detected in three much longer HRI pointings (~ 40.9 ks, Jan. 1997; ~ 15.2 ks, Sep. 1996; ~ 9.3 ks, Jan. 1992) and in a ~ 17.8 ks PSPC pointing in Sep. 1992. Only another source was present in the Sep. 1995 pointing, so the boresight correction for this source should be taken with care. The nearest optical catalog source is at $\sim 32''$ ($\sim 3.4\sigma$), while in the digitized blue and red images there is a source not present in catalogs at $\sim 29''$ ($\sim 3.1\sigma$; object A in Figure 2.6).

2.4 Two σ Failed Blank Field Sources

The Failed Blank Field Sources of this subsection have the nearest off-band counterpart between 2σ and 3σ. Using two dimensional circular Gaussian statistical properties, the probability that a source is displaced by more than 2σ from its off-band counterpart is $\sim 14\%$. With such numbers, a counterpart between 2σ and 3σ can neither be excluded nor confirmed. All these sources have very large positional errors, therefore boosting the probability of by-chance, spurious associations (Rutledge et al. [207]). The properties of these sources are shown in Table 2.4. Note that the reported f_X/f_{BJ} limit assumes that the real counterpart is beyond the survey limiting depth (22.5 in the North emisphere, 23 in the South emisphere). Table 2.5 summarizes the properties of off-band objects distant less than 3σ from the X-ray position (positions are from USNOB1.0, magnitudes from USNOB1.0 and 2MASS). None of these sources, has the same characteristics of BFS transient candidates (1.3.6, 1.4.3), i.e. it has not been observed in longer pointings; however, there are strong clues of variability for 1BMW160549.4+615557. Generally speaking, these five sources could be BFS with by chance off-band counterparts. Therefore, all the hypothesis on their nature made in Chapter 1 are valid. However, since we expected a priori $\sim$ 180 sources of the 1340 left after our selection masks to have a displacement $> 2\sigma$ from their true position (see 1.5), the strongest hypothesis for these five objects is simply that the X-ray position if $> 2\sigma$ far away from the position of

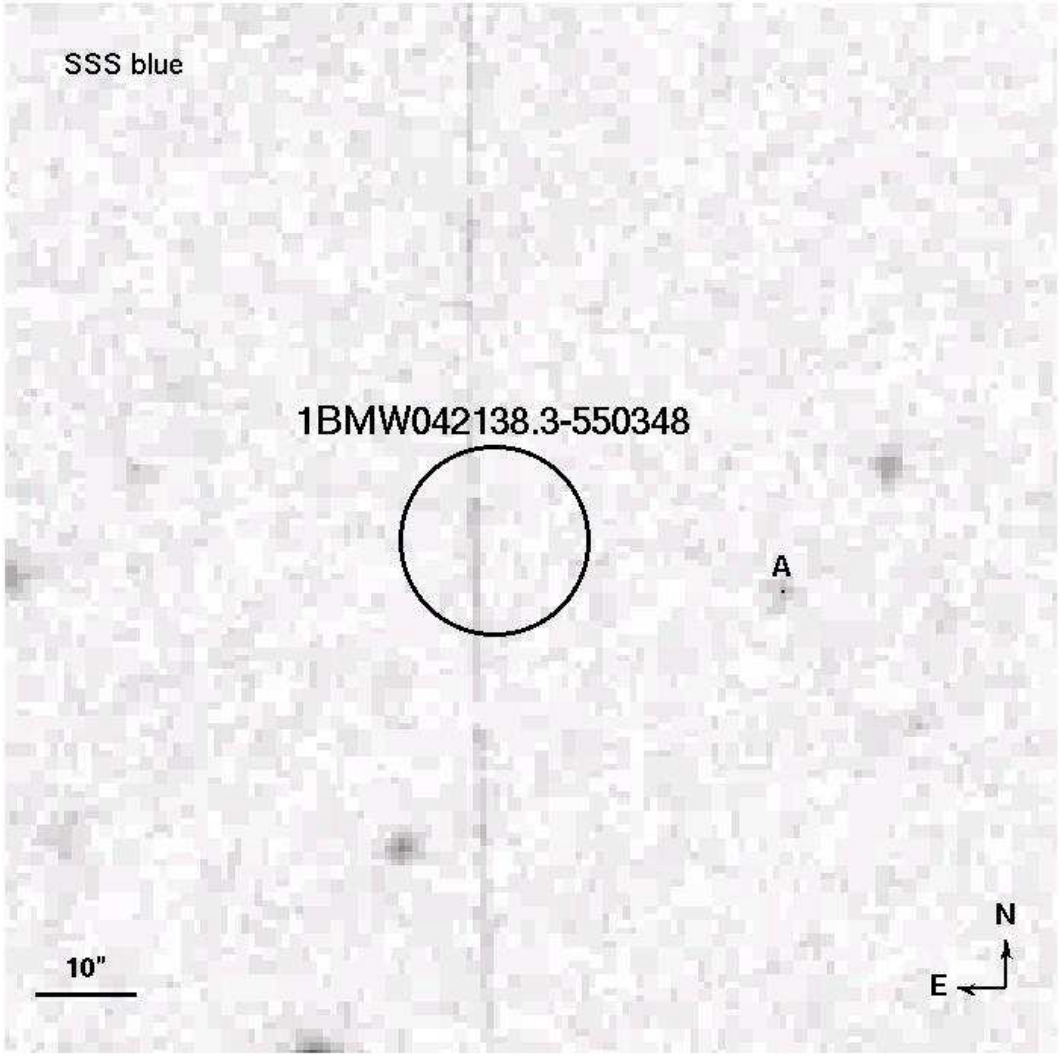

Figure 2.6 The X-ray position of 1BMW042138.3-550348 superimposed to the corresponding blue image along with its 1σ error circle.

the offband counterparts.

Table 2.4 Two σ FBFS parameters.

Name	R.A.	Dec	Err. rad.	Flux	Cts
	bII	N_H	Close ass.	f_X/f_{BJ}	Prob.
	J2000	J2000	$''$	erg cm^{-2} s^{-1}	
		10^{20} cm^{-2}	(sigma)		σ
1BMW012007.7+302626	01 20 07.77	+30 26 26.6	8.06	4.5×10^{-13}	50
	-32.02	5.95	2	>61	4
1BMW071944.5-570646	07 19 44.19	-57 06 47.9	9.04	4.21×10^{-13}	38
	-18.87	8.84	2.2	>91	3.4
1BMW160549.4+615557	16 05 50.25	+61 55 57.0	9.32	3.97×10^{-13}	54
	42.78	1.78	2.3	>54	3.4
1BMW033327.1-620343	03 33 27.16	-62 03 47.9	7.98	2.90×10^{-13}	50
	-46.05	3.24	2.2	>63	3.9
1BMW004057.9+481824	00 40 58.30	+48 18 22.0	3.81	2.85×10^{-13}	184
	-14.53	12.4	2.9	>39	7.8

Table 2.5 Off-band sources at $\leq 3\sigma$ from the X-ray position

1BMW012007.7+302626				
Label	R.A.	Dec	Magnitude	Distance
	J2000	J2000		″
A	01 20 08.80	+30 26 09.0	O=18.8;BJ=18;E=17.9;RF=18.4;I=16.6;J=16.8; H=16; K=15	22.1
B	01 20 06.04	+30 26 33.0	O=19.9;BJ=19.2;E=20.6;RF=19.3;I=18.2;J=16.6; H=15.7; K=15.4	23.2
1BMW071944.5-570646				
Label	R.A.	Dec	Magnitude	Distance
	J2000	J2000		″
A	07 19 46.08	-57 06 34.6	BJ=21.3; RF=19.7(ESO); RF=20.1(AAO); I=18.8	20.3
1BMW160549.4+615557				
Label	R.A.	Dec	Magnitude	Distance
	J2000	J2000		″
A	16 05 53.08	+61 55 50.2	BJ=21; RF=19.6	21.1
B	16 05 53.21	+61 55 47.8	BJ=20.5; RF=19.5	22.8
C	16 05 47.61	+61 56 16.0	O=21; BJ=21.7	26.6
1BMW033327.1-620343				
Label	R.A.	Dec	Magnitude	Distance
	J2000	J2000		″
A	03 33 29.61	-62 03 45.2	BJ=19.5; RF=18.4(ESO); RF=18.7(AAO); I=17.9	17.5
B	03 33 24.98	-62 03 56.3	BJ=20; RF=17.2; I=18.1;J=16.9; H=15.8; K=15.4	17.5
C	03 33 27.53	-62 03 23.8	BJ=16.4; RF=14.5(ESO); RF=14.6(AAO); I=14.9;J=13.9; H=13.4; K=13.2	24.2
D	03 33 29.56	-62 03 44.5	BJ=19.8; RF=17.9(ESO); RF=18.3(AAO); I=18.1	17.2
E	03 33 25.10	-62 03 58.7	BJ=21; RF=17.6; I=18.5	18.05
F	03 33 24.84	-62 03 56.4	BJ=19.3; RF=17.6(ESO); RF=17.1(AAO); I=16.9	18.4
1BMW004057.9+481824				
Label	R.A.	Dec	Magnitude	Distance
	J2000	J2000		″
A	00 40 59.19	+48 18 14.4	O=15;E=12.1;BJ=14.8;RF=12.4;I=11.7;J=10.6; H=9.9; K=9.7	11.7

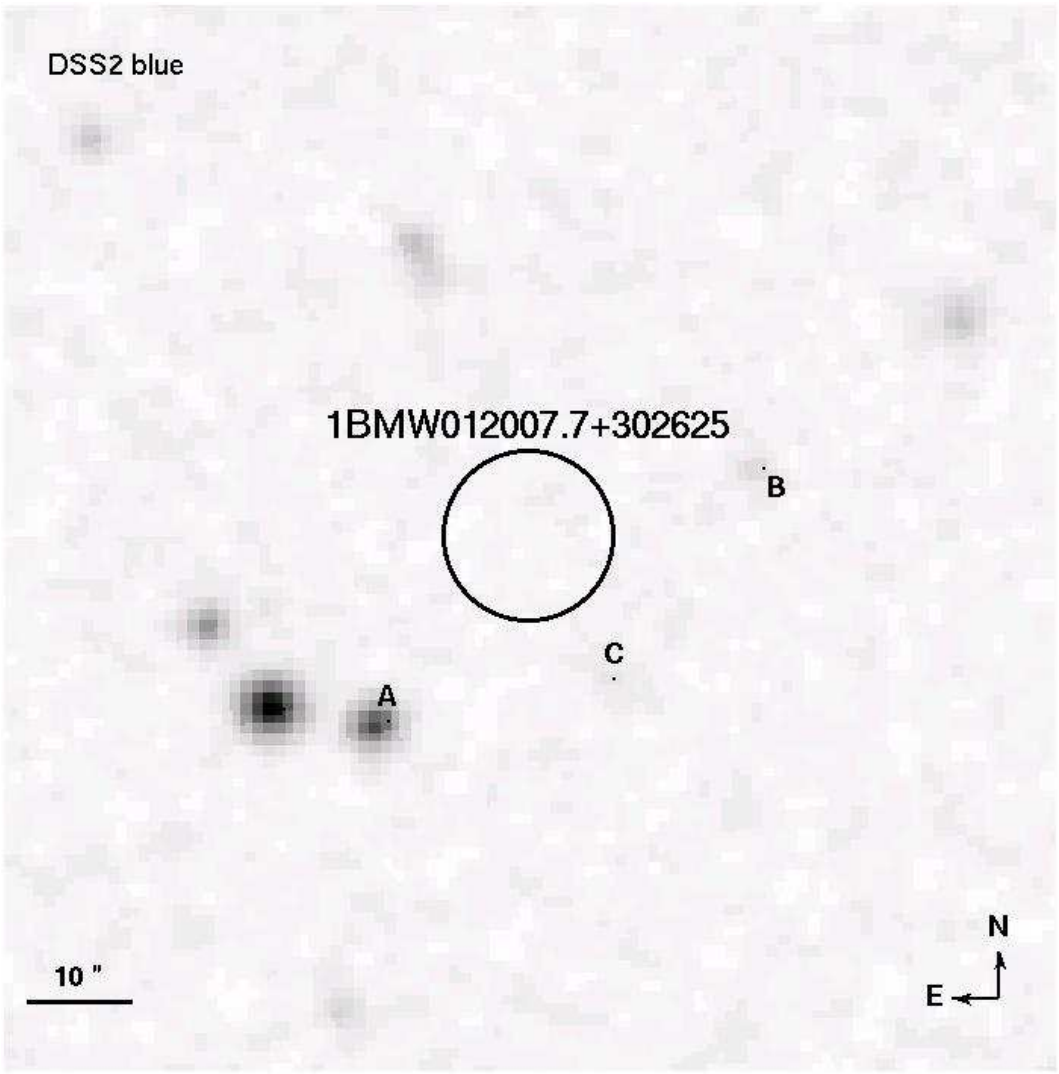

Figure 2.7 The X-ray position of 1BMW012007.7+302626 superimposed to the corresponding blue image along with its 1σ error circle.

1BMW012007.7+302626. The boresight correction has been done with the only other source detected in the pointing, yielding a still quite large error on the source position ($\sim 8''$). Despite this, the nearest catalog source is at $\sim$ 2.7 σ (see Figure 2.7 and Table 2.5). A third source (object C in Figure 2.7 and 2.8) at $\sim 2\sigma$ is barely visible at the plate limit in the DSS2 BJ image, while it is not apparent at any other wavelength. It is not clear if object C is slightly extended or not.

1BMW071944.5-570646. The detection probability for this source is 3.36 σ, the lowest in our sample, giving the highest possibility of a spurious detection. After the boresight correction, made using the center of the pointing and another

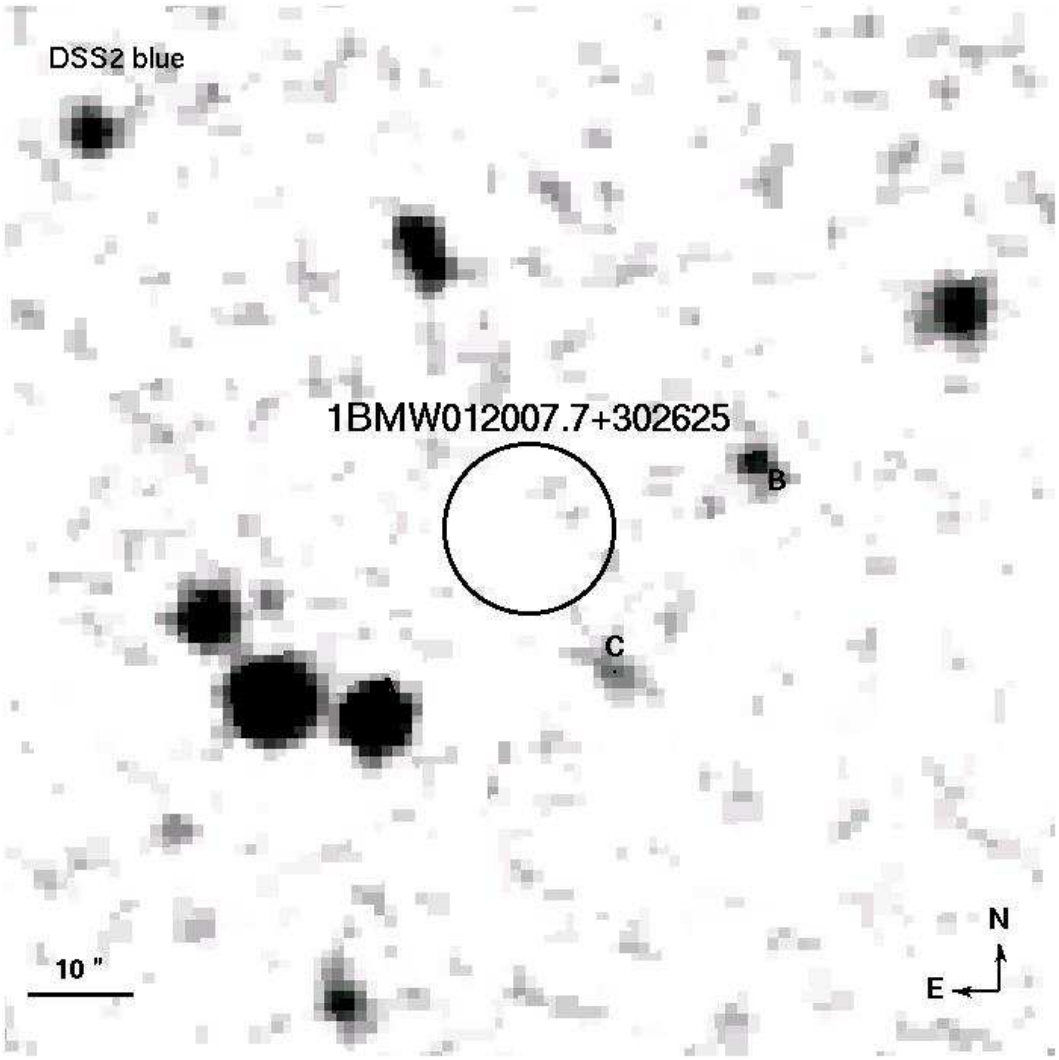

Figure 2.8 The same as above, in logarithmic scale to evidence source C.

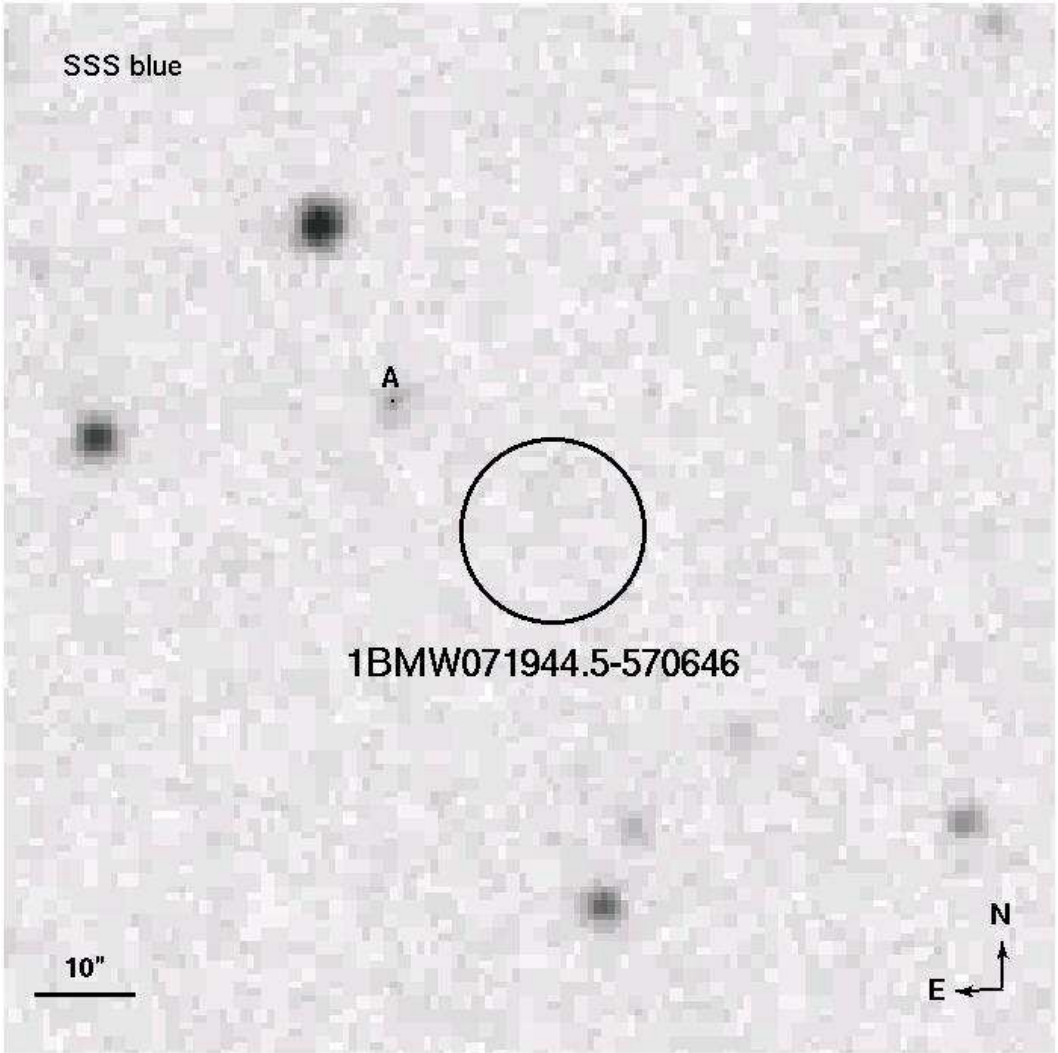

Figure 2.9 The X-ray position of 1BMW071944.5-570646 superimposed to the corresponding blue image along with its 1σ error circle.

source, this source has still a poor position determination (error radius $\sim 9''$). There is an USNO B1.0 entry at $6.7''$ (BJ= 22, I=19.1), i.e. well inside the 1 σ error radius. We believe that this source is actually fake, on the basis both of unusual colors (no red RF detection) and on the absence in the deeper GSC2 catalog, putting the nearest object at more than 2 σ (see Figure 2.9 and Table 2.5).

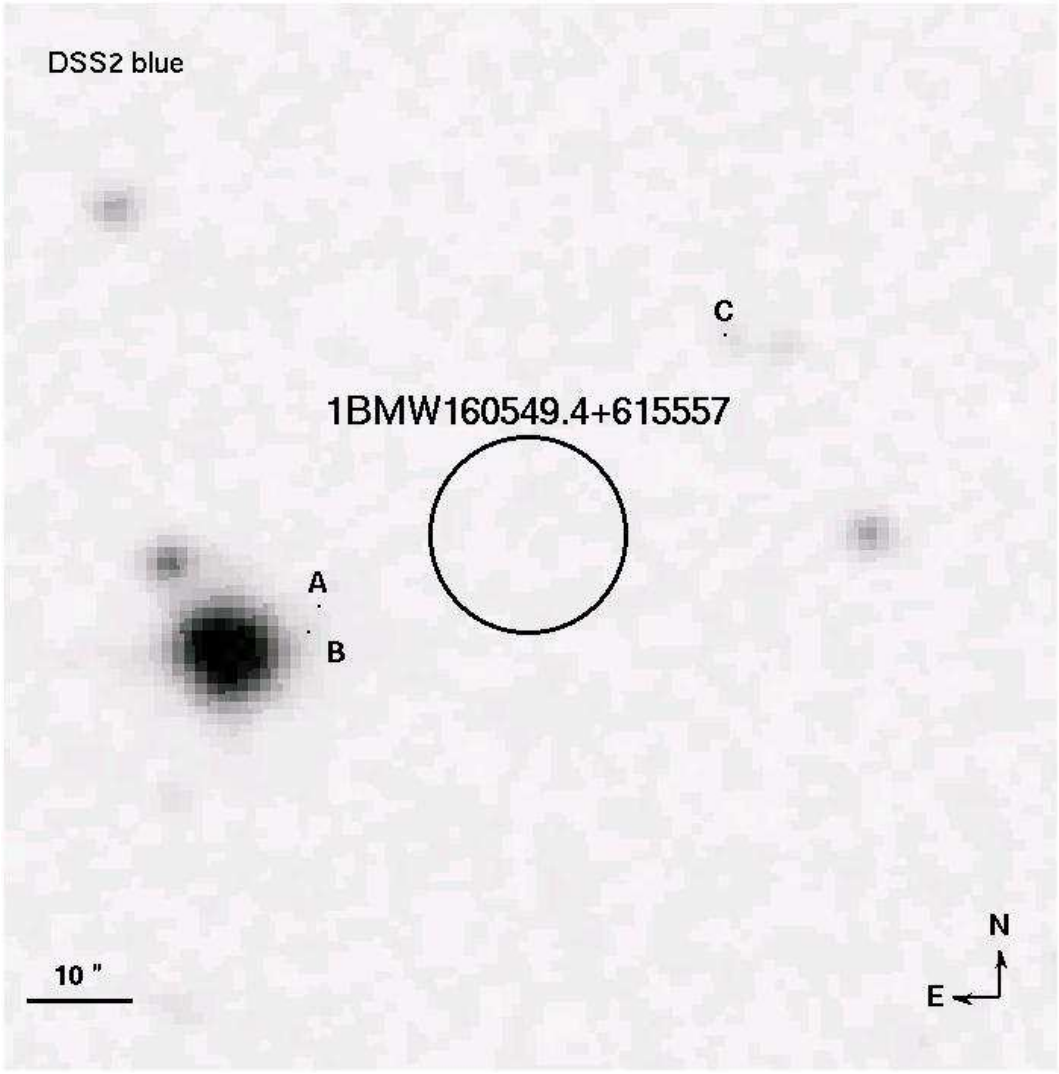

Figure 2.10 The X-ray position of 1BMW160549.4+615557 superimposed to the corresponding blue image along with its 1σ error circle.

1BMW160549.4+615557. This source has the second lowest detection probability in our sample, 3.44σ. However, there is a RASS Faint Source Catalog entry, 1RXS J160544.7+615557, with which it is tentatively identified. The

boresight correction was applied with the only other source in the pointing. The nearest optical object is at more than 2 σ, despite the poor precision on the position (9.3 $''$; see Figure 2.10 and Table 2.5). Using a counts-to-flux RASS conversion factor of 5.6 $\times$ 10^{-12} erg cm^{-2} s^{-1} cts^{-1}, 1RXS J160544.7+615557 is at $\sim$ 2.7$\times$ 10^{-14} erg cm^{-2} s^{-1}, a factor $\sim$ 15 fainter than the HRI observation. Even rejecting the identification of 1BMW160549.4+615557 and 1RXS J160544.7+615557, the flux of the latter can be used as upper limit on the flux of the former at the epoch of the RASS observation. Unfortunately, the faintness of the source makes RASS hardness ratio weakly significant. Using RASS FSC conventions, HR1=0.22, HR2=1, indicating that most photons are hard. The f_X/f_{BJ} value obtained using the HRI flux and the optical flux of the objects in Table 2.5 is still near to ten. Thus, we consider unlikely a flaring star identification (disfavoured also by an hard emission). Flux variations are natural in most accretion powered sources. However, the source is too faint to be a Galactic X-ray binary in high state during the HRI observation (unless undiscovered low luminosity transients exist; see 1.5), and the f_X/f_{BJ} still exceeds values common for cataclysmic variables. 1BMW160549.4+615557 could therefore be an highly variable AGN, either radio quiet or with a radio emission fainter than the FIRST limit. Note that putting 1BMW160549.4+615557 in the BL Lac sequence, with the optical flux of object A in Table 2.5, would need a radio flux barely beyond the FIRST limit. If instead we reject the possible optical counterparts of 1BMW160549.4+615557, the variability still suggest an accretion powered source, either an extreme BL Lac or a type II QSO.

1BMW033327.1-620343. The other three sources detected in the same pointing were used for the boresight correction of1BMW033327.1-620343. The obtained error on the position is 8". There are five objects between 2 σ and 3 σ radius (see Figure 2.11 and Table 2.5). At $\sim$ 37$''$, a bright star (BJ=13.59, R=12.01 in the GSC2.2) saturates the optical images.

1BMW004057.9+481824. The position determination of the faintest source in our sample is quite accurate (3.8$''$ error radius). The boresight correction was made by means of other three sources detected in the same pointing. The low galactic latitude, bII= -14.53, and the Galactic column density in excess of 10^{21} cm^{-2} points to a galactic object. This source appears to be in a hole in a star crowded region, the closest being at 2.9 σ (see Figure 2.12 and Table 2.5).

2.5 Failed Blank Field Sources with a radio counterpart

The four sources of this Section where not associated with radio counterparts by the automatic BMW cross identification procedure, but did not escape a deeper examination. In particular, two of the four sources in this Section, 1BMW081203.8+025543 and 1BMW080727.0+755027, coincide with the pe-

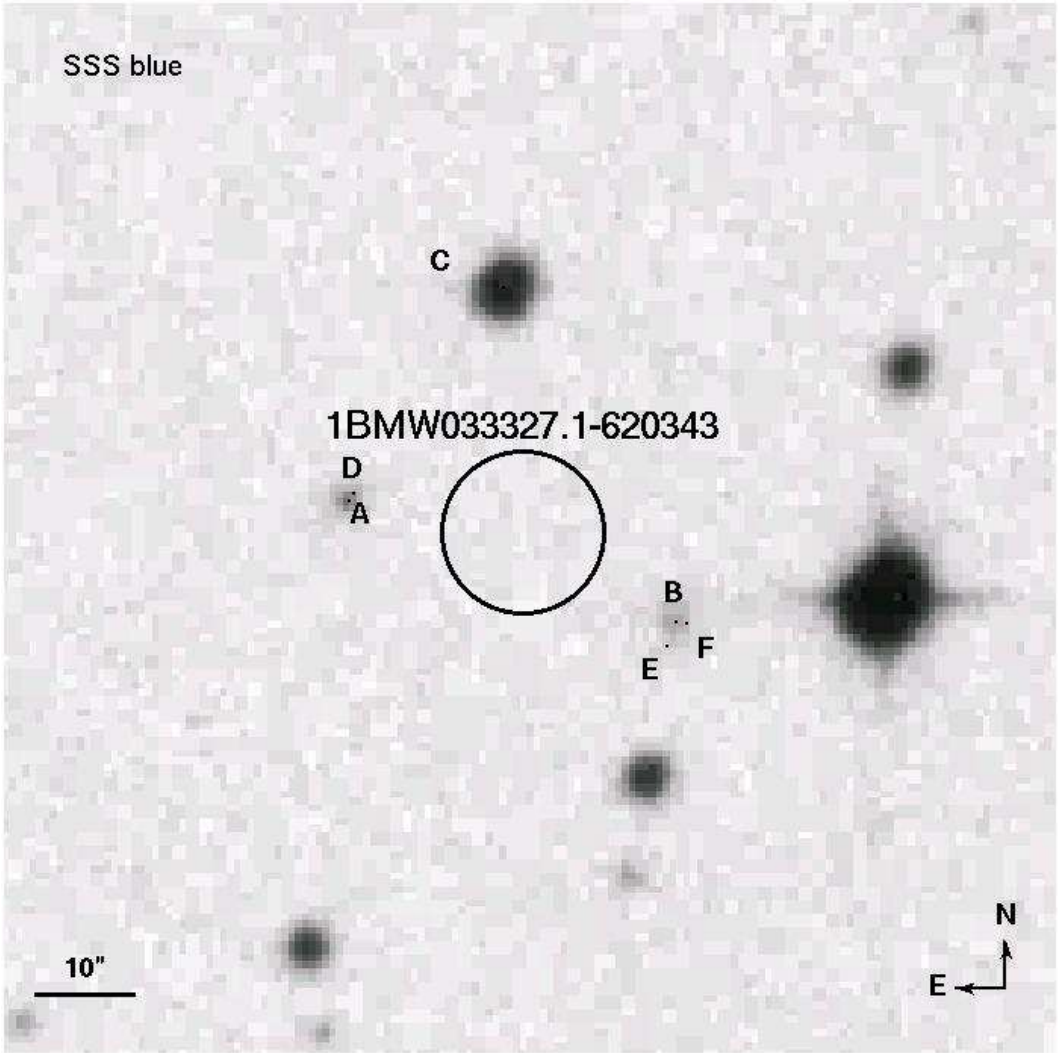

Figure 2.11 The X-ray position of 1BMW033327.1-620343 superimposed to the corresponding blue image along with its 1σ error circle.

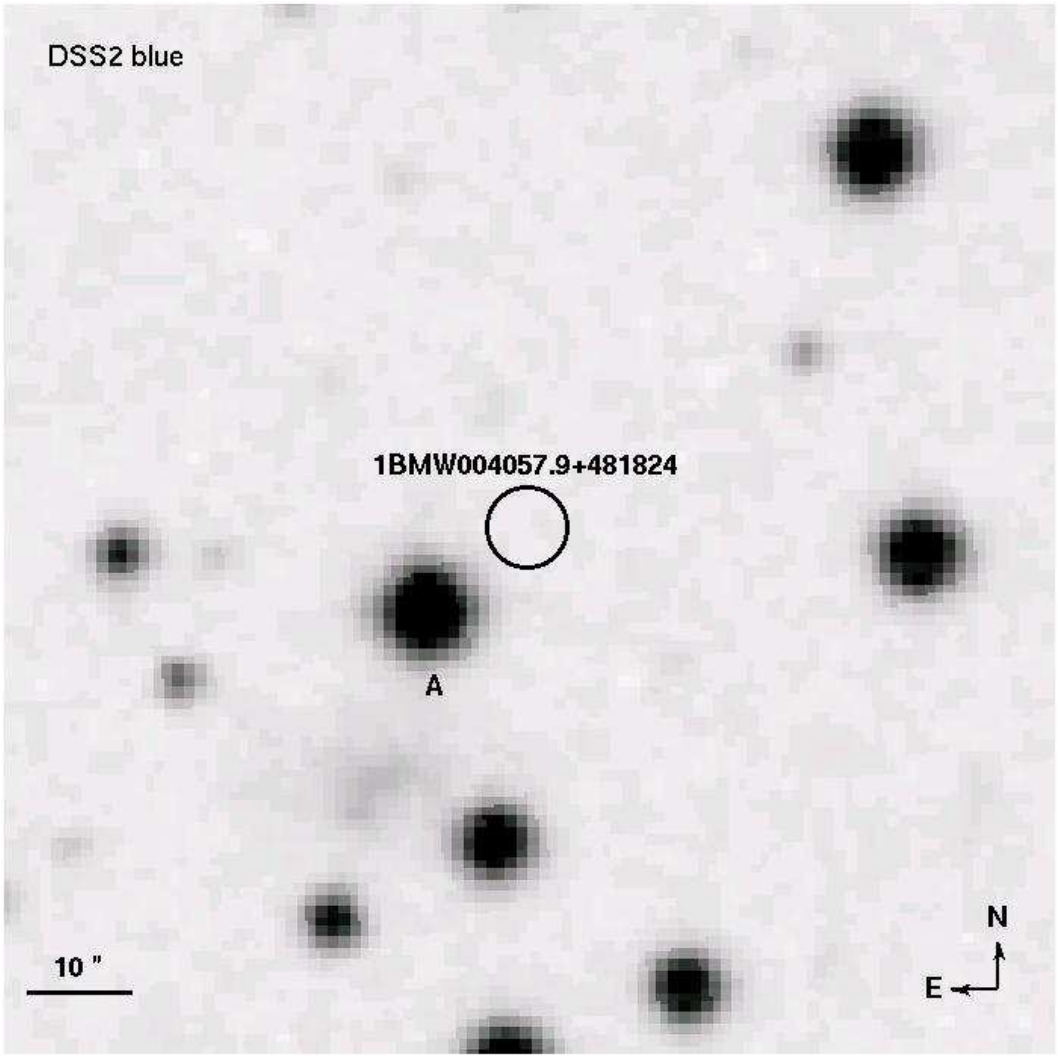

Figure 2.12 The X-ray position of 1BMW004057.9+481824 superimposed to the corresponding blue image along with its 1σ error circle.

riphery of extended NVSS sources. Both are in the portion of the sky at present not covered by the FIRST. In the third case, 1BMW104929.5+553926, there is a possible association with a source detected only in the FIRST 2003 version (i.e. in the part of sky not covered by the old 2000 version used for automatic BMW cross identification). Finally, the X-ray source corresponding to the three BMW entries 1BMW101542.8+594449, 1BMW101541.8+594442 and 1BMW101543.0+594426 could be associated with an extended radio emission, resolved by the FIRST image in a core plus lobes morphology.

Table 2.6 Parameters of FBFS with radio counterpart.

Name	R.A.	Dec	Err. rad.	Flux	Cts
	bII	N_H	Radio ass.	Opt. ass	Prob.
	J2000	J2000	$''$	erg cm^{-2} s^{-1}	
		10^{20} cm^{-2}	(sigma)	(sigma)	σ
1BMW081203.8+025543	08 12 04.16	+02 55 44.0	4.35	3.39×10^{-13}	81
	19.24	3.46	6.5	2.5	5
1BMW080727.0+755027	08 07 27.49	+75 50 25.7	6.05	2.79×10^{-13}	184
	30.87	3.02	2.3	2.1	5.1
1BMW104929.5+553926	10 49 29.33	+55 39 28.2	3.22	3.8×10^{-13}	117
	54.01	0.78	2.8	2.8	8.2
1BMW101542.8+594449	10 15 42.82	+59 44 48.7	3.41	5.33×10^{-13}	735
	47.96	0.92	-	-	7.7
1BMW101541.8+594442	10 15 41.38	+59 44 45.5	3.17	2.78×10^{-13}	428
	47.96	0.92	-	-	9.3
1BMW101543.0+594426	10 15 42.67	+59 44 31.6	4.42	2.37×10^{-13}	294
	47.96	0.92	-	-	3.8

1BMW081203.8+025543. This source has been detected also as a RASS Bright Sources entry, 1RXS J081203.7+025528. With a counts-to-flux RASS conversion factor of 5.6×10^{-12} erg cm^{-2} s^{-1} cts^{-1}, the flux of 1RXS J081203.7 +025528 is 3.92×10^{-13} erg cm^{-2} s^{-1}; therefore both detections are at roughly the same flux level. The boresight correction to the BMW position of this source has been applied with six other X-ray positions. The distance between the boresight corrected position of 1BMW081203.8+025543 and the centroid of NVSS081204+025612 (Table 2.7) is $\sim 29''$, i.e. $\sim 6.5\sigma$. However the radio source is fairly extended (54" major axis, 29" minor axis), so the X-ray position coincides with the periphery of the radio emission. The radio emission is asymmetric. It is not clear if the poor resolution of NVSS masks a lobed source, like 1BMW101542.8+594449/1BMW101541.8+594442/1BMW101543.0+594426. It seems that no optical emission is associated with the centroid of radio emission (see Figure 2.13; in Table 2.7 we reported the distance of the closest optical source). However the region corresponding to the radio emitting area is rather rich in optical sources. Some of these sources appear definitely non stellar, as confirmed by catalogs. Thus it seems that NVSS081204+025612 and

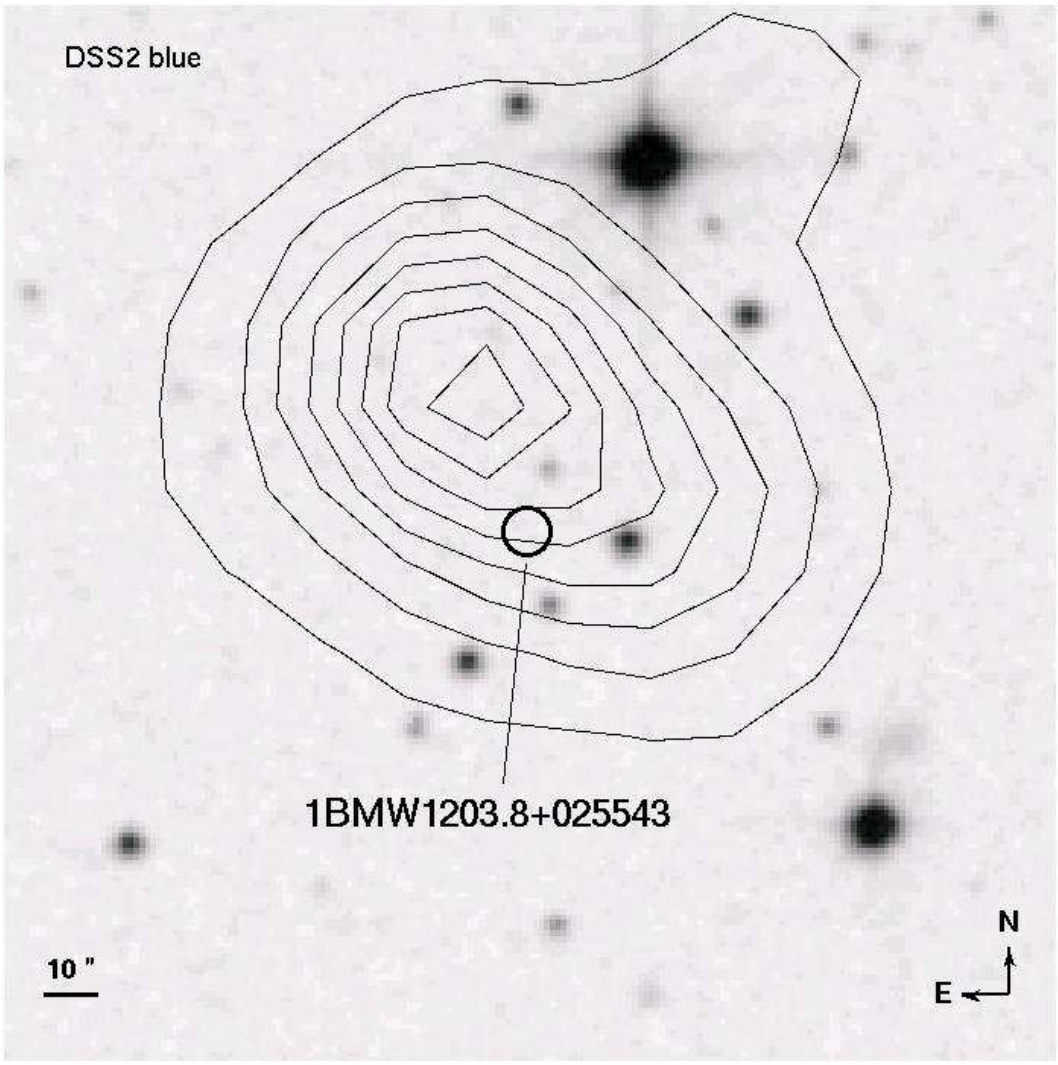

Figure 2.13 The X-ray position of 1BMW081203.8+025543 superimposed to the corresponding blue image, along with its 1σ error circle and a radio NVSS contour map showing NVSS081204+025612.

1BMW081203.8+025543 could both be associated with a group of galaxies.

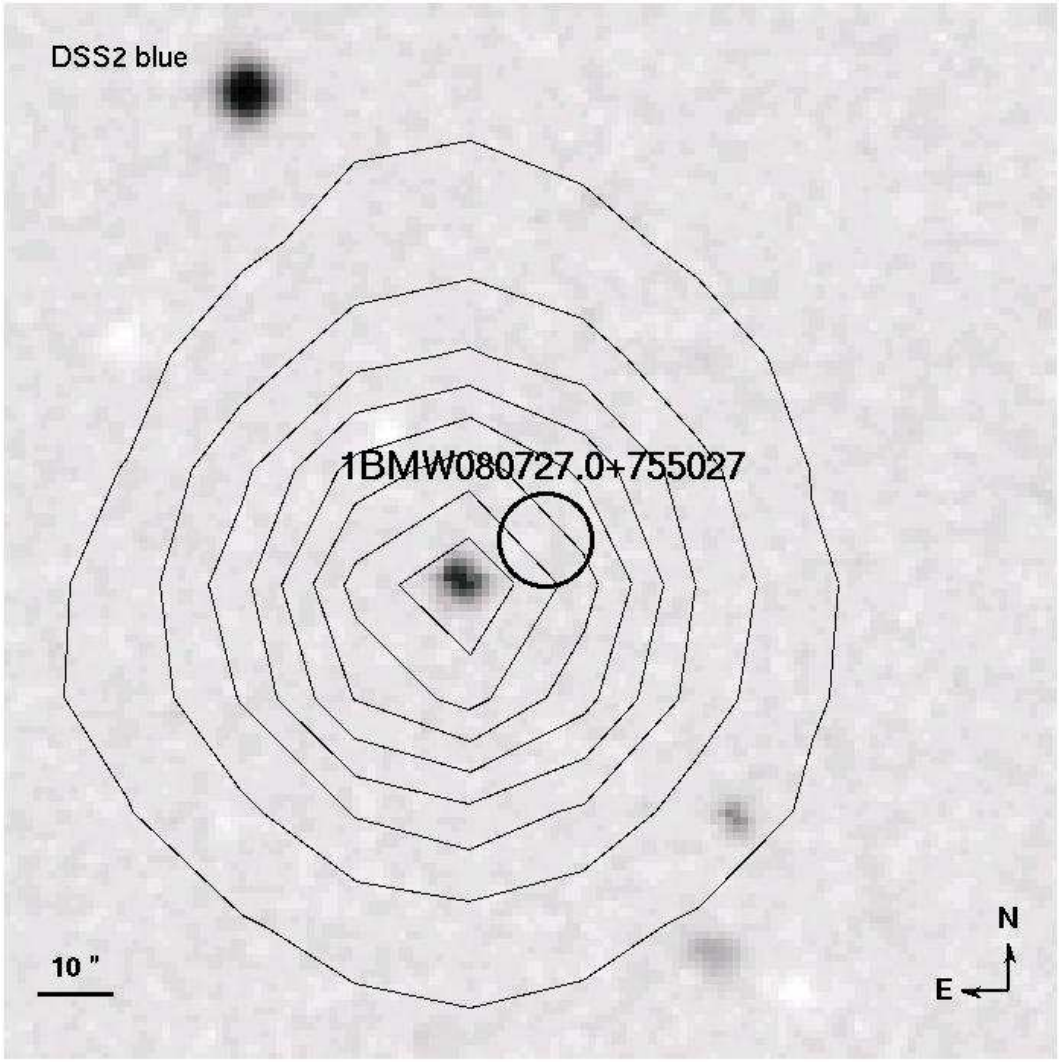

Figure 2.14 The X-ray position of 1BMW080727.0+755027 superimposed to the corresponding blue image, along with its 1σ error circle and a radio NVSS contour map showing NVSS080730+755017.

1BMW080727.0+755027. The position of 1BMW080727.0+755027 has been corrected with nine more source positions in the same pointing. There is a NVSS entry, NVSS080730+755017 (see Table 2.8, Figure 2.14) at $\sim 2.3\sigma$ from the boresight corrected position. The radio emission appears slightly extended (major and minor axes are both $\sim$ 20"), but it is possible that the apparent extension is due to the poor NVSS imaging capabilities. The radio emission is associated with an optical source (BJ=16.4, RF=15.3 in the GSC2; see Figure 2.14). 1BMW080727.0+755027 have also been detected in two PSPC pointings

(1WGA0807.4+7550 and 1WGA0807.5+7550) with respectively 14, 17 and 18 photons and 23, 14 and 29 photons in the WGA soft, mid and hard bands. The flux reported for 1WGA0807.4+7550 is 1.78×10^{-13} erg cm^{-2} s^{-1}, while the one reported for 1WGA0807.5+7550 is 5.51×10^{-13} erg cm^{-2} s^{-1}. According to the WGA catalog, the detection of 1WGA0807.4+7550 is good but it is near to the PSPC inner support structure, the detection of 1WGA0807.5+7550 is good but due to non-optimal rebinning the source is split in two. Therefore we consider scarcely significant the flux variation. The X-ray/radio/optical cross identification is also reported in the QORGCAT (Flesch & Hardcastle [71]), in which the source is considered a probable (83%) AGN. We note that, if this is the case, it would be posed at the lower end of the AGN f_X/f_{opt} range.

1BMW104929.5+553926. 1BMW104929.5+553926 has been detected also as a RASS Faint Source (1RXS J104929.1+553921) and in one PSPC pointing (1WGA J1049.4+5539). The reported WGA flux is 5.22×10^{-13} erg cm^{-2} s^{-1}, while the RASS flux is somewhat lower. The WGA entry has a rather soft spectrum (100, 47 and 37 photons in the low, mid and high bands). We carried out the boresight correction using other six sources. There is a FIRST entry near to the boresight corrected position,FIRST J104928.2+553927 (2.9; Figure 2.15). The relative distance is 8.85" (2.75 σ). The FIRST radio source is faint and pointlike. It almost coincides with an optical source (BJ=18.2, RF=17.8 in the GSC2.2; Figure 2.15). The correlation is reported in the QORGCAT, with an 88% probability of being an AGN. We note that 1BMW104929.5+553926 would be in the middle of the locus of the BL Lac sequence.

1BMW101542.8+594449/1BMW101541.8+594442/ 1BMW101543.0+594426.
This source corresponds to three different BMW entries. After the boresight correction (performed with respectively 12, 15 and 12 sources), the resulting positions are still rather different (Figure 2.16, Figure 2.17). In particular, the positions of 1BMW101542.8+594449 and 1BMW101541.8+594442 are compatibles at 2σ, while all the three positions are compatible at 2.5σ. The source is also a RASS Bright Source (1RXS J101540.8+594450), with a flux of $\sim 5 \times 10^{-13}$ erg cm^{-2} s^{-1} cts^{-1}, and a WGA entry (1WGA J1015.6+5944), with a flux of $\sim 6.6 \times 10^{-13}$ erg cm^{-2} s^{-1} cts^{-1}. The 684 counts detected in the WGA make spectral hardness ratio reliable. The source seems to be definitely soft, with respectively 452, 117 and 115 photons in the low, mid and high bands. There is no evidence of dramatic flux variation from the comparison between these detections. The non-detection in a further, shorter duration (about an half) HRI pointing, however, seems to indicate a level of variability much stronger.Complex radio emission is associated with this source (Figure 2.16 and Figure 2.17, Table 2.10). In particular, the FIRST image and the corresponding contour map show a source with two lobes and a central core. The eastern lobe is the brightest (FIRSTJ101543.3+594439), while the core component is the faintest of the three. This brings to the simple interpretation in terms of a radio galaxy, for

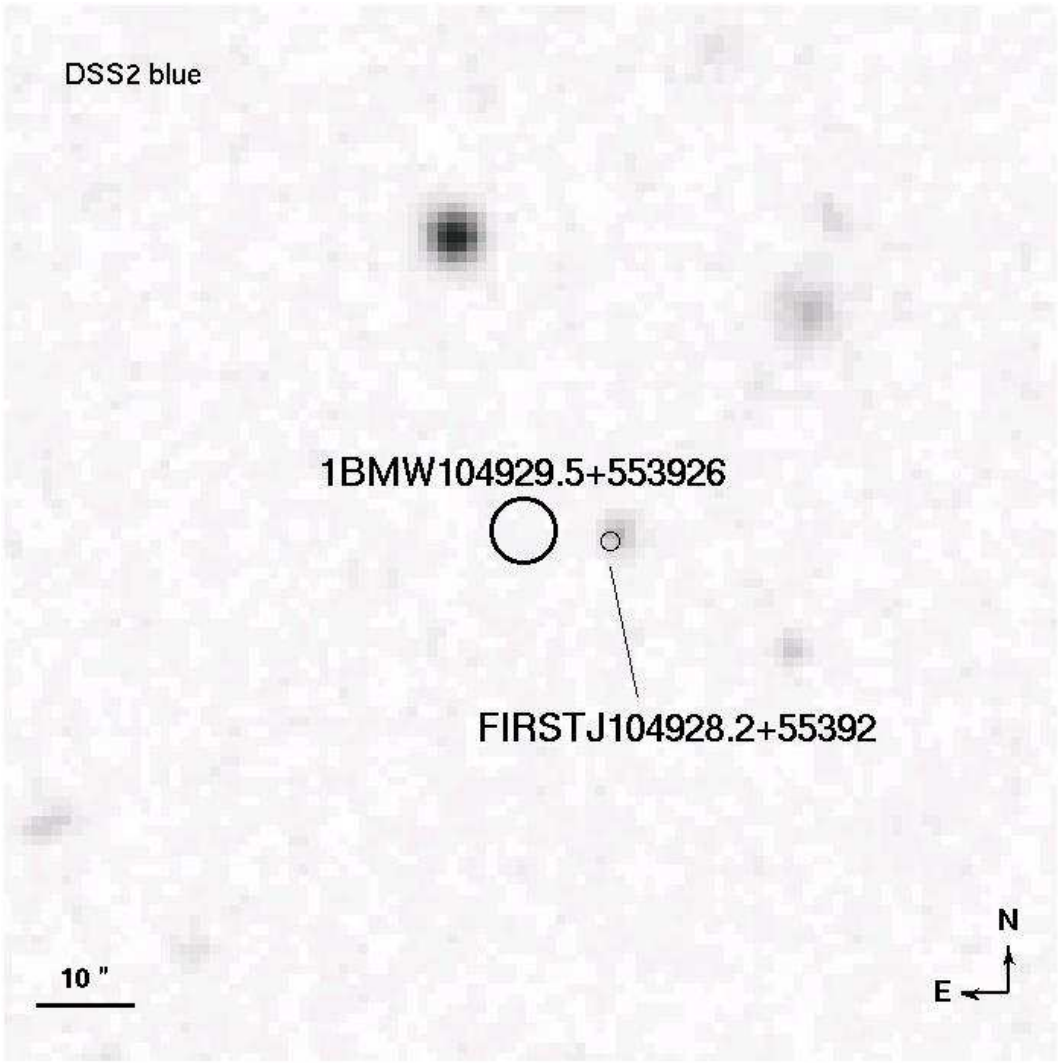

Figure 2.15 The X-ray position of 1BMW104929.5+553926 superimposed to the corresponding blue image, along with its 1σ error circle and a radio FIRST contour map showing FIRST J104928.2+55392.

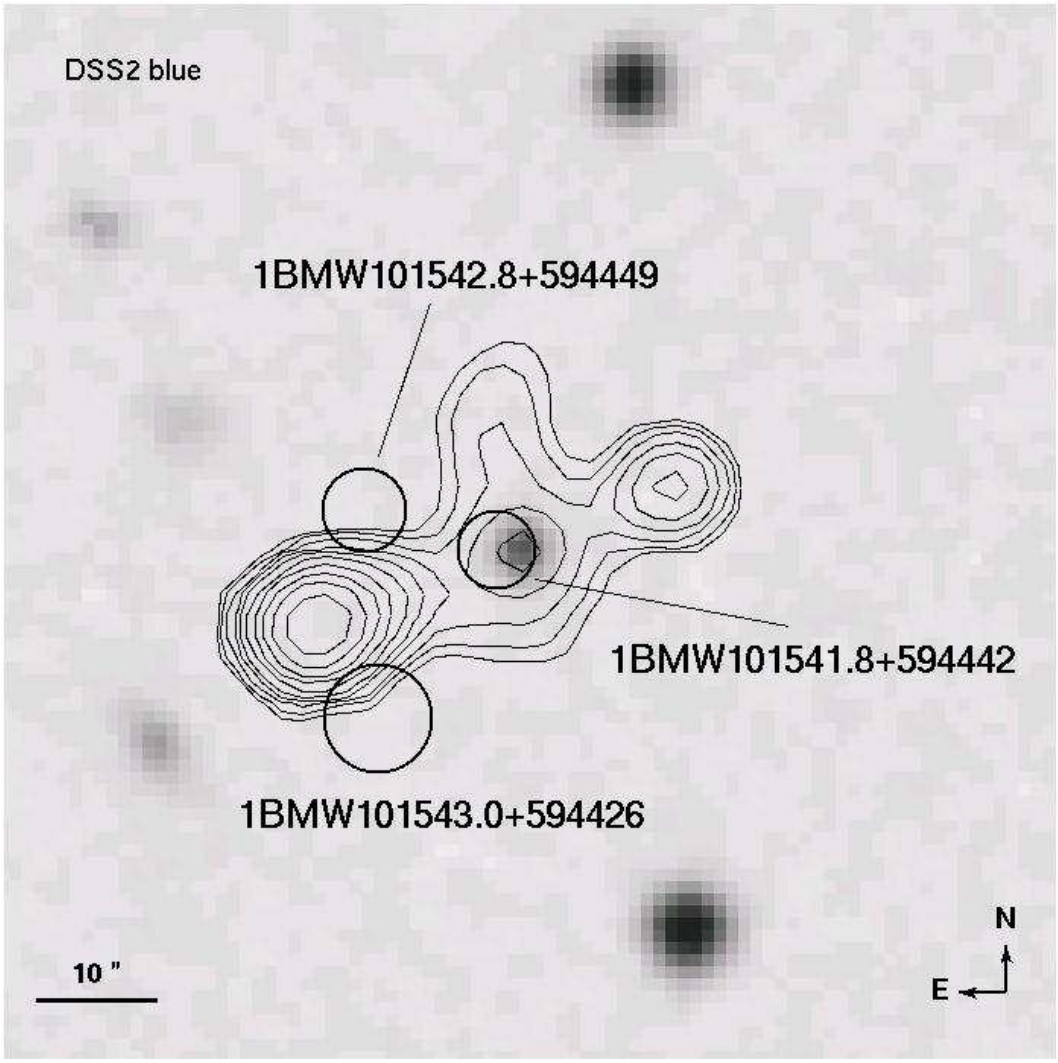

Figure 2.16 The X-ray positions of 1BMW101542.8+594449, 1BMW101541.8+594442 and 1BMW101543.0+594426 superimposed to the corresponding blue image, along with their respective 1σ error circles and a radio FIRST logarithmic contour map showing the two lobes plus core and plume (see text for details).

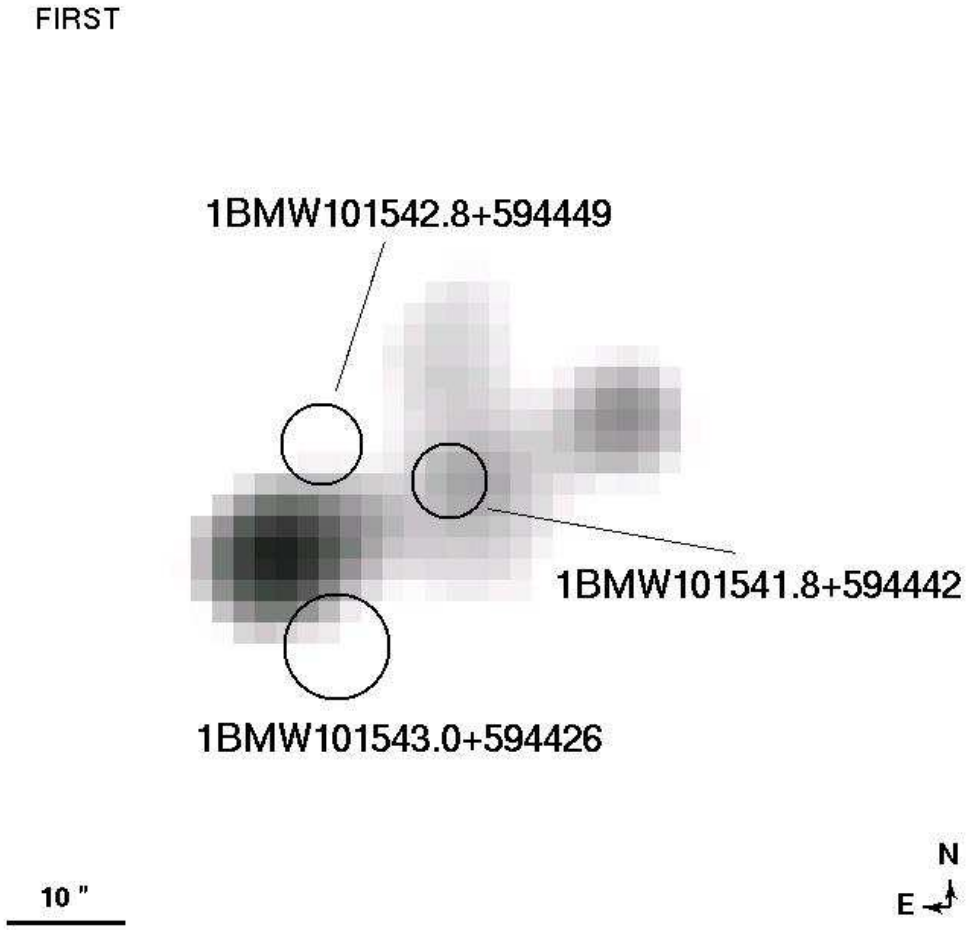

Figure 2.17 The X-ray positions of 1BMW101542.8+594449, 1BMW101541.8+594442 and 1BMW101543.0+594426 superimposed to the corresponding radio FIRST image (in logarithmic scale).

which we see both an approaching and a receding jet, and the galaxy core. An additional feature is present, an extended, faint emission that surrounds the core and elongates itself in a plume in the North direction. An optical source is also associated with the core of radio emission, with BJ=18.1, RF=17.9. Finally we note that this association is present in the QORGCAT, where is correctly identified with a probable AGN and classified (reductively) as a two lobes radio source.

Table 2.7 **NVSS081204+025612**

Name	R.A.	Dec	$\sigma_{R.A.}$	σ_{Dec}	Int. flux 1.4GHz	Maj axis	Min axis	dist
NVSS	J2000	J2000	sec	arcsec	mJy	arcsec	arcsec	arcsec
081204+025612	08 12 04.50	+02 56 12.3	0.06	0.8	52.2	54	23.9	28.7

Table 2.8 **NVSS080730+755017**

Name	R.A.	Dec	$\sigma_{R.A.}$	σ_{Dec}	Int. flux 1.4GHz	Maj axis	Min axis	dist
NVSS	J2000	J2000	sec	arcsec	mJy	arcsec	arcsec	arcsec
80730+755017	08 07 30.75	+75 50 17.3	0.16	0.7	36.9	22.1	19.3	13.8

Table 2.9 **FIRSTJ104928.2+55392**

Name	R.A.	Dec	Err. (90%)	Peak 1.4GHz	Int. 1.4GHz	Maj axis	Min axis	dist
FIRSTJ	J2000	J2000	arcsec	mJy	mJy	arcsec	arcsec	arcsec
104928.2+55392	10 49 28.292	+55 39 27.21	0.91	1.37	0.99	0.00	0.00	8.85

Table 2.10 **FIRST sources near to 1BMW101542.8+594449**

Name	R.A.	Dec	Err. (90%)	Peak 1.4GHz	Int. 1.4GHz	Maj axis	Min axis
FIRSTJ	J2000	J2000	arcsec	mJy	mJy	arcsec	arcsec
101541.6+594444	10 15 41.611	+59 44 43.86	1.45	6.92	42.80	20.32	6.67
101543.3+594439	10 15 43.306	+59 44 39.23	0.16	140.21	162.75	3.12	0.53
101539.4+594451	10 15 39.448	+59 44 50.62	0.12	13.42	14.02	1.98	0.00

2.6 Failed Blank Field Sources: optically identified transient candidates

The six sources of this section are characterized by a possible transient behaviour, i.e. they have been observed in some HRI pointing, but not observed in some other longer HRI or PSPC pointing, like the sources of Section 2.3. At odds with the BFS of Section 2.3, however, these sources, after the boresight correction , have a possible optical counterpart less than 2σ distant. Most of these sources are likely to be stars caught in an X-ray flare. However, some case deserves probably further investigation. The f_X/f_{BJ} reported in Table 2.11 is calculated with the catalog optical association(s) of Table 2.12; for sources without BJ magnitude, the GSC2 limit of BJ=22.5 (in the northern sky) or BJ=23 (in the southern sky) are considered.

Table 2.11 Parameters of transient candidates with optical counterpart.

Name	R.A.	Dec	Err. rad.	Flux	Cts
	bII	N_H	Close ass.	f_X/f_{BJ}	Prob.
	J2000	J2000	$''$	erg cm^{-2} s^{-1}	
		10^{20} cm^{-2}	(sigma)		σ
1BMW223126.9+113658	22 31 27.0	+11 36 59.9	10.4	6.87×10^{-13}	107
	-38.68	5.13	1.3	14	3.5
1BMW070011.0-554424	07 00 10.51	-55 44 19.9	13.06	6.47×10^{-13}	51
	-20.85	6.54	1.5	2-142	5.2
1BMW184854.5+331445	18 48 54.74	+33 14 43.1	8.15	3.78×10^{-13}	47
	14.63	7.72	0.5	0.01-52	5.8
1BMW111537.7-613227	11 15 38.01	-61 32 20.2	4.96	3.33×10^{-13}	41
	-0.93	134	1.8	0.06-73	4.3
1BMW160633.2+175628	16 06 33.6	+17 56 34.0	8.94	3.22×10^{-13}	41
	43.75	3.55	0.6	10	4
1BMW200925.6-662647	20 09 25.34	-66 26 47.3	8.09	2.79×10^{-13}	58
	-32.94	4.94	1.6	1.5	4.2

Table 2.12 Possible optical counterparts of transient candidates.

1BMW223126.9+113658				
Label	R.A.	Dec	Magnitude	Distance
	J2000	J2000		″
A	22 31 27.66	+11 37 08.5	BJ=20.4;RF=17.5	13
1BMW070011.0-554424				
Label	R.A.	Dec	Magnitude	Distance
	J2000	J2000		″
A	07 00 11.58	-55 44 37.7	BJ=20.8, RF=18.8 (ESO), RF=19.3 (AAO), I=18.1	20
B	07 00 09.68	-55 43 58.7	BJ=18.4; RF=17.5(ESO); RF=17.9(AAO); I=17.5;J=16.9; H=16.2; K=15.6	22.3
C	07 00 13.06	-55 44 11.7	RF=20.4;I=18.8	23
1BMW184854.5+331445				
Label	R.A.	Dec	Magnitude	Distance
	J2000	J2000		″
A	18 48 55.04	+33 14 45.4	O=20.8; E=19.7	4.3
B	18 48 55.88	+33 14 43.0	O=19.5; E=17.7; BJ=20.4; RF=18.6; I=18.2	14.3
C	18 48 55.59	+33 14 32.6	O=13.7; E=12.8; BJ=13.3; RF=12.8;I=12.2;J=12.1; H=11.9; K=11.9	14.9
1BMW111537.7-613227				
Label	R.A.	Dec	Magnitude	Distance
	J2000	J2000		″
A	11 15 38.78	-61 32 13.1	J=16.7; H=15.7; K=14.7	8.9
B	11 15 39.40	-61 32 20.1	BJ=15.2; RF=14.3; I=13.9; J=12.9; H=12.4; K=12.3	9.9
1BMW160633.2+175628				
Label	R.A.	Dec	Magnitude	Distance
	J2000	J2000		″
A	16 06 33.91	+17 56 36.8	E=19.4;BJ=20.9;RF=19.5;I=18.7	5.3
1BMW200925.6-662647				
Label	R.A.	Dec	Magnitude	Distance
	J2000	J2000		″
A	20 09 25.46	-66 26 34.3	BJ=19;RF(ESO)=19;RF(AAO)=18.9;I=18.3	13.5

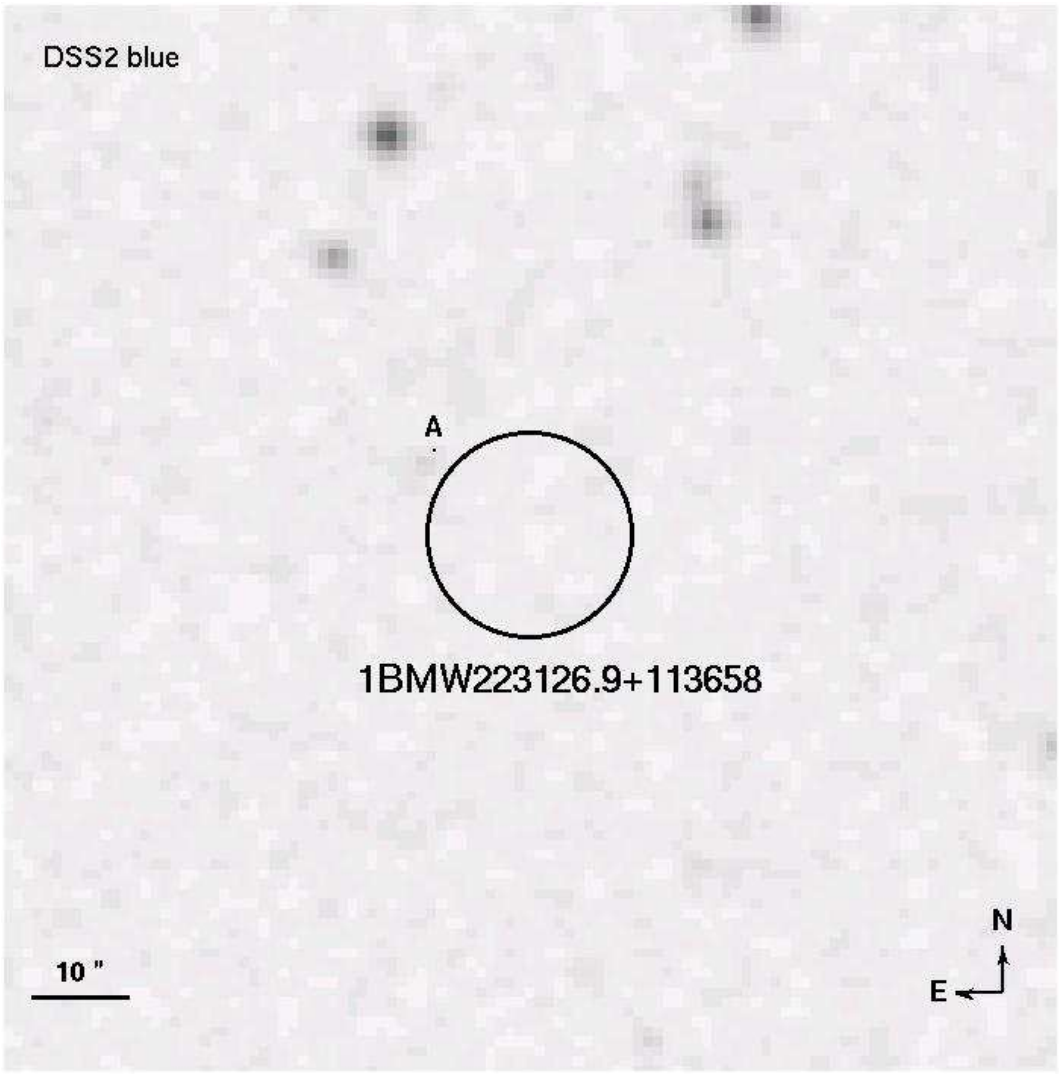

Figure 2.18 The X-ray position of 1BMW223126.9+113658 superimposed to the corresponding blue image along with its 1σ error circle.

1BMW223126.9+113658. This source has been observed in a $\sim$ 2.5 ks pointing in Dec. 1995, and has not been detected in any of the other 13 HRI pointings of the same target (the γ-ray blazar CTA 102), of duration 1-4 ks, performed at a distance of days. We applied the boresight correction to this source with the optical position of the target. The error on the position of 1BMW223126.9+113658 is larger than usual, 10.38". This source seems to coincide with a rather rich region at the limiting magnitude of the surveys. The closest catalog entry to the X-ray position is in the APM-North catalog (McMahon, Irwin & Maddox [144]), at $\sim 0.9\sigma$. In DSS2 digitized images nothing can be seen in correspondence of the APM-North entry. At 13" (1.25 σ) there is

a USNOB1.0 source (object A in Figure 2.18 and Table 2.12). It is also possible to individuate one source in the blue image and two in the red image well inside the 1σ error circle, in both cases at the plate limits.

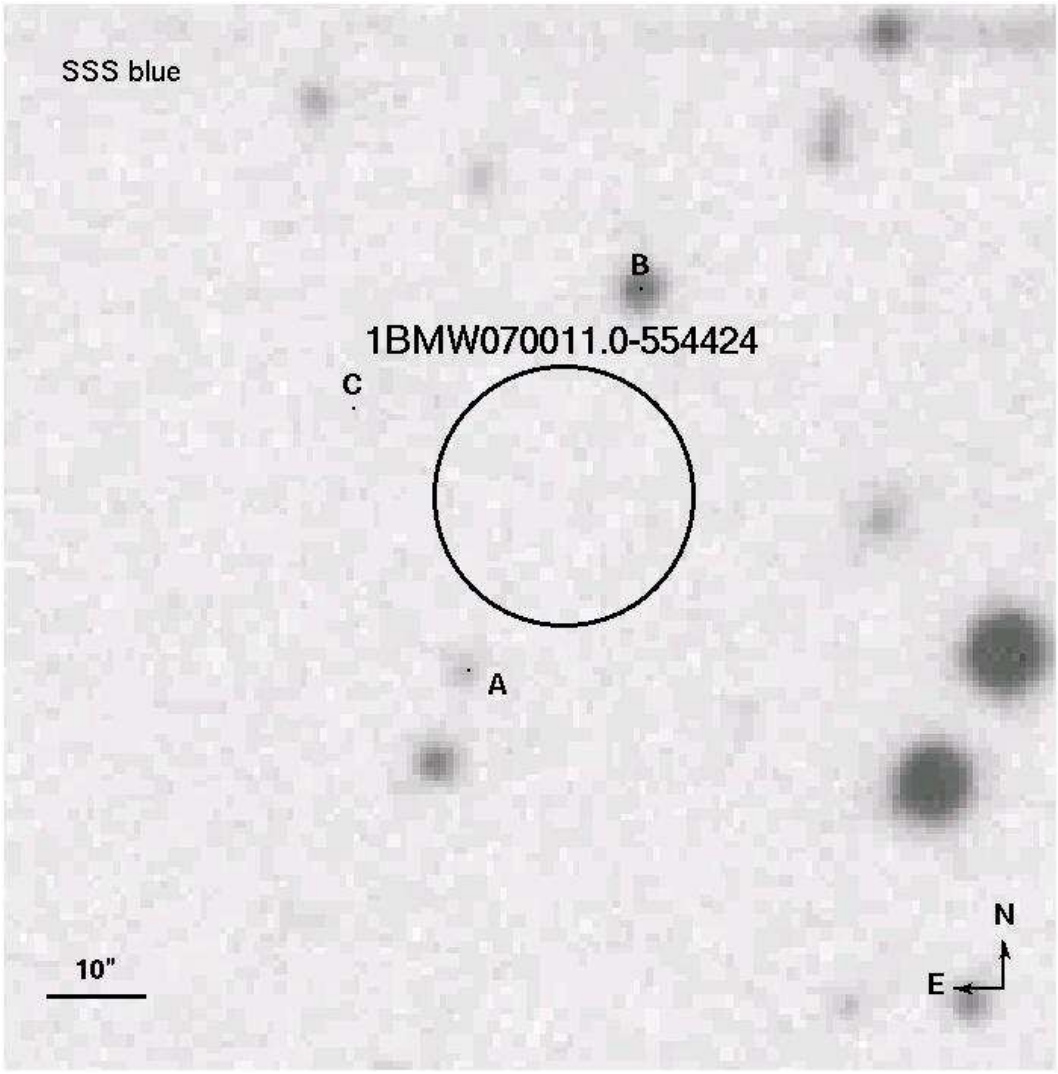

Figure 2.19 The X-ray position of 1BMW070011.0-554424 superimposed to the corresponding blue image along with its 1σ error circles.

1BMW070011.0-554424. This source has been detected in a short ($\sim$ 1 ks) pointing of the galaxy cluster 1E 0657-55.8, while neither a 50 ks HRI pointing nor a 4 ks PSPC pointing showed anything. After the boresight correction (applied with three sources), the closest off-band counterpart is at $\sim$ 20", i.e. $\sim 1.53\sigma$, using the USNOB1.0 optical position (object A in Figure 2.19 and Table 2.12). However there are other two sources less than 2σ distant, objects

B and C in Figure 2.19 and Table 2.12.

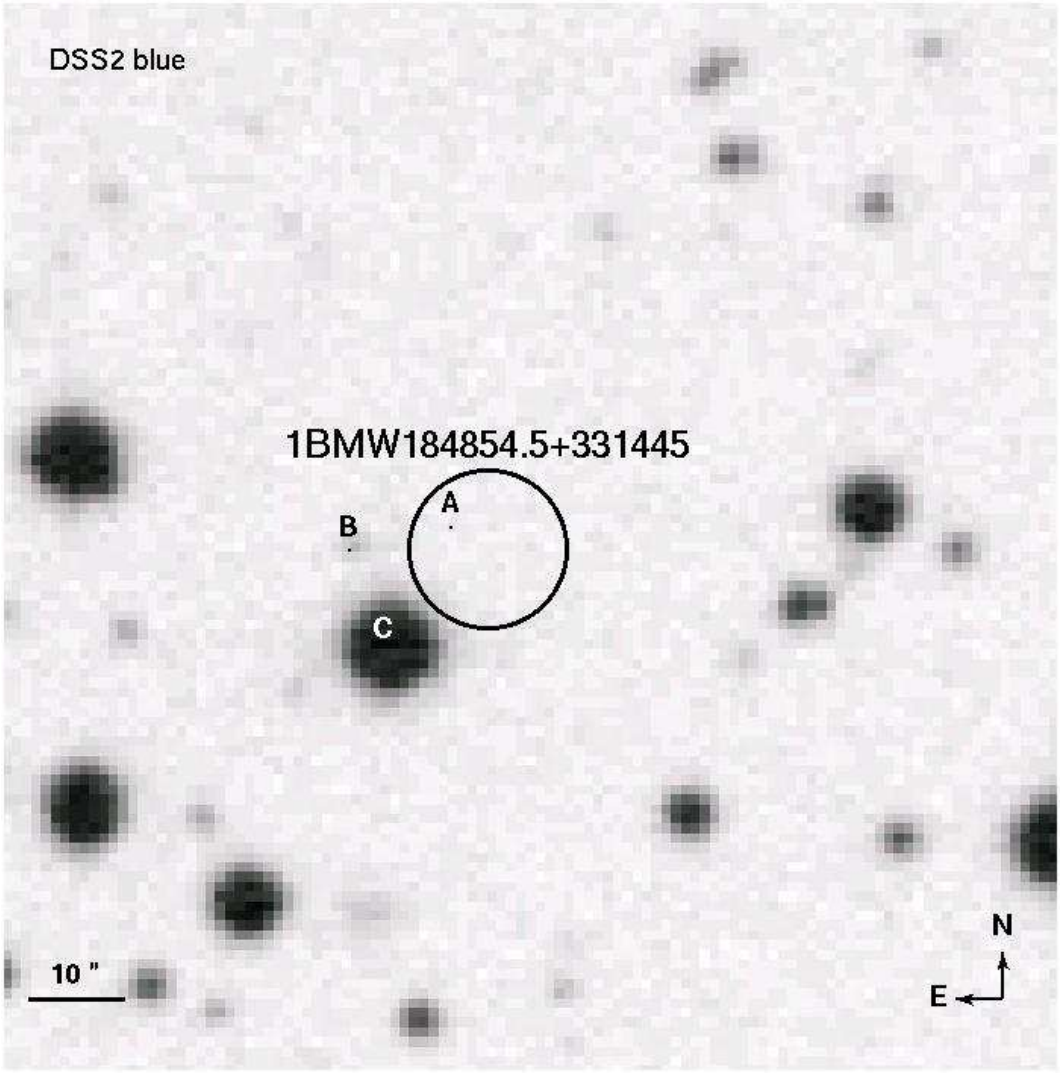

Figure 2.20 The X-ray position of 1BMW184854.5+331445 superimposed to the corresponding blue image along with its 1σ error circles.

1BMW184854.5+331445. This source has been detected in a $\sim$ 2000 s HRI pointing of the eclipsing binary HD 174638 in Nov 1995, while it has not been detected in other 13 HRI observations of the same field (from $\sim$ 500 to $\sim$ 5000 s, some at $\sim$ few days distance). We performed the boresight correction for 1BMW184854.5+331445 with other 5 sources detected in the same pointing. There is a USNOB1.0 entry at about 4.3" ($\sim 0.5\sigma$; object A in Figure 2.20 and Table 2.12), detected only from POSS I scans, not POSS II. If both the X-ray and the optical source are real, there would be evidence of fading for both; this

could strongly support the identification. There are other two sources at ~ 1.8 σ, objects B and C in Figure 2.20 and Table 2.12.

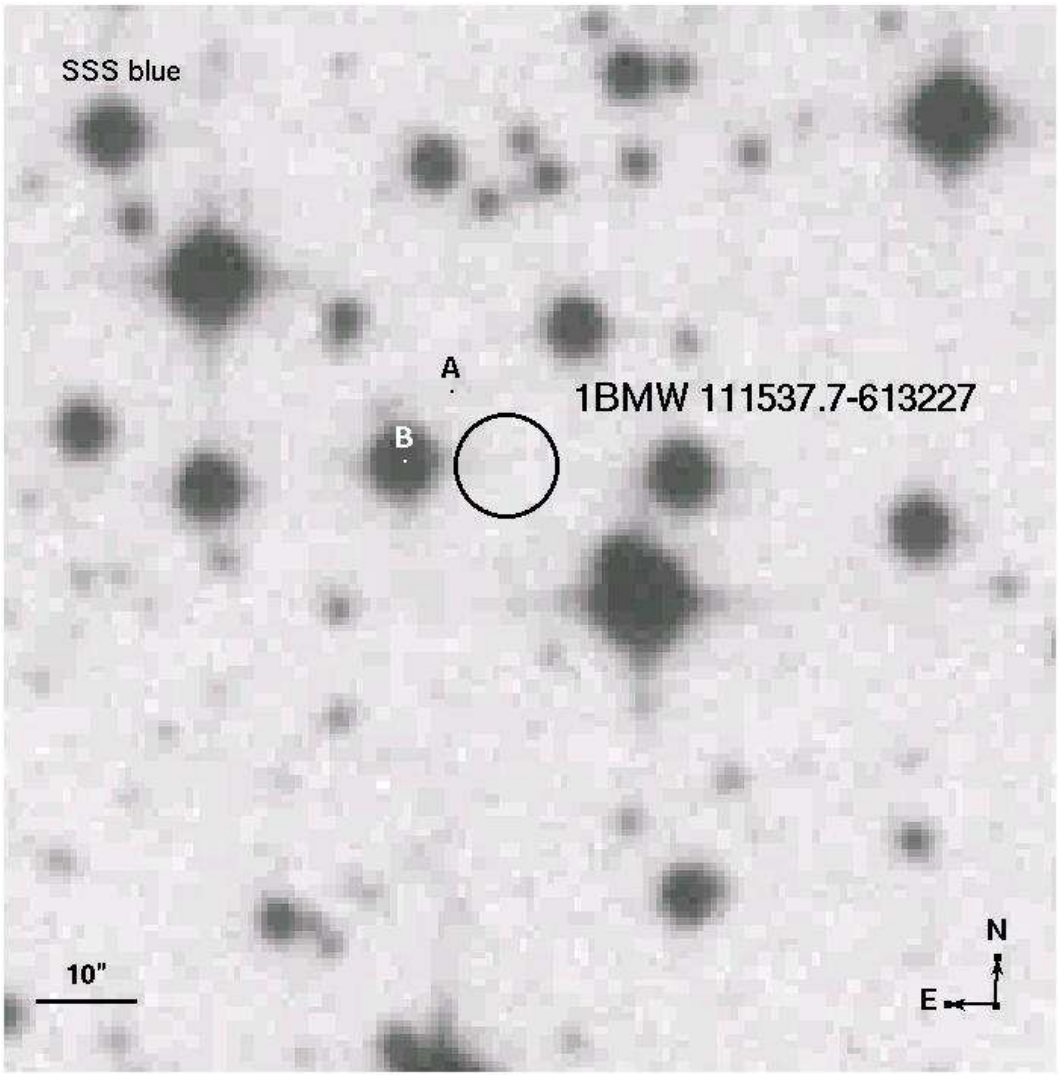

Figure 2.21 The X-ray position 1BMW111537.7-613227 superimposed to the corresponding blue image along with its 1σ error circle.

1BMW111537.7-613227. This source has been detected in a ~ 2 ks pointing in Feb. 1996, while it has not been detected in a $\sim$ 44ks pointing in Aug. 1998, and in a ~ 12 ks PSPC pointing in Jun. 1993. It is on the Galactic plane, with bII$\sim$-1 and Galactic column density 1.34 $\times 10^{22}$ cm^{-2}. We performed the boresight correction using the only one (out of three) other source in the Feb. 1996 pointing not associated with extended emission. The closest optical/near IR source is at $\sim 2\sigma$ (10.2", i.e. 2.07 σ, using USNOB1.0 position, 9.9", i.e. 2

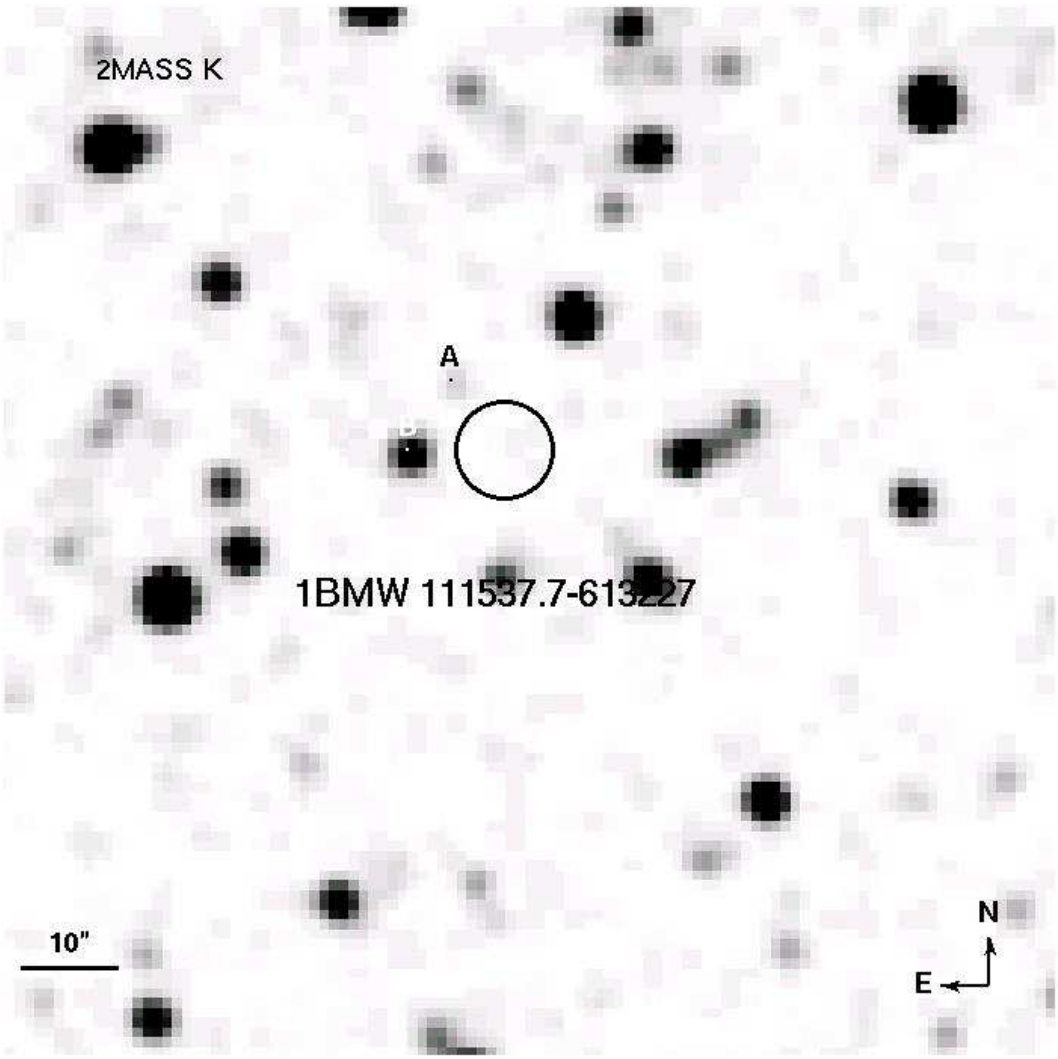

Figure 2.22 The X-ray position 1BMW11537.7-613227 superimposed to the corresponding K image along with its 1σ error circle.

σ, using 2MASS position; object B in Figure 2.21, Figure 2.22 and Table 2.12). In the 2MASS, but not in optical surveys, is present a fainter, redder (K-H$\sim$H-J$\sim$1) and closer source (object A in Figure 2.22 and Table 2.12). We note that the heavy absorption can increase the relative efficiency of near IR surveys in respect to optical surveys, and that the poorly determined X-ray position of 1BMW111537.7-613227, in such a crowded region, hampers at present any hypothesis on the counterpart.

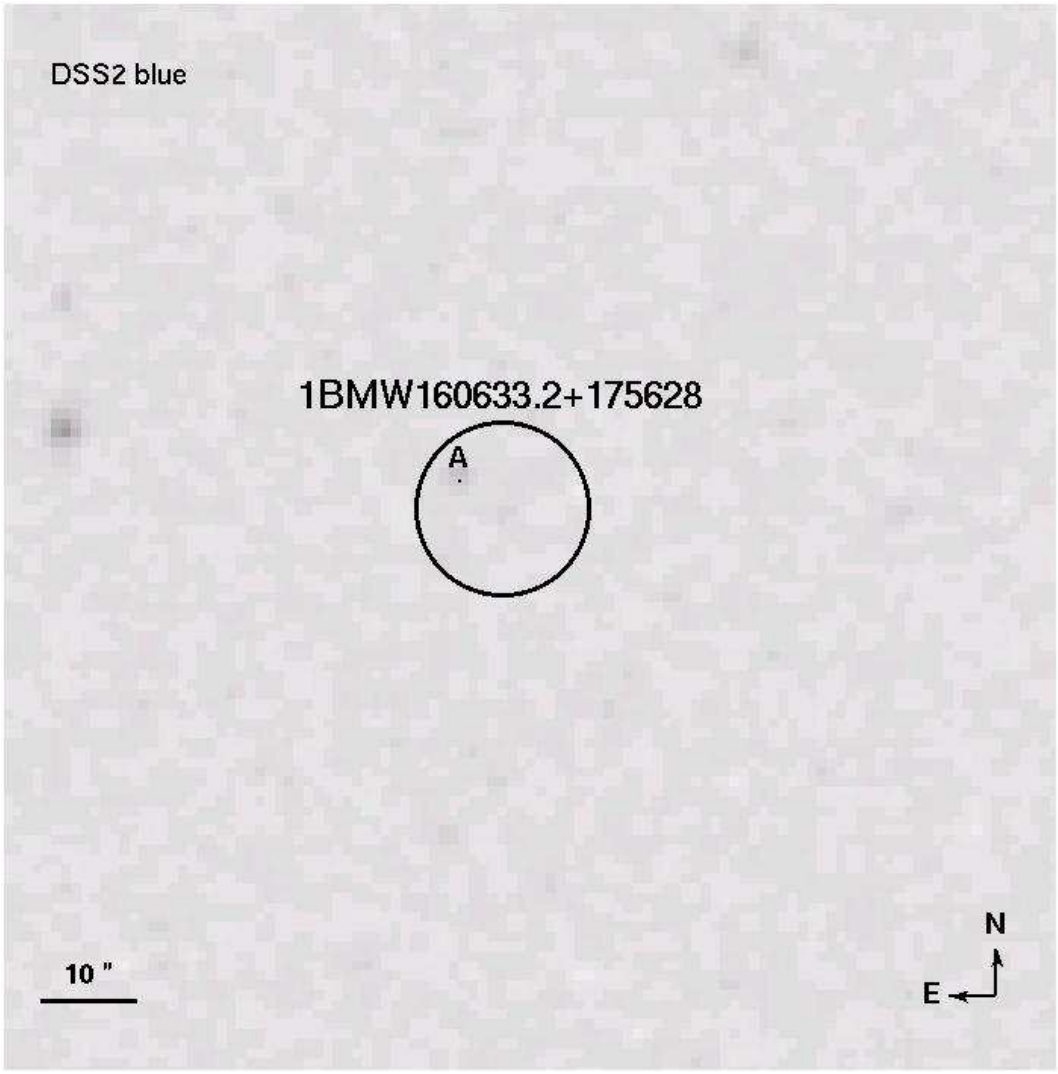

Figure 2.23 The X-ray position of 1BMW160633.2+175628 superimposed to the corresponding blue image along with its 1σ error circle.

1BMW160633.2+175628. This source has been detected in a 2.2 ks pointing in Feb. 1997, while it has not been detected in a much longer one

(55 ks) in Aug. of the same year, nor in a 12 ks PSPC pointing in Aug. 1993. The boresight correction has been effected with the only other source detected in the Feb. 1997 pointing. There is a USNOB1.0 source at only 5.3" (0.6 σ; object A in Figure 2.23 and Table 2.12) from the X-ray position, and no other source in a 3σ radius.

Figure 2.24 The X-ray position of 1BMW200925.6-662647 superimposed to the corresponding blue image along with its 1σ error circle.

1BMW200925.6-662647. 1BMW200925.6-662647 was observed in a ~ 3.6 ks pointing in Jul. 1999, while it has not been detected in a ~ 4.4 ks pointing in Dec. 1998. The boresight correction has been applied using other two sources of the Jul. 1999 pointing. The nearest optical source is at 13.5", i.e. at $\sim 1.6\sigma$,

and it is quite blue (object A in Figure 2.24 and Table 2.12). There are no other catalog sources in a circle of 3σ radius.

2.7 Failed Blank Field Sources with an optical counterpart

This section is dedicated to some BMW sources without automatic cross identifications, but that now, after visual inspection of associated optical images and application of the boresight correction procedure, have a candidate optical identification (see Table 2.13).

Table 2.13 Failed Blank Field Sources with optical counterpart.

Name	R.A.	Dec	Err. rad.	Flux	Cts
	bII	N_H	Close ass.	f_X/f_{BJ}	Prob.
	J2000	J2000	$''$	erg cm^{-2} s^{-1}	
		10^{20} cm^{-2}	(sigma)		σ
1BMW192149.0-585821	19 21 49.42	-58 58 24.1	4.2	1.2×10^{-12}	191
	-27.37	5.12	1.9	0.3	7.4
1BMW023222.3-440010	02 32 22.22	-44 00 09.3	4.44	4.94×10^{-13}	557
	63.44	2.48	0.25	$\geq$108	4.5
1BMW152542.6+705757	15 25 42.64	+70 57 56.6	5.46	4.08×10^{-13}	74
	41.26	2.61	1.6	0.3	4.6
1BMW125848.1+471536	12 58 47.93	+47 15 38.0	4.07	3.22×10^{-13}	211
	70.05	1.13	2.6	1.1-16	5.9
1BMW125848.0+471556	12 58 48.16	+47 15 53.3	4.55	1.71×10^{-13}	471
	70.04	1.13	2.2	0.6-9	4.2

1BMW192149.0-585821. The boresight corrected position of this source is obtained with the position of the center of the pointing, since no other objects were detected. The new BMW-HRI position is compatible (7.9" distant) with the nucleus of the galaxy PGC374930 (Paturel et al. [181]; see Figure 2.25). The optical properties of PGC374930 are shown in Table 2.14. The galaxy is also an IRAS source, IRAS FSC F19174-5904 (Table 2.15). 1BMW192149.0-585821 has been observed also in the RASS (1RXS J192152.3-585818), in two PSPC pointings (1WGA J1921.7-5858a, 1WGA J1921.7-5858b) and by the ASCA GIS (1AXG J192154-585 in the ASCA Medium Sensitivity Survey; Ueda et al. [233]). Positions, fluxes and count rates of associated X-ray sources are resumed in Table 2.16. The X-ray fluxes are compatible with no flux variations. The hardness ratios of the various ROSAT detections point toward a rather hard source, in particular for 1WGA J1921.7-5858b were collected 447, 239 and 74 respectively in the high ($\sim 0.9-2$ keV), mid($\sim 0.4-0.9$ keV) and low($\sim 0.1-0.4$) keV bands. Moreover, the ASCA GIS detection allow us to infer the presence of significant emission harder than the ROSAT passband (the inferred 2-10 keV

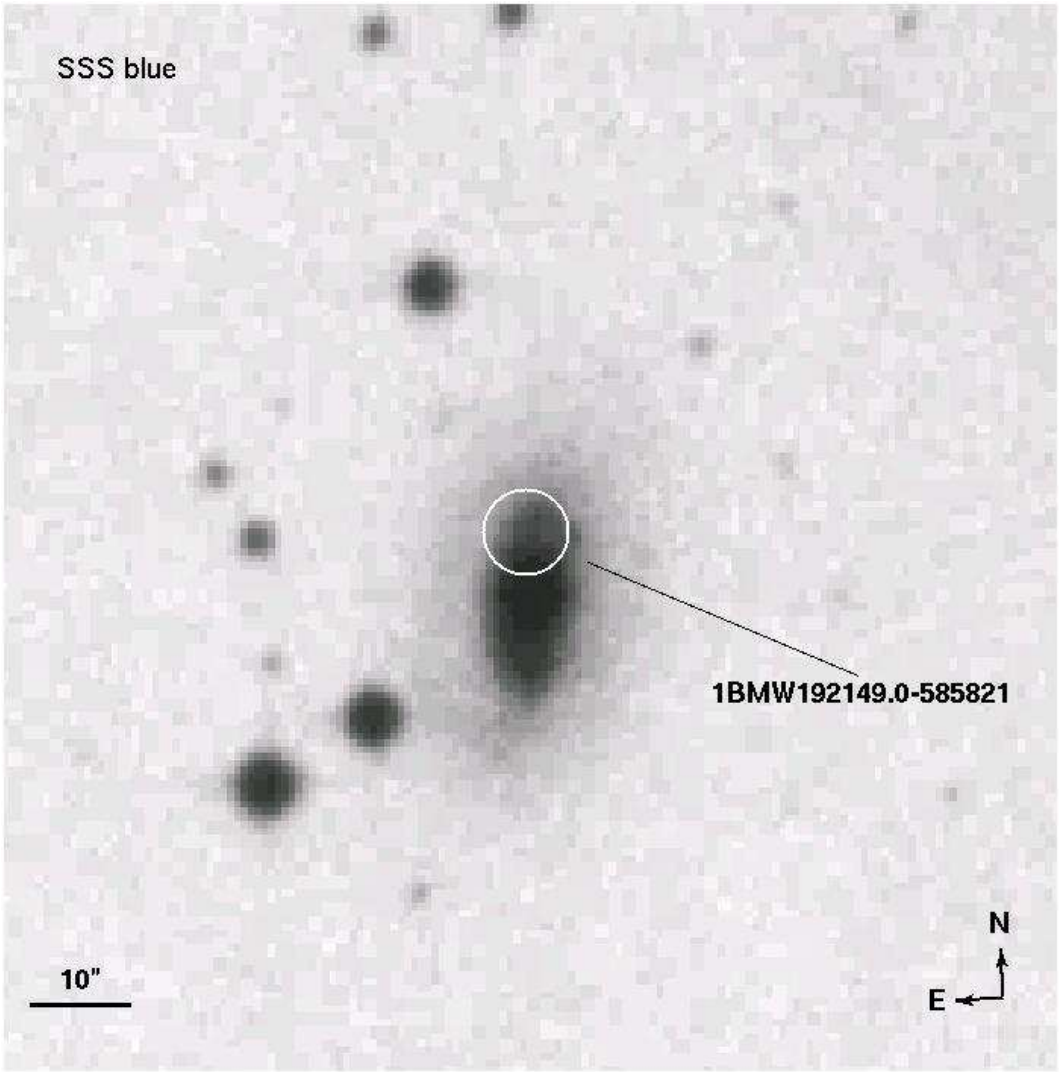

Figure 2.25 The X-ray position of 1BMW192149.0-585821 superimposed to the corresponding blue image along with its 1σ error circle.

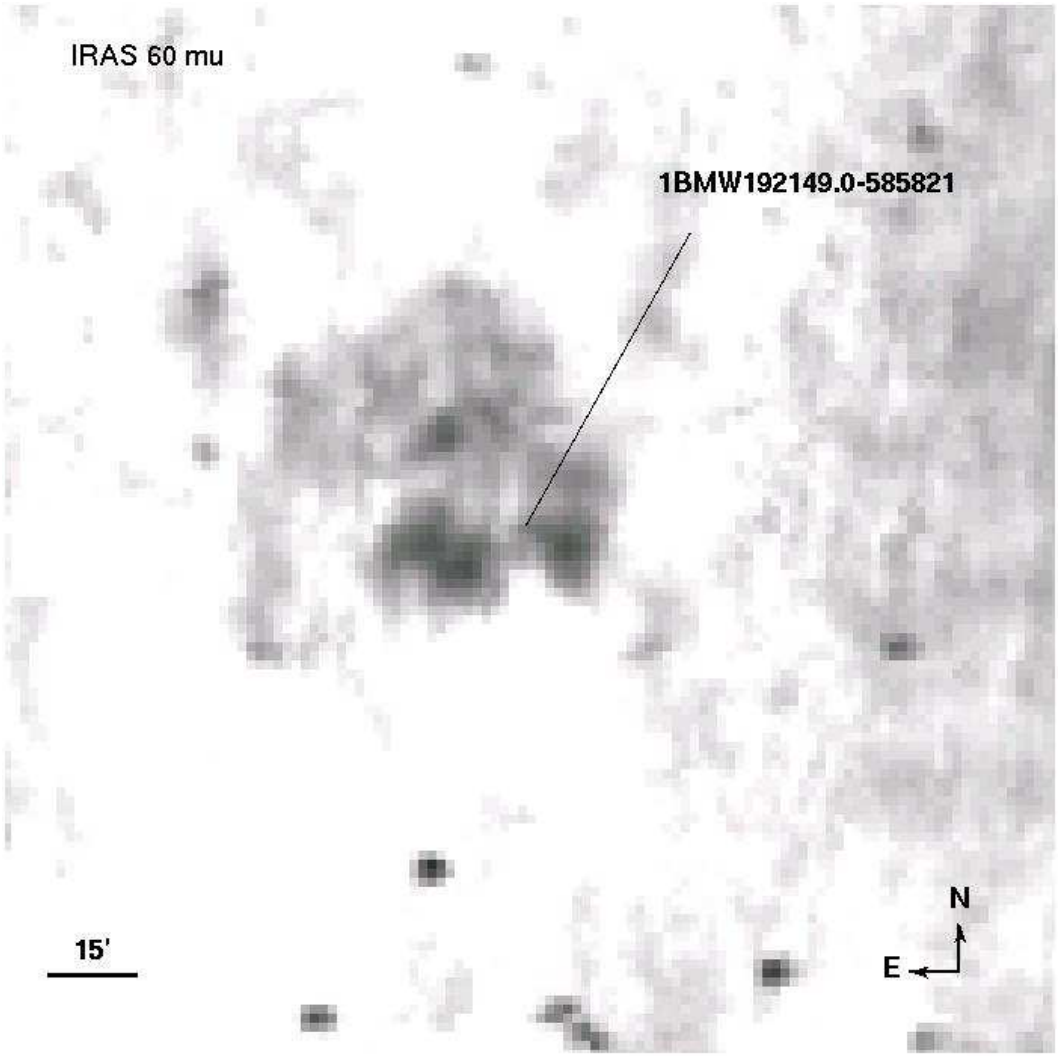

Figure 2.26 An IRAS 60μ image of the region surrounding 1BMW192149.0-585821. The extended source at the center is the dark cloud DCld 338.0-26.9

to 0.7-2 keV flux ratio is 2.5). The f_X/f_{BJ} reported in Table 2.13 is calculated with the HRI f_X of Table 2.13 and the magnitude of Table 2.14. The hard emission and the IRAS source could hint presence of dust. In fact IRAS images show that the source is in the dark cloud DCld 338.0-26.9 (Otrupcek, Hartley & Wang [174], Figure 2.26). Since the galaxy is not obscured in the blue image, it is also possible that is seen through a hole in the cloud. From the optical images (Figure 2.25) the galaxy seem elongated with a bright core and a visible halo. Probably, it is a disk galaxy nearly edge-on. Therefore, we tentatively identify 1BMW192149.0-585821 a Seyfert, even if we need information on the galaxy redshift and more detailed spectrsl analysis to confirm the identification.

Table 2.14 **1BMW192149.0-585821 associations: PGC374930**

Name	R.A.	Dec	logd25	logr25	bt	incl
	J2000	J2000			magn	deg
PGC374930	19 21 49.4	-58 58 32	0.84	0.24	15.71	56.1

Table 2.15 **1BMW192149.0-585821 associations: IRAS FSC F19174-5904**

Name	R.A.	Dec	σ_{maj}	σ_{min}	angle	flux 12μ	flux 25μ	flux 60μ	flux 100μ	dist
	J2000	J2000	arcsec	arcsec	deg	Jy	Jy	Jy	Jy	arcsec
F19174-5904	19 21 43.3	-58 58 36	14	4	90	0.13	0.17	0.38	4.46	48.81

Table 2.16 **1BMW192149.0-585821: associated X-ray sources**

Name	R.A.	Dec	σ	distance	counts	flux
	J2000	J2000	arcsec	arcsec		erg cm^{-2} s^{-1}
1RXS J192152.3-585818	19 21 52.30	-58 58 18.5	25	22.9	23	1×10^{-12} (0.1-2.4 keV)
1WGA J1921.7-5858a	19 21 47.6	-58 58 34	50	17.2	63	1.7×10^{-12}(0.1-2.4 keV)
1WGA J1921.7-5858b	19 21 47.1	-58 58 05	50	26.2	760	2.7×10^{-12}(0.1-2.4 keV)
1AXG J192154-5858	19 21 54.6	-58 58 53	44.4	49.4	1730	5.6×10^{-12}(0.7-7 keV)

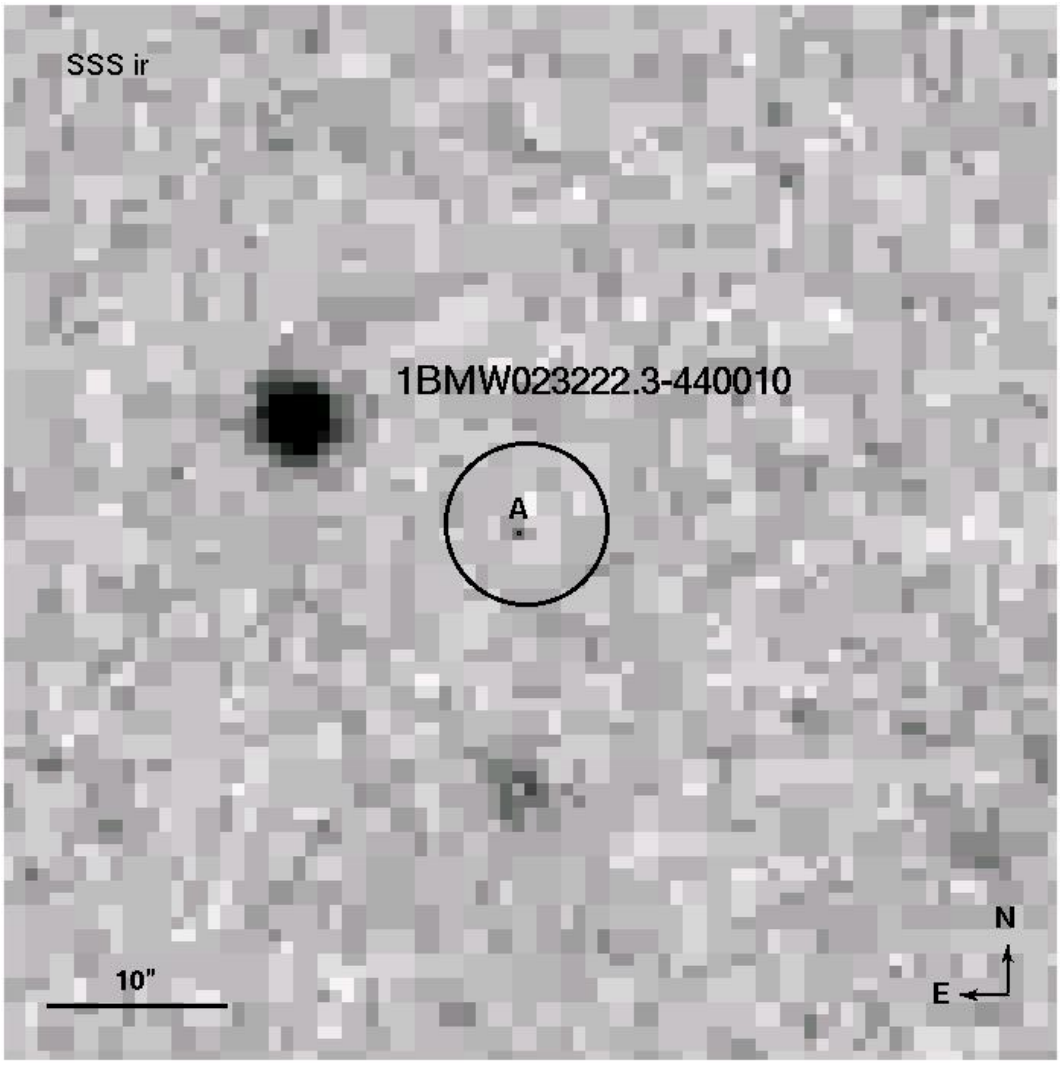

Figure 2.27 The X-ray position of 1BMW1023222.3-440010 superimposed to the corresponding I image along with its 1σ error circle.

1BMW023222.3-440010. The boresight corrected BMW-HRI position of this source has been obtained with five X-ray/optical matches. The source was observed in a 19 ks HRI pointing as well as in a 13 ks PSPC pointing (1WGA J0232.3-4359) and in the RASS (1RXS J023224.1-440008), while it was not observed in two other 11 ks and 9 ks HRI pointings and in a 4 ks PSPC pointing. This implies a variable behaviour, with a timescale of at minimum $\sim$15 days (the separation between the 19 ks and the 9 ks HRI pointings). The reported flux of 1WGA J0232.3-4359 is 6.7×10^{-13} erg cm^{-2} s^{-1}, i.e. roughly the same of the BMW entry, while the RASS flux is slightly higher. The spectrum of 1WGA J0232.3-4359 shows a soft excess, with 356, 288 and 600 photons

observed in high, mid and low bands. There is a faint, not catalogued source at only $\sim 0.5\sigma$ from the boresight corrected X-ray position, in the SSS I image (object A in Figure 2.27). If we do not consider object A, the closest sources are at a distance $> 3\sigma$. The lower limit on the f_X/f_{BJ} written in Table 2.13 assumes the limiting GSC2 value of BJ=23. If we exclude the possibility of a large ($> 3\sigma$) displacement between the X-ray and the real position, the hypotheses put forward for variable BFS have to be considered for 1BMW023222.3-440010 too. In particular, a BL Lac nature would be strongly favoured on a type-2 QSO due to the soft excess in PSPC data, or alternatively a low luminosity transient could be invoked.

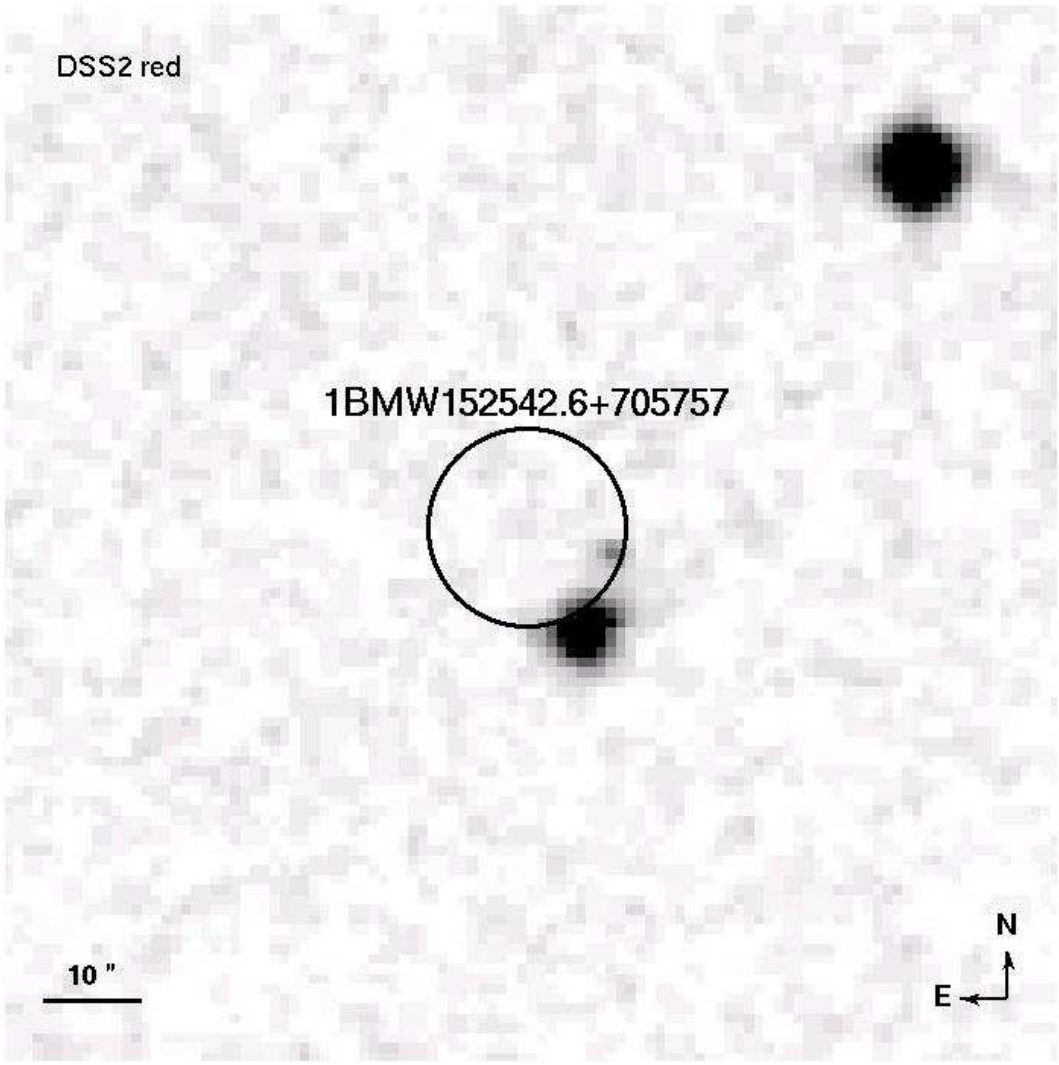

Figure 2.28 The X-ray position of 1BMW152542.6+705757 superimposed to the corresponding red image along with its $10''$ fiducial boresight error circle.

1BMW152542.6+705757. It has not been possible to apply a boresight correction to this source, because it was the only one detected in the pointing. Furthermore, there are no other X-ray observations of this field. Near to the BMW position there is an optical catalogued source, at $\sim 11.5''$ ($\sim 2\sigma$), with magnitude values of O=17.3; E=15.4; BJ=16.7; RF=15.3; I=14.9; J=15.4; H=14.8; K=14.4. This source is reported to have non-stellar (i.e. extended) brightness profile in all the bands. In Table 2.13 we put the f_X/f_{BJ} obtained with this BJ value of 16.7. The inspection of the DSS2 red image, however, shows that this source is actually split in two separated nearby objects (see Figure 2.28), the brighter extended and coincident with the catalog positions, the fainter at about 15 25 40.87 +70 57 54.21, i.e. at $\sim 9''$ (1.6 σ), too faint to judge its extension. In the blue DSS2 image and in the 2MASS images, the fainter source is not seen (probably it is beyond the image limit).

1BMW125848.1+471536/1BMW125848.0+471556. These nearby BMW entries have been observed respectively in a 9.6 ks and in a 53 ks pointing. After the application of the boresight correction procedure (with, respectively, 7 and 12 other positions) we found positions 15.4" distant, i.e. compatibles at 2 σ. The combination of both positions seems to favor the faint object A in Figure 2.29 and Table 2.17, at $\sim$ 10.6" from 1BMW125848.1+471536, $\sim$ 10" from 1BMW125848.0+471556, while the brighter object B in Figure 2.29 and Table 2.17 is almost as close to 1BMW125848.1+471536, at $\sim$ 13.6", but $\sim$ 22.1" distant from 1BMW125848.0+471556. Both A and B seem not stellar in DSS2 images. The BMW flux in the 9.6 ks pointing is a factor $\sim$ 2.5 larger than its equivalent in the 53 ks pointing. Table 2.13 reports the f_X/f_{BJ} values calculated with the BJ magnitudes of Table 2.17. Besides the two HRI pointings, this object has been observed also in a 47 ks PSPC pointing (1WGA J1258.7+4715), with a flux of 2.2×10^{-13} erg cm^{-2} s^{-1}, i.e. in between the two HRI fluxes. The WGA source is soft, with 144, 196 and 513 counts collected in high, mid and low bands. We conclude that the evidence for variability is not compelling, that the source is soft and likely to be connected with optically extended emission (probably object A). The most obvious candidate to satisfy this requisites is some kind of AGN without excess of absorption, though a Galactic nature can not be excluded.

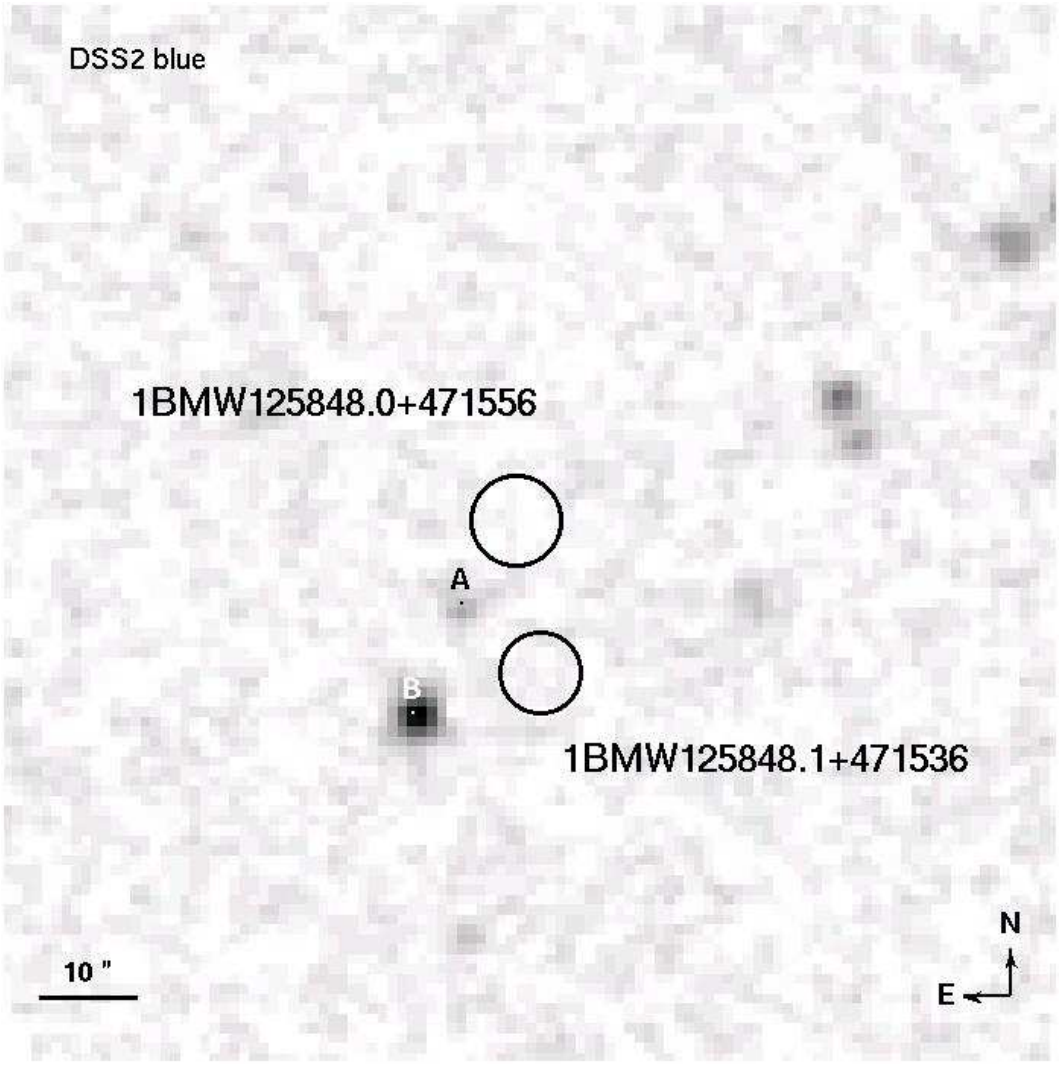

Figure 2.29 The X-ray positions of 1BMW125848.1+471536 and 1BMW125848.0+471556 superimposed to the corresponding blue image along with their 1σ error circles.

Table 2.17 Possible optical counterparts of 1BMW125848.1+471536/1BMW125848.0+471556.

Label	R.A.	Dec	Magnitude	Distance
	J2000	J2000		$''$
A	12 58 48.71	+47 15 45.0	E=20.2;BJ=21.4;RF=20.1	10.6/10
B	12 58 49.19	+47 15 33.9	O=20.2;E=17.9;BJ=18.5; RF=17.2; I=17.6;J=16.7; H=16; K=15.1	13.6/22.1

2.8 Conclusion

All the sources presented in this chapter are peculiar to some degree. While they probably represent populations more common than BFS, the additional information coming from possible cross-identifications balance partially the loss of rarity, and in some cases allow us to propose a tentative, broad class identification. Further observations of these source are required to confirm or refute the identifications and the significance of peculiarities.

Chapter 3

The Ultraluminous X-ray Source NGC 1313 X-2 (MS0317.7-6647) and its Environment[1]

3.1 Introduction

First revealed by the *Einstein* Observatory (see e.g. [66]), point-like, off-nuclear X-ray sources with luminosities significantly exceeding the Eddington limit for one solar mass are being progressively discovered in the field of many nearby galaxies. To date, hundreds of such sources have been found in dozens of galaxies, both ellipticals and spirals (e.g. Colbert & Ptak [49]). These powerful objects, commonly referred to as ultraluminous X-ray sources (ULXs), do not appear to have an obvious Galactic counterpart. Despite some of them have been identified with supernovae or background active galactic nuclei, the nature of most of these sources remains unclear. X-ray spectra have been obtained with the *Einstein*, *ROSAT*, *ASCA* and recently *XMM-Newton* and *Chandra* satellites. Although the statistics is rather poor, in many cases fitting with simple models indicates that the spectral properties are consistent with those of Galactic black hole binaries (e.g. Foschini et al. [72]). About half of them show some degree of variability in the X-ray flux. Among the various possibilities, the most favored explanation is that ULXs are powered by accretion and that they are

[1]We report here Zampieri, L., Mucciarelli, P., Falomo, R., Kaaret, P., Di Stefano, R., Turolla, R., Chieregato, M. & Treves, A.: "The Ultraluminous X-ray Source NGC 1313 X-2 (MS0317.7-6647) and its Environment", 2004, ApJ 603, 523, adapted to the one-column format. A shortened version can be found in Zampieri, L., Mucciarelli, P., Falomo, R., Kaaret, P., Di Stefano, R., Turolla, R., Chieregato, M. & Treves, A.: "Optical counterpart of the ultraluminous X-ray source NGC 1313 X-2", 2004, NuPhS 132, 387. Some ulterior information can be found in Turolla et al. [229], here repoerted as Appendix C.

somewhat special X-ray binaries, either containing an intermediate mass black hole (BH) with $M_{BH} \gtrsim 100\,M_{\odot}$ (e.g. Colbert & Mushotzky [48]; Kaaret et al. [112]) or having beamed emission toward us (e.g. King et al. [122]; Kaaret et al. [113]). For a recent review on the properties of ULXs we refer to Fabbiano & White [68].

Optical observations are of fundamental importance to better assess the nature of these sources but they are still rather scarce (see e.g. Cagnoni et al. [36]; Foschini et al. [73]). Some ULXs have optical counterparts in the Digitized Sky Survey or Hubble Space Telescope images (e.g. NGC 5204 X-1; Roberts et al. [205], Goad et al. [81]) and some appear to be embedded in emission nebulae a few hundred parsecs in diameter Pakull & Mirioni[178].

NGC 1313 X-2 was one of the first sources of this type to be found. It was serendipitously discovered in an *Einstein* IPC pointing toward the nearby SBc galaxy NGC 1313 (Fabbiano & Trinchieri [65]). Originally included in the *Einstein* Extended Medium Sensitivity Survey as MS 0317.7-6647, it is located $\sim 6'$ south of the nucleus of NGC 1313. [218] investigated the nature of MS 0317.7-6647 on the basis of X-ray, optical and radio observations. They identified a possible optical counterpart and concluded that the source could be either a Galactic isolated neutron star or a binary containing a massive BH in NGC 1313. Spectral fits to *ROSAT* PSPC data (Stocke et al. [218],Colbert et al. [47], Miller et al. [152]) yielded results consistent with many single component models. *ASCA* observations (Petre et al. [187], Makishima et al. [135]) are described successfully by a multi-color disk blackbody (MCD) model, representing thermal emission from a standard accretion disk around a BH. A very recent analysis of a *XMM* EPIC-MOS observation of NGC 1313 (Miller et al. [149]) indicates that two spectral components, soft and hard, are required to fit the spectrum of NGC 1313 X-2 and the normalization of the soft component yields a conspicuous mass of the black hole $M_{BH} \gtrsim 830 M_{\odot}$.

We present new optical[2] and *Chandra* observations of NGC 1313 X-2, with the aim to shed further light on its enigmatic nature. In Section 3.2 we present *Chandra* data and re-analyze all the available X-ray observations of NGC 1313 X-2. In Section 3.3 optical observations of the field of this ULX are reported. Finally, the implications of our results on the nature of NGC 1313 X-2 are discussed in Section 3.4.

[2]Based on observations collected at the European Southern Observatory, Chile, Program number 68.B-0083(A).

Table 3.1. Positions of NGC 1313 X-2 and positions and optical magnitudes of field objects

Observatory/Instr.	Object[a]	RA[J2000]	DEC[J2000]	R magnitude (Bessel-Cousins)	Ref.
ROSAT/HRI	NGC 1313 X-2	03 18 22.00±0.50	-66 36 02.3±3.0	–	[211]
XMM/EPIC-MOS	NGC 1313 X-2	03 18 22.34±0.33	-66 36 03.7±2.0	–	[149]
Chandra/ACIS-S	NGC 1313 X-2	03 18 22.18±0.12	-66 36 03.3±0.7	–	this work
ESO/3.6m	A	03 18 21.97±0.05	-66 36 06.5±0.3	19.8±0.2	this work
ESO/3.6m	B	03 18 21.56±0.05	-66 36 00.9±0.3	20.7±0.2	this work
ESO/3.6m	C	03 18 22.34±0.05	-66 36 03.7±0.3	21.6±0.2	his work
ESO/3.6m	D	03 18 20.96±0.05	-66 36 03.7±0.3	17.8±0.2	this work

[a]See Figure 3.3.

3.2 X-ray Data

NCG 1313 X-2 was first observed by *Einstein* with the IPC instrument in 1980. It was then pointed several times by *ROSAT* (PSPC and HRI) between 1991 and 1998 (Stocke et al.[218], Colbert et al. [47], Miller et al. [152], Schlegel et al. [211]), by *ASCA* (SIS and GIS) in 1993 and 1995 (Petre et al. [187], Makishima et al. [135]) and by *XMM* (EPIC) in 2000 (Miller et al. [149]). Most recent data are from a 2002 *Chandra* (ACIS-S) pointing, reported here for the first time. The *Chandra* observation began on 13 Oct 2002 and had a duration of 19.9 ks. The primary goal of the observation was to study sources near the center of the galaxy, but the aim-point was adjusted to also place NGC 1313 X-1, NGC 1313 X-2, and SN 1978K on the S3 chip of the ACIS-S. In addition, we present here a complete analysis of the *XMM* observation, including the EPIC-PN data, which were not considered by Miller et al. ([149]).

3.2.1 X-ray astrometry

An accurate determination of the X-ray position of NCG 1313 X-2 can be obtained from the 2002 *Chandra* pointing, using the *Chandra* aspect solution. Chandra data were extracted from the S3 chip on the ACIS-S and subjected to standard processing and event screening. No strong background flares were found, so the entire observation was used. Because the source is $5'$ off axis, the point spread function was fitted with an ellipsoidal Gaussian ($1.9''$ and $1.1''$ along the two axes, rms values). Also, the pixel with the highest number of counts is offset by $0.8''$ from the center of the fitted ellipse. Taking these uncertainties into account, we conservatively estimate a positional error of $0.7''$ (1-σ). The final *Chandra* position is: α = 03h 18m 22.27s$\pm$0.12s, δ = -66^0 36$'$ 03.8$''\pm0.7''$.

In order to check the accuracy of the *Chandra* aspect solution, we exploited the presence in the field of view of a quite peculiar supernova, SN 1978K, that shows powerful radio and X-ray emission. The *Chandra* position of SN 1978K is α = 03h 17m 38.69s, δ = -66^0 33$'$ 03.6$''$ (J2000), within $0.46''$ from the accurate ($0.1''$) radio position of Ryder et al. ([208]). This is consistent with the expected *Chandra* aspect accuracy.

The position of NGC 1313 X-2 was previously determined from the *ROSAT* HRI ([218, 211]) and *XMM* EPIC-MOS [149] images. Typical 1-σ error boxes are $\sim 3''$ for *ROSAT* HRI and $\sim 2''$ for *XMM* EPIC-MOS. The *ROSAT* and *XMM* positions and corresponding error boxes are summarized in Table 3.1.

3.2.2 X-ray spectrum and lightcurve

We analyzed the *XMM* EPIC data from both the MOS and PN cameras (operated with the medium filter). The EPIC-PN spectrum is reported here for the first time and was extracted directly from the observation data file because

the automatic pipe-line processing failed to produce a standard event list for the EPIC-PN camera. Both reduction procedures (`epchain` and `epproc`) were used to extract the data obtaining similar results (differing typically by a few percents). Data screening, region selection and event extraction were performed using standard software (XMMSELECT v 2.43.2). An analysis of the MOS and PN light curves shows that solar flares are present in both datasets. They were filtered out using the standard criterion (total off-source count rate above 10 keV < 5 counts s^{-1} for MOS and < 15 counts s^{-1} for PN). We extracted the source counts from a circle of $40''$ and $30''$ for the MOS and PN cameras, respectively. The proximity of the source to one of the CCD edges in the EPIC-MOS data requires some care. We eliminated the area of a box aligned and superimposed to the CCD boundary to avoid contamination from bad pixels close to the source. The background was selected from a circle of $60''$ in a nearby source-free region of the same CCD. Ancillary and response files were produced using the appropriate XMMSELECT tasks. Data were grouped to require at least 20 counts per bin for the MOS data and 40 counts per bin for the PN data, and were then analyzed and compared with different models using XSPEC (v 11.2.0). To minimize the effects of possible relative calibration uncertainties, the fit of the MOS1, MOS2 and PN spectra were performed with an overall normalization constant (those of the two MOS cameras differ by $\sim 10\%$, while that of the PN instrument is larger by $\sim 25\%$). The count rates are 0.08 counts s^{-1} for the MOS cameras and 0.25 counts s^{-1} for the PN.

In order to reconstruct the X-ray variability history of NGC 1313 X-2, we have carefully re-analyzed also the *ROSAT* and *ASCA* observations. Extraction regions for the *ASCA* SIS data were chosen with care to avoid contamination from the CCD edges and SN 1978K. Spectra were grouped to require at least 15 counts per bin for the *ROSAT* data and 20 counts per bin for the *ASCA* data.

The results of the spectral analysis are listed in Table 3.2. The statistics of the *XMM* EPIC spectrum is significantly improved including the EPIC-PN data (the PN camera has almost twice more counts than each single MOS instrument). An absorbed power-law does not provide a satisfactory fit of the joint MOS1, MOS2 and PN spectra ($\chi^2_{red} = 1.2$ for 249 *d.o.f.*). Two components models provide a significant improvement over single component ones. The best fit is obtained with an absorbed soft, thermal component plus a power-law. Adding a MCD model to the power-law results in an improvement of the fit which is significant at the $\sim 4.5/5$ (`epchain`/`epproc`) σ level. Figure 3.2 shows the results for a MCD+power-law fit. The resulting best fitting parameters are $kT = 200^{+50}_{-40}$ eV, $\Gamma = 2.23^{+0.15}_{-0.09}$ and $N_H = 3.13^{+0.92}_{-0.37} \times 10^{21}$ cm^{-2} for the inner disk temperature, photon index and column density, respectively (see Table 3.2). There are residuals in the fit (mainly in the EPIC-PN spectrum) that suggest the possible presence of emission lines. We emphasize that the EPIC-PN data provide marginal evidence for the presence of a soft component even at low metallicities. Reducing the abundances of the absorbing gas at 0.5 solar,

a simple power-law fit of the EPIC-PN data has $\chi^2_{red} = 1.24$ (89 *d.o.f.*), while a MCD+power-law fit gives $\chi^2_{red} = 1.15$ (87 *d.o.f.*). Finally, it is worth noting that the value of kT is $\sim 25\%$ larger (although consistent within 1-σ) than that derived by Miller et al. ([149]).

In Figure 3.1 we report the X-ray flux derived from all the available observations of NGC1313 X-2. The fluxes were consistently derived from the best fit parameters of the X-ray spectral analysis reported in Table 3.2. An approximate estimate of the errors, based on counting statistics, is 5-10%. The *Chandra* point is not included in Figure 3.1 because of pile-up problems. The unabsorbed 0.2–10 keV flux from both the *XMM* EPIC-MOS and PN instruments agree within $\sim 20\%$ and give an average value of 2.4×10^{-12} erg cm^{-2}s^{-1}. This value is lower by a factor ~ 2 than that estimated by Miller et al. ([149]). Variability of up to a factor 2 on a timescale of months is clearly present and it is reminiscent of the behavior observed in Galactic X-ray binaries. If uncertainties in the best-fitting spectral parameters are taken into account, the amplitude of variability is reduced but not eliminated. This suggests that a compact object is present in NGC 1313 X-2. If the emission is isotropic and the distance is that of the host galaxy ($\simeq 3.7$ Mpc; Tully [228]), the X-ray luminosity in the 0.2–10 keV range is $L_X \simeq (3-6 \pm 0.5) \times 10^{39}$ erg s^{-1}. If at maximum the source radiates at the Eddington limit L_{Edd}, the BH mass is $\sim 50\, M_\odot$. Sub-Eddington accretion would imply an even larger mass.

Interestingly, comparing data from the first and second epoch *ASCA* observations, the X-ray flux of NGC 1313 X-2 appears to increase with increasing spectral hardness (see Table 3.2). This behavior is similar to that observed in the ULXs of the Antennae galaxy (Fabbiano et al. [67]) and it is opposite to what is usually seen in Galactic BH X-ray binaries (e.g. Cyg X-1).

Table 3.2. Parameters of the fit of *ROSAT*, *ASCA* and *XMM* observations

Observatory/Instr.	Obs. Id.	Model	N_H (10^{21} cm^{-2})	Parameters	χ^2_{red} (dof)	F_X^a (10^{-12} erg cm^{-2} s^{-1})	$F^b_{0.2-10\,\mathrm{keV}}$ (10^{-12} erg cm^{-2} s^{-1})
ROSAT/PSPC	rp600045n00	Power-law	$1.06^{+2.14}_{-0.50}$	$\Gamma = 2.40^{+1.40}_{-0.60}$	0.83 (20)	1.4	2.6
		Blackbody	$0.17^{+0.20}_{-0.15}$	$kT = 0.27^{+0.05}_{-0.03}$	1.01 (20)	0.34	0.38
ROSAT/PSPC	rp600504n00	Power-law	$1.74^{+2.95}_{-1.31}$	$\Gamma = 2.20^{+1.50}_{-0.90}$	1.43 (22)	1.5	1.8
		Blackbody	$0.09^{+0.23}_{-0.09}$	$kT = 0.35^{+0.05}_{-0.07}$	1.32 (22)	0.37	0.44
ASCA/GIS+SIS	60028000	Power-law	$4.24^{+0.41}_{-0.41}$	$\Gamma = 1.99^{+0.03}_{-0.09}$	0.99 (171)	1.3	3.2
		MCD	$1.15^{+0.35}_{-0.34}$	$kT = 1.38^{+0.07}_{-0.07}$	0.89 (171)	2.1	2.6
ASCA/GIS+SIS	93010000	Power-law	$4.74^{+0.50}_{-0.50}$	$\Gamma = 2.43^{+0.09}_{-0.07}$	1.28 (139)	0.50	2.2
		MCD	$1.06^{+0.31}_{-0.31}$	$kT = 1.08^{+0.04}_{-0.04}$	1.31 (139)	0.86	1.0
XMM/EPIC-MOS+PN	0106860101	Power-law	$2.69^{+0.18}_{-0.16}$	$\Gamma = 2.42^{+0.07}_{-0.07}$	1.20 (249)	2.1	
		MCD	$0.70^{+0.06}_{-0.06}$	$kT = 0.90^{+0.02}_{-0.02}$	2.29 (249)	0.86	
		CompTT[c]	$1.67^{+0.43}_{-0.45}$	$kT = 3.00^{+0.11}_{-0.09}$ $T_0 = 0.15^{+0.03}_{-0.03}$ $\tau = 4.69^{+0.10}_{-0.10}$	1.11 (248)	1.2	
		MCD+Power-law	$3.13^{+0.92}_{-0.37}$	$kT = 0.20^{+0.04}_{-0.05}$ $\Gamma = 2.23^{+0.15}_{-0.09}$	1.09 (247)	2.4	
		MCD+Power-law[d]	$3.67^{+0.94}_{-0.52}$	$kT = 0.20^{+0.10}_{-0.07}$ $\Gamma = 2.23^{+0.12}_{-0.08}$	1.07 (247)	2.0	

[a]Unabsorbed flux in the 0.1–2.0 keV (*ROSAT*), 2.0–10.0 keV (*ASCA*) and 0.2–10.0 keV (*XMM*) energy bands

[b]Unabsorbed flux extrapolated in the 0.2-10.0 keV band using the web interface to PIMMS (v 3.3)

[c]Thermal comptonization model with Wien soft photon input

[d]Abundance 0.5 solar

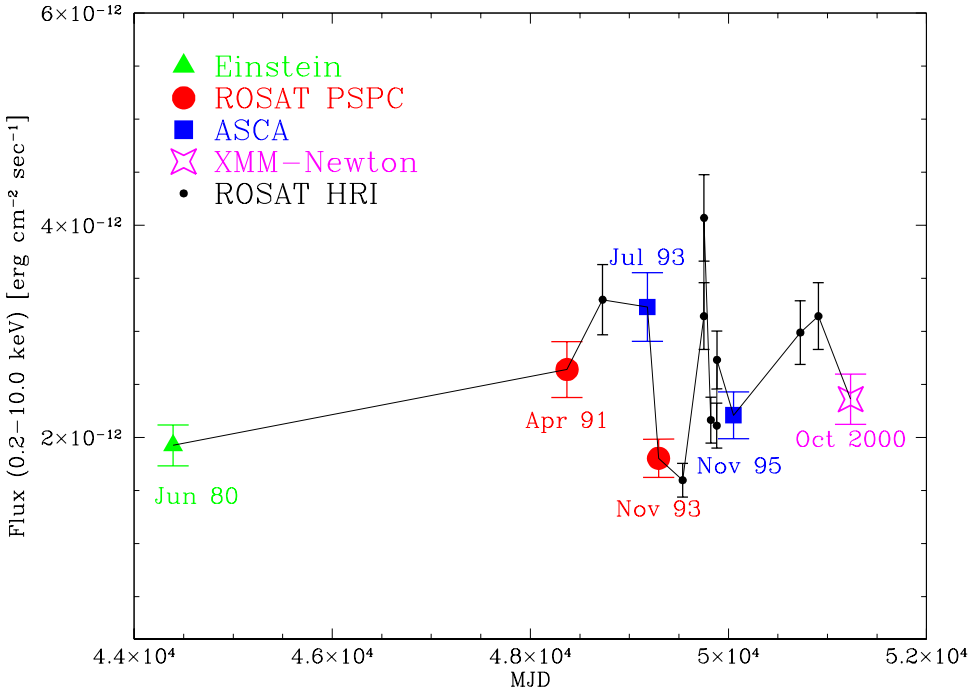

Figure 3.1 The 0.2-10 keV light curve of NGC 1313 X-2 from all presently available data. Fluxes were de-absorbed and, when necessary, extrapolated in the 0.2–10 keV interval using the web interface to PIMMS (see Table 3.2). For the *Einstein* IPC observation, we adopt the value reported by [79]. For the *ROSAT* PSPC and *ASCA* GIS+SIS observations, the fluxes were derived from the best fit parameters of the power-law model reported in Table 3.2. For the *ROSAT* HRI data ([211]) a power-law spectrum with $\Gamma = 2$ and $N_H = 3 \times 10^{21}\,\mathrm{cm}^{-2}$ was assumed (in agreement with the best fit parameters derived from the spectral analysis). For the *XMM* EPIC data, the flux is calculated from the best fit MCD+power-law model reported in Table 3.2.

3.3 Optical Observations

Optical images of the field of NGC 1313 X-2 in the R-band (Bessel filter) were taken on 16 January 2002 with the 3.6 m telescope of the European Southern Observatory (ESO) at La Silla (Chile). We used EFOSC2 with a Loral/Lesser CCD of 2048×2048 pixels yielding a field of view of $\sim 5' \times 5'$ at a resolution of $0.314''$/pixel (re-binned by a factor 2). The night was clear with a seeing of about $1''$. Four images were obtained for a total exposure time of 1320 s. Standard reduction of the data (including bias subtraction and flat-field correction) was performed within the IRAF (v 2.12) environment.

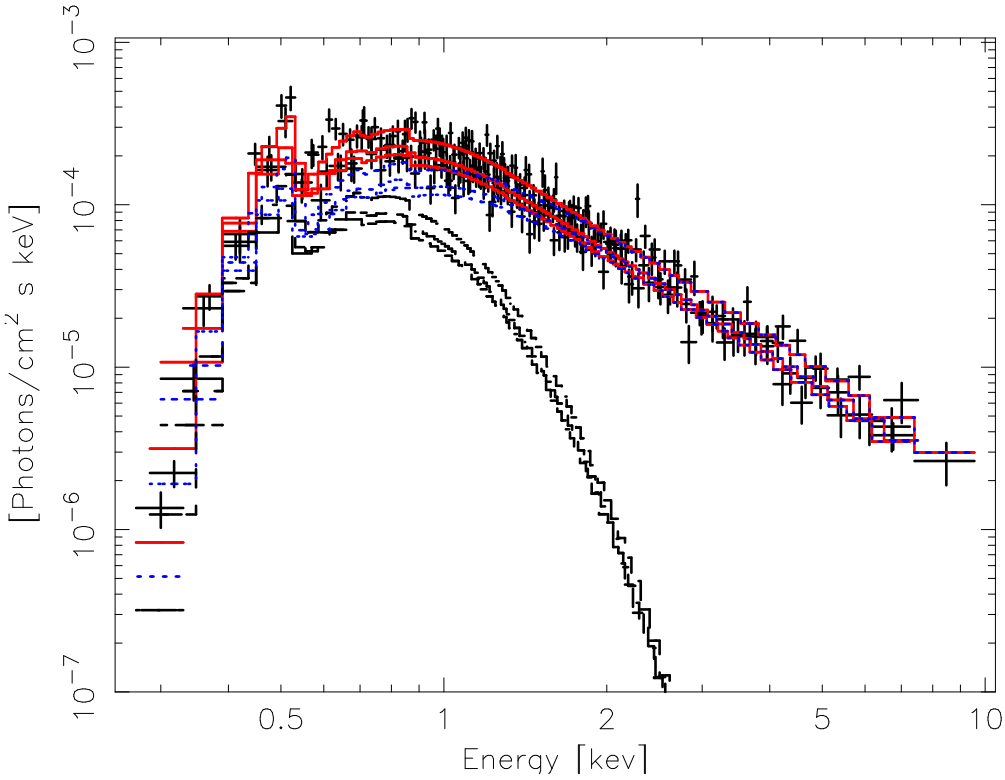

Figure 3.2 X-ray spectrum of NGC 1313 X-2 from the *XMM* EPIC-MOS and PN cameras. The solid line represents the combined best fitting model spectrum, while the dashed and dotted lines are the MCD and power-law components respectively.

A spectrum of one of the field objects (object A; see below) was secured on the same night. We performed low-resolution (13.4 A, grism#4) spectroscopy for a total exposure time of 1200 s. After applying standard corrections and sky subtraction, cosmic rays were removed and the spectrum was corrected for atmospheric extinction. At the time of the optical observations object A had already been imaged at the 1.1 m Las Campanas telescope by Stocke et al. ([218]) and was considered a possible counterpart of NGC 1313 X-2. Although the new accurate *Chandra* position rules out an association with this object (see below), the spectrum can be used to gain insight on the properties of a surrounding nebula, possibly associated with the X-ray source (see e.g. Pakull & Mirioni[178]).

3.3.1 Astrometry and photometry of field objects

Our four ESO images were astrometrically calibrated using an IRAF task (PLTSOL) and performing a polynomial interpolation starting from the positions of GSC2 ESO field stars. The internal accuracy of this procedure was estimated

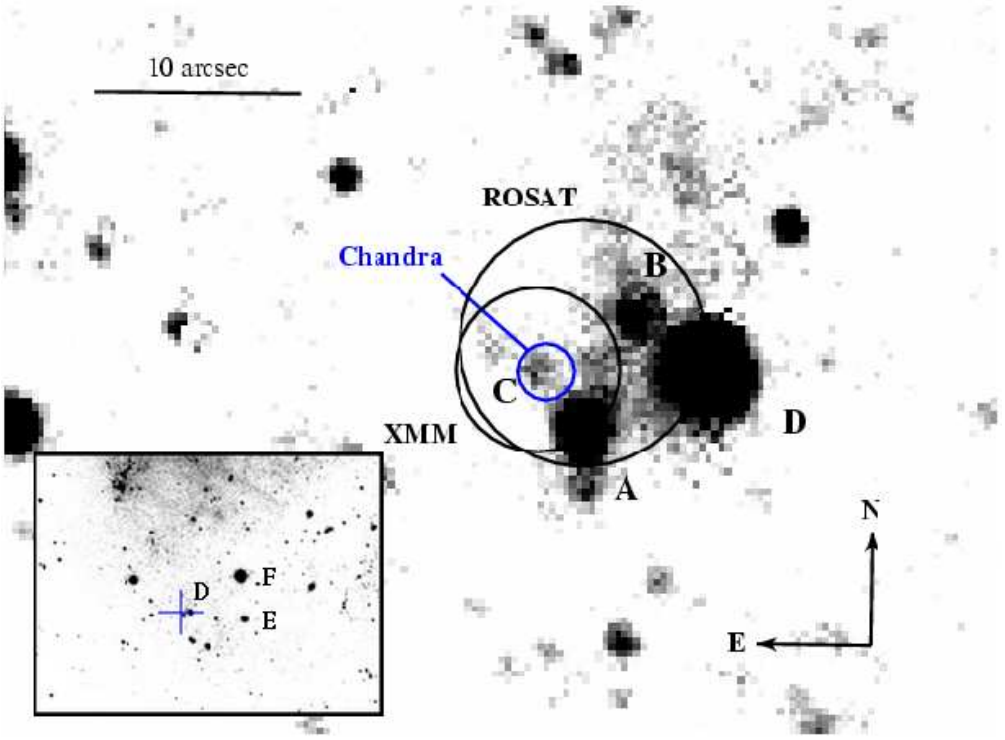

Figure 3.3 ESO 3.6m R-band (Bessel filter) image of the field of NGC 1313 X-2. The circles show the *ROSAT* HRI, *XMM* EPIC-MOS and *Chandra* ACIS-S positions. The estimated 90% confidence radii are 6″ for HRI, 4″ for EPIC-MOS and 1.4″ for ACIS-S. Labels A, B, C and D mark the four field objects inside or close to the X-ray error boxes. The insert at the bottom-left shows a larger portion of the image with the position of the X-ray source (*cross*).

comparing the actual positions of a number of GSC2 stars not used for astrometric calibration with the positions contained in the catalog. The accuracy is 0.3" (1-σ). The four calibrated images were then summed together and the resulting image is shown in Figure 3.3.

In order to check for the relative systematics between the optical and X-ray astrometric calibrations, we used again the position of SN 1978K. This supernova is inside the *Chandra* field of view but outside our optical image. Thus, we analyzed also an archival image of SN 1978K (from the Padova-Asiago Supernova Archive) taken on 13 September 1999 with the same telescope and a similar instrumental set-up (ESO 3.6m+EFOSC/2.9+R#642, exposure time 180 s). After calibrating the archival image, the position of SN 1978K is $\alpha =$ 03h 17m 38.605s, $\delta =$ -66^0 33′ 03.13″ (J2000). This is within 0.28″ from the radio position of [208], improving significantly upon the previous optical position by the same authors. The difference between the centroids of the optical and *Chandra* positions of SN 1978K is 0.69″ ($\alpha_{opt} - \alpha_X =$ -0.085s, $\delta_{opt} - \delta_X =$

-0.47″). Although this difference is small and comparable with the statistical errors, we decided to apply this correction to the *Chandra* position of NGC 1313 X-2 to eliminate any systematic error between the optical and X-ray astrometric calibrations. The resulting *Chandra* position of NGC 1313 X-2 is reported in Table 3.1.

The photometry of the objects in our optical image was performed calibrating the frame with the *R*-band magnitudes of 23 stars from the SuperCosmos Sky Survey (Hambly, Irwin & MacGillivray [97]) homogeneously distributed over the field of view. The internal accuracy of this calibration is 0.2 mag. Aperture (5″ radius) magnitudes are reported in Table 3.1.

3.3.2 Spectroscopy of the emission nebula

The two-dimensional spectrum of the field around object A (Figure 3.4) shows clear emission lines extending for tens of arcsecs from east to west, confirming the existence of an extended ($\sim$ 400 pc) optical emission nebula that was first found in deep H_α images by Pakull & Mirioni ([178]). A one-dimensional spectrum of the field was extracted over an aperture of 0.9″ (3 pixels) from two regions east-ward and west-ward of the position of object A and adjacent to it (Figure 3.5). Wavelength and relative flux calibration were applied to the data. The one-dimensional spectrum shows strong emission lines of H_α, H_β, [SII] $\lambda\lambda$ 6717–6731 A, [OI] λ 6300 A and [OIII] $\lambda\lambda$ 4959-5007 A. The shift of the centroid of the lines ($\sim$ 10 A) is consistent with the recession velocity of the galaxy and indicates that the emission nebula is located in NGC 1313.

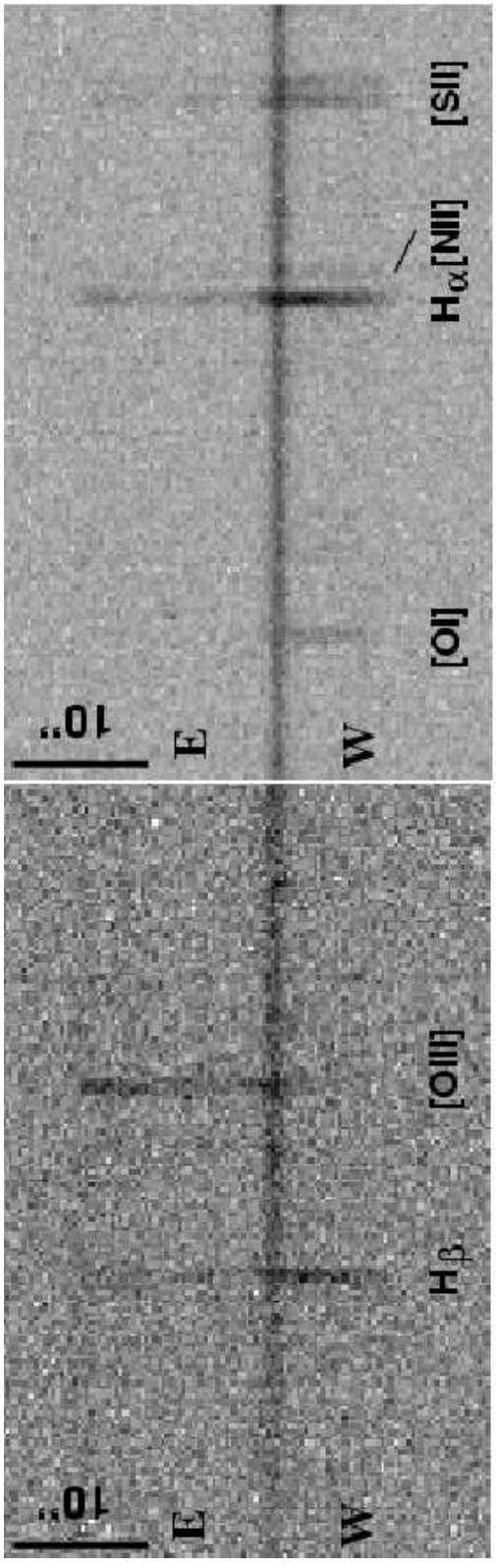

Figure 3.4 Two-dimensional spectrum (ESO 3.6m+EFOSC2+grism#4) of the field around object A. The slit (1.2″) is oriented in the east-west direction. The wavelength intervals are 4500–5300 A (left panel) and 6150–6900 A (right panel).

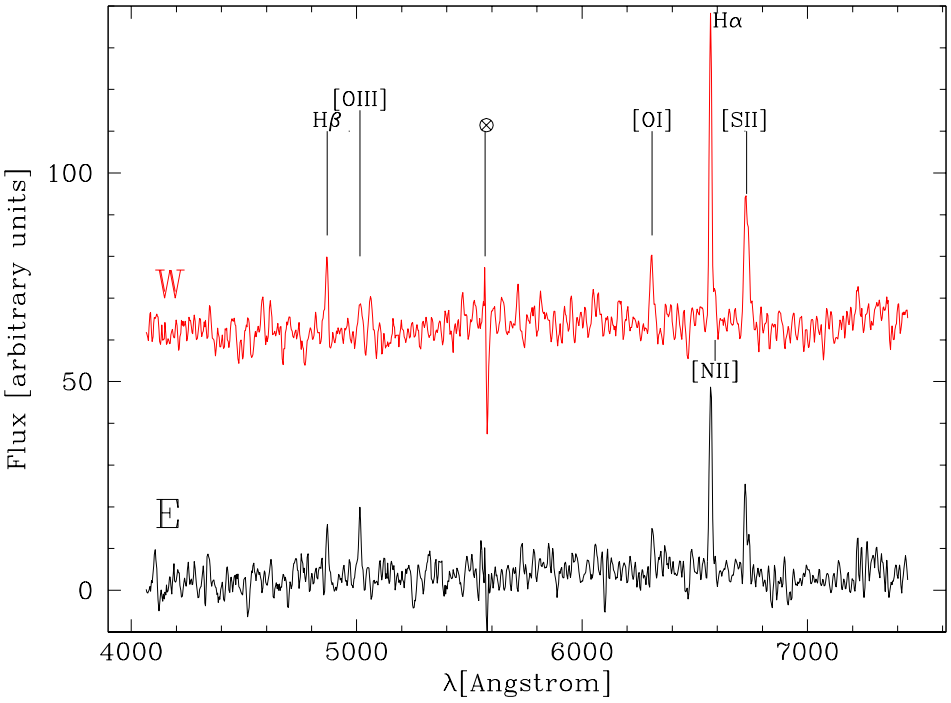

Figure 3.5 One-dimensional spectrum (F_λ) of the nebula around NGC 1313 X-2. The lower (upper) spectrum is extracted in a region east-ward (west-ward) of the position of object A (see text for details). The symbol $\otimes$ marks a residual contamination from an emission line of the sky.

It is worth emphasizing the abrupt change in the absolute and relative intensity of the emission lines from east to west, indicating variations in the physical conditions and/or geometry of the emission nebula. In particular, strong emission from [OIII] is present on the east side but almost absent on the west side, while emission from H_α, [SII], [OI] and other elements is present on the west side but weaker or absent on the east side. A careful inspection of the line intensity profiles (in particular those of H_α and [SII]) reveals a fairly symmetric, broadly peaked profile, centered at $\sim 2''$ west of the position of object A, and a weaker, roughly constant intensity component extending in the east direction.

3.4 Discussion

Our *Chandra* position of NGC 1313 X-2 (Table 3.1) is shown in Figure 3.3, together with the *ROSAT* HRI [211] and *XMM* EPIC-MOS [149] error boxes, overlaid on our ESO image. All measurements are consistent within 1-σ. The distance of the centroids of objects A, B and D with respect to the *Chandra* position is $3.6''$, $4.1''$ and $7.3''$, respectively. Even taking into account the statis-

tical error on the optical positions ($0.3''$), these three objects can be ruled out at a significance level of at least 3-σ. On the other hand, object C is inside the Chandra error box and its position coincides within 1-σ with that of NGC 1313 X-2, making it a likely counterpart.

From the maximum absorbed X-ray flux of NGC 1313 X-2 ($f_X \sim 2 \times 10^{-12}$ erg cm^{-2} s^{-1}) and optical magnitude of object C ($R = 21.6$), we estimate $f_X/f_{opt} \sim 500$. This value is very high, in agreement with the suggestion by [35] that ULXs can be selected on the basis of their large f_X/f_{opt}. Only Isolated Neutron Stars (INSs), heavily obscured AGNs and luminous X-ray binaries can reach such large values of the X-ray/optical flux ratio. INSs are extreme in this respect, with $B \approx 25$ optical counterparts and typical X-ray-to-optical flux ratios $\gtrsim 10^5$ (see e.g. Kaplan, Kulkarni, S.R. & van Kerkwijk ([116]) The presence of the relatively bright ($R \sim 21.6$) object C in the *Chandra* error box makes this possibility unlikely. Furthermore, known INSs exhibit different spectral properties with no significant variability. On the other hand, a heavily obscured AGN is expected to have a rather hard X-ray spectrum and to emit significantly in the near-infrared (see e.g. Brusa et al. [32]). Given the X-ray luminosity of NGC 1313 X-2, an infrared magnitude $K \approx 12$ is expected were it an obscured AGN. The lack of any IR counterpart on a K image of the 2MASS All Sky Image Service down to a limiting magnitude $K \simeq 14$ (10-σ) and the softer X-ray spectrum of NGC 1313 X-2 make this possibility unlikely, although a low resolution optical spectrum of object C is definitely required to settle this issue. Our accurate *Chandra* position and optical identification favor a very luminous X-ray binary in NGC 1313 as the likely explanation for NGC 1313 X-2. As a reference, the X-ray/optical flux ratio of persistent BH binaries at maximum is $\gtrsim 10 - 100$, while that of soft X-ray transients in outburst can reach 2000 (Masetti [138]). This is in line with the alleged binary nature of ULXs and is consistent with the observed properties of this source, such as the X-ray variability and the observed X-ray spectrum, including the presence of a soft component probably produced by an accretion disk.

If indeed NGC 1313 X-2 is a black hole binary, the X-ray spectral parameters, in particular the temperature of the MCD fit (hereafter referred to as T_{MCD}), can be used to estimate the BH mass. This is similar to what done by Miller et al. ([149]) using the normalization of the MCD fit and, as discussed below, we reach similar conclusions. The effective temperature of a standard accretion disk depends on radius as $T^4 = (3GM_{BH}\dot{M}/8\pi\sigma r_{in}^3)(r_{in}/r)^{3/4}[1 - (r_{in}/r)^{1/2}]$, where $\dot{M}$ is the accretion rate and r_{in} is the innermost disk radius (e.g. Frank, King & Raine [75]). Assuming that T_{MCD} represents an estimate of the maximum disk temperature, it is $(3GM_{BH}\dot{M}/8\pi\sigma r_{in}^3)^{1/4} = \alpha T_{MCD}$, with $\alpha \simeq 2$. Neglecting relativistic corrections and assuming that the disk terminates at the innermost stable circular orbit of a Schwarzschild BH, it is: $M_{BH}/M_\odot = (\dot{M}c^2/L_{Edd})f^4(\alpha T_{MCD}/1.5 \times 10^7\,\mathrm{K})^{-4}$, where f is a color correction factor ($f \sim 1.6 - 1.7$, Shimura & Takahara[215], Zampieri, Turolla, & Szuszkiewicz

[250]). Given the strong dependence of M_{BH} on temperature, any uncertainty in the accretion physics and radiative transfer may induce significant errors in the resulting value of M_{BH}. So, the inferred spectroscopic measurement of the BH mass should be taken simply as an approximate estimate. The low inner disk temperature obtained from the two-components fit to the *XMM* EPIC spectrum ($kT \sim 200$ eV) implies $M_{BH} \approx 90 f^4\, M_\odot$ ($\alpha \simeq 2$) for Eddington limited accretion, somewhat larger than that derived from the flux. This result removes the need for a rapidly spinning BH (invoked by Makishima et al. [135] from an analysis of the *ASCA* data) and agrees with the conclusion of Miller et al. ([149]) that NGC 1313 X-2 contains an intermediate mass BH. The large inferred BH mass does not require beamed emission. Then, the estimated accretion rate (assuming 10% efficiency) is $\dot{M} \sim 10^{-7}\, M_\odot\, \mathrm{yr}^{-1}$, forcing the mass reservoir to be a companion star.

From the apparent magnitude ($R = 21.6$) and absorption ($A_R \simeq 1.7$, computed from the X-ray best fitting column density $N_H \sim 3 \times 10^{21}$ cm^{-2}; Bohlin, Savage & Drake [26]) of object C, we estimate an absolute magnitude $M_R \simeq -7.9$ and a luminosity in the range $\sim 7 \times 10^4 - 10^6 L_\odot$, depending on the adopted bolometric correction. If this originates from the companion star, the inferred luminosity is consistent with a $\approx 20 M_\odot$ main sequence star or a $\sim 15 - 20 M_\odot$ evolved OB supergiant (e.g. Bowers& Deeming [28]), making NGC 1313 X-2 a high-mass X-ray binary. In luminous Galactic X-ray binaries, the reprocessed optical emission from the disk may be significant. Assuming that 20–30% of the X-ray flux produced in the innermost part of the accretion disk intercepts the outer regions, for realistic values of the albedo ($\gtrsim 0.9$; e.g. de Jong, van Paradijs & Augusteijn [56]) few percents of the X-ray luminosity ($\approx 10^{38}$ erg s^{-1}) can be absorbed and re-emitted in the optical band. Characteristic emission lines of X-ray-ionized H, He or N, typically seen in luminous Galactic X-ray binaries should then be detectable in the optical spectrum. Also X-ray heating of the companion star itself may contribute to the optical emission. If the optical luminosity comes in part from X-ray re-irradiation, the mass of the companion would be lower. Taking $M_2 \sim 20 M_\odot$ as an upper limit for the mass of the companion, the mass ratio of the binary is $q = M_2/M_{BH} \lesssim 0.4 f^{-4} \ll 1$. Writing the binary separation as $a = 2.16 R_2 [q/(1+q)]^{-1/3}$ (Paczyński [175]), the orbital period of the system is $P \gtrsim 0.15 (R_2/100\, R_\odot)^{3/2} f^2 (M_{BH}/50\, M_\odot)^{-1/2}$ yr. According to King et al. ([122]), the system should not be a persistent X-ray source.

Although difficult to reconcile with the properties of the environment surrounding NGC 1313 X-2 (see below), we can not rule out also that the optical emission detected in the *Chandra* error box originates from a stellar cluster (see e.g. the case of a ULX in NGC 4565; Wu et al. [247]), in which case NGC 1313 X-2 may be a low-mass X-ray binary in the cluster.

The mass accretion rate required to produce the observed luminosity may in principle be provided by Roche-lobe overflow from an evolved companion or by a wind from a supergiant. In the first case, evolutionary swelling of the companion

keeps pace with the increase in Roche lobe size and the system remains self-sustained: accretion is likely to proceed through a disk. In the second case, assuming 10% accretion efficiency and that the BH can capture $\sim 1\%$ of the mass outflow, the wind must be very powerful ($\dot{M} \sim 10^{-5}\, M_{\odot}\, \mathrm{yr}^{-1}$). A lower efficiency would require too high a gas supply, so a disk is needed even in a wind-fed system. In this case, however, the disk is probably much smaller than in a Roche-lobe overflow system and the optical emission dominated by the supergiant. On the other hand, in a Roche-lobe overflow system, an extended, possibly re-irradiated accretion disk should contribute heavily in the UV and B bands, producing strong emission lines. Thus, the two modes of mass supply are likely to be distinguishable by optical spectroscopy.

We now turn to discuss how our optical observations can be used to constrain the environment of NGC 1313 X-2. Figures 3.4 and 3.5 reveal that NGC 1313 X-2 is likely to be associated with an optical emission nebula, recognizable also in a H_{α} image taken by Pakull & Mirioni ([178]). From the velocity (80 km s^{-1}) and flux of H_{β}, they derive an impressive mechanical energy of $3 - 10 \times 10^{52}$ erg for the expanding ionized gas, and suggest that the nebula is inflated by a relativistic jet from NGC 1313 X-2. Our measured ratio of [SII]/H_{α} (~ 0.5) is consistent with that expected from a shock-ionized supernova remnant, a stellar wind-shocked nebula or diffuse ionized gas (Matonick & Fesen [139]). However, the inferred diameter and energy of the nebula are too large to be consistent with a single supernova event, unless it was produced by a hypernova similar to SN 1998bw (see e.g. Iwamoto et al. [108]). In fact, it could be the result of several explosion events (multiple supernova remnant) or be originated by the intense wind of hot stars, possibly the parent stellar association of NGC 1313 X-2. As discussed in the previous section, the nebula appears to have some internal structure: a comparatively brighter, fairly symmetric component west of the position of NGC 1313 X-2 and a weaker, slightly elongated one extending in the east direction. The brighter part of the nebula has [SII]/H_{α}=0.58, the weaker one has [SII]/H_{α}=0.44 and intense [OIII] emission. Different possibilities may explain the irregular appearance of the nebula. As suggested by Pakull & Mirioni ([178]), the varying line intensity may be caused by reprocessed emission from the X-ray ionized interstellar medium where the physical conditions (in particular the density) vary on a scale ~ 100 pc. However, the nebular emission may also arise from two physically distict components: a wind-shocked nebula produced by a possible parent stellar association of NGC 1313 X-2 and a multiple supernova remnant. This hypothesis seems to be confirmed also by the marginal detection of (possibly extended) UV emission in an image of the *XMM* Optical Monitor (see Figure 3.6), in coincidence with the brighter component. Clearly, the weaker component may still be a jet-inflated nebula, as suggested by Pakull & Mirioni ([178]).

Finally, we note that, although NGC 1313 X-2 is somewhat hotter and much more luminous, the [OIII] signature in the eastern portion of the nebula is

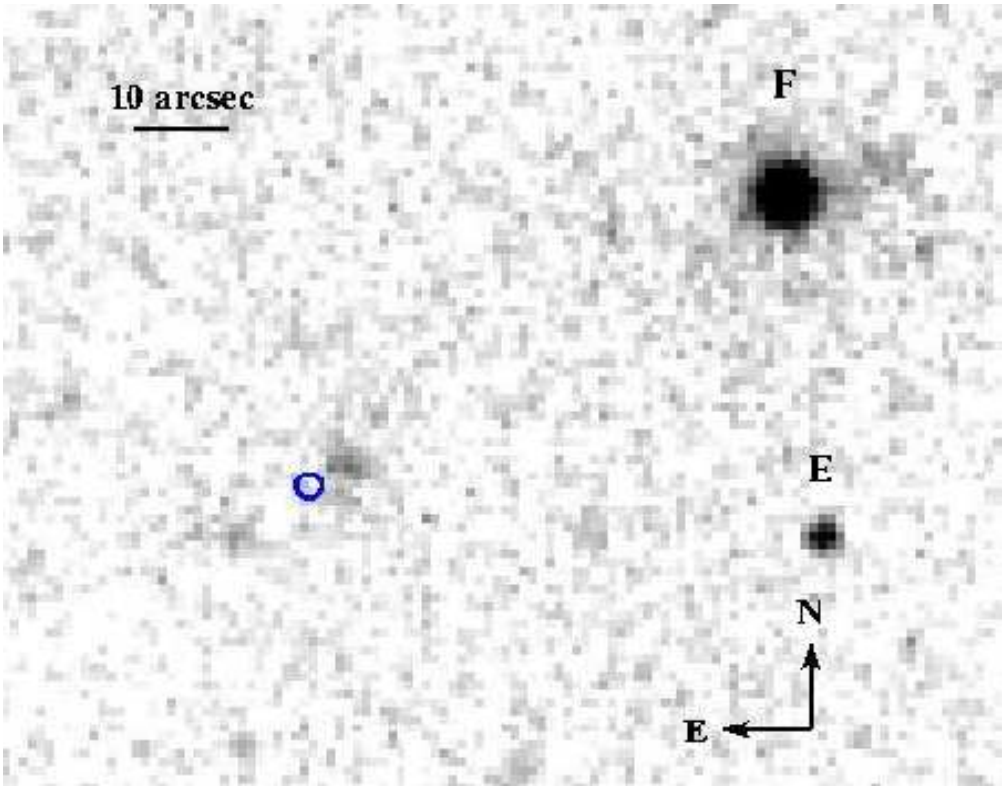

Figure 3.6 UV-band (UVW1 filter, 1800–3200 A) exposure of the field of NGC 1313 X-2, obtained with the *XMM* Optical Monitor. The circle shows the *Chandra* position (90% confidence level). A region of possible diffuse emission is visible NW of the *Chandra* error box.

reminiscent of predictions for the radiation-limited nebulae around supersoft sources (Di Stefano, Paerels & Rappaport [61]; Chiang & Rappaport [43]).

It is interesting to note that object A, the possible association of which with NGC 1313 X-2 was discussed by Stocke et al. ([218]), lies very close both to the *Chandra* error box and the point where the intensity of the nebular emission lines suddenly changes. The continuum spectrum of this object, obtained after subtracting off the emission line spectrum of the nebula in the adjacent regions, was compared to template stellar spectra (Pickles [189]) and turns out to be in fair quantitative agreement with that of a G-M supergiant, but not with that of late-type dwarfs. This result is independent of reddening. The absolute magnitude of object A is $M_R \simeq -9.7$, and the luminosity $L \sim 5 \times 10^5 L_\odot$ (assuming a bolometric correction appropriate for a K star). Object A may be a very massive ($\sim 30 M_\odot$) G-M supergiant of radius $\sim 1000 R_\odot$ or a cluster in NGC 1313. The first interpretation would support the conclusion that the region in which NGC 1313 X-2 is located is an active star forming region, in which the initial mass function is top-heavy. On the other hand, the second

possibility appears more likely because $\sim 30 M_{\odot}$ massive stars are extremely rare. However, the red color would indicate a rather evolved cluster that would be projected by chance on the active star forming environment in which NGC 1313 X-2 appears to be embedded.

A crucial question is how a binary system containing an intermediate mass BH may have formed (see e.g. van der Marel [235]). The BH progenitor must have been rather massive. This is consistent with the fact that NGC 1313 is likely to have lower than solar metallicity ($Z \sim 0.5$; Zaritsky, Kennicutt & Huchra [256]) and hence mass loss was less intense. Such a massive BH may have formed through direct collapse without producing a supernova. In this way, if the system was born as a binary, it may have survived after the collapse of the primary. Although less likely, it is also possible that the companion might have been captured from a nearby stellar association. In this case, it is not possible to exclude that the BH may have formed from an early episode of star formation (population III).

It is worth noting that, although the large BH mass does not require that the emission is beamed, we cannot rule out that a moderate jet activity, producing radio emission (and possibly inflating the emission nebula), is present in NGC 1313 X-2 (see e.g. the case of an ULX in NGC 5408; Kaaret et al. [113]). However, presently available radio images of the field of NGC 1313 X-2 (Sydney University Molonglo Sky Survey at 843 MHz and Australia Telescope Array at ~ 5 GHz; (Stocke et al. [218]) are not sufficiently deep to allow detection.

Optical spectroscopy of object C, narrow band imaging of the nebula, deep radio observations and an analysis of the short timescale X-ray variability are essential to better assess the physical properties of NGC 1313 X-2 and its environment. In particular, even a moderate resolution spectrum of object C will make it possible to detect any characteristic absorption and/or emission line, and then determine its properties and redshift. These observations will allow us to strengthen the identification of NGC 1313 X-2 with an intermediate mass BH and foster our understanding of ULXs.

Chapter 4

XMM-Newton Detection of Pulsations and a Spectral Feature in the X-ray Emission of the Isolated Neutron Star 1RXS J214303.7+065419/RBS 1774[1]

4.1 Introduction

Over the last decade *ROSAT* observations have led to the discovery of seven very soft X-ray sources with quite particular characteristics. The extreme values of the X ray-to-optical flux ratio ($\gtrsim 10^4$), the low hydrogen column densities ($n_H \approx 10^{20}\,\mathrm{cm}^{-2}$) and the detection of pulsations in the range $\sim 5-10$ s in four objects (five with the present one) strongly favor the possibility that these sources are close-by, X-ray emitting, dim, isolated neutron stars (XDINSs; see e.g. Treves et al. ([226]) and Haberl ([88]) for reviews and Table 4.1 for a summary).

XDINSs stand apart with respect to other known classes of bona fide isolated neutron stars detected at X-ray energies. All of them are radio-silent, they are not associated with supernova remnants and exhibit a soft X-ray spectrum without evidence of a power-law hard tail. The origin of their X-ray emission has not been fully clarified as yet. The recent measurement of relatively large

[1]We report here Zane, S., Cropper, M., Turolla, R., Zampieri, L., Chieregato, M., Drake, J. J. & Treves, A.: "*XMM-Newton* Detection of Pulsations and a Spectral Feature in the X-ray Emission of the Isolated Neutron Star 1RXS J214303.7+065419/RBS 1774", 2005, ApJ 627, 397, adapted to the one-colum format.

proper motions in three sources, implying transverse velocities $\gtrsim 150\,\mathrm{km\,s^{-1}}$ (Kaplan, van Kerkwijk & Anderson [114]; Motch, Zavlin & Haberl [163]; Motch et al. [164]), makes it unlikely that these are old ($\gtrsim 10^7$ yr) neutron stars accreting from the interstellar medium (see e.g. Treves et al. [226]). Most probably the X-rays arise from the cooling of younger objects with an inferred age of $\approx 10^5$–10^6 yr.

XDINSs play a key role in compact objects astrophysics being the only sources in which we can have a clean view of the compact star surface, without contamination from magnetospheric emission or emission from a binary companion or a supernova remnant. They appear to be truly "isolated" neutron stars, and only a small number of them has been detected so far. Detailed multiwavelength studies of the largest possible sample of XDINS candidates are therefore fundamental for tracking the evolutionary history of galactic neutron stars, and for shedding light on their thermal and magnetic surface properties.

Spectral analysis carried out so far has convincingly shown that the broadband X-ray emission from XDINSs is well represented by a blackbody continuum, challenging the predictions of conventional atmospheric models. The absence of spectral lines appears to be well established in the brightest XDINS, RX J1856.5-3754 (Drake et al. [62]; Burwitz et al. [33]), while absorption features have been increasingly reported in the spectra of other sources, including RX J1308.6+2127, RX J0720.4-3125, RX J1605.3+3249, RX J0806.4-4123, RX J0420.0-5022 (Haberl et al. [92]; Haberl et al. [94]; Van Kerkwjik et al. [236]; Haberl et al.[93]). The absorption features are quite broad, in contrast with the atomic spectral lines predicted by atmospheric models, and they appear at energies $\sim 200 - 500$ eV. Their nature is still uncertain but the intriguing identification with a proton cyclotron resonance has been suggested. Should this interpretation prove correct, it makes XDINSs highly magnetized objects with fields of the order of, or exceeding, a few $\times 10^{13}$ G. In this respect, the case of RX J0720.4-3125 is particularly interesting: the magnetic field strength derived by line energy, assuming it is a proton cyclotron feature, is in good agreement with that implied by the spindown measure ($\dot{P} \sim 3 - 6 \times 10^{-14}\,\mathrm{s\,s^{-1}}$; Zane at al. [254]; Kaplan et al. [115]; Cropper et al. [54]).

We are still at a stage where every newly discovered XDINS holds important information for understanding the properties of the whole class and may also show some peculiarities which import unique information. RBS 1774 (1RXS J214303.7+065419) has been the most recent XDINS to be found (Zampieri et al. [251]). The source is listed in the *ROSAT* Bright Source catalog, and lies about $48'$ off-axis in a PSPC pointing of the BL Lac MSS 2143.4+0704. The *ROSAT* observation had a limited statistics (~ 500 net counts), but it had been sufficient to reveal a very soft X-ray spectrum, to which an absorbed blackbody provides an acceptable fit ($kT \sim 92\,\mathrm{eV}$, $n_H \sim 4.6 \times 10^{20}\,\mathrm{cm^{-2}}$). No modulation with amplitude $\gtrsim 30\%$ has been found in the PSPC data. Optical follow-up observations have shown no plausible optical counterpart in the X-ray error box

Table 4.1. Summary of XDINSs properties

Source	kT_{bb}^{∞} eV	n_H 10^{20} cm^{-2}	E_{line} eV	P s	Semi-Ampl.[a]	Ref.[b]
RX J1856-3754	56.7	0.18	no	no	no	1
RX J0720-3125	85.2	1.38	270	8.39	11%	2
RX J1605.3+3249	94.1	0.68	493	no	no	3
RX J1308.6+2127	85.8	4.10	290	10.31	18%	4
RX J0420-5022	44.9	1.02	329	3.45	13%	5
RX J0806-4123	95.6	0.41	460	11.37	6%	5
RBS 1774	101.4	3.65	700	9.44	4%	6

[a]Semi amplitude of the folded light curve.

[b]1) [33]; 2) [94]; 3) [236]; 4) [92]; 5) [93]; 6) this paper.

down to $R \sim 23$, implying an X-to-optical flux ratio $\gtrsim 10^3$. All these properties are very similar to those of the already established XDINSs and make RBS 1774 worth of further investigation.

In this Chapter we report results from a recent *XMM-Newton* observation of RBS 1774 and compare the newly measured properties of this source with those of other known members of this class.

4.2 X-ray Observations

RBS 1774 was observed with *XMM-Newton* on 2004 May 31 for 30 ks (EPIC PN). All the three EPIC detectors were configured in small window mode. We processed the data using the *XMM-Newton* SASv6.0.0. We selected periods of low background, with the Good Time Interval (GTI) file leaving an effective exposure of 23 ks (EPIC PN). The same GTI was used for the spectral and timing analysis.

The source is clearly visible in EPIC PN, MOS1 and MOS2 with count rates of 2.054 ± 0.011, 0.346 ± 0.004 and 0.328 ± 0.004 counts s^{-1} respectively (0.2-2 keV band). In the EPIC image, the source is slightly off axis since the pointing was requested based on the revised position published by Zampieri et al. ([251]). The position obtained with *XMM-Newton* (J2000 coordinates) is $\alpha = 21^h43^m03.3^s$, $\delta = +06^\circ54'17''$, with a 90% uncertainty radius of $3''$. Within 3σ, previous estimates based on *ROSAT* data (see again Zampieri et al. [251]) are consistent with the XMM position. In particular, the position from the *ROSAT* ASS Bright Sources Catalogue ($\alpha = 21^h43^m03.7^s$, $\delta = +06^\circ54'19.5''$, 90% uncertainty radius of $18''$; labelled with RASS in Zampieri et al. [251]) is within $\sim 7''$ from the present XMM position. Figure 4.1 shows the *ROSAT* and *XMM-Newton* error boxes overlayed on the optical image (discussed below). We

note the small difference in the position of the RASS error box with respect to that reported by Zampieri et al. ([251]).

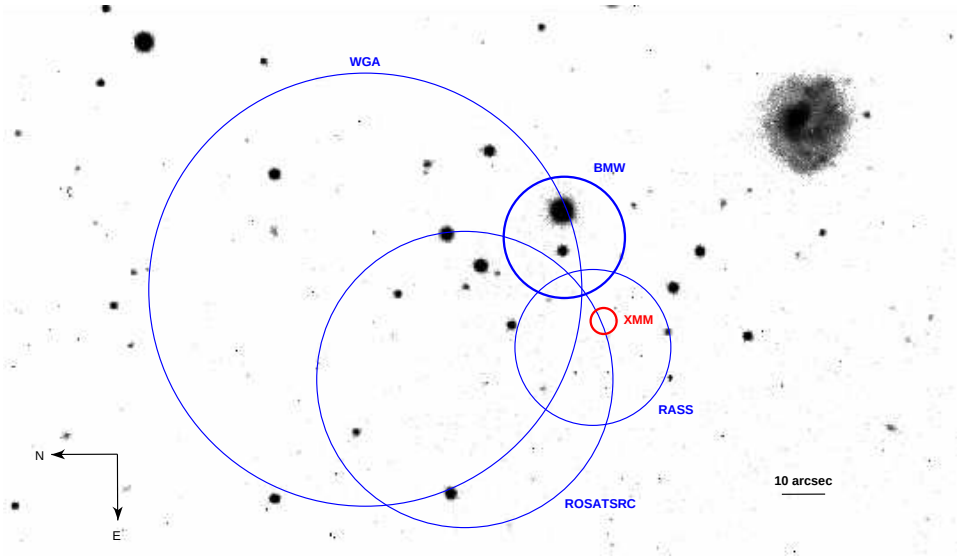

Figure 4.1 R-band NTT image of the field around RBS 1774 (limiting magnitude ~ 22.8, see text and Zampieri et al. [251]). The red circle (3" radius) shows the source position as derived from our recent *XMM-Newton* observation, while the blue circles show the position inferred from past data (see the electronic version for a full color image). Positions (see Zampieri et al. [251] for all details) are taken from: White, Giommi & Angelini ([241]) Catalogue (WGA); *ROSAT* ASS Bright Sources Catalogue (RASS, Voges et al. [239]), *ROSAT* SRC Catalogue (ROSATSRC, Zimmermann [263]), RASS field analized with a Brera Multiscale Wavelet alghoritm (BMW, Lazzati et al. [129]). Error circles represent the 90% confidence intervals.

4.2.1 Spectral analysis

For the EPIC PN, we extracted single and double events (PATTERN ≤ 4, FLAG=0) within a circle of $25''$ radius for source and within two circular regions (to avoid out-of-time events) with radius $50''$ for background. For the EPIC MOS1 and 2, we extracted up to quadruple events (PATTERN ≤ 12, FLAG=0) with a $25''$ and $32''$ radius for the source respectively with two rectangular background regions to exploit the limited window size more effectively. In order to account for the slightly off-axis position, we generated the appropriate off-axis response and ancillary response matrices. Data were grouped, ensuring a minimum of 30 counts per energy bin.

We performed a spectral analysis by fitting data from the three EPIC detectors simultaneously. We find that the broadband spectrum can be represented by

a single absorbed blackbody, with $kT = 0.1014$ keV and $n_H = 3.65 \times 10^{20}$ cm^{-2} (see Figure 4.2, Table 4.2). Both parameters are consistent with those measured in the past using *ROSAT* data, although better constrained. The unabsorbed EPIC-PN flux in the $0.1-2.4$ keV band is 6.05×10^{-12} erg cm^{-2} s^{-1}, slightly less than that reported by Zampieri et al. for *ROSAT* PSPC (8.7×10^{-12} erg cm^{-2} s^{-1} (the difference is likely to be due to the large off-axis angle of RBS 1774 in the *ROSAT* observation). Assuming a typical luminosity of 5×10^{31} erg/s gives a distance ~ 280 pc. The value of the column density is similar to, but slightly lower than, the total Galactic absorption in the source direction ($n_H = 5 \times 10^{20}$ cm^{-2}, Dickey & Lockman [60]). The resulting reduced $\chi^2 = 1.36$ is not fully satisfactory and an inspection of the residuals suggests that the largest discrepancies between model and data are above ~ 0.6 keV.

As discussed by many authors (see e.g. Zavlin & Pavlov [258], Treves et al. [226] for reviews), realistic model spectra of the cooling atmosphere surrounding an unmagnetized ($B \lesssim 10^9$ G) neutron star exhibit a distinctive hardening with respect to a blackbody and deviate significantly from a Planckian shape. When accounting for a magnetic field of moderate strength ($B \sim 10^{12} - 10^{13}$ G), the hard tail present in nonmagnetic models with comparable luminosity is partially suppressed and the X-ray spectrum, although still harder than a blackbody at the neutron star effective temperature, T_{eff}, is more Planckian in shape.

Models of fully ionized, pure H neutron star cooling atmospheres, as computed by Pavlov, Shibanov & Zavlin ([182]) and Zavlin, Pavlov & Shibanov ([257]), are currently implemented in XSPEC (*nsa* model) for three different values of the magnetic field: $B = 0$ (unmagnetized models) and $B = 10^{12}, 10^{13}$ G. In the attempt to improve the spectral fit we tested all the three sets of models, but in all cases the resulting χ^2 was worse than that obtained using a simple blackbody model (see Table 4.3). The star mass and radius have been fixed at $M = 1.4 M_\odot$ and $R = 10$ km, but the effects of gravity on the emergent spectra are too small to produce any appreciable difference in the fits.

Similarly, no improvement is obtained adding a power-law component or a second blackbody. However, we find that adding a gaussian line in absorption at ~ 0.7 keV produces a statistically significant ($\Delta\chi^2 = 56$; 7σ) improvement[2], leading to a reduced $\chi^2 = 1.20$. The best fitting energy of the line is $E_{line} = 0.754$ keV; the line width and depth are $\sigma_{line} = 0.027$ keV and $\tau_{line} = 4.8$, respectively. The latter two parameters are mutually degenerate and not well constrained, because, at least for narrow or moderately narrow lines, the energy resolution is insufficient to strongly distinguish between width and depth. A slightly better (reduced $\chi^2 = 1.17$) but similar fit is obtained by using an absorption edge instead of a gaussian line (see Figure 4.3): in the edge model there is one parameter less, therefore the depth is well constrained. At

[2]The F-test has been widely used to test the significance of spectral lines, although this is strictly inappropriate (see Protassov et al. [197]). Only for completeness, we report that we have checked the F-test statistics value and probability, obtaining 12.1 and 1.8×10^{-7}, respectively.

this level the data do not have enough resolution to allow us to discriminate between the two kinds of spectral features, in terms of their physical meaning. The best fitting energy of the edge is $E_{edge} = 0.694$ keV and the optical depth is $\tau_{edge} = 0.25$. In both cases, the blackbody temperature is essentially unchanged with respect to the single blackbody fit. The best fit parameters are reported in Table 4.2. The flux in the line/edge has been computed by fitting data with the models above, then switching the optical depth to zero and calculating the difference in flux, yielding 8.6×10^{-14} erg cm^{-2}s^{-1} (edge) and 3.3×10^{-14} erg cm^{-2}s^{-1} (gaussian line).

Table 4.2. Model Fit Parameters: blackbody (bb) model.[a]

Model	n_H 10^{20} cm^{-2}	kT_{bb}^{∞} eV	$E_{edge/line}$ eV	τ_{edge}; τ_{line}	σ_{line} eV	f_X[b] erg cm^{-2} s^{-1}	χ^2/d.o.f.
bb	$3.65^{+0.16}_{-0.13}$	$101.4^{+0.5}_{-0.6}$				5.16×10^{-12}	1.36
bb+abs.edge	$3.60^{+0.21}_{-0.16}$	$104.0^{+0.6}_{-0.7}$	694^{+5}_{-11}	$0.25^{+0.03}_{-0.03}$		5.07×10^{-12}	1.17
bb+gauss.line	$3.74^{+0.14}_{-0.10}$	$102.1^{+0.5}_{-0.3}$	754^{+8}_{-9}	$4.8^{+1.0}_{-0.5}$	27^{+15}_{-8}	5.20×10^{-12}	1.20

[a]All fits have been obtained by fitting simultaneously data from EPIC PN, MOS1 and MOS2; the absorption model is *TBabs* in XSPEC. The reported errors are the 68% (1σ) confidence range. The number of degrees of freedom (d.o.f.) is: 286 (bb), 284 (bb+abs. edge) and 283 (bb+gauss. line), in the three cases respectively.

[b]Unabsorbed flux measured with EPIC-PN in the $(0.2 - 2)$ keV band.

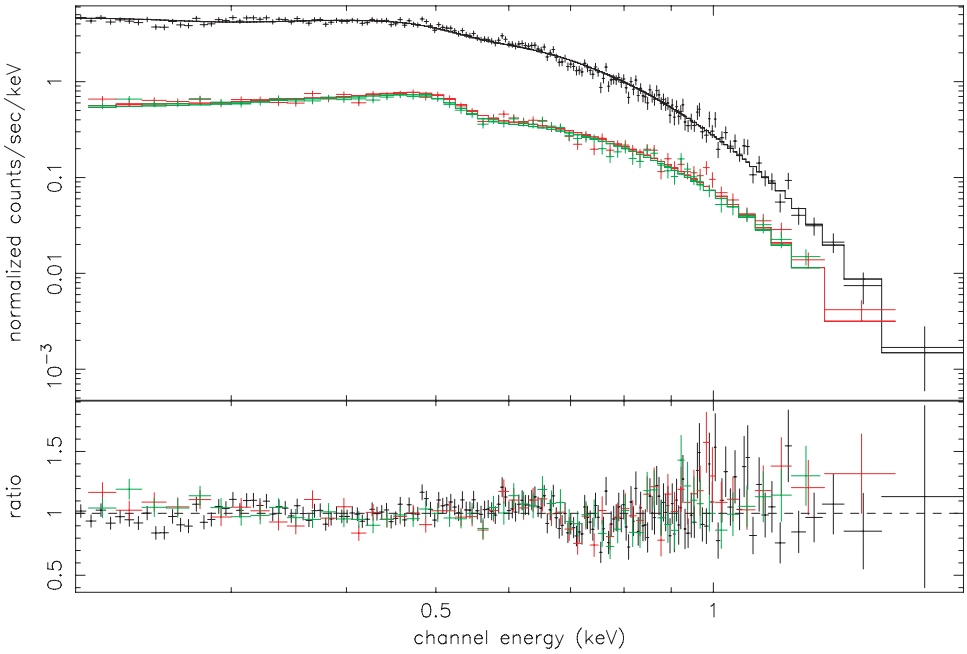

Figure 4.2 The top panel shows the count rate spectrum of RBS 1774 obtained with EPIC PN (black) and the two EPIC MOS (light green, red in the color version) detectors, with the best single blackbody combined model fit (parameters are given in Table 4.2). The bottom panel shows the data to model ratio.

4.2.2 Timing analysis

The high throughput of *XMM-Newton* provides a much more stringent check than the *ROSAT* PSPC on whether RBS 1774 is pulsating. For the timing analysis, we extracted the counts within a 30″ radius aperture in both PN and MOS1 and MOS2 but with the aperture truncated by a chord where it approached the edge of the CCD window in each case: this maximised the counts while avoiding any edge effects. A background area was selected using as much as possible of the small window mode image area while avoiding the edge of the window and the out-of-time events. This resulted in event files containing 38485, 9738 and 9500 events available for data analysis for PN, MOS1 and MOS2 respectively.

We analysed PN, MOS1 and MOS2 data both individually and combined using the Maximum Likelihood Periodogram technique described in Zane et al. ([254]) and Cropper et al. ([54]). We searched periods from 10000 s to 30 ms, ensuring that in each case the period grid was 2.5 times better sampled than the Nyquist frequency. Below 0.3 s the time resolution even in small window mode of MOS prevents them being used, so only the PN data were used for periods shorter than this.

Table 4.3. Model Fit Parameters: atmospheric models[a]

B 10^{12} G	n_H 10^{20} cm^{-2}	kT^{∞} eV	χ^2/d.o.f.
0	$8.4^{+0.3}_{-0.2}$	$29.8^{+0.3}_{-0.3}$	1.94
1	$8.3^{+0.2}_{-0.2}$	$47.3^{+0.5}_{-0.4}$	1.99
10	$8.6^{+0.1}_{-0.2}$	$50.0^{+0.4}_{-0.4}$	2.19

[a]All fits have been obtained by fitting simultaneously data from EPIC PN, MOS1 and MOS2; the absorption model is *TBabs* in XSPEC. The reported errors are the 68% (1σ) confidence range, and the number of degrees of freedom (d.o.f.) is 286 in all the three cases. The star mass and radius have been fixed at 1.4 $M_{\odot}$ and 10 km, respectively. The temperature measured by a distant observer, T^{∞}, and the effective temperature obtained by the model fit, T_{eff}, are related by $T^{\infty} = (1+z)^{-1}T_{eff}$, where $(1+z)^{-1} = [1-2.95(M/M_{\odot})/(R/10\,\mathrm{km})]^{1/2}$ is the gravitational redshift factor.

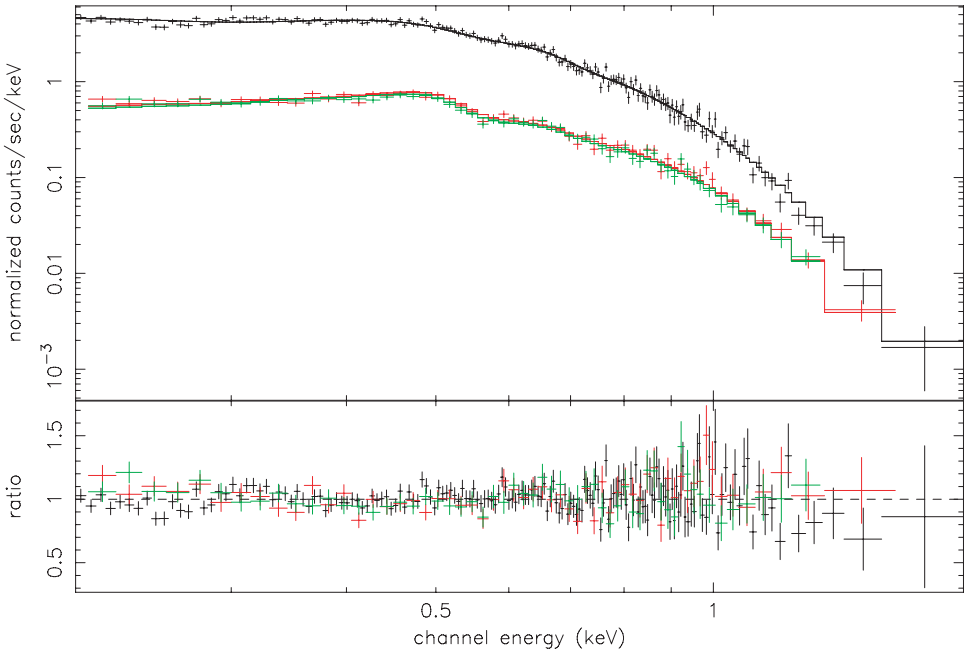

Figure 4.3 Top panel: the count rate spectrum of RBS 1774 obtained with EPIC PN and the two EPIC MOS detectors. The best fit model is an absorbed blackbody with an absorption edge at ~ 0.7 keV (parameters are given in Table 4.2). The bottom panel shows the data to model ratio.

The search revealed a significant period at 9.437 s. This is illustrated for the combined MOS and PN dataset in Figure 4.4, where the dotted lines show confidence intervals of 68% and 90%. The $\Delta\chi^2$ between the maximum and the noise floor is 40 in the combined dataset, while for the PN alone $\Delta\chi^2 = 36$. The peak is evident in the combined MOS1 and MOS2 data, with $\Delta\chi^2 = 9.5$. We have checked whether the reduced significance of the MOS1+2 peak is consistent with that in the PN data, given its greater sensitivity, by selecting (at random) event data from the PN event list to generate a reduced dataset with the same number of events as MOS1+2. In this reduced PN dataset the noise levels are similar to the MOS1+2 dataset, and the 9.437 s peak is no longer the most significant in the 9–10 sec period range. This indicates that the lower significance of the peak in the MOS1+2 dataset is consistent with its reduced statistics with respect to the PN dataset and that no additional bias is introduced because of event selection.

$\Delta\chi^2 = 40$ corresponds to a $> 6\sigma$ result ($\sigma = \sqrt{\Delta\chi^2}$ for 1 degree of freedom). However, we need to consider the random probability of a peak occurring given the large number of periods searched. In the interval between 1 and 1000 seconds, there are 59638 independent periods, and the probability of a 6σ peak will occur once in 1.5×10^5 cases, corresponding to a $\Delta\chi^2 = 18.7$ or $> 4\sigma$ result.

We therefore consider the peak to be significant, although with the caveat that in [91] a 4σ detection was claimed for a 22.69 s periodicity in RX J0420.0-5022, which has since been shown to have a 3.45 s periodicity.

We have consequently folded the data on the 9.437 s period and binned them in phase. This is shown in Figure 4.5 for PN separately, for the combined MOS data, and then for all three instruments together. The MOS data taken separately are noisy, with a variation which would not be considered significant in its own right, but which nevertheless shows an amplitude and phasing which is consistent with that from the PN. This is evident (equivalently) from our periodogram analysis where the $\Delta\chi^2$ increases from 36 to 40 when the MOS1+2 data are added to the PN data, and adds weight to our conclusion that this pulsation is real.

The pulsation is approximately sinusoidal, and the amplitude of the variation is remarkably small: fitting a sinusoid yields a semiamplitude of 0.036 ± 0.006 (0.072 peak-to-peak). In the attempt to confirm the periodicity, we re-analysed the archival *ROSAT* data taken in May 1991 (Zampieri et al. [251]). This observation is divided into two segments of duration ~ 1800 s each; the interval between the two segments is ~ 4000 s. No statistically significant peak is present in the power density spectrum of the two separate segments, due to the poor statistics. No modulation with amplitude $\gtrsim 30\%$ has been found in the PSPC data, and this limit is consistent with the *XMM-Newton* detection.

4.3 Possible nature of the spectral feature

The quality of the blackbody fit to the phase-averaged EPIC data of RBS 1774 is not completely satisfactory. Adding an absorption edge or a gaussian line in absorption significantly improves the spectral fit, suggesting the presence of an absorption feature similar to those observed in RX J1308.6+2127, RX J0720.4-3125, RX J1605.3+3249, RX J0806.4-4123, RX J0420.0-5022 (Haberl et al. [92]; Haberl et al. [94]; Van Kerkwjik et al. [236]; Haberl et al. [93]). However, the absorption features detected in these other sources appear at energies below 500 eV, while in the case of RBS 1774 it is at ~ 700 eV (for the purpose of the discussion we use the energy of the feature obtained by the blackbody plus edge fit, which is slightly better constrained). This makes the detection in RBS 1774 less sensitive to the uncertainties in the EPIC-PN spectral calibration, since residual systematic calibration effects are mainly present below ~ 0.5 keV. We note that a feature at this energy has been detected in the spectrum of the neutron star 1E 1207.4-5209 (Sanwal et al. [210]; Mereghetti et al. [146]; Bignami et al. [19]; Hailey & Mori [95]; Mori, Chonko & Hailey [158]; Zavlin, Pavlov & Sanwal [259]). The comparison between the properties of the XDINSs and those of 1E 1207.4-5209 must be done carefully, given the fact that the latter is probably younger: it has a shorter period, it is still associated with a supernova remant and it shows an additional harder spectral component in the X-ray

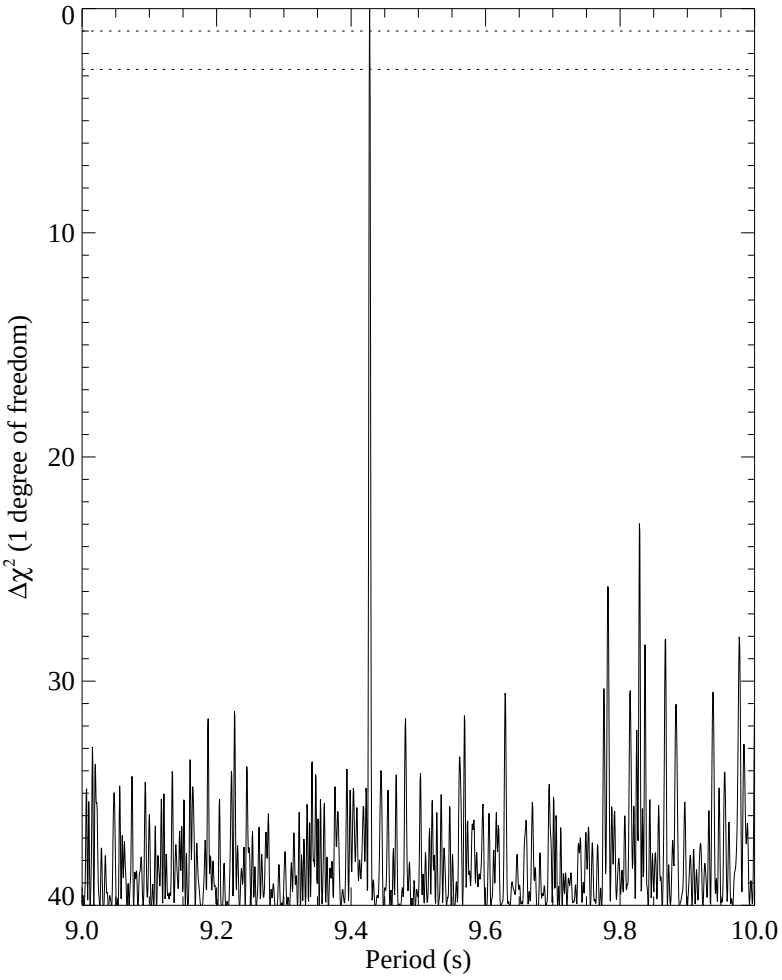

Figure 4.4 Maximum Likelihood Periodogramme from the combined EPIC MOS and PN data of RBS 1774 (see text for details).

spectrum. Also, 1E 1207.4-5209 is unique since it exhibits at least two spectral lines, with harmonic spacing. However, as will be discussed further on, some of the models proposed for this source can be applied to RBS 1774 as well.

Strong atomic absorption features are predicted by low-field atmospheric

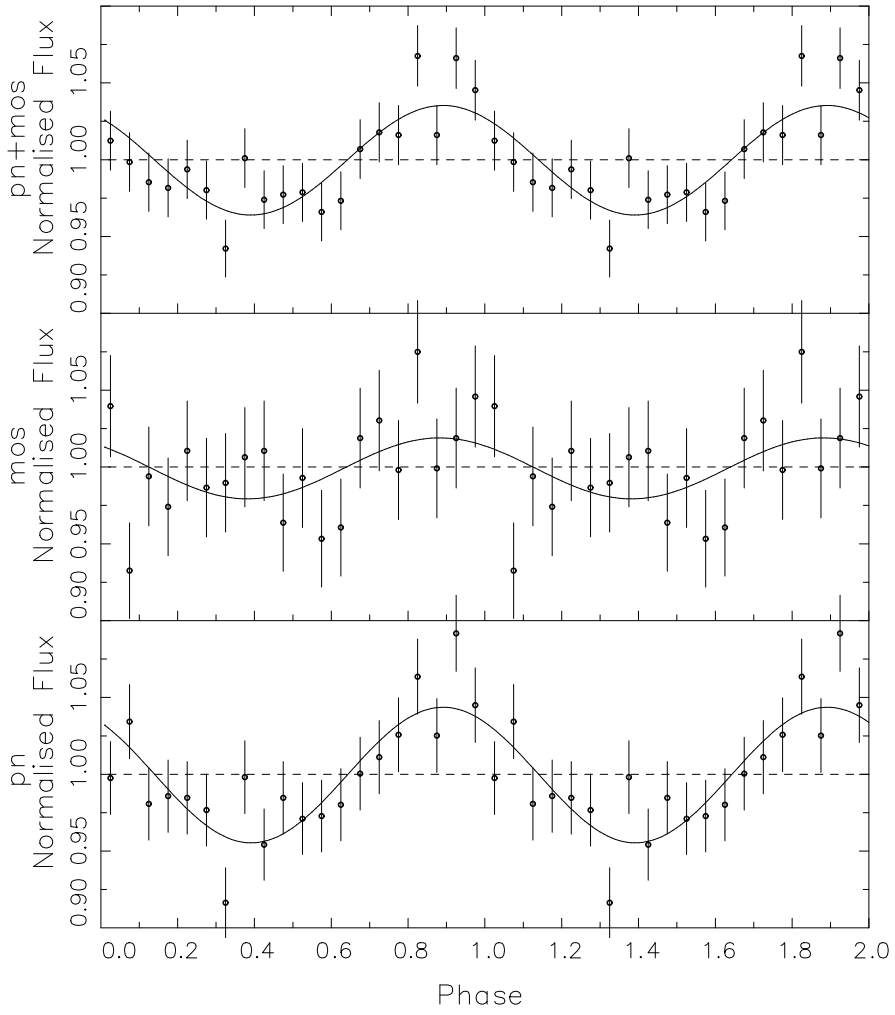

Figure 4.5 Folded 0.15-3 keV EPIC PN and MOS light curve of RBS 1774.

models with significant metal abundances (either solar, or pure iron, see Ra-

jagopal & Romani [198]; Zavlin, Pavlov & Shibanov [257]). The predictions for strongly magnetized metal-enriched atmospheres are more difficult to assess, due to the lack of detailed calculations. However, the strongly magnetized pure Fe spectra presented by Rajagopal, Romani & Miller ([199]) also show a significant number of absorption lines. The main difficulties faced by these models is that they exhibit a variety of rather narrow lines, in contrast with the single feature observed in RBS 1774.

Other possible interpretations are discussed below and can be divided in two groups, requiring either a superstrong ($B \sim 10^{14}$ G) or a moderate ($B \sim 10^{10} - 10^{12}$ G) magnetic field.

4.3.1 Super-strong magnetic fields

A plausible hypothesis is that the feature in the spectrum of RBS 1774 is associated with a proton cyclotron line. An interpretation in terms of a proton resonance has been recently put forward for the lines observed in other XDINSs, and, at least for RX J0720.4-3125, it is supported by the agreement between the magnetic field strength independently inferred from spin-down measurements and line energy (Cropper et al. [54]). In the case of RBS 1774, this would imply an ultra-strong magnetic field of $B \sim (E_{edge}/0.63\,\mathrm{keV})(1+z) \times 10^{14}\,\mathrm{G} \sim 1.4 \times 10^{14}$ G, assuming a gravitational redshift factor at the star surface of $(1+z)^{-1} = \sqrt{1-2GM/c^2R} \sim 0.8$. Such a field strength is comparable (although a factor $\sim 30\%$ higher) with that estimated in a similar way for RX J1605.3+3249 and RX J0806.4-4123 ($\sim 9 \times 10^{13}$ G, see Van Kerkwjik et al. [236]; Haberl et al. [93]), and is well above the critical value, $B_Q \simeq 4.4 \times 10^{13}$ G, at which QED effects become important.

An alternative interpretation is that we are detecting an absorption feature due to a bound-bound or bound-free transition in the hydrogen atom. A strong magnetic field can significantly increase the atomic binding energies and radiative transition rates, moving the H ionization edge into the soft X-ray band. First calculations of hydrogen atmospheres with bound atoms have shown that broad spectral lines become prominent if the atmospheric temperature drops below $\sim 10^6$ K. The strongest line corresponds to the transition between the ground state and the lowest excited state at an energy of $\approx 75[1 + 0.13\ln(B/10^{13}\ \mathrm{G})] + 63(B/10^{13}\ \mathrm{G})$ eV (Zavlin & Pavlov [258]). If applied to the ~ 0.7 keV line detected in RBS 1774, this interpretation yields a magnetic field of $B \approx 10^{14}$ G, again in the ultra-magnetized range. More detailed atmospheric models which include partially ionized hydrogen have been computed by Ho et al. ([103]), accounting for magnetic field effects and using the latest available equation of state. They have shown that, for $B = 5 \times 10^{14}$ G and $T = 5 \times 10^6$ K, two broad absorption features, due to bound-free transitions to different continuum states, are present at ~ 0.76 and 4 keV, respectively. The latter is much stronger, but it would not be visible in the spectrum of RBS 1774 which has negligible emission above ~ 2 keV. At somewhat lower

fields ($B \sim 10^{14}$ G) Ho & Lai ([104]) found that the dominant atomic features in the 0.2–2 keV band are those due to the low-energy bound-free transition, which is barely visible at 0.54 keV, and the bound-bound transition discussed above at 0.74 keV. These authors argue that at super-strong field strengths ($B \gtrsim 10^{14}$ G) vacuum polarization may efficiently suppress these lines, in which case the above conclusions can be (at least partially) invalidated. However, current treatment of this QED effect is too crude to make a definite statement.

At present, accurate atmospheric models for chemical compositions other than hydrogen are unavailable for $B \gtrsim 10^{12}$ G. In the case of 1E 1207.4-5209, attempts to interpret the ~ 0.7 keV feature as a transition in ions other than H have been made, simply based on the latest theoretical results on the characteristics of bound-bound and bound-free transitions in He-like and H-like ions in strong fields. In this case, a ~ 0.7 keV feature may be associated with a transition between the ground level ($m = 0, \nu = 0$, where m and ν are the magnetic and longitudinal quantum numbers) and the lowest excited tightly-bound level ($m = 0, \nu = 1$) of He^+. The required magnetic field is $\sim 1.4 \times 10^{14}$ G, for $(1 + z)^{-1} \sim 0.81$ (Sanwal et al. [210]; Zavlin, Pavlov & Sanwal [259]). Taken overall, these results show that if RBS 1774 has a magnetar-like field, $B \approx 10^{14}$ G, the feature at ~ 0.7 keV may be due to a proton cyclotron resonance, or bound-bound transitions in H or H-like He, or a blend of these.

4.3.2 Moderate magnetic fields

An obvious scenario involving a moderate magnetic field is that in which the observed feature is associated with electron (instead of proton) cyclotron resonance. Would this be the case, the surface magnetic field is necessarily much lower, $B \sim (E_{edge}/11.6\,\mathrm{keV})(1 + z) \times 10^{12}\,\mathrm{G} \sim 7.5 \times 10^{10}\,\mathrm{G}$ for $(1 + z)^{-1} \sim 0.8$.

A further possibility is that of an atomic transition out of the ($m = 0$, $\nu = 0$) ground state to the ($m = 0$, $\nu = 1$) excited state or to the continuum in a mid-Z H-like ion, such as C VI, N VII or O VIII. Such an interpretation has been put forward by Hailey & Mori ([95]) again in connection with the lines in 1E 1207.4-5209 and yields $B \sim 10^{11}$ G (we refer in particular to their solutions B; see also their discussion about the possibility of having elements other than H in the neutron star atmosphere). Both these models are conceivable, although the required field strength is well below that estimated for RX J0720.4-3125 and well below the average fields measured in ordinary radio pulsars (only $\sim 20\%$ of the pulsar population has $B \leq 6 \times 10^{11}$ G).

4.4 Comparison with other thermally emitting Neutron Stars and open issues

In this paper we have reported on the results of a recent *XMM-Newton* observation of RBS 1774. Spectral and timing analysis of the high-quality PN and

MOS data confirm the association of this source with an isolated neutron star (as originally reported by Zampieri et al. [251]). The spectrum is thermal and there is evidence at a significance level $> 4\sigma$ that the source is an X-ray pulsar, with spin period of 9.437 s. The EPIC-PN X-ray light curve is single peaked and approximately sinusoidal, in agreement with what is seen in most of the other XDINSs (see Cropper et al. [52]; Haberl et al. [93]; RX J1308.6+2127 is the only XDINSs with double peaked X-ray pulse). However, both the relatively low level of significance of the periodicity and the small amplitude variation in the folded data prevented us from performing pulsed phase spectroscopy.

The deepest available optical pointing of the field is that obtained with the New Technology Telescope (NTT) at la Silla on 2001 May 27. The faintest source in this image is object D, as listed in Table 2 by Zampieri et al. ([251]), with $R = 22.77$. This, combined with the unabsorbed *XMM-Newton* X-ray flux ($f_X = 5 \times 10^{-12}$ erg cm^{-2}s^{-1} in the 0.2-2 keV band for $n_H = 3.6 \times 10^{-20}$ cm^{-2}) allows a lower limit to be placed on the X-to-optical flux ratio of $f_X/f_R \sim 1700$. When using the absorbed flux $f_X = 2.8 \times 10^{-12}$ erg cm^{-2}s^{-1} and the same X-ray energy band, we get $f_X/f_R \sim 1000$.

Taken overall, the characteristics of RBS 1774 are remarkably similar to those of an other XDINS recently studied in detail, RX J0806.4-4123 (see Haberl et al. [93]). Both sources have a similar EPIC-PN count rate of $\sim 1.7-2.0$ counts s^{-1} and a similar period (~ 10 s).[3] Also, they have a blackbody temperature of ~ 100 eV, among the highest observed from the XDINs, and exhibit the smallest pulsed fractions of the group (semiamplitude of 4% and 6% respectively) which makes the detection of significant spectral variations with phase difficult. Intriguingly, and if related, the two latter characteristics may be suggestive of a nearly pole-on viewing geometry, with the spin and magnetic axes fairly closely aligned. This appears also broadly consistent with the fact that the energy of the spectral feature is the highest in RBS 1774, RX J0806.4-4123 and RX J1605.3+3249. If the feature energy is sensitive to the field strength, then, both the temperature and the average magnetic field are higher in the polar regions.

As discussed in Section 4.3, many of the viable interpretations for the feature detected at ~ 0.7 keV require a magnetar-like field strength, $B \sim 10^{14}$ G. For a period of 9.437 s, this implies a dipole spin-down rate (at present) of $\dot{P} \sim 11 \times 10^{-13}$ s/s, and a spin-down age of 1.4×10^5 yrs (assuming B constant). In order to investigate if such a high magnetic field strength is compatible with the cooling age of the source, we considered the evolutionary tracks in the B-$\dot{P}$ diagram by repeating the simple computation discussed in Cropper et al. ([54]). We computed the source age, τ_d, and the value of the magnetic field at the birth of the neutron star, B_0, obtaining $B_0 \approx 1.6 \times 10^{15}$ G and $\tau_d \approx 10^4$ yrs for Hall cascade; $B_0 \approx (1.1$ or $1.5) \times 10^{14}$ G and $\tau_d \approx (1.4$ or $1.1) \times 10^5$ yrs for ambipolar diffusion in the solenoidal or irrotational mode, respectively. The

[3] RX J1308.6+2127 also has a similar count rate, but a much higher pulsed fraction.

situation is therefore very similar to that of RX J0720.4-3125 (Cropper et al. [54]): ambipolar diffusion predicts a magnetic field which is relatively constant over the source lifetime, while Hall cascade gives a scenario compatible with a superstrong field at the star's birth ($B_0 \sim 10^{15}$ G). The corresponding star's ages are compatible with the cooling age of a neutron star with mass ≈ 1.35 $M_\odot$ or slightly larger, $1.4 - 1.5$ $M_\odot$ (see Fig. 2 in Yakovlev et al. [248]).

Should the strength of the magnetic field be confirmed by future observations, this will make RBS 1774 the XDINS with the highest field discovered so far. RX J1605.3+3249 and RX J0806.4-4123 may possess magnetic fields of comparable strength ($B \sim 9 \times 10^{13}$ G, Van Kerkwjik et al.[236]; Haberl et al. [93]), and this raises the question of whether or not a highly magnetized neutron star may remain for long periods without any sign of some kind of transient activity. Very recently, a few radio pulsars with $B > B_Q$ and long period ($\approx$ few seconds) have been discovered (see e.g. McLaughlin et al. [140]; Morris et al. [160]; Camilo et al. [38]). On the other hand, non-thermal magnetospheric emission from XDINSs is so far undetected, although this may simply reflect the fact that it falls below the detection threshold of present instruments. In fact, if XDINSs are similar to the standard radio-pulsars the relation between rotational energy and non-thermal X-ray luminosity would be $L_X \approx 10^{-3}\dot{E}$. Taking the above value for the magnetic field gives $\dot{E} \approx 10^{31}$ erg/s, for RBS 1774, implying $L_X \approx 10^{28}$ erg/s.

XDINSs were unanimously believed to be steady sources, as indicated by several years of observations for the brightest of them. Only recently, and quite surprisingly, *XMM-Newton* observations revealed a substantial change in the spectral shape and pulse profile of RX J0720.4-3125 over a timescale of ~ 2 yr (de Vries et al. [58]; Vink et al. [238]). Possible variations in the pulse profile of RX J0420.0-5022 over a similar timescale (~ 0.5 yr) have also been reported Haberl et al. ([93]), although at a much lower significance level. Even more recently, timing analysis of *Chandra* and *XMM-Newton* data of 1E 1207.4-5209 revealed non-monotonic variations in the spin period, possibly related to glitches occurring on a timescale of $\sim$ 1-2 yr (Zavlin, Pavlov & Sanwal [259]). Also the monitoring of anomalous X-ray pulsars (AXPs), previously believed to be steady emitters, has now revealed X-ray variability: both short energetic bursts and long-lasting variations in the X-ray emission of some of these sources have been reported (see Gavriil, Kaspi & Woods [76], Woods et al. [245], and Mereghetti et al. [148] for the cases of 1E 2259+58 and 1E 1048-59). Quite interestingly, the long-term changes observed in RX J0720.4-3125 bear some resemblance to those reported in 1E 2259+58 and 1E 1048-59, with the difference that in RX J0720.4-3125 the spectral and lightcurve evolution is not accompanied by any flux variation.[4]

Further timing studies of XDINSs will be of key importance in securing new

[4]And again, we caveat that given the several spectral and timing differences, a direct comparison between XDINSs and AXPs or sources like 1E 1207.4-5209 must be done with caution.

spin-down measurements: this will provide a second independent measurement of the field strength and also will bring further insights on the long-term behavior of XDINSs. Should the presence of ultra-strong fields and the variability be confirmed, the putative relation between XDINSs and AXPs, put forward on the basis of the similarity in spin periods (see e.g. Mereghetti et al. [147], Haberl [88]), becomes much firmer. In turn, this relation may provide the "missing link" among XDINSs and SGRs. If indeed XDINSs are the descendants of SGRs/AXPs, as their lower temperature may suggest, then explaining why evolution produces "quiet" magnetars is still a challenge.

Chapter 5

Gravitational Lensing

Gravitational lensing refers to light deflection by gravitational fields. Einstein's General Relativity predicts light propagation along null geodesics of space-time. The presence of mass-energy modifies the structure of space-time, and therefore the shape of null-geodesics. Rays of light can be considered as traveling in straight lines at infinity (actually, this is not completely true in a non-trivial cosmology, like in the one most widely used today, the so-called concordance cosmological model), and to be bent by the gravity of astrophysical objects to which they pass nearby. In practice, in astrophysically relevant situations there is no need to use exact, complex, general relativistic calculations, but it is possible to rely on a suitable number of approximations, such as the use of linearized equations and of thin lens and small angle approximations. After a more than three hundred years long historical development (see e.g. Schneider, Ehlers & Falco [212]), nowaday gravitational lensing is achieving impressive results in a wide number of astrophysical research fields, from cosmological parameters estimates to the search of extrasolar planets, passing through the search for baryonic dark matter and the use of lenses as telescopes for quasar host galaxies and for Galactic Bulge stars. Meanwhile, a huge amount of theory has been developed on the subject. A comprehensive review of all observational and theoretical aspects of gravitational lensing would go far beyond the scope of this short introduction, that is intended only to give to the readers the tools to understand the following two chapters. A lot of books, monographs and reviews on the subject are available for those who want to dive in deeper; a by no means exhaustive list consists of Jetzer ([111]), Schneider, Ehlers & Falco ([212]), Kochanek, Schneider, & Wambsganss ([125]), and Narayan & Bartelmann ([170]). The next paragraphs follow strictly the exposition of Jetzer ([111]), compatibly with the above exposed philosophy, i.e. trying to avoid parts not used in Chapters 6 and 7. We added in Section 5.2 some more information on mass models relevant for strong lensing, and in Section 5.3.4 some recent results in the rapidly evolving field of bulge microlensing.

5.1 Basic of gravitational lensing

In what follows we will assume that the geometry of the universe is described in good approximation by the Friedmann-Lemaître-Robertson-Walker metric, with inhomogeneities treated as small perturbations of the metric. In this framework, we can divide the trajectory of a ray of light in three pieces: one in which the light coming from the source travels in a flat unperturbed space time, one near to the lens in which the trajectory is bent by the lens gravitational potential and finally another one in which the light propagates again in unperturbed space time until it is seen by the observer. In most cases of astrophysical interests, the Newtonian potential of the lens Φ is small, which means $\mid \Phi \mid \ll c^2$ (c being the velocity of light), and the peculiar velocity v of the lens is negligible as compared to c. Therefore, we can describe the zone near to the lens as a flat Minkowskian space time with small perturbations induced by the gravitational potential of the lens. The effect of the space-time curvature on light propagation in this first order post-Newtonian approximation can be treated in a way analogous to geometrical optics by means of the introduction of an effective refraction index, given by

$$n = 1 - \frac{2}{c^2}\Phi = 1 + \frac{2}{c^2} \mid \Phi \mid \ . \tag{5.1}$$

The Newtonian potential is negative and vanishes asymptotically. The refraction index $n > 1$ means that the light travels with a speed which is less than its speed in the vacuum. We define the effective speed of light in a gravitational field as

$$v = \frac{c}{n} \simeq c - \frac{2}{c} \mid \Phi \mid \ . \tag{5.2}$$

The travel time gets longer as compared to the propagation in the empty space. The expression for the total time delay Δt is obtained by integrating along the light trajectory from the source till the observer, as follows

$$\Delta t = \int_{source}^{observer} \frac{2}{c^3} \mid \Phi \mid dl \ . \tag{5.3}$$

The integration of the gradient component of n perpendicular to the trajectory itself gives the deflection angle

$$\vec{\alpha} = -\int \vec{\nabla}_\perp n \ dl = \frac{2}{c^2} \int \vec{\nabla}_\perp \Phi \ dl \ . \tag{5.4}$$

We will assume that the deflection angle is extremely small (as in all astrophysical phenomena). Therefore $\vec{\nabla}_\perp n$ can be integrated along an unperturbed path, rather than the effective perturbed path, introducing only a negligible error.

5.1.1 Thin lens approximation

A further approximation is to assume that the region in which the light is deflected (the second part of the light of ray trajectory in the above paragraph)

is much smaller than the distance between the observer and the lens and the lens and the source, respectively; i.e. the lens is thin in comparison to the full length of the light trajectory. In this thin lens approximation, it is possible to consider the mass of the lens projected on a plane perpendicular to the line of sight (between the observer and the lens) and going through the center of the lens. This plane is usually called the lens plane, and similarly one can define the source plane. The two-dimensional mass density (the projection of the lens mass on the lens plane) is obtained by integrating the mass density ρ along the direction perpendicular to the lens plane

$$\Sigma(\vec{\xi}\,) = \int \rho(\vec{\xi}, z)\ dz\ , \tag{5.5}$$

where $\vec{\xi}$ is a two dimensional vector in the lens plane and z is the distance from the plane. The deflection angle at the point $\vec{\xi}$ is then given by summing over the deflection due to all mass elements in the plane as follows

$$\vec{\alpha} = \frac{4G}{c^2} \int \frac{(\vec{\xi} - \vec{\xi}')\Sigma(\vec{\xi}')}{\mid \vec{\xi} - \vec{\xi}' \mid^2}\ d^2\xi'\ . \tag{5.6}$$

If it is further assumed that the lens has circular symmetry on the lens plane, the problem becomes one-dimensional, and the deflection angle is a vector directed towards the center of the symmetry with absolute value given by

$$\alpha = \frac{4GM(\xi)}{c^2\xi}\ , \tag{5.7}$$

where ξ is the distance from the center of the lens and $M(\xi)$ is the total mass inside a radius ξ from the center, defined as

$$M(\xi) = 2\pi \int_0^{\xi} \Sigma(\xi')\ \xi'\ d\xi'\ . \tag{5.8}$$

5.1.2 Lens equation

Figure 5.1 shows a typical lensing situation.

A light ray from a source S (in $\vec{\eta}$) is deflected by the lens by an angle $\vec{\alpha}$ (with impact parameter $\mid \vec{\xi}\, \mid$) and reaches the observer located in O.

The angle between the optical axis (arbitrarily defined) and the true source position is given by $\vec{\beta}$, whereas the angle between the optical axis and the image position is $\vec{\theta}$. The distances between the observer and the lens, the lens and the source, and the observer and the source are, respectively, D_d, D_{ds} and D_s. From Figure 5.1 one can easily derive (assuming small angles) that $\theta D_s = \beta D_s + \alpha D_{ds}$.

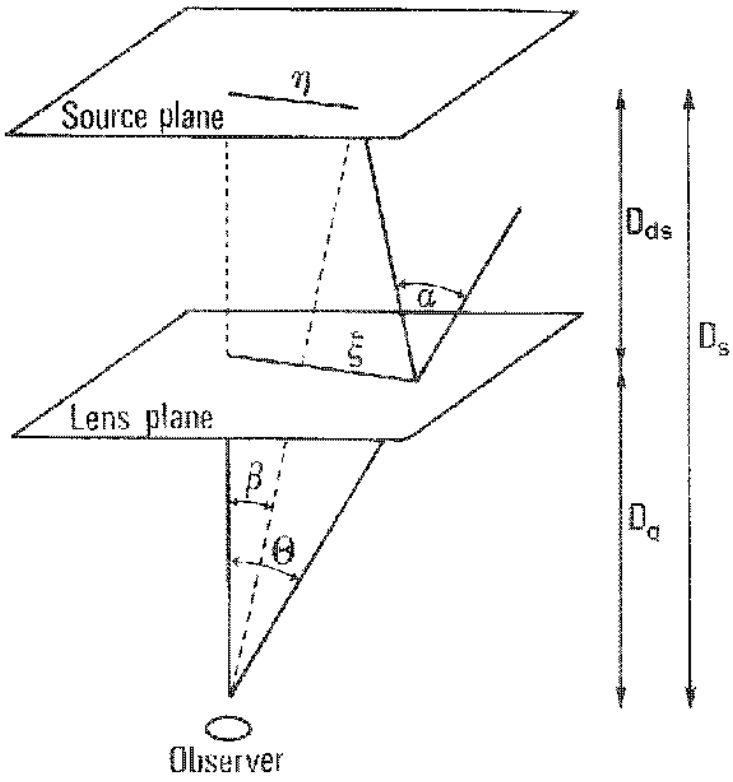

Figure 5.1 Notation for the lens geometry.

Thus the positions of the source and the image are related by the following equation

$$\vec{\beta} = \vec{\theta} - \vec{\alpha}(\vec{\theta}\,)\frac{D_{ds}}{D_s}\ , \tag{5.9}$$

which is called the *lens equation*. It is a non-linear equation so that it is possible to have several images $\vec{\theta}$ corresponding to a single source position $\vec{\beta}$.

5.1.3 Lens equation with Fermat principle

It is possible to derive the lens equation 5.9 with the Fermat principle, as in geometrical optics, but with the refraction index as defined in eq.(5.1). The light trajectory is then given by the variational principle

$$\delta \int n\ dl = 0\ . \tag{5.10}$$

That is, a ray of light travels in such a way that the traveling time will be extremal. Suppose that source S emits a light of ray at time $t = 0$. The ray travels in a straight line until the location I of the lens, where it is deflected, and then again in a straight line until the observer in O. The corresponding equation is

$$t = \frac{1}{c}\int\left(1 - \frac{2\phi}{c^2}\right) dl = \frac{l}{c} - \frac{2}{c^3}\int \phi \; dl \tag{5.11}$$

where l is the Euclidean distance. The term containing ϕ has to be integrated along the light trajectory. From Figure 5.1 we see that

$$\begin{aligned} l &= \sqrt{(\vec{\xi} - \vec{\eta})^2 + D_{ds}^2} + \sqrt{\vec{\xi}^2 + D_d^2} \\ &\simeq D_{ds} + D_d + \frac{1}{2D_{ds}}(\vec{\xi} - \vec{\eta})^2 + \frac{1}{2D_d}\vec{\xi}^2 \; , \end{aligned} \tag{5.12}$$

where $\vec{\eta}$ is a two dimensional vector in the source plane. If we consider a surface mass density $\Sigma(\vec{\xi}\,)$ (as defined in eq.(5.5)) the integral containing the potential term is (neglecting higher order contributions)

$$\frac{2}{c^3}\int \phi \; dl = \frac{4G}{c^3}\int d^2\xi' \; \Sigma(\vec{\xi'}) \; ln\frac{\mid \vec{\xi} - \vec{\xi'} \mid}{\xi_0} \; , \tag{5.13}$$

where ξ_0 is a characteristic length in the lens plane and the right hand side term is defined up to a constant. The sum of eq.(5.12) and eq.(5.13) minus the travel time without deflection from S to O gives the difference in the arrival time between the "with lens" and "without lens" situation. This way one gets

$$c\Delta t = \hat{\phi}(\vec{\xi}, \vec{\eta}) + const. \; , \tag{5.14}$$

where $\hat{\phi}$ is the *Fermat potential* defined as

$$\hat{\phi}(\vec{\xi}, \vec{\eta}) = \frac{D_d D_s}{2D_{ds}}\left(\frac{\vec{\xi}}{D_d} - \frac{\vec{\eta}}{D_s}\right)^2 - \hat{\psi}(\vec{\xi}\,) \tag{5.15}$$

and

$$\hat{\psi}(\vec{\xi}) = \frac{4G}{c^2}\int d^2\xi' \; \Sigma(\vec{\xi'}) \; ln\left(\frac{\mid \vec{\xi} - \vec{\xi'} \mid}{\xi_0}\right) \tag{5.16}$$

is the *deflection potential*, which does not depend on $\vec{\eta}$. The Fermat principle can thus be written as $\frac{d\Delta t}{d\vec{\xi}} = 0$, and inserting eq.(5.14) one gets again the lens equation

$$\vec{\eta} = \frac{D_s}{D_d}\vec{\xi} - D_{ds} \; \vec{\alpha}(\vec{\xi}\,) \; , \tag{5.17}$$

where $\vec{\alpha}$ is defined in eq.(5.6). (If we define $\vec{\beta} = \vec{\eta}/D_s$ and $\vec{\theta} = \vec{\xi}/D_d$ we get eq.(5.9)). One can also write eq.(5.17) as follows

$$\nabla_{\vec{\xi}} \, \hat{\Phi}(\vec{\xi}, \vec{\eta}) = 0 \; , \tag{5.18}$$

which is an equivalent formulation of the Fermat principle.

The arrival time delay of light rays coming from two different images (due to the same source in $\vec{\eta}$) located in $\vec{\xi}^{(1)}$ and $\vec{\xi}^{(2)}$ is given by

$$c(t_1 - t_2) = \hat{\Phi}(\vec{\xi}^{(1)}, \vec{\eta}) - \hat{\Phi}(\vec{\xi}^{(2)}, \vec{\eta}) \ . \tag{5.19}$$

5.1.4 Adimensional lens equation

Equation (5.9) it is often written in a dimensionless form. Let ξ_0 be a length parameter in the lens plane (whose choice will depend on the specific problem) and let $\eta_0 = (D_s/D_d)\xi_0$ be the corresponding length in the source plane. We set $\vec{x} = \frac{D_d\vec{\theta}}{\xi_0}$, $\vec{y} = \frac{D_s\vec{\beta}}{\eta_0}$ and

$$\kappa(\vec{x}) = \frac{\Sigma(\xi_0\vec{x})}{\Sigma_{crit}} \ , \qquad \vec{\alpha}(\vec{x}) = \frac{D_d D_{ds}}{\xi_0 D_s}\hat{\vec{\alpha}}(\xi_0\vec{x}) \ , \tag{5.20}$$

where we have defined a critical surface mass density (also called convergence)

$$\Sigma_{crit} = \frac{c^2}{4\pi G}\frac{D_s}{D_d D_{ds}} \tag{5.21}$$

Then eq. (5.9) reads as follows

$$\vec{y} = \vec{x} - \vec{\alpha}(\vec{x}) \ , \tag{5.22}$$

with

$$\vec{\alpha}(\vec{x}) = \frac{1}{\pi}\int_{R^2} \frac{\vec{x} - \vec{x}'}{\mid \vec{x} - \vec{x}' \mid^2}\kappa(\vec{x}')d^2x' \ . \tag{5.23}$$

The critical surface mass density has also a physical meaning, as we will see later. In fact, a surface mass density with $\kappa(\vec{x}) \geq 1$ somewhere, i.e. $\Sigma(\xi_0\vec{x}) \geq \Sigma_{crit}$, is able to map some source positions into multiple images.

5.1.5 Magnification and distortion

We rewrite again the lens equation (5.9) in a slightly different shape. Defining $k(\vec{\theta}\,) := \Sigma(\vec{\theta}D_d)/\Sigma_{crit}$, the lens equation is

$$\vec{\beta} = \vec{\theta} - \vec{\tilde{\alpha}}(\vec{\theta}\,) \ , \tag{5.24}$$

with

$$\vec{\tilde{\alpha}}(\vec{\theta}\,) = \frac{1}{\pi}\int_{R^2} d^2\theta' \ k(\vec{\theta'}) \ \frac{\vec{\theta} - \vec{\theta'}}{\mid \vec{\theta} - \vec{\theta'} \mid^2} \ . \tag{5.25}$$

Moreover

$$\vec{\tilde{\alpha}}(\vec{\theta}\,) = \nabla_{\vec{\theta}}\,\Psi(\vec{\theta}\,) \tag{5.26}$$

where

$$\Psi(\vec{\theta}\,) = \frac{1}{\pi}\int_{R^2} d^2\theta' k(\vec{\theta'})\; ln \mid \vec{\theta} - \vec{\theta'} \mid \;\; . \tag{5.27}$$

The Fermat potential is given by

$$\Phi(\vec{\theta}, \vec{\beta}\,) = \frac{1}{2}(\vec{\theta} - \vec{\beta}\,)^2 - \Psi(\vec{\theta}\,) \tag{5.28}$$

and we get then the lens equation from

$$\nabla_{\vec{\theta}}\, \Phi(\vec{\theta}, \vec{\beta}) = 0 \;. \tag{5.29}$$

Notice that

$$\nabla^2 \Psi = 2k \geq 0 \tag{5.30}$$

(using $\nabla^2\; ln \mid \vec{\theta}\mid = 2\pi\delta^2(\vec{\theta}\,)$), since k as a surface mass density is always positive (or vanishes). Until geometric optics approximation stays valid, gravitational lensing light deflection is achromatic (principle of equivalence: photons with different energies are deflected in the same way by a gravitational field). Liouville's theorem states that in absence of emission and absorption of photons, the quantity $I_\nu \nu^{-3}$ is invariant, with I_ν specific intensity. Therefore gravitational lensing conserves specific intensity, and also surface brightness I, defined as $I = \int I_\nu d\nu$, i.e. for a surface brightness distribution in the source plane $I(\vec{\beta})$, the corresponding image surface brightness distribution is

$$I(\vec{\theta}) = I(\vec{\beta}(\vec{\theta}))A(\vec{\theta}\,) = \frac{d\vec{\beta}}{d\vec{\theta}} \tag{5.31}$$

In general, the deflection of a surface brightness distribution in the source plane lends to a distorted surface brightness distribution in the image plane. Solving the lens equation for each light emitting point of the source, one finds the shape of the image. In practice, if the source is much smaller than the angular scale for which the lens properties change, it is possible to linearize locally the equation. The distortion of the images is then determined by the Jacobian matrix of the lens mapping,

$$A(\vec{\theta}\,) = \frac{d\vec{\beta}}{d\vec{\theta}} \;\; (A_{ij} = \frac{d\beta_i}{d\theta_j} = \delta_{ij} - \Psi_{,ij}) \;, \tag{5.32}$$

(where $\Psi_{,ij} = \partial_i\partial_j\Psi$) Hence, if $\vec{\theta_0}$ is a point of an image, corresponding to a source point $\vec{\beta_0} = \vec{\beta}(\vec{\theta_0})$, the conservation of surface brightness and the linearized lens equation give

$$I(\vec{\theta}) = I(\vec{\beta_0} + A(\vec{\theta_0}\,) \times (\vec{\theta} - \vec{\theta_0})) \tag{5.33}$$

Circular isophotes are mapped in ellipses, and the ratio between ellipses semiaxes and the radius of a source isophote is given by the inverse of the eigenvalues of $A(\vec{\theta_0}\,)$. The flux of a source, located in $\vec{\beta}$, in the solid angle $d\Omega(\vec{\beta}\,)$ is given by

$$S(\vec{\beta}\,) = I\; d\Omega(\vec{\beta}\,) \;. \tag{5.34}$$

$S(\vec{\beta}\,)$ is the flux one would see if there were no lensing. On the other hand the observed flux from the image located in $\vec{\theta}$ is

$$S(\vec{\theta}\,) = I\ d\Omega(\vec{\theta}\,)\ . \tag{5.35}$$

The ratio of the fluxes is the magnification factor $|\mu|$, and is thus given by the ratio

$$|\mu| = \frac{d\Omega(\vec{\theta}\,)}{d\Omega(\vec{\beta}\,)} = \frac{1}{|detA(\vec{\theta}\,)|}\ , \tag{5.36}$$

The inverse of the Jacobian is called the magnification tensor

$$M(\vec{\theta}\,) = A(\vec{\theta}\,)^{-1} \tag{5.37}$$

Therefore

$$|\mu| = |detM(\vec{\theta}\,)| \tag{5.38}$$

Note that the $\mu = detM(\vec{\theta}\,)$ can be of either sign. The sign of μ is the parity of the image. Note also that if the image stays unresolved, i.e. if it is point-like in the observations, the only apparent effect will be a change in magnification, whereas deformation will be observed only for extended objects. In particular, let's consider the case of a quasar within its host galaxy. The quasar image will stay unresolved (in the optical band), while the host galaxy will be stretched. The apparent effect will be that of a magnified point source superimposed to an extended, deformed source; in the latter the total flux will increase because the image will appear more extended, but the surface brightness will stay unchanged.

5.1.6 Critical curves and caustics

For some values of $\vec{\theta}$, $detA(\vec{\theta}\,) = 0$ and thus $\mu \to \infty$. The points (or the curve) $\vec{\theta}$ in the lens plane for which $detA(\vec{\theta}\,) = 0$ are defined as *critical points (or critical curve)*. At these points the geometrical optics approximation used so far breaks down. The corresponding points (or curve) of the critical points in the source plane are the so called *caustics*.

The qualitative behaviour of gravitational lensing can be greatly aided by the study of critical curves and caustics. In fact the number of images that a source can produce is completely determined by its position in respect to the caustics. Suppose to move a source in the lens plane. Everytime it will cross a caustic, the number of images produced will be increased or reduced by two. The inner and the outer side of each caustic are defined in such a way that crossing the caustic from the outside to the inside will decrease the number of images, while crossing it from the inside to the outside will decrease the number of images. This behaviour can be qualitatively explained in the following way: suppose that the source is far away from the lens. The deflection angle will go to low value, up to be zero at infinity. Therefore such a source will have only an image at $\vec{\theta} \sim \vec{\beta}$. Suppose to move the source at smaller impact parameter with

the lens. The lens mapping will stay locally invertible until the determinant of the Jacobian will not be null, $detA \neq 0$, so there will be still only one image until a caustic that corresponds to $detA = 0$ will be crossed. The number of images will always change of ± 2, in agreement with the odd image theorem. The two image created by a caustic crossing are always on opposite side of the corresponding critical curve. Since μ changes sign at the critical curve, these images must also have opposite parity. In general, critical curves are closed and smooth. Caustics instead are not necessarily smooth, but they can develop cusp. Suppose in fact $\vec{\theta}(\lambda)$ to be a parametrization of the critical curve. The corresponding caustic is $\vec{\beta}(\vec{\theta}(\lambda))$. The tangent vector to the critical curve and the caustic are respectively

$$\dot{\vec{\theta}}(\lambda) \equiv \frac{d\vec{\theta}(\lambda)}{d\lambda} \tag{5.39}$$

and

$$\frac{d\vec{\beta}(\vec{\theta}(\lambda))}{d\lambda} = \frac{\partial \vec{\beta}}{\partial \vec{\theta}} \times \frac{d\vec{\theta}(\lambda)}{d\lambda} \tag{5.40}$$

In the case in which the tangent to the critical curve, $\dot{\vec{\theta}}(\lambda)$, is parallel to the eigenvector of A whose eigenvalue is 0, the tangent to the caustic can vanish. Such a point is a cusp. Apart from the cusps, the caustics are smooth curves called fold caustics.

5.1.7 Images classification and theorems

If we consider a fixed value for $\vec{\beta}$, then the Fermat potential $\Phi(\vec{\theta}, \vec{\beta})$ defines a surface for the arrival time of the light. Ordinary images, for which $detA(\vec{\theta}) \neq 0$, are formed at the points $\vec{\theta}$, where $\nabla_{\vec{\theta}} \Phi(\vec{\theta}, \vec{\beta}) = 0$. Thus the images are localized at extremal or saddle points of the surface $\Phi(\vec{\theta}, \vec{\beta})$ and are classified as follows.

Images of type I:
correspond to minima of Φ, with $detA > 0$, $trA > 0$. Images of type I are always magnified (at least as bright as the source) and have positive parity.

Images of type II:
correspond to saddle points of Φ, with $detA < 0$. Images of type II can be either magnified or demagnified, but they have negative parity.

Images of type III:
correspond to maxima of Φ, with $detA > 0$, $trA < 0$. Like type II images, they can be either magnified or demagnified; however, they have negative parity.

Let's consider a thin lens with a smooth surface mass density $k(\vec{\theta})$, which decreases faster than $|\vec{\theta}|^{-2}$ for $|\vec{\theta}| \to \infty$. For such a lens the total mass is finite and the deflection angle $\vec{\alpha}(\vec{\theta})$ is continuous and tends to zero for $|\vec{\theta}| \to \infty$,

therefore $\vec{\alpha}$ is bounded: $\mid \vec{\alpha} \mid \leq \alpha_0$. Moreover, lets denote by n_I the number of images of type I for a source located in $\vec{\beta}$, similarly for n_{II} and n_{III} and define $n_{tot} = n_I + n_{II} + n_{III}$. If these conditions are fulfilled than the following theorems hold.

Theorem 1

If the above conditions hold and $\vec{\beta}$ is not situated on a caustic, the following conditions apply:

a) $n_I \geq 1$
b) $n_{tot} < \infty$
c) $n_I + n_{III} = 1 + n_{II}$
d) for $\mid \vec{\beta} \mid$ sufficiently large $n_{tot} = n_I = 1$.

It thus follows from c) that the total number of images $n_{tot} = 1 + 2n_{II}$ is odd. The number of images with positive parity $(n_I + n_{III})$ exceeds by one those with negative parity (n_{II}); $n_{II} \geq n_{III}$ and $n_{tot} > 1$ if and only if $n_{II} \geq 1$. The number of images is odd, however, in practice some images may be very faint or be covered by the lens itself and are thus not observable.

Theorem 2

The image of the source which will appear first to the observer is of type I and it is at least as bright as the unlensed source would appear $(\mu(\vec{\theta_1}) \geq 1)$.

See e.g. Schneider, Ehlers & Falco ([212]) for a proof of the two theorems.

5.1.8 Necessary and sufficient conditions for multiple images formation

There are two general criteria to establish if a mass distribution with a surface dimensionless density $k(\vec{\theta})$ can or cannot form multiple images:
Criterion I
An isolated and transparent lens can produce multiple images if and only if there is a point $\vec{\theta}$ for which $detA(\vec{\theta}) < 0$. This can be shown as follows: suppose $detA(\vec{\theta}) > 0 \; \forall \; \vec{\theta}$, then the lens mapping is globally invertible and no more than one image can be formed. By converse, if $\exists \; \vec{\theta}_0$ for which $detA(\vec{\theta}) < 0$, then a source in $\vec{\beta}(\vec{\theta_0})$ must form a saddle point image in $\vec{\theta}_0$, and therefore at least other two images for the odd number theorem.

Criterion II
A sufficient but not necessary condition to form multiple images is the existence of a point $\vec{\theta}$ for which $k(\theta) > 1$. We refer to e.g. Schneider, Ehlers & Falco

([212]) for a proof.

5.2 Simple mass models

In this Section we will discuss the lensing properties of simple mass models. In general, the lens equation must be solved numerically. Simplifying assumptions for the mass surface density permit to treat lensing quantities analytically, instead of numerically. We will treat three models, a point mass lens, relevant especially for microlensing, a Singular Isothermal Sphere (SIS) and a Singular Isothermal Ellipsoid (SIE). The second two models are often used for lens galaxy modeling, either alone or as building blocks for more complex distributions. We will not discuss other models, sometimes almost as simple, that are often used in literature, especially for spiral galaxies or for dark matter dominated structures (e.g. Kochanek, Schneider & Wambsganss [125] and references therein).

5.2.1 Axisymmetric lenses

When the surface mass density of a lens is axially symmetric, $\Sigma(\vec{\xi}) = \Sigma(\mid \vec{\xi} \mid)$, the lens equation reduces to a one-dimensional equation. By symmetry we can restrict the impact vector $\vec{\theta}$ to be on the positive θ_1-axis, thus we have $\vec{\theta} = (\theta, 0)$ with $\theta > 0$. We can then use polar coordinates: $\vec{\theta'} = \theta'(cos\phi, sin\phi)$ (thus $d^2\theta' = \theta' d\theta' d\phi$). With $k(\vec{\theta}) = k(\theta)$ we get for eq.(5.25)

$$\alpha_1(\theta) = \frac{1}{\pi} \int_0^\infty \theta' \; d\theta' k(\theta') \; \int_0^{2\pi} d\phi \; \frac{\theta - \theta' cos\phi}{\theta^2 + \theta'^2 - 2\theta\theta' cos\phi} \; , \tag{5.41}$$

$$\alpha_2(\theta) = \frac{1}{\pi} \int_0^\infty \theta' \; d\theta' k(\theta') \; \int_0^{2\pi} d\phi \; \frac{-\theta' sin\phi}{\theta^2 + \theta'^2 - 2\theta\theta' cos\phi} \; . \tag{5.42}$$

Due to the symmetry $\vec{\alpha}$ is parallel to $\vec{\theta}$ and with eq. (5.42) we get $\alpha_2(\theta) = 0$. A two dimensional analog of the Birkhoff theorem is valid: only the mass inside the disc of radius θ around the center of the lens contributes to the light deflection. In practice, from eq. (5.41) one finds

$$\alpha(\theta) \equiv \alpha_1(\theta) = \frac{2}{\theta} \int_0^\theta \theta' \; d\theta' k(\theta') \equiv \frac{m(\theta)}{\theta} \; . \tag{5.43}$$

where we introduced the adimensional mass inside radius θ, $m\theta$. Analogously,

$$\alpha(\xi) = \frac{4G}{c^2} \frac{2\pi}{\xi} \int_0^\xi \xi' \; d\xi' \Sigma(\xi') \equiv \frac{4GM(\xi)}{c^2 \xi} \; . \tag{5.44}$$

with $M(\xi)$ is the dimensional mass inside a radius ξ. The lens equation is thus

$$\beta = \theta - \alpha(\theta) = \theta - \frac{m(\theta)}{\theta} \tag{5.45}$$

for $\theta \geq 0$. Due to the axial symmetry it is enough to consider $\beta \geq 0$. Since $m(\theta) \geq 0$ it follows that $\theta \geq \beta$ (for $\theta \geq 0$). Instead of eq. (5.27) we get

$$\Psi(\theta) = 2 \int_0^\theta \theta' \; d\theta' \; k(\theta') \; ln \left(\frac{\theta}{\theta'} \right) \; , \tag{5.46}$$

whereas the Fermat potential can be written as

$$\Phi(\theta, \beta) = \frac{1}{2}(\theta - \beta)^2 - \Psi(\theta) \; . \tag{5.47}$$

This way we get the lens equation (5.45) from

$$\frac{\partial \Phi(\theta, \beta)}{\partial \theta} = 0 \; . \tag{5.48}$$

To get the Jacobi matrix we write: $\vec{\alpha}(\vec{\theta}) = \frac{m(\theta)}{\theta^2}\vec{\theta}$ (with $\vec{\theta} = (\theta_1, \theta_2)$ and $\theta = \mid \vec{\theta} \mid$) and thus

$$A = \begin{pmatrix} 1 & 0 \\ 0 & 1 \end{pmatrix} - \frac{m(\theta)}{\theta^4} \begin{pmatrix} \theta_2^2 - \theta_1^2 & -2\theta_1\theta_2 \\ -2\theta_1\theta_2 & \theta_1^2 - \theta_2^2 \end{pmatrix} - \frac{2k(\theta)}{\theta^2} \begin{pmatrix} \theta_1^2 & \theta_1\theta_2 \\ \theta_1\theta_2 & \theta_2^2 \end{pmatrix} \; , \tag{5.49}$$

where we made use of $m'(\theta) = 2\theta k(\theta)$. The determinant of the Jacobi matrix is given by

$$detA = \left(1 - \frac{m}{\theta^2}\right) \left(1 - \frac{d}{d\theta}\left(\frac{m}{\theta}\right)\right) = \left(1 - \frac{m}{\theta^2}\right) \left(1 + \frac{m}{\theta^2} - 2k\right) \; . \tag{5.50}$$

5.2.2 Tangential and radial critical curves

The critical curves for an axisymmetric lens are circles. Two cases are possible:

(i) $\frac{m}{\theta^2} = 1$: defined as *tangential critical curve*;

(ii) $\frac{d}{d\theta}\left(\frac{m}{\theta}\right) = 1$: defined as *radial critical curve*.
The names of the critical curves refer to the preferential direction images formed near to the critical curve are distorted. The corresponding caustics inherit the same name, *tangential caustic* and *radial caustic*. Using the lens equation in the form (5.45) it is immediate to see that the tangential caustic reduces to a point ($\beta = 0$). This degeneracy is broken by any perturbation of the axial symmetry. The total mass $M(\xi_t)$ inside the tangential critical curve is thus

$$M(\xi_t) = \pi \xi_t^2 \Sigma_{crit}. \tag{5.51}$$

This shows that the average density $\langle \Sigma \rangle_t$ inside the tangential critical curve is equal to the critical density Σ_{crit}. This provides an immediate estimate of the lens mass when Einstein rings can be traced (see the following subsection).

5.2.3 Einstein radius

If we write dimensionally the lens equation (5.7) for an axisymmetric lens, we get

$$\beta(\theta) = \theta - \frac{D_{ds}}{D_s D_d} \frac{4GM(\theta)}{c^2 \theta} \ , \tag{5.52}$$

The tangential critical curve is a circle of radius

$$\theta_E = \left(\frac{4GM(\theta_E)}{c^2} \frac{D_{ds}}{D_d D_s} \right)^{1/2} \ , \tag{5.53}$$

θ_E is called *Einstein radius*. The corresponding linear quantity is often used

$$R_E = R_E = \theta_E D_d = \left(\frac{4GM}{c^2} \frac{D_{ds} D_d}{D_s} \right)^{1/2} \tag{5.54}$$

and it is also called Einstein radius. A source posed in the degenerate tangential caustic is imaged in a ring of radius θ_E, called *Einstein ring* ([45]; also discussed by Einstein in 1911, see [204]). The Einstein radius depends, as we see from (5.53) both on lens parameters and on the distances of the lensing situation. The Einstein radius sets a natural scale for the angles entering the description of the lens. The formation of Einstein rings depends crucially on the tangential caustic degeneracy. Therefore, one would not expect to see Einstein rings in real situations due to small deviations from axial symmetry. It turns out instead that Einstein rings are indeed observed (see Figure 5.2). The current model for Einstein rings requires lensing of an extended source by an asymmetric mass ([125]). Non axisymmetric sources form an astroid tangential caustic; Einstein rings form when the source and the astroid caustic are of comparable extent.

5.2.4 Point mass lens

The simplest lens is a point mass M. For the Birkhoff's theorem, it is equivalent to consider the outside region of a finite spherical mass distribution of total mass M. We put the origin of the lens plane in the same place of the point M. The surface density is $\Sigma(\vec{\xi}) = M\delta^2(\vec{\xi})$, where $\delta^2(\vec{\xi})$ is the two-dimensional Dirac's delta, and thus $m(\theta) = \theta_E^2$. The lens equation (5.45) becomes

$$\beta = \theta - \frac{\theta_E^2}{\theta} \ , \tag{5.55}$$

where θ_E is given by eq. (5.53). This equation has two solutions

$$\theta_\pm = \frac{1}{2}(\beta \pm \sqrt{\beta^2 + 4\theta_E^2}) \ . \tag{5.56}$$

Therefore, there will be two images of the source located on the opposite sides of the lens. The image on the same side of the source, in θ_+, is further away

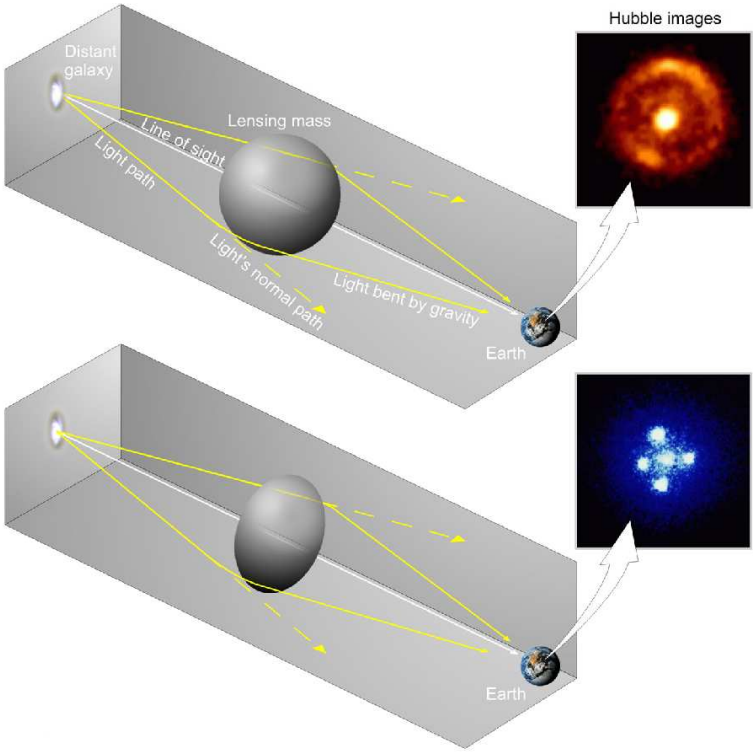

Figure 5.2 An illustrative view of lensing of a source exactly aligned with the center of the lens. If the source is asymmetric, the Einstein ring breaks in four images, the Einstein cross (adapted from Hubble European Space Agency Information Centre).

from the lens than the other one. In fact, the image in θ_+ is outside the Einstein radius, while the image in θ_- is inside the Einstein radius. For a lens with axial symmetry the amplification is given by

$$\mu = \frac{\theta}{\beta}\frac{d\theta}{d\beta} \, . \tag{5.57}$$

Substituting β with eq.(5.56) we obtain

$$\mu_\pm = \left[1 - \left(\frac{\theta_E}{\theta_\pm}\right)^4\right]^{-1} = \frac{u^2+2}{2u\sqrt{u^2+4}} \pm \frac{1}{2} \, . \tag{5.58}$$

with $u = \beta/\theta_E$. We can see that the image in θ_+ has positive parity and is always magnified, while the image in θ_- has negative parity and can be either magnified or demagnified. The total amplification is given by the sum of the absolute values of the amplifications for each image

$$\mu = \mid \mu_+ \mid + \mid \mu_- \mid = \frac{u^2+2}{u\sqrt{u^2+4}} \, . \tag{5.59}$$

For $\beta = \theta_E$, $\mu = 1.34$. Note that the odd images theorem is not applicable, since we supposed a non-smooth mass distribution. If we use a smooth mass distribution, like a very sharp but finite circular gaussian, a third image is formed, very demagnified and near to the lens.

5.2.5 Singular Isothermal Sphere

In this subsection we will discuss the simplest model that can be applied to galaxies, the Singular Isothermal Sphere (SIS). The SIS is a spherical mass distribution with density

$$\rho(r) = \frac{\sigma_v^2}{2\pi G r^2} \tag{5.60}$$

The physical meaning of the SIS is that of a distribution of self-gravitating particles with, at every radius, a Maxwellian velocity distribution with one-dimensional velocity dispersion σ_v (i.e. "the same kinetical temperature at every radius"). The corresponding three-dimensional velocity dispersion is $\sqrt{3}\sigma_v$, and the Keplerian rotational velocity is $\sqrt{2}\sigma_v$. The mass distribution described by the 5.60 have two pathological properties: it diverges in the center as $\rho \propto r^{-2}$, and the total mass of the distribution diverges as $r \to \infty$. The former feature can be cured introducing a finite core radius, while the second does not affect lensing properties at smaller radii. The SIS projected mass density is

$$\Sigma(\xi) = \frac{\sigma_v^2}{2G}\frac{1}{\xi} \ , \tag{5.61}$$

where ξ is the distance (in the lens plane) from the center of mass.

For the light deflection angle we get

$$\hat{\alpha} = 4\pi\frac{\sigma_v^2}{c^2} = 1.4'' \left(\frac{\sigma_v}{220\ km\ s^{-1}}\right)^2 \tag{5.62}$$

independent of the position ξ ($220\ km\ s^{-1}$ is a typical value for the rotation velocity in spiral galaxies).

The Einstein radius R_E is given by

$$R_E = 4\pi\frac{\sigma_v^2}{c^2}\frac{D_{ds}D_d}{D_s} = \hat{\alpha}\frac{D_{ds}D_d}{D_s} = \alpha D_d \ . \tag{5.63}$$

Multiple images occur only if the source is located within the Einstein radius. Let be $\xi_0 = R_E$, then $\Sigma(\xi) = \Sigma(x\xi_0)$ where $x = \xi/\xi_0$. This way the lens equation becomes

$$y = x - \frac{x}{\mid x \mid} \ . \tag{5.64}$$

For $0 < y < 1$ we have two solutions: $x = y + 1$ and $x = y - 1$. For $y > 1$ (the source is located outside the Einstein radius) there is only one image: $x = y + 1$. The images with $x > 0$ are of type I, whereas the ones with $x < 0$ are of type

II. If the singularity in $\xi = 0$ is removed then there will be a third image in the center.

The amplification of an image in x is given by

$$\mu = \frac{\mid x \mid}{\mid x \mid -1} \tag{5.65}$$

(the circle $\mid x \mid = 1$ corresponds to a tangential critical curve). For $y \to 1$ the second image (corresponding to the solution $x = y - 1$) gets very faint.

5.2.6 General features of non axisymmetric lenses

Some feature of the non axisymmetric lenses can be treated in generality. In particular, the degenerate tangential caustic is unstable to any loss of symmetry. In general, whatever the exact source of the asymmetry be(ellipticity of the potential, of the isothermal mass distribution, inclination of a disk distribution, external mass that introduce a directional shear), the tangential caustic develop four cusps, assuming an astroid shape, that can be further bent if there is symmetry loss in different directions. The presence of two non degenerate caustics with an interior (defined as in 5.1.6) make the lens capable to produce up to five images. Indeed, if the source stays in the center of the lens caustics, an Einstein Cross is produced (see Figure 5.2). Another general feature is the extreme complexity. Very few lens models can be solved analytically in the general case (i.e. if the source is not on a symmetry axis). Finally, it is useful to remark that very different lens models with different parameters can originate the same caustic/critical curve structure, and are therefore difficult to discriminate. This applies in particular to the two most studied classes of non axisymmetric models, axisymmetric lenses with external shear and elliptical mass distributions.

5.2.7 Singular Isothermal Ellipsoid

One of the simplest non axisymmetric model is the Singular Isothermal Ellipsoid (SIE; e.g. Kassiola & Kovner [117], Kormann, Schneider & Bartelmann[128], Keeton & Kochanek [119])[1]. In general, the surface density of a generic isothermal elliptic mass distribution is

$$k = constant \times (c_0^2 + c_1^2 x^2 + c_2^2 y^2)^{-1/2}. \tag{5.66}$$

In the case singular (vanishing core), c_0=0, and we can rewrite the surface density introducing the elliptical radius r_{em},

$$r_{em}^2 = \frac{x^2}{(1+\epsilon)^2} + \frac{y^2}{(1-\epsilon)^2} \tag{5.67}$$

[1]It should be specified if it refers to potential or to mass distribution, because a) parameters are different b) for large enough ellipticities, the Singular Isothermal Ellipsoidal potential do not correspond to a Singular isothermal mass distribution. We will use here the Singular Isothermal Mass Distribution

where ϵ is related to the axis ratios by the

$$\frac{b}{a} = \frac{1+\epsilon}{1-\epsilon} \tag{5.68}$$

The resulting expression of the convergence $k(\vec{\theta})$ is

$$k(\vec{\theta}) = k(r_{em}) = constant' \times (r_{em}^2)^{-1/2}. \tag{5.69}$$

For a surface mass density of this shape, the magnification is simply:

$$\mu(\vec{\theta}) = \frac{1}{1-2k(\vec{\theta})}. \tag{5.70}$$

The tangential critical curve k=1/2 defines a "pseudo-Einstein radius" E_0, i.e.

$$E_0^2 = r_{em,crit}^2. \tag{5.71}$$

The components of the deflection angle are:

$$\frac{\partial\Phi}{\partial x} = \frac{E_0(1-\epsilon^2)}{2\sqrt{\epsilon}} sin^{-1}\left(\frac{2\sqrt{\epsilon}}{1+\epsilon} cos\phi\right) \tag{5.72}$$

$$\frac{\partial\Phi}{\partial y} = \frac{E_0(1-\epsilon^2)}{2\sqrt{\epsilon}} sinh^{-1}\left(\frac{2\sqrt{\epsilon}}{1+\epsilon} sin\phi\right) \tag{5.73}$$

with the usual ϕ of polar coordinates.

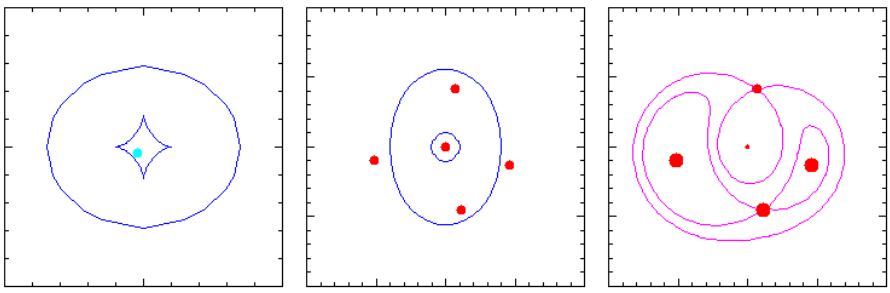

Figure 5.3 Illustration of caustics and critical curves for an ellipsoidal lens. Left: source plane. The blue curves are caustics, the light blue dot is the source. Center: image plane. The blue curves are critical curves, the red dots are image. Right: image plane. The red dots are images, with area proportional to magnification, the blue curves are contours of light travel time. Made with SimpLens software ([209])

5.3 Microlensing

Let's suppose to have a source located in the Large Magellanic Cloud and a point lens of mass M located in the galactic halo at a distance of $D_d \sim 10$ kpc. The Einstein radius will be

$$\theta_E = (0.9'' \times 10^{-3}) \left(\frac{M}{M_\odot}\right)^{1/2} \left(\frac{D}{10\ kpc}\right)^{-1/2} \tag{5.74}$$

where $D = D_d D_s / D_{ds}$. Thus, the scale of this kind of lensing can easily be the scale of microarcsec, hence the denomination microlensing. In microlensing the angular separation between the two images is far too small to be observable. What can be detected is magnification: when the motion of the lens is such that the source will be in its Einstein ring, a sharp brightness increase will happen, followed by a sharp decrease when the source will go out from the Einstein ring. Actually, microlensing was the first application of gravitational lensing considered (Chwolson [45]; Einstein [63]); but after Zwicky ([264];[265]) suggested to look for lensing galaxies instead, it remained more or less forgotten (with some remarkable exception: Liebes [131], Refsdal [200], Refsdal [201], Chang & Refsdal([42]) until Paczyński paper in 1986 ([176]), who understood the potential of microlensing in searches for baryonic dark matter. Some years later, both theoretical progress (De Rújula, Jetzer & Massó [57],Griest [85]) and large observational efforts (the collaborations MACHO, OGLE, EROS) started the MACHOs era (an acronym for Massive Compact Halo Object). It would go beyond the scope of the present thesis to resume the debate about the results of microlensing searches. What instead it is important to remark is that meanwhile the scientific world attention was concentrated on LMC microlensing, the Galactic Bulge was used as control for the experiment, in order to verify the theoretical expectation of microlensing. It turned out that bulge microlensing, despite of this mild start, is applicable to diverse field of astrophysics (see 5.3.4). In the following sub-sections a brief summary of microlensing events features and observable is presented.

5.3.1 Microlensing formalism

A distinctive trait of microlensing in respect to other lensing situation is its dynamicity. The typical situation that we consider is that of a lens in motion in respect to the line of sight (we neglect motions of the source). The total magnification factor for a point lens $\mu(u)$(eq. 5.59) becomes $\mu(u(t))$. Given the respective size of the distances in play, we can safely neglect the radial motion of the lens and consider fixed in time the Einstein radius of the lens. It is convenient to introduce the impact parameter r, i.e. the distance between the lens and the line of sight. Since $r = \beta \times D_d$, we can write $u = \frac{r}{R_E}$ (remembering eq. 5.54). If we indicate with $v_\perp$ the transverse velocity of the lens, i.e. the component of lens velocity perpendicular to the line of sight, with b the minimum distance

between the lens trajectory and the line-of-sight and with t_0 the time of closest approach, we can write

$$u^2(t) = \frac{b^2 + [v_\perp (t - t_0)]}{R_{\rm E}^2} \equiv u_{\rm min}^2 + \left[\frac{(t - t_0)}{T}\right]^2 \tag{5.75}$$

The situation is illustrated in Figure 5.4 and Figure 5.5.

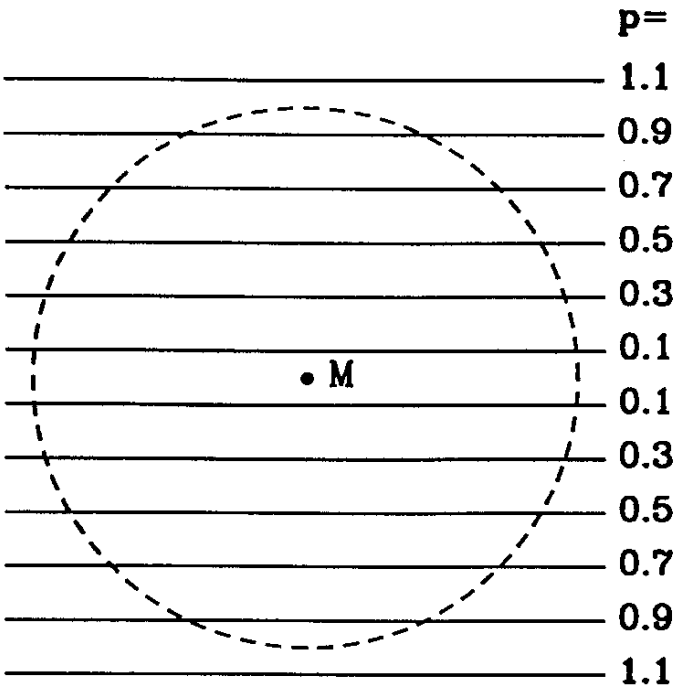

Figure 5.4 Einstein ring (dashed) and some possible relative orbits of a background star with projected minimal distances $p = r/R_E = 0.1$, 0.3, ..., 1.1 from a MACHO M (from Paczyński [176]).

The Einstein ring crossing time sets a natural time scale for the microlensing event duration:

$$T_E \equiv \frac{R_{\rm E}}{v_\perp} = \frac{1}{v_\perp}\sqrt{\frac{4\,G\,M}{c^2}\frac{D_{\rm ls} D_{\rm ol}}{D_{\rm os}}}, \tag{5.76}$$

(T_E is sometimes called Einstein time). In particular, T_E is the width of the microlensing lightcurve between the two points corresponding to magnification 1.34 (i.e. a ~ -0.3 rise in magnitude). An important concept in microlensing is the *optical depth*, τ. The optical depth is the probability that a source is found

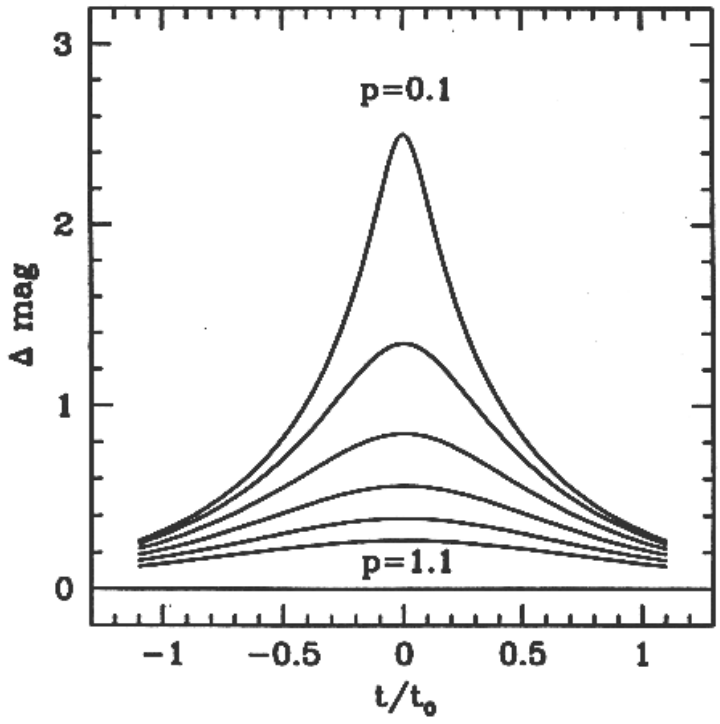

Figure 5.5 Light curves for the different cases of Figure 5.4. The maximal magnification is $\Delta m = 0.32$ mag, if the star just touches the Einstein radius ($p = 1.0$). For smaller values of p the maximum magnification gets larger. t is the time in units of t_0 (from Paczyński [176]).

within a circle of radius $r \leq R_E$ around a lens. It is defined as

$$\tau = \int_0^1 dx \frac{4\pi G}{c^2} \rho(x) D_s^2 x(1-x) \tag{5.77}$$

with $\rho(x)$ being the mass density along the line of sight at distance $s = xD_s$ from the observer. With the optical depth it is possible to evaluate the probability of having microlensing events for a fixed Galactic model. It is interesting to note that the optical depth does not depend on mass function, i.e. models with the same smoothed density can not be discriminated by means of the optical depth. The values of τ are very low, of the order of $10^{-7} - 10^{-6}$; therefore experiments need to monitor several millions of stars. For an experiment of duration $t_{\rm obs}$ that monitors N_* stars, we can write the *differential number of events* $dN_{\rm ev}$ like

$$dN_{\rm ev} = N_* t_{\rm obs} d\Gamma, \tag{5.78}$$

where $d\Gamma$ is the differential rate at which a single star is microlensed by a compact object and it is just equal to

$$d\Gamma = 2v_t f_t(v_t) D_S R_{\rm E} \frac{dn}{dm} dm dv_t dx \tag{5.79}$$

where $f_t(v_t$ is the transverse velocity distribution, the mass m is adimensional (in $M_\odot$ units) and $\frac{dn}{dm}$ is the mass function of the lenses.

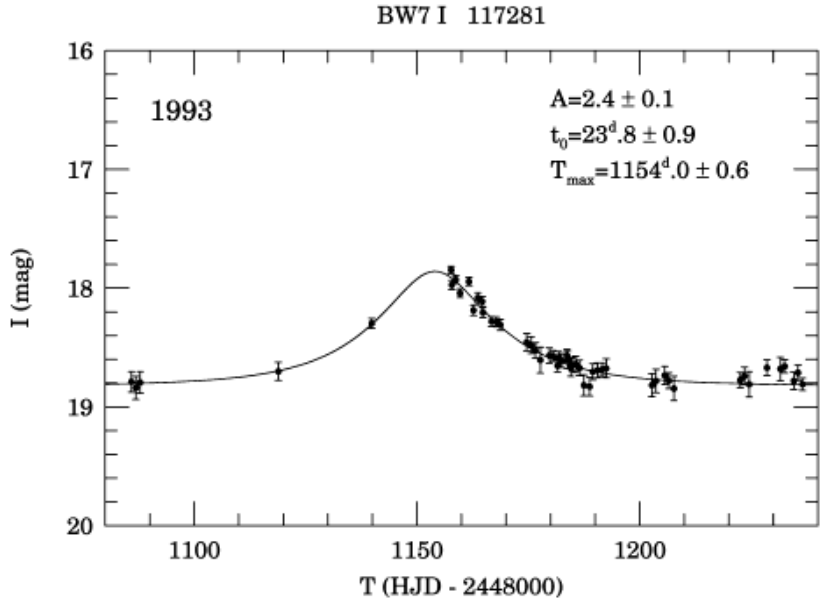

Figure 5.6 The lightcurve around maximum of the first bulge candidate microlensing event (from Udalski et al. [230])

5.3.2 Microlensing features

With such large numbers, it is paramount to individuate strong criteria to recognize microlensing events against the noise of variable stars. The criteria are essentially three, plus two criteria on the data ensemble, i.e.:
Achromaticity
Achromaticity is connaturated to gravitational lensing (but absorption can change the situation, e.g. Bozza et al. [29]), while instead stellar variability should be always chromatic.
Light curve shape
The microlensing light curve is symmetric, at odds with variable stars lightcurves, and it has a peculiar shape (see Figure 5.6).
Event unrepeatability

With such values of the optical depth the probability of repeat an event is too low. By converse, most variable stars have different flaring episodes.

The criteria on the data ensemble are:

Maximum magnification distribution

The maximum magnification distribution depends on the minimum impact parameter distribution, that is equiprobable.

Lensed star population

The population of microlensed stars should reflect the parent population of the target of the observational campaign.

In practice, the task of assessing the validity of a microlensing events is much harder. First, the sampling is not always sufficient to exclude different light curve shapes; second, binary sources, binary lenses, finite source size effects can perturb the light curve shape; finally, it is possible that unknown variable stars cannot be discriminated on the usual basis. This last risk is increased by the unprecedented size of the microlensing experiments monitoring, and since the number of events is low, even a rare new variable star could severely contaminate the sample. In fact, it was recently discovered by the EROS collaboration that MACHO-LMC-23 flared again after seven years, and it is therefore a new kind of variable star (Glicenstein [80]; Griest & Thomas [87]).

5.3.3 Degeneracy of microlensing

Finally, two quantities come out from an event, the event duration and its maximum amplification. Unfortunately, the event duration depends on four quantities. Even if we consider as fixed the source distance, still the lens mass, the lens transverse velocity and the lens distance are entangled in the event duration (note that the maximum magnification depends also on the minimum impact parameter, so it cannot be used to break the degeneracy). One cunning way to break microlensing degeneracy in a statistical way is the method of mass moments. With this method, it is possible to extract mean values and other information on the lens mass function extracting integrals of powers of lens masses (mass moments) from integrals of powers of event duration (time moments; see De Rújula, Jetzer & Massó [57] for the first formulation, Grenacher et al. [84] for an application). For individual events, the best bet within current observational capabilities is to detect in the light curve parallax effects (Alcock et al. [7]; Smith et al. [216]; see Figure 5.7). This method works only for long events, and has been used as the primary method to find black hole candidates. It is possible to break degeneracies also if the lens is binary. This is particularly relevant for exoplanets microlensing searches.

5.3.4 Learning from bulge microlensing

The first issue to which bulge microlensing applies is of course the study of galactic structure. The comparison between the foreseen optical depth and the

observed one is a powerful test for the validity of Milky Way Galaxy models. First model calculations, including only disk contribution, found $\tau = 0.5 \times 10^{-6}$ (Paczyński [177]; Griest [86]). Soon after the first event detection (Udalski et al. [230]), Kiraga & Paczyński ([123]) found $\tau = 0.85 \times 10^{-6}$ adding a bulge contribution. However, the first measurements were significantly higher: $\tau \geq 3.3 \pm 1.2 \times 10^{-6}$ (Udalski et al. [231]) from OGLE, $\tau = 3.9^{+1.8}_{-1.2} \times 10^{-6}$ from MACHO (Alcock et al. [8]). These results opened the so-called bulge optical depth problem. A lot of theoretical work focused on different models of Galactic structure, especially with the addition of a bar (e.g., Zhao, Spergel & Rich [260]; Zhao & Mao [261]; Bissantz et al. [21]; Nair & Miralda-Escudé [169]; Binney, Bissantz & Gerhard [20]; Evans & Belokurov [64];Han & Gould [98]; Bissantz, N., Debattista & Gerhard [23]). Values forecast for τ by these models reached $2.5 - 3 \times 10^{-6}$. Meanwhile, measurements of the optical depth with different sample selection methods ranged from $0.93 \pm 0.29 \times 10^{-6}$ (Afonso et al. [2]) to $3.36^{+1.11}_{-0.81} \times 10^{-6}$ (Sumi et al. [220]). One reason of this discrepancy between measurements is the use of different methods to circumvent the blending problem. Bulge fields are so crowded by stars that it is often not easy to pinpoint the real microlensing source. In presence of blended stars, the event is attributed to the blended source, not to the true, fainter one. Therefore its duration can be significantly underestimated. Two ways have been developed to deal with this bias; the Difference Image Analysis technique and the selection of red clump giants events only. In the first, image subtraction is applied to recover the real lightcurve (the contamination by blending should not change between the two images). The second uses the interesting property of red clump giants, a subclass of very bright stars, of occupying only a tiny region of the HR diagram (6.3). Once a sample of red clump giant events is selected by means of color information, since source absolute magnitude is known, a sample almost cleansed from blending bias is obtained. The last observational results on bulge optical depth, with larger samples and more efficient rejection of blended events seem to settle a more robust value. Specifically,

- the MACHO collaboration (Popowski et al. [195]) found $\tau = 2.17^{+0.47}_{-0.38} \times 10^{-6}$ at (l,b)=(1.50°, -2.68°), with latitude and longitude gradient of $(1.06 \pm 0.71) \times 10^{-6}$ deg^{-1} and $(0.29 \pm 0.43) \times 10^{-6}$ deg^{-1}, respectively (from 42 clump giant events; Popowski et al. [195]);

- the OGLE collaboration reported $\tau = 2.55^{+0.57}_{-0.46} \times 10^{-6}$ at (l,b)=(1.16°, -2.75°), with latitude gradient $\tau = [(4.48 \pm 2.37) + (0.78 \pm 0.84) \times b] \times 10^{-6}$(from 32 clump giant events; Sumi et al. [221];

- the EROS group obtained $\tau = [(1.62 \pm 0.23)\exp(-(0.43 \pm 0.16)/(\|\mathrm{b}| - 3\mathrm{deg}))] \times 10^{-6}$ in the range $1.4° < |b| < 7.0°$ (from 120 clump giant events; Hamadache et al. [96]).

All three estimate are compatible between themselves and with most Galactic models (see the discussion in Hamadache et al. [96]).

Other two applications of bulge microlensing are particularly appealing. One is the search for exoplanets. The first exoplanet candidate from microlensing is OGLE 2003-BLG-235/MOA 2003-BLG-53 (Bond et al. [27]; see Figure 5.8). The relative importance of different methods of exoplanet searches is questionable. What is certain is that at the present state microlensing can probe a much more distant sample of stars, so to provide a data ensemble much less biased by Solar neighborhood peculiarities, and therefore precious for planet formation studies.

The other one is the search for compact objects, black holes and neutron stars (Gould [82]). Being sensitive to mass, not light, microlensing is a suitable tool for individuate isolated black holes, that can accrete only from interstellar medium. Black hole events should stand out from the bulk of sub-solar mass lenses, but the degeneracy due to transverse velocities and distances acts to smear out the Einstein times ([82]). Nevertheless, for some very long events the parallax analysis resulted in a black hole candidate. Up to now, three candidates have been found (OGLE-99-BUL-32/MACHO-99-BLG-22, see Mao et al. ([137]), Bennett et al. ([16]), MACHO-96-BLG-5 and MACHO-98-BLG-6, see Bennett et al. ([15]); see however Agol et al. ([4]) for criticism). The main problem is that the unrepeatability of microlensing events hampers confirmations of mass estimates. Some of these candidates has already been observed by X-ray satellites, without revealing any source. However, accretion from interstellar medium is far from being fully understood. In particular, if a disk do not form (an issue not completely clear, see Agol & Kamionkowski [3]) accretion should take the inefficient Bondi-Hoyle path, originating a very dim source even if the black hole is very massive and the interstellar medium is very dense (the case of Sgr A* is emblematic). A further limitation could set a maximum threshold density of the interstellar medium surrounding the black hole. In fact, chromatic effects and changes in the shape of microlensing lightcurve are expected when the lens is embedded in a dense medium (Bozza et al. [29]), resulting in a rejected event. The confirmation of one of such candidates with an X-ray observation would be a major breakthrough not only as a confirmation for the whole goodness of the method, but especially because it would set interstellar medium accretion parameter with which large programs of isolated black holes searches could be calibrated.

Microlensing of isolated neutron stars up to now has been somehow overlooked, with some exceptions (Agol et al. [4] evaluated the likelihood of a neutron star mass for the three microlensing black hole candidates, Mollerach & Roulet [153] studied kicked neutron stars microlensing in direction of the LMC, Schwarz & Seidel [214] considered neutron stars for bulge microlensing). In regard to isolated neutron stars most of the above considerations remain valid, but there are four substantial differences. First, isolated neutron stars are likely to outnumber isolated black holes, even if the exact proportion of the two populations is currently hard to quantify, since it relies on a number of uncertain

parameters (what is the cut-off mass of the progenitor star, how it evolved with the metallicity in the history of the Galaxy, what is the kick velocity distribution of neutron stars and how many of them evaporate from the Galaxy...). This means that neutron star microlensing events should proportionally outnumber black hole microlensing events (e.g. Gould [82]). Second, black hole events are likely to stand out much more than neutron star events against the noise of "normal" events. In other words, the degeneracies intrinsic to microlensing are likely to drown most of neutron star events in the uncertainties on lens distance and transverse velocity. Third, the initial kicks are likely to drastically change the isolated neutron stars transverse velocity distribution in respect to the "background" one (usually taken from some Galactic model), valid from stars and probably for black holes. This phenomenon has been taken in consideration by Mollerach & Roulet ([153]) for an evolved distribution, but only for halo microlensing, and by Schwarz & Seidel ([214]) in the context of bulge microlensing, but with the rather crude use of a young radio pulsars velocity distribution as representative of the entire neutron stars population (dominated instead by older objects). Both event rates and Einstein times are very sensitive to the assumed kick distribution. In general, it is the low transverse velocity tail of neutron stars that can produce most of the long duration events, recognizable from the bulk of events. However, for the single event the impact of the kick velocity could actually be opposite (for example, the kick could counteract the transverse velocity of the progenitor star). Fourth, the confirmation of an isolated neutron star candidate found with microlensing would have to keep in account differences in the emission in respect to black holes. There a lot of light emitting isolated neutron stars powered by mechanisms different from accretion (the most important by all means is the radio pulsar phenomenon), but they are just a tiny minority in the overall neutron stars population, so it is likely that one would have to rely again on accretion from the interstellar medium. Radial accretion on a neutron star is in principle much more efficient in respect to radial accretion on a black hole, due to the presence of a rigid surface instead of an event horizon (the kinetic energy of the infalling material is radiated away once it hits the surface, and can not be advected through the horizon). However, the Bondi-Hoyle accretion rate can be strongly reduced by the boost of the neutron star velocities due to the initial kicks. Furthermore, magnetic fields and rapid rotation complicate the interaction of neutron stars with the surrounding medium, generating a sequence of different interaction phases, even more observationally elusive than the accreting one. The overall effect is to make more difficult the observation of isolated neutron stars (see Treves et al. [226] for an extensive review on accreting isolated neutron stars). In any case, as for black holes, even a single confirmed microlensing neutron star could constitute a paradigm for calibrating accretion parameters of future searches.

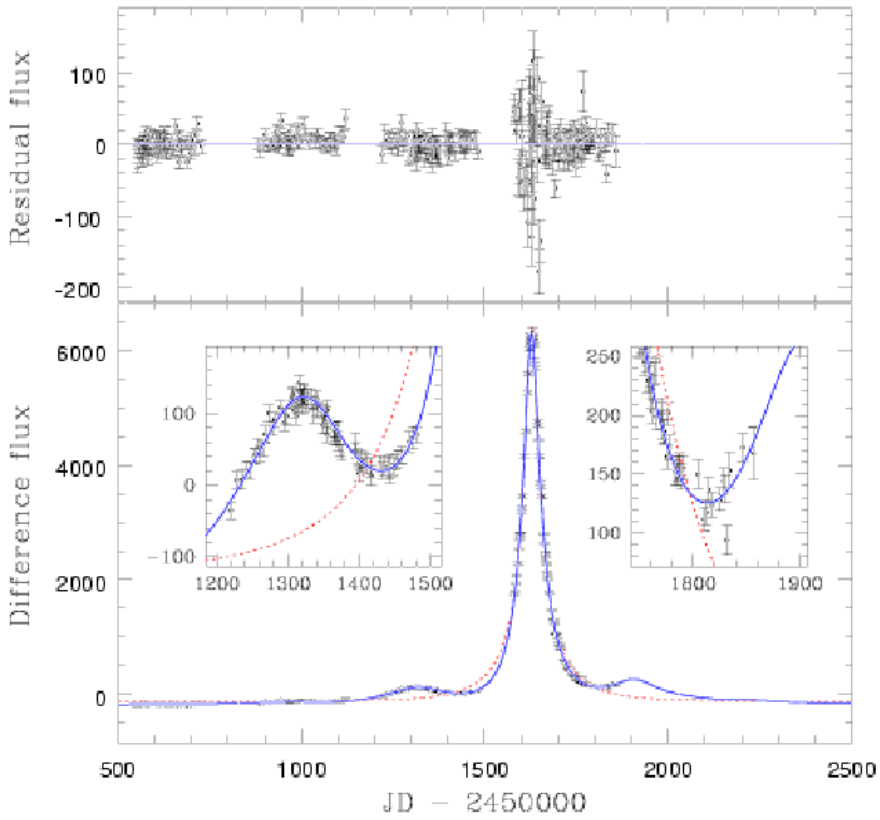

Figure 5.7 The lightcurve of the parallax microlensing event OGLE-1999-BUL-19. The thin dashed line is the microlensing curve fit without parallax effect, the solid blue line is the fit with parallax effects (from Smith et al. [216])

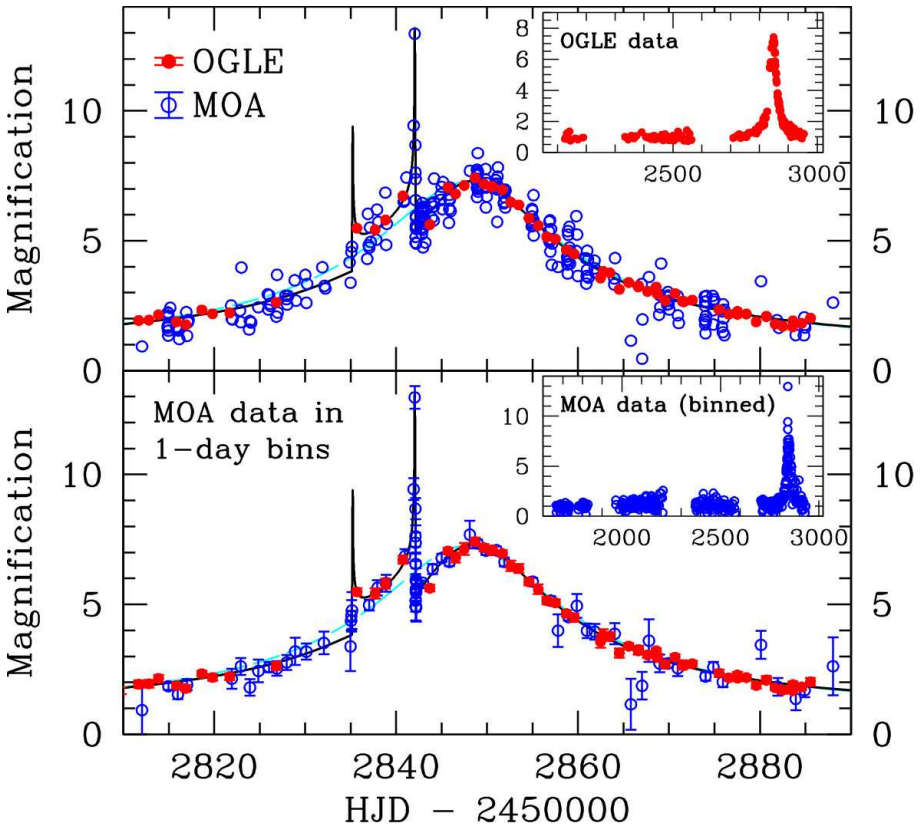

Figure 5.8 The lightcurve of the first exoplanet candidate microlensing event, OGLE 2003-BLG-235/MOA 2003-BLG-53 (Bond et al. [27]). Red dots are from the OGLE collaboration, blue dots are from the MOA collaboration (from Bond et al. [27]).

Chapter 6

Microlensing toward the Galactic Bulge

This chapter reports on the status of a work-in-progress on microlensing that we are conducting. Recent data releases of microlensing events in direction of the Galactic Bulge (MACHO, Thomas et al. [224]; EROS, Hamadache et al. [96]; 5.3.4) and optical depth estimates (MACHO, Popowski et al. [195]; OGLE, Sumi et al. [221]; EROS, Hamadache et al. [96]) have greatly increased the quality of data available to the scientific community. In summary, existing data releases from various collaborations are:

- 45 events from the first year of MACHO observations (Alcock et al. [8]);
- 99 events from Difference Image Analysis from three years of MACHO observations in eight fields (Alcock et al. [9]);
- 214 events from three years of OGLE-II observations (Udalski et al. [232]);
- 520 events from the same three years of OGLE-II observations, but with a different, Difference Image Analysis based, detection technique (Woźniak et al. [246]);
- 500 events from seven years of MACHO observation (Thomas et al. [224]);
- 62 red clump giant events taken from the same MACHO database (Popowski et al. [195]);
- 120 red clump giant events observed in six years by EROS-2 (Hamadache et al. [96]).

Both OGLE-II and MACHO released large data samples. Until recently, OGLE-II data were not provided with sampling efficiency, therefore severely limiting the amount of information that could be extracted. The situation changed with the work of Sumi et al. ([221]), that made available efficiency

for the full 520 DIA events from Woźniak et al. ([246]). The MACHO database of Thomas et al. ([224]) is comparable to the OGLE-II one. Unfortunately, full efficiency curves have been published only for red clump giant events (Popowski et al. [195]), and it is not easy to evaluate how much difference it can make for the whole data sample, though some information on the efficiency can be found in Thomas et al. ([224]). Finally, Hamadache et al. ([96]) provided the largest sample of red clump giant events (free from blending bias). Overall, the above numbers indicate a strong increase in data quality, that still have to produce most of its scientific impact. In the following sections we report on the aims and the present status of the (still in progress) works on microlensing that we are conducting, especially in light of the new data.

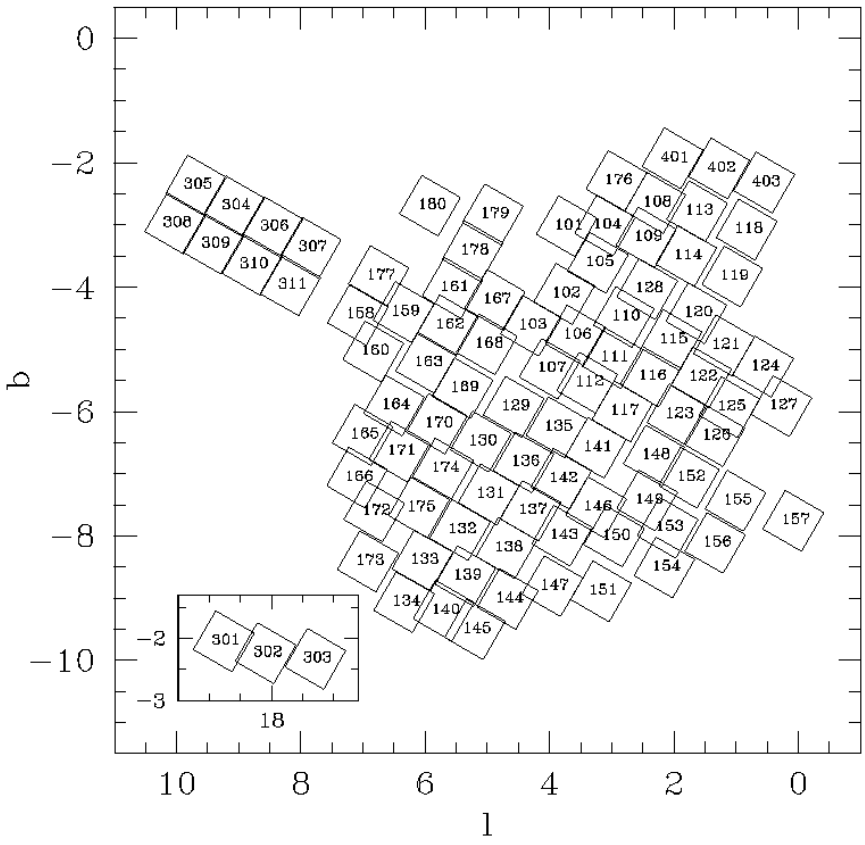

Figure 6.1 The MACHO bulge fields.

6.1 The field 104 anomaly

Soon after the first years of Galactic Bulge microlensing observations, it became clear the presence of a somewhat unexpected large number of long events. The analysis of these events, that can be sufficiently long to incorporate parallax effect (see 5.3.4) has opened the hunt for isolated black holes with microlensing. Popowski ([194]) noted an anomalous clustering of long events in one single field of the MACHO data, field 104 (see Figure 6.1). Here we summarize the anomalous features:

- **Too many red clump giants events.** 9 out of 62 events of Popowski et al. ([195]) sample are in field 104.
- **Too large optical depth.** The τ for field 104 is $8.76 \pm 3.73 \times 10^{-6}$. Errors are always large in determining the optical depth field by field, due to the poor statistics. The second largest optical depth value is $5.13 \pm 2.13 \times 10^{-6}$ for field 401.
- **Too many long red clump giant events.** Four out of ten of the event with $T_E > 50$ days are in field 104. Of the three longest events, two are in field 104.

The anomaly is much less apparent, at least at first sight, when the overall events are considered. Only 27 of the overall 515 events of Thomas et al. [224]) belong to field 104. Seven events in field 104 have $T_E > 50$, a threshold crossed by 58 events in the overall sample.

Sumi et al. ([221]) reported a similar long duration excess in their field BUL_SC30 ($\sim$ 1 deg away from field 104) in respect to the neighbouring fields, but they do not unbalance themselves on its significance.

Hamadache et al. ([96]) have also considered the field 104 anomaly; they do not find any evidence of anomaly in the corresponding direction. Comparing their sample with the 9 red clump giant events of Popowski et al. ([195]) they find that 5 events happened before the start of EROS-2 and two further events are outside EROS fields. They then conclude that the anomaly is purely a statistical fluctuation, remarking the fact that in three years after the end of MACHO they observed no anomaly.

The significance of the anomaly has been verified statistically by Popowski et al. ([195]) with a Wilcoxon two samples test on the clump giant events. They obtained a 2σ anomaly. They concluded that the statistical significance of the anomaly is too low to be meaningful, and therefore they favor an explanation based on statistical fluctuations.

6.1.1 Significance test

To investigate further the issue, we tried a different approach. First, we used the Kolmogorov-Smirnov test instead of the Wilcoxon one. The Kolmogorov-

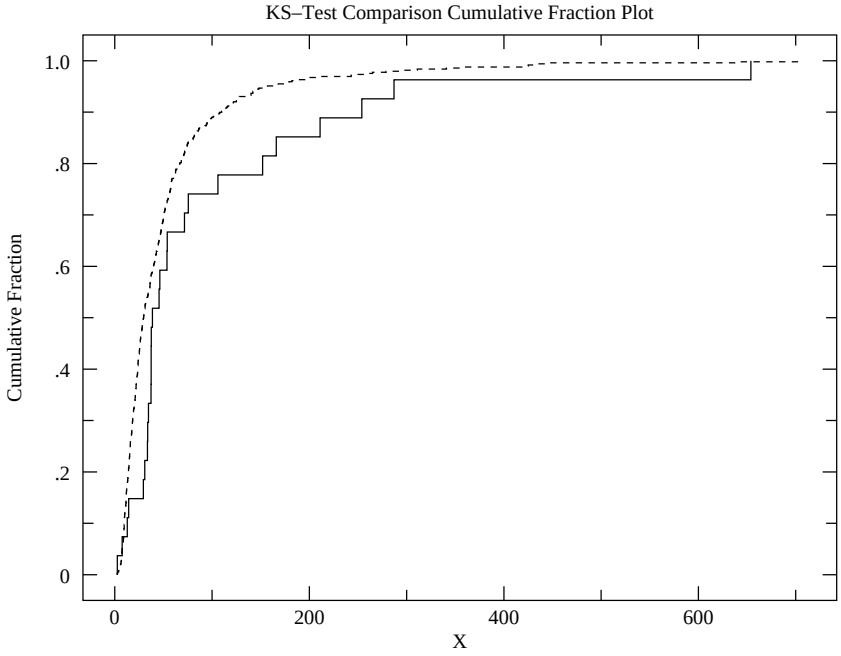

Figure 6.2 The Kolmogorov-Smirnov cumulative fraction plot of field 104 and non-field 104 microlensing events.

Smirnov test evaluates the maximum difference between cumulative distributions, and is known to be sensitive to difference in distribution shape, besides to difference in central tendency. Since we suspect some kind of strong contamination in field 104, the wings of the distribution could be as well altered. Second, we used all the events instead of the red clump giants only. In fact, there is no reason to suspect that the contamination and the blending are somewhat related. The Kolmogorov-Smirnov run on the 27 events in field 104 and the 488 unique events not in field 104 resulted in a 0.3 % probability of the data being picked from the same underlying distribution (Figure 6.2). We conclude that indeed the anomaly is meaningful. A proper statistical analysis should be conducted on efficiency weighted data. However, as argued by Popowski et al. ([195]), the main difference for sampling efficiency should be an underestimate of the number of short duration events due to scarcely sampled fields, and therefore the use of non efficiency-weighted data is likely to give a lower limit on the significance; thus our conclusion is still valid.

Our conclusion on anomaly significance should not be altered by the EROS result. As Hamadache et al. ([96]) wrote, they simply did not examine the anomalous red clump giants data; furthermore, as we said, there is no reason

to restrict the analysis only to red clump giants. Finally, the time intervals of MACHO and EROS do not coincide; transient astrophysical phenomena are often more the rule than the exception, and therefore it seems hazardous to conclude that there was no anomaly in MACHO data on the basis that in the three following year no anomaly appeared.

6.1.2 Possible causes of the anomaly

The statistical test of the previous subsection calls for a difference in the distribution of events duration, and not specifically for a difference in the mean duration. Furthermore, it does not give any information on a possible excess in number of events (that, as we already stressed, is apparent when only red clump giant events are considered). However, looking at event durations in field 104, we will consider as a working hypothesis that some kind of contamination in field 104 caused an excess of events skewed to long durations. Let us concentrate first on event duration, putting aside the excess in number. We recall eq. 5.76. Relative distances between observer, lens and source, transverse velocity of the lens in respect to the observer-source line of sight and lens mass are all entangled in the expression for the characteristic time. However, it is possible to make some consideration able at least to individuate which parameters are likely to be anomalous. A lot of events in field 104 are red clump giant events. Since red clump giants absolute magnitude intrinsic spread is very small (see Figure 6.3), it is possible to assess their distance; therefore, it is difficult to fiddle with source distance for red clump giant events. Therefore, source distance alone cannot be responsible for the anomaly of field 104. Consider then lens distance. Since we do not know the distribution of lens distances for the overall events, we cannot assess how much strong can be the impact of a change in lens distance. However, we note that if we pose sources at $\sim$ 8 kpc, we have the maximum Einstein ring radius for lenses at $\sim$ 4kpc, and that the effect of change in the lens distances distribution is larger if the original distribution is mostly composed by nearby and/or very faraway lenses, i.e. disk lenses and/or bulge lenses. At first sight, while a lens population extremely skewed toward disk or toward bulge seems not convincing, a combination of nearby disk and faraway bulge lens could be plausible. However, it is not clear if difference in the distribution of velocities would produce a bimodal events duration distribution, that is not observed. Next parameters we consider is the transverse velocity of lenses. It seems difficult to invoke an overall velocity dispersion reduction in direction of field 104. A much more likely hypothesis could be the presence of some bound substructure imposing its own peculiar velocity over the Galactic velocity fields. Note that there is no need of a slow substructure, it is possible to have a small angle between the substructure velocity and the line of sight. Last but not least, the presence of an excess of dark, massive objects (compact remnants) would produce easily an increase in long duration events.

Let us consider now the excess in number of events. Since in eq. 5.79 the

Einstein ring appears at numerator, lens mass and distance can increase in the same way the number of events. Since the transverse velocity appears as $v_t f_t(v_t)$, it is not immediate to assess that a velocity distribution skewed toward lower values can increase the number of events.

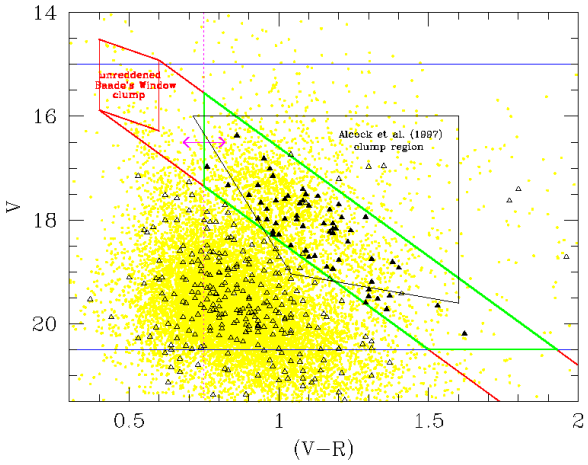

Figure 6.3 Color-magnitude diagram of MACHO objects (yellow). The unreddened red clump giants locus is shown in the top left of the diagram. Filled triangles are red clump giant events, empty triangles are other events (from Popowski et al. [195].)

6.1.3 Objects in field 104

Figure 6.4 shows the field 104. Since its proximity (l= 3.01, b=-3.11) to the Galactic center, the richness of the field is not surprising. The mean extinction over the field is smaller than in the surrounding, so that sometimes this zone is dubbed "the small Baade's window". Two known substructures are in the field of view, the open cluster NGC 6520 and the globular cluster NGC 6540.

NGC 6520

NGC 6520 is an open cluster, with a distance estimate of ~ 1.6 kpc, a quite high proper motion (3.54 ± 0.81 mas/yr in RA $\times$ *cos* (DEC), -1.74 ± 1.03 mas/yr in declination; Kharchenko et al. [121]) and an age estimate ranging from 10^7 to 10^9 yrs (Carraro et al.[41]; Loktin, Matkin & Gerasimenko [132]; Ahumada & Lapasset [6]; Dias et al. [59]). NGC 6520 is known to be associated with at least two H_α sources. The surroundings of NGC 6520 are quite complex. In Figure 6.4 it is clearly visible the dark nebula Barnard 86 at about $5'$ from NGC 6520. The nebula is dusty, and it could be an active star forming region or a remnant of a past star formation episode. A bright radio source with a complex morphology seems to be centered at the edge of the dark nebula, and covers also NGC 6520 area. As an open cluster, it seems unlikely that NGC 6520 can be the

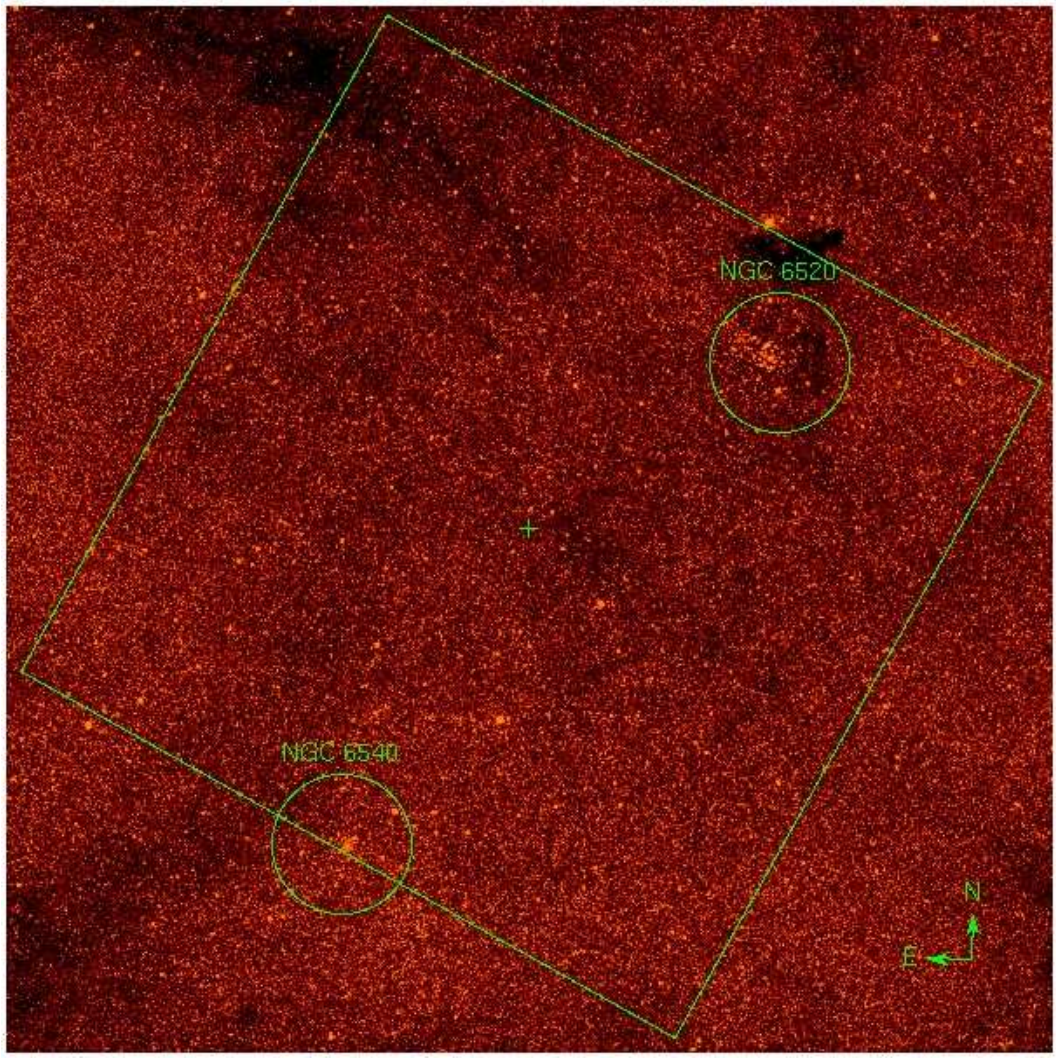

Figure 6.4 Field 104 (green square) superimposed to the corresponding DSS2 red image. The square side is 43 ′. The locations of NGC 6520 and NGC 6540 are also shown.)

reason for the anomaly of field 104. The high proper motion seems to exclude a strong reduction of transverse velocity, the distance is quite far away from the maximization value of 4 kpc (1.9 ± 0.1 Kpc, according to Carraro et al. [41]). The open cluster could be associated with a top heavy mass function; but the proper motion point in the same direction of the field center (that is, if it seeded is path with compact remnants, most of the path is outside field 104; obviously if the compact remnants are neutron stars, kick velocities can easily overwhelm this objection). Furthermore, the strongest objection is that the amount of mass in an open cluster is limited; Carraro et al. ([41]) estimated a mass of 364 ± 54

$M_\odot$) for NGC 6520, a value not sufficient to change sensibly the optical depth, for example, and it seems very unlikely that it can modify in a visible way the events duration distribution. More promising seem the dark structure nearby, Barnard 86. It is not clear if there is a physical link between NGC 6520 and this dark nebula; however the proper motion could suggest that the nebula is the birthplace of the cluster. Star formation could easily be associated with an overproduction of young, optically dark, compact objects. The complex radio morphology could indicate a supernova remnant, or be due to a superposition of different sources. In the hypothesis of an association with NGC 6520, Carraro et al. ([41]) estimated the mass of Barnard 86 to be 600 $M_\odot$ from CO observations, and 3000 $M_\odot$ from the virial theorem (they conclude that the cloud is likely not to be virialized).

NGC 6540

NGC 6540 has been identified as a globular cluster by Bica et al. ([17], while before it was considered an open cluster. It has a peculiar morphology, with a very dense nucleus with FWHM 10", elongated in the E-W direction by two clumps of bright giant stars. The outer parts of the cluster are instead elongated in the N-S direction. The distance to NGC 6540 is 3 kpc (Barbuy, Bica & Ortolani [12]. Bica et al. ([17]) argued that the very dense core of the cluster suggests a post-core collapse cluster, and that the apparently twisted structure are likely to be intrinsic to the cluster (not caused by differential extinction). They also suggest a possible merger between two globular clusters. Globular clusters have been extensively treated from a microlensing perspective, both as sources and lens (e.g. Jetzer, Strässle & Wandeler [110]). A globular cluster can significatively contribute to the optical depth (Jetzer, Strässle & Wandeler [110]), especially if its distance is near to half the distance between the Earth and the bulge (where source are located). The same distance value can in principle produce a sensitive increase in long duration events (it can be safely assumed that all cluster lenses are at the same distance). For NGC 6540, the distance is quite near to the maximizing value (the lens distance dependent factor in eq. 5.76 is 92% of the maximum). Furthermore, the presence of NGC6540 could also be responsible of a change in the transverse velocity field. It is remarkable the fact that Jetzer et al. ([110]) already noted, at the time, an excess of events near to NGC 6540. However, there are two problems in identifying NGC 6540 as the cause of field 104 anomaly. The first is that NGC 6540 is located at the border of field 104 (see Figure 6.4 and Figure 6.1), and it should therefore produce an anomaly as well in field 105, that is not apparent. The second is that long duration events in field 104 seem not to cluster near to the location of NGC 6540, where instead there are many short duration events (see Figure 6.5). Long duration events do not show evidence of clustering, but seems distributed in a line across the field.

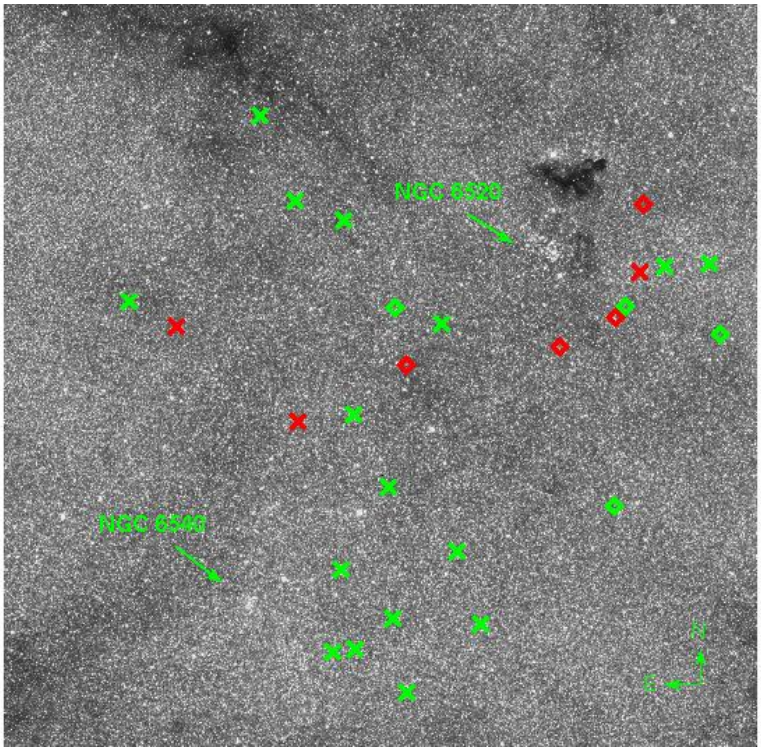

Figure 6.5 Microlensing events (crosses, diamonds) in field 104 superimposed to the corresponding DSS2 red image. Diamonds are clump giant events, crosses other events. Events with $T_E > 50$ days are shown in red color.

6.1.4 Conclusion

From our analysis the anomaly of the distribution of events duration in field 104 is significant. However, the cause of the anomaly still has to be clarified. The field itself is very rich, containing an open cluster, a dark nebula, a globular cluster. Furthermore, other, still unidentified structures could be present in the field. It seems unlikely that the open cluster NGC 6520 can significantly alter the distribution of events. Other possibilities definitely need a more thorough exploration. We note that, if the anomaly has a transient behavior, as one could infer from our statistical analysis and its absence in EROS data, a transient cause has to be searched for. A change in the optical depth in a timescale of years would seem to indicate a local cause, may be tied to some high velocity lens. An alternative explanation of the negative EROS result could be that of an anomaly clustered in a small solid angle, so to escape detection in EROS fields. However, as already showed in the above paragraph, long events do not appear clustered in some part of field 104. A thorough, comparative study of the events of MACHO, OGLE and EROS could cast some light on the anomaly.

6.2 Bulge mass function and compact remnants

As we already stressed in Section 5.3.3, the intrinsic degeneracy in microlensing observables can be broken in a statistical way with the mass moments method. Therefore, starting from an observational sample and a density-velocity Galactic model, the lens mass function can be inferred. Grenacher et al. [84] applied the mass moments method to the 41 bulge events from the first year of MACHO observations (Alcock et al. [8]), finding a mass function for bulge and disk lenses in the shape of a power law with index $\alpha \sim 2$ in both cases, and minimum mass respectively of 0.01 $M_{\odot}$ and of 0.02 $M_{\odot}$. The availability of sample of events more than ten times larger opens new interesting perspectives. Two approaches are possible. The first is to cleanse the sample of events. In particular, the 62 MACHO and the120 EROS red clump giant events are respectively 1.5 and 3 times larger than the sample of Grenacher et al. [84]. The use of a clean sample of clump giant events only would allow to get rid of blending biases. Moreover, since the location of events in which the source is a red clump giant is known (e.g. Figure 6.3), the noise introduced by events with a disk source or with a source behind the bulge would be eliminated. In such a way much more reliable parameters for the mass function would be picked up. The second approach involves instead the use of the full event MACHO sample, with the aim to search for large residuals in the mass function. In fact, using stars as lenses, fitted mass functions are generally truncated at $M_{max} = 1M_{\odot}$ to obtain a dark lens. However, a certain percent of events should be due instead to compact remnant lenses: black holes, neutron stars, white dwarfs. The lens mass function is therefore well described by a four component function: a power law with some M_{min} and $M_{max} = 1M_{\odot}$ representing the stellar population, a sharp gaussian function peaked at $\sim 0.5M_{\odot}$ representing white dwarfs, another sharp gaussian function peaked at $\sim 1.4M_{\odot}$ to take in account neutron stars and finally a fourth high mass component of which we know very little, the signature of black holes (Gould [82]; see Figure 6.6). Microlensing observables degeneracies smear out the structure of such a mass function, i.e. at fixed mass, the possible spread of Einstein times is so large to lose memories of the mass value (Gould [82]). However, with sufficient statistics, deviations from the stellar power law mass function should be individuated. One building block of such an analysis is a density-velocity Galactic model. We are using the COBE-DIRBE model (Bissantz et al. [23]; Bissantz & Gerhard [22]). The use of such a state of art numerical model already tested with previous MACHO optical depth estimate would allow a self-consistent treatment of the problem, minimizing uncertainties due to the use of poorly constrained parametric models. This ambitious project is still in the phase of numerical development.

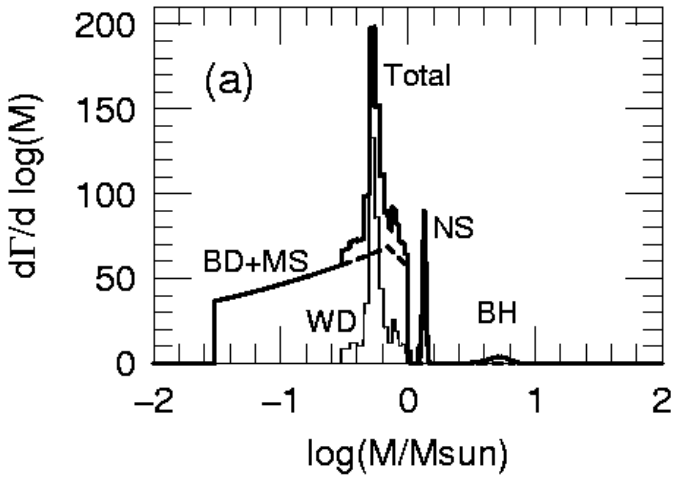

Figure 6.6 Distribution of microlensing events per unit log mass, as a function of log mass and classified by type of object (taken from Gould [82]).

Chapter 7

Q0045-3337: a candidate for strong lensing by a spiral galaxy[1]

7.1 Introduction

The number of known strong lensed quasars boosted in the last years up to the current value of ~ 90 (Kochanek, Schneider & Wambsganss [125]; CASTLES web site, http://cfa-www.harvard.edu/castles/). The reason of this increase is mainly the availability of new observational facilities, in particular the Hubble Space Telescope, of dedicated surveys (CLASS, Myers et al. [168], Browne et al. [31]) and of large public observational databases, like the FIRST (White et al.[242]) and in particular the Sloan Digital Sky Survey (York et al. [249], Adelman-McCarthy et al. [1]).

The lion's share in lenses population is made by early-type galaxies. In fact, up to now, only 5 systems are confidently identified with spiral galaxies: first of all, the Einstein cross, Q2237+0305 (Huchra et al. [105]), then B1600+434 (Jackson et al. [109]), PMNJ2004-1349 (Winn, Hall, & Schechter [244]), B0218+357 (Patnaik et al. [180]) and PKS 1830-211 (Pramesh Rao & Subrahmanyan [196]). Each of these systems has its own peculiarities (inclination of the lens galaxy, richness of the lens environment, etc.), up to the point of making it unique, and can therefore bring its own precious contribution on knowledge of spiral galaxies mass distribution.

The discovery of a late-type galaxy at $\sim 1.2''$ from Q0045-337 (Falomo et al. [69]) pointed up the existence of another spiral lens candidate. In fact, while there is no evident image splitting, under reasonable hypotheses on galaxy redshift and mass-to-light ratio, Falomo et al. inferred a galaxy Einstein radius

[1]This chapter has been submitted to A&A as Chieregato, M., Miranda, M. & Jetzer, P.: "Q0045-3337: a candidate for strong lensing by a spiral galaxy"

of size comparable to the distance between the galaxy and the QSO (considering the galaxy as a point mass).

Existing, limited data hampers detailed modeling of Q0045-3337. We investigated some simple configurations compatible with the known properties of the system, in the hope to restrict the range of possibilities and to focus future observations.

7.2 Observational parameters

Q0045-3337 (R.A. = 00 47 41.85, DEC = -33 20 55.1) is a radio quiet quasar with a reported redshift of z=2.14 (Iovino, Clowes & Shaver [106]) and a V magnitude of 18.75 (Véron-Cetty & Véron [237]). The NAOS-CONICA VLT K band image of Q0045-3337 (Falomo et al. [69]) revealed a galaxy at 1.14″ SE from the quasar (respectively A and B in Figure 7.1). The K magnitude of the QSO is 17.80, while the one of the galaxy is 16.97 (see the following paragraph for a discussion of the galaxy surface photometry). The only other object seen in the field apart from the guide star is source C, with a K magnitude of 20.90, 3.5 ″ N of A.

The quasar itself appears noticeably, elliptical (see Section 7.5.2 for a discussion on the ellipticity). There is no redshift measurement for the galaxy. However, Falomo et al. (Falomo et al. [69]) estimated a redshift range of 0.4-1 from an educated guess on the galaxy absolute K magnitude (-24 to -26) and effective radius (2 to 3 kpc).

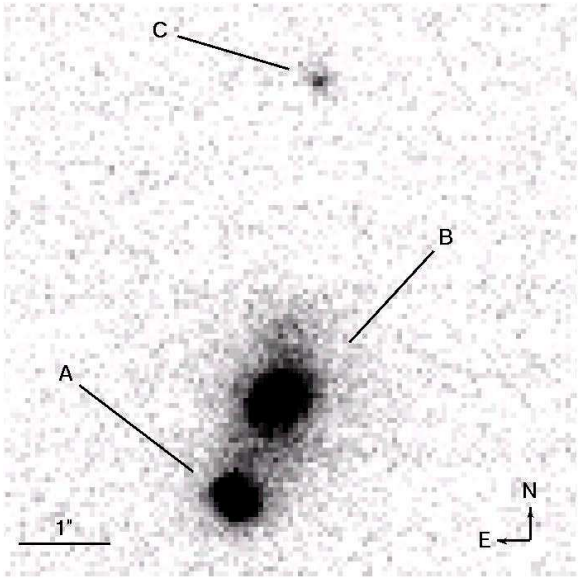

Figure 7.1 **Q0045-3337 and its foreground galaxy.** A close-up of the NAOS-CONICA image of Q0045-3337 and its foreground galaxy.

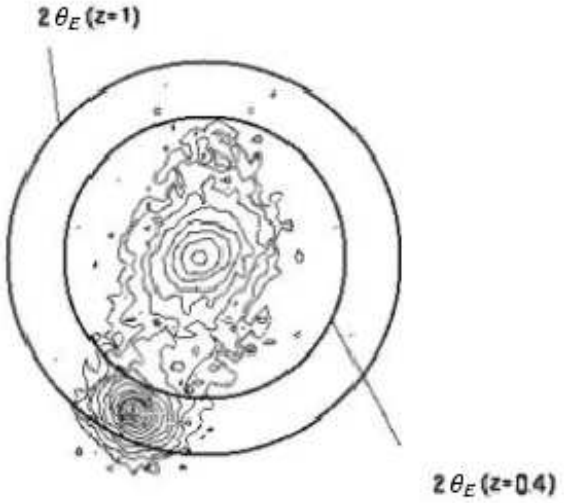

Figure 7.2 **Contour map and Einstein radii.** Contour map from the NAOS-CONICA image, with superimposed the doubled Einstein radii for SIS with dispersion velocities calibrated with the Tully-Fisher law (see text for details).

7.3 Surface photometry and galaxy image subtraction

We performed two-dimensional surface photometry on the NAOS CONICA image of the galaxy with the aid of the software GALFIT (version 2.0.3c; Peng et al. [183]). Two dimensional photometry for adaptive optics is complicated by the peculiarities of Point Spread Function (PSF). In fact, each extended component of the GALFIT models is usually convolved with the PSF of the image; moreover, the PSF is used to fit point-like sources. It is a well known feature of adaptive optics that the PSF can assume complex shapes, in particular it usually varies with angular distance from the guide star, and it can be elongated in direction of the guide star. Usually, analytical modelling of the PSF from ancillary data is not possible, though the situation is likely to change in the future (see Clénet et al. [46] for the NaCo case). What should be done is therefore to infer a PSF template from observations of bright stars at similar angular distance from the guide star, observations performed just before and after the one to be analyzed. Unfortunately, this part of the program was not done for the NaCo observation of Q0045-3337 (see Falomo et al. [69]).

The QSO itself, besides being "contaminated" from light from the galaxy, appears visibly elliptical, and it is not clear if its ellipticity is an effect of PSF elongation or it is due to a different cause (Figure 7.2; Section 7.5.2). The only other source, object C, is too faint and irregular, and its point-like or extended

nature is not well determined.

We therefore fitted with GALFIT simultaneously the galaxy and the QSO without convolving a PSF, and using GALFIT models also for the QSO light distribution.

A two component model it is required to account for the galaxy light distribution (plus other two components to fit the QSO); in particular, we obtained the best results with two Sérsic models of integrated magnitude 17.19 and 18.80, both with Sérsic index 0.63 (1 is the exponential disk, 0.5 the gaussian) and R_e respectively $13.5''$ and $3.4''$. The inner model is tilted of 50 degrees in respect to the outer.

After galaxy model subtraction, the main residual feature is an irregularly shaped object at $0.85''$ N of the galaxy centroid ($\sim 2\,''$ from the QSO; see Figure 7.3). The residual is very elongated, but due to its faintness (K $\sim$ 22.6) it is not possible to firmly establish its point-like or extended nature.

We checked the robustness of our results using PSF templates obtained from the QSO, keeping in mind the already mentioned caveat. In particular, we used both the background subtracted QSO cropped image and the best fit QSO analytical profile (this last case should be less contaminated from galaxy light; however, it has the additional difficulty that the QSO fit is not perfect, leaving a noticeable residual).

Even using these PSF templates, the need of two components to account for the galaxy light distribution stands still. In particular, the large difference in orientation between the outer and inner ellipsoids is unchanged.

The residual component is also unchanged. The only appreciable difference is a slight change in the two Sérsic indexes; the inner one becomes steeper (0.71), the outer one shallower (0.57).

7.4 Single image or multiple images

The zero-th order question that Q0045-3337 and its foreground galaxy pose to us is whether the lensing effect is strong, i.e. whether there are other, still unseen, source images, and eventually where they should be looked for.

In fact, if truly there is no image splitting, only a reduced number of information can be extracted on the galaxy (e.g. Narayan & Schneider [171], Le Brun et al. [130]), though still useful, in our case, to probe the behaviour of the strong lensing cross section for a spiral galaxy.

The simplest galaxy lens model with some physical meaning is the singular isothermal sphere (SIS; see 5.2.5). Within the SIS framework, all lens and source quantities are tied by simple analitycal relations. In particular, necessary and sufficient condition for multiple images formation is that the Einstein radius θ_E has to be greater than half of θ_I, the distance of the brightest image from the lens ($\theta_E \geq 1/2\theta_I$; Narayan & Schneider [171]). The Einstein radius is defined as $\theta_E = 4\pi \times (\sigma_v/c)^2 \times D_{ds}/D_s$, where σ_v is the velocity dispersion of the SIS,

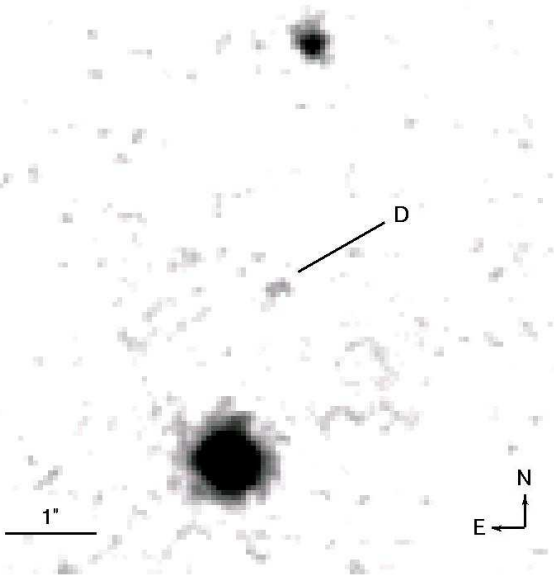

Figure 7.3 **Q0045-3337 galaxy subtracted.** The NAOS-CONICA image of Q0045-3337 after galaxy model subtraction, top-hat smoothing and contrast enhancing, in logarithmic scale. The residual feature (D) is well visible midway between object C and QSO.

$D_{\rm ds}$ is the angular diameter distances between the source and the lens and $D_{\rm s}$ is the angular diameter distance between the source and the observer. The $0.57''$ discriminating threshold corresponds to a SIS velocity dispersion of 167 km s $^{-1}$ for a lens galaxy redshift of 0.4, and of 228 km s $^{-1}$ for a redshift of 1. The mass enclosed in θ_I is respectively 7.8 $\times 10^{10}$ $M_\odot$ inside 6.1 kpc and 2.2 $\times 10^{11}$ $M_\odot$ inside 9.1 kpc. Since the companion galaxy of Q0045-3337 is a spiral, the Tully-Fisher relationship (Pierini & Tuffs [190]) can be used to infer a circular velocity range of 218-351 km s $^{-1}$ from the (guessed) absolute magnitude. Under the assumption that the $\sigma_{\rm v}$ parameter of the SIS mass distribution is $1/\sqrt{2}$ of the maximum circular velocity, the obtained $\sigma_{\rm v}$ are 154 km s $^{-1}$ and 248 km s $^{-1}$, and the inferred Einstein radius ranges from $0.49''$ to $0.68''$ (Figure 7.2). Such values do not allow to confirm or reject image splitting, keeping in mind the intrinsic dispersion in the Tully-Fisher relationship, the possibility of evolutionary effects and in particular the extreme simplification used in assuming a SIS model.

If the lensing is weak, its effects are magnification of point sources and tangential stretching of extended sources. We will treat later on the stretching effect. In the SIS framework the maximum magnification without image splitting is 2. Much higher values can be reached, at least in principle, with different mass models (Keeton & Kochanek [120]).

7.5 Multiple images

In this section we investigate the hypothesis that additional, yet unseen (or not recognized) images are produced. We slightly complicate the galaxy model abandoning the spherical symmetry. Singular and non-singular Isothermal Ellipsoidal Mass Distribution (SIEMD, PIEMD) and ellipsoidal potential have been studied in some details in the last $\sim$ 15 years (e.g. Kassiola & Kovner [117], Schramm [213], Kormann, Schneider & Bartelmann [128]; see 5.2.7). The structure of the caustic curves of non-spherical models is changed qualitatively, with the appearance of the astroid-shaped tangential caustic. The odd image theorem needs no more infinite demagnification of the central image, and the presence of two caustics allows the production of up to five images. These models should be more realistic than the SIS oversimplification; however, they still miss "on the field" tests for spiral lenses, due to the already mentioned paucity of known cases.

Our goal in this section is not to make a detailed model of the galaxy mass distribution, but only to check if strong, image splitting, lensing configurations can be compatible with the constraint that no other image is seen in the NAOS-Conica data, and if that is the case to track the way for future observations. To reproduce the qualitative behaviour of different cases, we widely used the Java applet SimpLens (Saha & Williams [209]). Subsequently, we ran some simple simulation with the Gravlens software (Keeton [118]) to verify if the proposed configurations require a non-realistic choice of parameters. We focused mainly on SIEMD, but we also tried finite core models, models with shear, non-isothermal models (the so-called α-models) and exponential models (that represent a constant mass-to-light disk).

7.5.1 Three images

The easiest, and therefore favoured by the Ockham's razor, image splitting configuration is a three image configuration (like the one shown in Figure 7.4, top panels). In this case, the source has to be positioned between the external, tangential caustic and the internal cusp. The minimum, demagnified image is hidden by the lens galaxy bulge. Let us suppose that the residual image found in Section 7.3is unrelated. If this is the case, the absence of other point sources requires a large magnification ratio between the maximum and the saddle point images. The easiest way to enhance the magnification ratio is to suppose the mass of the galaxy almost aligned with the straight line connecting the galaxy center and the quasar. In such a way, putting the source arbitrarily close to the astroid cusp, you can obtain an arbitrarily high magnification ratio, until the breakdown of geometrical optics validity.

The required misalignment between mass and light in such a case could be mimicked by the presence of shear, or be due to the aftermath of a major merger; this last hypothesis could be supported by the isophotal twisting and core-disk

misalignment of the galaxy. If we strictly adhere to a mass-light alignment condition, using plausible parameters, the magnification ratio between the maximum and the saddle point images is of the order of 20 (as obtained by a Gravlens simulation of a SIE with the galaxy image ellipticity, b/a=0.67, eps=0.33), and thus is not clear if it is compatible with the absence of any visible trace of the saddle point image. However, there are other ways to boost the magnification ratio. In particular, the saddle point image could be hidden by a strong obscuration if there is enough dust in the galaxy (even if no evidence of dust lane is found from the surface photometry), or the maximum image could be enhanced by substructure lensing, microlensing and by the QSO variability itself.

Let us consider instead the hypothesis that the residual image is the saddle point image.

The elongated shape of the residual seems to contradict this speculation; however, since we are dealing with an object near to the plate limit, obtained after subtraction of an extended component and possibly absorbed, and after all we have no firmly established PSF shape, the morphological evidence can not be decisive. In the same way the position and the faintness (magnification ratio $\sim$ 30) of the residual are less than conclusive clues against the saddle point image interpretation. If indeed the residual feature marks the saddle point image, a mass-light misalignment is compulsory to reproduce the positions of images; the absorption is likely less effective in boosting the magnification ratio, since the third image is not so close to the galaxy core.

We envisaged also the possibility that the object C is a third image. It seems that somehow this interpretation creates more problems than it solves. In fact the system size of $\sim 4.7''$ is excessive for a single galaxy lens. Furthermore, fitting object C in a configuration like that of Figure 7.4, top panels, would require a reversed magnification ratio (A would be the saddle point image), very difficult to produce. Finally, it is not clear if object C is truly point-like, since it seems to have a slightly smeared light profile, and the uncertainty on the PSF prevents us from a definite conclusion in this sense.

In the three image configuration, the elongation of the quasar has to be of instrumental origin, as it is explained in the following subsection.

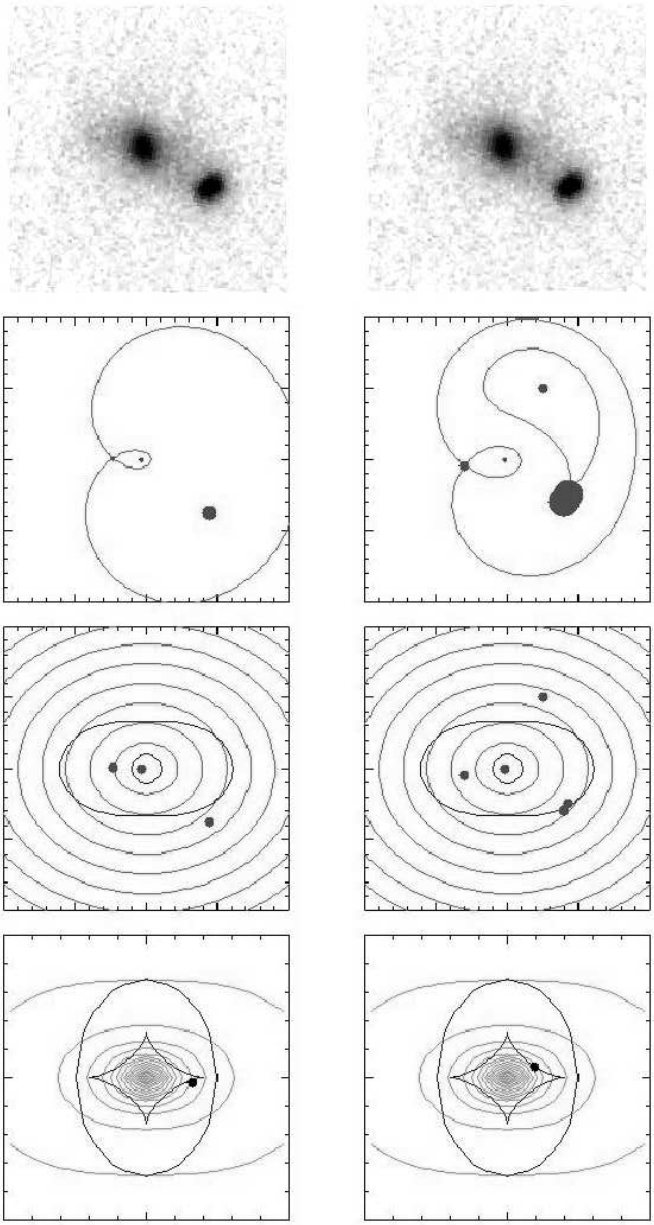

Figure 7.4 **Lensing scenarios for Q0045-3337.** A qualitative representation of lensing scenarios for Q0045-3337. From up to down: three images case with the third image hidden; five images case with two images merged and two images hidden. From left to right: SimpLens source position (point), isodensity contours (light curves) and caustics (grey curves); SimpLens images positions (points) and critical curves (grey curves); SimpLens image positions (points) with area proportional to the magnification and virtual light-travel time contours (grey curves); Q0045-337 and foreground galaxy, properly rotated and scaled to be directly comparable with the SimpLens images. The SimpLens model used is a non-singular isothermal ellipsoidal potential, with a core radius of 0.01 and an ellipticity of 0.37.

7.5.2 Quasar ellipticity

The first, most obvious, explanation for the elllipticity of Q0045-3337 in the NACO image is instrumental, i.e. due to adaptive optics PSF deformation (see 7.3. As noted by Falomo et al. ([69]), Q0045-3337 is elongated in a direction almost aligned to the vector radius of the guide star, but not equal (with a difference of $\sim 10-15$ degrees). The galaxy itself, and its brightest core in particular, do not appear to suffer of similar deformation, but since their intrinsic brightness distribution is not radially symmetric, no definite conclusion can be drawn. If the ellipticity is real and not an instrumental artifact, a gravitational lensing effect should be invoked. In principle, image deformation can be produced by lensing of resolved sources, since in that case lensing conserves surface brightness, stretching the sources in the tangential directions and originating the well known arclets. However, it seems unlikely that this can be the case for Q0045-3337. In fact, while we stress one last time that the PSF in an adaptive optical image can be intrinsically complex, a magnified point source superimposed to a tangentially stretched extended source (like a QSO with its host galaxy) should result in a sharp bright core with a faint extended wing, i.e. the image should appear more elliptical at low brightness, and less at the brightness peak, where it should be dominated by the point source. This is exactly the opposite of what we see for Q0045-3337 (see the contour map of Figure 7.2). The only way in which gravitational lensing can produce such a behaviour is by means of merging two or more images, unresolved by the NACO observation (note that the merging of two equal circular PSF produce an elliptical PSF with stronger ellipticity at the peak and weaker at the periphery). In the following subsection we will explore in some more detail this possibility.

7.5.3 Five images

If we require a lensing explanation for the quasar ellipticity, we need to produce five images. This can be obtained in any model with two at least partially nested caustic curves. For our purpose, we want the merging of two (or even three images) near to the tangential critical curve, in such a way that the NACO observation is not sufficient to resolve the contribution of the different images (as in Figure 7.4, bottom panels). Images so close to a critical curve are strongly magnified. This can provide a explanation to the absence of the other images in the NACO observation based solely on strong lensing.

In particular, it is crucial to explain the non detection of the fifth image, that is foreseen quite far away from the galaxy and therefore can not be obscured. We estimate a conservative plate limit of 22.8 for such an undisturbed source using the barely visible 22.6 residual object, i.e. a magnification ratio between the merged images and the fifth image of ~ 40. Note that the centroids of the merged images have to be very close each other; to give an order of magnitude example, the plate scale of the NACO image is only $0.054''$, and the distance

between the two components used to fit the QSO with GALFIT in Section 7.3 is 0.052 ″.

We verified the viability of the five images scenario numerically with Gravlens simulations.

Unfortunately, Gravlens is not made to work with such extreme parameters; nevertheless we were able to force the program to reproduce similar configurations. In particular, we obtained a magnification ratio of ~ 41 between two merged images with a separation of 0.03 " and the fith, external image, using a SIE with ellipticity 0.11. Although such an high ellipticity can hardly represent the observational parameters we have, the simulation proves that in principle this scenario can produce very high magnification ratios. This can be further improved using different models of mass distribution, In particular, an exponential disk with k_0, q=0.67 and scale length R_d=0.5 with the two merged images separated by 0.023″ correspond to a magnification ratio of ~ 56.

7.6 Discussion

We performed two dimensional photometry on the galaxy near to Q0045-3337. We confirmed its spiral nature and found evidence for two components with different orientations. We found a residual image after model subtraction, that is most likely due to a spiral arm, even if more interesting possibilities can not be excluded. We then verified that no unusual parameters for the galaxy are required to produce or not image splitting. We also found some very simple strong lensing configuration capable to not contradict existing data, either assuming a) that no other image is seen and Q0045-3337 observed elongation is instrumental, b) that the residual image is truly another lensed image of Q0045-3337, and still the elongation is instrumental, c) that Q0045-3337 elongation is due to the merging of two or more images, and no other image is seen. These speculations can be easily verified observationally. In particular, another optically adaptive image with more information on the PSF behaviour would confirm or rule out the ellipticity of Q0045-3337 and en passant it would also verify if object C is point-like. A measurement of the galaxy redshift, while probably not conclusive, would help to constrain how likely is the production of multiple images. Deeper pointings could reveal additional images or put tighter constraints on required magnification ratios. If model c) turns out to be the most probable, an HST image could resolve the merged images. At present, strong lensing effects on Q0045-3337 can only be labelled as possible. Spiral strong lenses are rare objects. The current view assumes that the cross-section for image splitting it is not generally increased by the presence of a thin massive disk, at least once mediated on the inclination and once properly taken in account the current observational capabilities; furthermore, absorption biases strongly against the detection (Bartelmann & Loeb [11]; Keeton & Kochanek [119]; Perna, Loeb & Bartelmann [185]). In such a context, the galaxy close to Q0045-3337 can offer a

valuable help to our knowledge of spiral galaxy mass distributions and to lensing statistics too. Even in the case without image splitting, as it is likely both for the sample of Narayan & Schneider ([171]) and for the Lyman absorbers of Le Brun et al. ([130]), interesting upper limits can be casted on the galaxy mass inside the Einstein radius (once the redshift is known). Furthermore, the lensing effect of stretching of resolved sources could make Q0045-337 again a valuable target for deeper host galaxy studies (as it was originally selected by Falomo et al.([69]). As a final comment, it is interesting to note that this case can be a perfect example of edges and drawbacks of adaptive optics applied to strong lensing.

In the last years, HST has been the principal instrument in strong lensing studies, and it is interesting to evaluate if it can be -at least partially- surrogated by adaptive optics earth telescopes, especially in the case of a gap between the end of HST operations and the start of the James Webb Space Telescope operations. As Q0045-3337 and its neighbour galaxy tell us, a necessary condition to be fulfilled in this case is a correct PSF evaluation observational procedure (like it was at first proposed for Q0045-3337); otherwise, the unresolved uncertainty between real and instrumental deformations hampers the exploit of the optimal resolution for lensing studying purpose.

Appendix A

BFS $f_X/f_{offband}$ calculation and comparison with RASS-Hamburg optical identification program

A.1 Determination of the lower limits of the $f_X/f_{offband}$

In order to evaluate the f_X/f_{opt} lower limit from the non-detection of BFS in the GSC2, it is mandatory to calibrate the absolute photometry of the GSC2 BJ and F bands, i.e. to convert in fluxes the magnitude limits. This has been done with the aid of the Asiago Database of Photometric Systems (ADPS: Moro & Munari [159]; Fiorucci & Munari [70]; http://ulisse.pd.astro.it/Astro/ADPS/). According to the conventions there defined, the Vega (0 magnitude) BJ-POSS II band flux is given by:

$$f_{\lambda_{eff}\,Vega} \times W_{eff} \tag{A.1}$$

where, for the BJ band, λ_{eff} =4731 Å, W_{eff}= 1333 Å. The $f_{4731,Vega}$ value of 5.46×10^{-9}erg s^{-1}cm^{-2}/Åhas been obtained from Table II of Hayes ([102]), inferring $f_{BJ,Vega} = 7.274 \times 10^{-6}$erg s^{-1}cm^{-2}. Once calculated the Vega BJ flux, a straightforward applications of the Pogson formula ($m_2 - m_1 = 2.5 \log f_1/f_2$) gives the flux for the GSC2 limiting BJ magnitudes. The values found are respectively $f_{BJ} = 7.27 \times 10^{-15}$erg s^{-1}cm^{-2} for a 22.5 value and $f_{BJ} = 4.59 \times 10^{-15}$erg s^{-1}cm^{-2} for a 23 value. For the red F band, we made a similar calculation. A further complication comes from the fact that POSS II and SERC/AAO have slightly different filters, though the same emulsion. Supposing negligible the difference, we used ADPS POSS II parameters. In this case λ_{eff} =6555 Å, and W_{eff}= 767 Å. Using again Hayes ([102]), $f_{6555,Vega} = 1.73 \times 10^{-9}$erg s^{-1}cm^{-2} /Å, i.e. $f_{F,Vega} = 1.33 \times 10^{-6}$erg s^{-1} cm^{-2}.

The fluxes corresponding to GSC2 red limiting magnitudes are respectively

$f_{redF} = 6.35 \times 10^{-15}$erg s^{-1}cm^{-2} for a 20.8 value and $f_{redF} = 2.10 \times 10^{-15}$erg s^{-1}cm^{-2} for a 22 value. Note that this means that while the GSC2 magnitude limit is deeper in the blue band, the corresponding flux limit is deeper in the red band.

For the 2MASS near infrared bands, the absolute calibration has been taken from http://www.ipac.caltech.edu/2mass/, so the zero point magnitude flux is
J: $f_{0,J} = 5.079 \times 10^{-7}$erg s^{-1} cm^{-2},
H: $f_{0,H} = 2.791 \times 10^{-7}$erg s^{-1} cm^{-2},
K_s :$f_{0,K_s} = 1.124 \times 10^{-7}$erg s^{-1} cm^{-2},
and again from the Pogson formula the limiting fluxes are respectively $f_J = 2.43 \times 10^{-13}$erg s^{-1}cm^{-2} for the 15.8 J value, $f_H = 2.55 \times 10^{-13}$erg s^{-1}cm^{-2} for the 15.1 H value and $f_{K_s} = 2.141 \times 10^{-13}$erg s^{-1}cm^{-2} for the 14.3 K_s value.

A.2 Comparison with RASS-Hamburg optical identification program

The conversion for the X-ray and optical fluxes was done for each class of sources as follows:

$$\frac{f_{X,HRI}}{f_{BJ}} = \frac{f_{X,Hamburg-RASS}}{f_B} \times \frac{f_{X,HRI}}{f_{X,Hamburg-RASS}} \times \frac{f_B}{f_{BJ}} \quad (A.2)$$

Here $f_{X,HRI}$ means HRI flux in the 0.5-2 keV band using a power law spectral shape with index 2 and column density 5 x10^{19} atoms cm^{-2}, while $f_{X,Hamburg-RASS}$ is PSPC 0.1-2.4 keV flux computed assuming a "typical" spectral shape for each class of sources and galactic column density (Zickgraf et al. [262]). The ratio between the two fluxes has been calculated with XSPEC 11.2.0 using the HRI response matrices, taking only channels 2-9, and assuming that the typical spectral shape is the underlying real spectral shape of the sources. The ratio between the GSC2 BJ and the Johnson B fluxes is calculated with the relationship $BJ = B - 0.28 \times (B - V)$ (Reid et al. [202]). For each class of sources a couple of minimum and maximum typical B-V values are assumed (see Table 1.4). The ratio between the optical fluxes is calculated as:

$$\frac{f_B}{f_{BJ}} = \frac{f_{B,Vega}}{f_{BJ,Vega}} \times 10^{-\frac{m_B - m_{BJ}}{2.5}} = \frac{f_{B,Vega}}{f_{BJ,Vega}} \times 10^{-0.112 \times (B-V)} \quad (A.3)$$

with $\frac{f_{B,Vega}}{f_{BJ,Vega}} = \frac{5.982}{7.274} = 0.822$.

The converted f_X/f_{BJ} values are usually lower; this is mostly due to the narrower X-ray band and, in some cases, to the softer spectral shape. In particular, the maximum upper limit, still reached for Galaxy Clusters, is $f_X/f_{BJ} \sim 17$. In this case, the difference in spectral shape is strong, since clusters are usually hard sources (Zickgraf et al. [262] used a bremsstrahlung spectrum with kT=8 keV). In fact, while galaxy clusters are still the most extreme of source classes,

in most of the works their f_X/f_{opt} is boosted by the counts-to-flux conversion, using counts and magnitudes the limits reached are not so dramatic, if the X-ray band is soft as in our case. As discussed in Zickgraf et al. ([262]), borders between Galaxies and Clusters of Galaxies are somehow uncertain, i.e. some Cluster was probably misidentified as a Galaxy. We believe that this should not change substantially the f_X/f_{opt} values. We note that the AGN class includes BL Lacs, that, on average, have a different f_X/f_{opt} behavior; so the BL Lacs peculiarity is lost in the larger sample of AGNS. Finally, in Zickgraf et al. ([262]), stars are divided in different classes: bright (AB) stars, FG stars, K stars, M stars. Since we are interested only in high f_X/f_{opt} sources, we mixed up all the stars in a single category, taking the lowest lower limit and the highest upper limit.

Appendix B

Persistent and Transient Blank Field Sources [1]

B.1 Introduction

Isolated neutron stars, which have overcome the pulsar phase are elusive sources. In principle they can shine from some residual internal energy (coolers), or because of their interaction with the interstellar medium (e.g. accretors). Their number in the Galaxy should be very high, about one percent of the total number of stars. Their significance as a population is of the utmost interest: they are the end-point of the evolution of a vast class of stars.

It is just because of these considerations that the discovery of dim isolated neutron stars (DINS) by the ROSAT satellite has been a major achievement (see e.g. Treves et al. [226], Haberl [90], Zane et al. [254] Chapter 4).

DINS are one of the main attractions of this meeting, see in particular the presentations by Cropper and Popov. Their properties can be summarized as follows: softness $T \sim 100\,\mathrm{eV}$; closeness $d \sim 100\,\mathrm{pc}$; extremely dim optical counterparts ($V > 25$), periodicities of $5 - 10\,\mathrm{s}$; absorption features below 1 keV. The seven DINS discovered thus far are probably a mixed bag, in the sense that the above properties may not appear all together. For instance the prototype of the class 1856–37, has a perfect black body spectrum in the X-ray band with neither absorption lines nor indications of pulsations. Most likely they are all coolers (Neuhäuser R. & Trümper [172], Popov et al. [191]).

In order to further improve our knowledge of DINS it is mandatory to enlarge their sample. The procedure followed up to now to discover new DINS has been to search the ROSAT images for the so called "Blank Field Sources" (BFS, cagnoni et al. [35]), i.e. X-ray sources without counterparts in other spectral

[1] Here we report Treves, A., Campana, S., Chieregato, M., Moretti, A., Nelson, T. & Orio, M.: "Persistent and Transient Blank Field Sources", 2006, to appear in Ap&SS, in the proceedings of "Isolated Neutron Stars: from the Interior to the Surface", edited by D. Page, R. Turolla and S. Zane, astro-ph/0609194

Table B.1 Blank Field Sources from the HRI Rosat catalogue, adapted from Table 1.2

Source	Flux $10^{-13}\frac{\text{erg}}{\text{cm}^2\text{s}}$	Prob. σ	Cts	f_X/f_{opt}	Opt. σ
$0421-51$	6.5	14.0	742	>141	5.3
$1357+18$	3.5	4.2	112	>47	6.3
$2007-48$	3.0	4.3	55	>65	5.2

bands, and use the properties listed above to argue that the candidate belongs to the class. This line was pursued by a number of authors, we mention in particular the recent paper by Agueros et al. ([5]) where the ROSAT PSPC images are compared with the Sloan Digital Sky Survey.

Here we focus on progresses of our search of BFS in the ROSAT HRI images (Chieregato et al. [44], Chapter 1), concentrating on the possible detection of transient BFS.

B.2 The ROSAT-HRI Blank Field Sources

The ROSAT HRI fields cover $\sim 3\%$ of the sky but the advantage with respect to the PSPC is that the position of the source is much better determined, therefore the limit set by the absence of counterparts can be brought to a deeper level.

The $\sim$ 30000 sources of the ROSAT HRI Brera wavelet catalogue ([179]) have been searched for objects *a*) with extreme f_X/f_{opt}, *b*) not too faint, *c*) with total number of photon above a given threshold. Excluding known sources, three objects have been found which have a statistical significance $> 4\sigma$, and with the closest counterpart at $> 4\sigma$ (see Table B.1). With respect to Chieregato et al. ([44]; see Chapter 1) 0433+15 was excluded since it was recognized as spurious.

The brightest source is 0421–57. It is close to a bright star (see Figure 1.2). It has been detected with the PSPC at essentially the same level revealed by the HRI. The source is soft (0.2 keV) but not as soft as other typical DINS. The two other sources are much weaker, and they have not been detected with HRI or PSPC when observed at a different epochs. We will refer to them as transient BFS. Their light curve have been examined and we can exclude spike-like emission of duration of seconds or minutes.

B.3 New Observations

A program of *X*-ray observation of the three sources with the SWIFT XRT is ongoing (P.I. Moretti). We observed all three BFS: 0421–57(11 ks), 1357+18(9 ks)and 2007–48 (8 ks). The last two sources were not detected, resulting in $0.3-10$ keV 3σ upper limits of 1.8×10^{-3} counts s^{-1} and 2.2×10^{-3} counts

s^{-1}, respectively. Assuming a power law spectrum with photon index 2 and a Galactic column density (2.1 and 5.1 $\times$ 10^{20} cm$-$2) we obtained 5 $\times$ 10^{-14} and 8 $\times$ 10^{-14} erg cm$-$2 s$-$1 as upper limit on the unabsorbed flux in the 0.3-10 keV band. In the case of 0421–57 we detect the source at a rate of (2.2$\pm$ 0.2) $\times$ 10^{-2} counts s^{-1} (about 200 counts) but we are evaluating the contamination from a bright star closeby. The spectrum is very soft and consistent either with a black body (250$\pm$30 eV) or a double Raymond-Smith model.

Several optical campaigns are now in progress. 1357+18 was observed with the I and R filters and the MiniMo camera with the 3.5 WIYN telescope in 10 minutes exposures on 2004 June (P.I. M. Orio). The seeing was about 1.2 arcsec. No optical counterparts were observed in the 3σ spatial error circle, with a 5σ upper limit $R > 23.4$. VLT ESO observations of 2007–48 were performed in May 2006 (P.I. R. Mignani), but are not yet analyzed.

B.4 Discussion

We consider in particular the two transient BFS (1357+18, 2007–48). Note that the statistical significance is formally 4σ, and the total number of photons $\sim$ 100. It is obvious that one must be extremely cautious about the reality of the sources, and because they are supposedly transient, one can't test with further observations.

In the following we suppose that the sources are real: the optical counterparts are dim indeed. What can transient BFS be? An extragalactic origin seems unlikely, because if they were some kind of BL Lac object, a persistent radio-emission would be expected. Gamma ray bursts are probably to be excluded too, because as noted above the light curves is not spiky. One should exclude also binaries with a non collapsed companion, because this should show up in the optical band. One is left to systems consisting of collapsed objects. The key point is that the population of which we have tentatively detected two members could be quite numerous. In fact the HRI field is $\sim 0.2\,\mathrm{deg}^2$, the total exposure time was $\sim 3 \cdot 10^7$ sec. If the distribution of sources were isotropic this would translate in a rate of 10^5 transient BFS per year, otherwise the number should be scaled with the solid angle. The large parent population points to isolated neutron stars or white dwarfs. In particular one may wonder if transient BFS are related to a sudden release of the internal energy of a neutron star, a process which may be at work in the recently discovered transient radio pulsar (McLaughlin et al. [141]; Lyne, this conference).

B.5 Conclusions

In the fifteen years of research about DINS the progress was remarkable, yet there are two basic points that have not yet been achieved:

- There is still no example of a DINS which is convincingly powered by the accretion of the interstellar medium. While there are a number of arguments indicating that these objects should be much rarer than originally estimated (Treves & Colpi[225], Blaes & Madau [24], Perna et al. [186] and references therein), these objects should finally show up, and their emission should be largely independent of the neutron star age. Neutron stars as old as the Galaxy could be a part of the lot.

- We have not yet any information on the cousins of DINS, i.e. isolated black holes (see e.g. Agol & Kamionkowski [3]).

The challenge for the future is obviously to explore the sky for DINS and their cousins, at a flux threshold which is an order of magnitude lower than that of ROSAT, and which is easily accessible to present generation X-ray telescopes. There is no doubt that the activity up to now has been rather slow, since X-ray and optical archives are already available.

Let us summarize the hopes for the future, which can derive from a thorough study of the existing data:

- discovery of accretion fed DINS;

- establishing or excluding the existence of transient BFS;

- discovery of isolated black holes;

- discovery of intermediate mass black holes possibly related to ultraluminous X-ray sources (e.g. Mapelli, Ferrara & Rea [136]).

Appendix C

The Ultraluminous X-ray Sources NGC 1313 X-1 and X-2[1]

C.1 Introduction

Point-like, off-nuclear X-ray sources with luminosities in excess of the Eddington limit for one solar mass are increasingly discovered in nearby galaxies. Despite the growing body of observational data, the mechanism which powers ULXs is still under debate. In several cases a variability on timescales of months/years has been detected, hinting towards the presence of a compact object. Were these sources X-ray binaries in the host galaxy, assuming Eddington-limited accretion, masses in the range $M_{\rm BH} \sim 100 - 1000 M_{\odot}$ are inferred for the compact object from the observed flux. IMBH may have originated from the collapse of a massive star formed in a low metallicity environment, or through merging of massive stars (or lower mass BHs) in a cluster (Miller & Colbert [151]). The BH mass estimates derived from considerations involving the Eddington limit are, however, questionable because these sources need not to be spherically symmetric, nor stationary. It has been proposed that many of the ULX properties can be explained assuming that they do not emit isotropically (King et al. [122]) or are dominated by emission from a relativistic jet (Kaaret et al. [113]). In this case, they may harbor stellar mass BHs and may be similar to Galactic microquasars.
Particularly interesting is the case of the three ULXs hosted in the nearby SBc galaxy NGC 1313. One of them is known to be associated with the interacting supernova SN 1978K (Schlegel et al. [211]). The other two have been extensively studied with several X-ray telescopes and, to date, provide some of the

[1]Here we report Turolla, R., Mucciarelli, P., Zampieri, L., Falomo, R., Chieregato, M. ,& Treves A.: "The Ultraluminous X-ray Sources NGC 1313 X-1 and X-2", 2006, to be published in AdSpR , astro-ph/0506341.

best evidence for the presence of a soft component in the X-ray spectrum of ULXs. Moreover, as discussed in Miller, Fabian & Miller ([150]) and Zampieri et al. ([252], Chapter 3), their continuum subtracted *XMM* EPIC-pn spectra show significant residuals especially in the 0.5–3 keV range.

C.2 X-ray Data

XMM-Newton observed NGC 1313 on October 17, 2000 for a total of ~ 42 Ks. The field was centered on the galaxy nucleus and contains all the three ULXs. The three *XMM* EPIC cameras operated in Prime Full Window mode with the medium filter. The analysis reported here follows that presented in Chapter 3. We consider only the EPIC-pn spectrum because it has twice as many counts as each single MOS instrument. The EPIC-pn spectrum was directly extracted from the observation data file because the automatic pipeline processing failed to produce an event list. Data screening, region selection and event extraction were performed with the standard software XMM-SAS v 6.0.0. In order to eliminate the possible contamination of solar flares (present during the observation), event files were filtered using the good time intervals when the total off-source count rate above 10 keV is less than 1 counts s^{-1}. This leave ~ 21 ks of useful time with an average count rate of 0.73 counts s^{-1} for NGC 1313 X-1 and 0.24 counts s^{-1} for NGC 1313 X-2.

The best fit of the *XMM* EPIC-pn continuum for both sources is obtained with an absorbed soft, thermal component (a multicolor disk blackbody, MCD) plus a power-law. In comparison with previous *ROSAT* and *ASCA* data the statistics is sufficiently good that two components models provide a significant improvement over single component ones (see Zampieri et al. [252], Chapter 3). The statistical improvement obtained adding a MCD component to a power-law model is significant above the 4.5σ level. The resulting best fitting parameters for NGC 1313 X-1 and X-2 are reported in Table C.1. The inferred inner disk temperature is much lower than that obtained for single component thermal models, as already found by Miller et al. ([149]). The X-ray luminosity in the 0.2–10 keV range, assuming isotropic emission and a distance of the host galaxy $\simeq 3.7$ Mpc, is $\simeq (1.4 \pm 0.2) \times 10^{40}$erg s^{-1} for NGC 1313 X-1 and $\simeq (6.0 \pm 0.5) \times 10^{39}$erg s^{-1} for NGC 1313 X-2. If at maximum the source radiates at the Eddington limit, the BH mass is $\sim 120\, M_{\odot}$ for X-1 and $\sim 50\, M_{\odot}$ for X-2. Sub-Eddington accretion would imply an even larger mass.

Residuals in the EPIC-pn spectra of NGC 1313 X-1 and X-2 suggest the presence of some emission lines in both sources. In order to test for the presence of spectral features, we added, one by one, gaussian components at different energies where residuals show evidence of some excess in emission.

For NGC 1313 X-1, the most significant residual is at around 0.6 keV, identified with a high ionization (He-like) Oxygen line (see Figure C.2). Adding a gaussian component, the improvement of the fit with respect to an absorbed

MCD+PL model is significant at the 3.5 σ level. The line energy is 0.58 keV, while the line width was frozen in the fit (0.01 keV). Residuals show also an excess of emission at energies of 1.8 and 4.7 keV (see Figure C.2). The first is the typical energy of highly ionized Silicon, while the second is not readily identified. Adding other two gaussian components for fitting these residuals does not give any further statistical improvement in the fit.

A similar analysis was performed also on the EPIC-pn spectrum of NGC 1313 X-2, following the same approach outlined above. Also in this case the spectrum shows some residuals at an energy of 0.6 keV. In order to test the influence of ISM absorption models (due to the neutral Oxygen absorption edge, see Miller, Fabian & Miller [150]) on the detection of an O line in NGC 1313 X-1, we repeated our analysis using the Tübingen-Boulder absorption model (TBABS; Wilms, Allen & McCray [243], Table C.1), that includes a treatment of gas-phase ISM with revised photoionization cross sections and revised abundances (plus the contribution of grain-phase ISM and molecules). The improvement obtained adding a gaussian component to a TBABS+MCD+PL continuum is at the $\sim 3.6\,\sigma$ level. The line energy is 0.6 keV, while the line width was frozen in the fit (0.01 keV). The significance of the line remains fairly high even performing a fit in a restricted energy region (0.3–1.0 keV) around the centroid of the gaussian. Fitting the continuum with an absorbed MCD+PL model, the addition of a gaussian component with fixed width (0.01 keV) gives an improvement at the $\sim 3\,\sigma$ level.

Additional information on the line properties were obtained analyzing the line profiles. After freezing the best fitting continuum of Table C.1 and removing the gaussian components, residuals (normalized to the continuum) were fitted with a constant (equal to unity) plus a gaussian profile, obtaining the lines centroid energies and equivalent widths. The energies are consistent (within the errors) with those derived from the spectral fits, while the equivalent widths are all below 100 eV. A thorough analysis of these data and new XMM observations of NGC 1313 X-1 and X-2 will be presented in Mucciarelli et al. ([165]).

Table C.1 Parameters of the fit of the *XMM*-EPIC observation of NGC 1313 X-1 and X-2

Model	$\frac{N_{\rm H}}{10^{21}\,cm^{-2}}$	Γ	kT [keV]	Parameters	$\chi^2_{\rm red}$(dof)
		NGC 1313 X-1			
WABS(MCD+PL)	$3.48^{+0.60}_{-0.25}$	$1.75^{+0.08}_{-0.04}$	$0.19^{+0.01}_{-0.03}$		1.12(301)
TBABS(MCD+PL)	$4.21^{+0.64}_{-0.32}$	$1.69^{+0.07}_{-0.05}$	$0.19^{+0.01}_{-0.02}$		1.10(301)
TBABS(MCD+PL+GAUSS)	$4.48^{+0.73}_{-0.31}$	$1.79^{+0.06}_{-0.05}$	$0.17^{+0.01}_{-0.02}$	$E = 0.60^{+0.02}_{-0.02}$ keV	1.04(299)
		NGC 1313 X-2			
WABS(MCD+PL)	$3.26^{+0.92}_{-0.25}$	$2.17^{+0.15}_{-0.09}$	$0.20^{+0.05}_{-0.04}$		1.21(109)

C.3 The optical counterpart of NGC 1313 X-2

Optical images of the field of NGC 1313 X-2 in the R-band were taken on 16 January 2002 with the 3.6 m telescope of the European Southern Observatory (ESO) at La Silla (Chile). Four images were obtained for a total exposure time of 1320 s (see Chapter 3 for details). The accuracy of the astrometric calibration, performed with GSC2 ESO field stars, is 0.3" (1-σ). The X-ray position of NCG 1313 X-2 was obtained from a 2002 *Chandra* pointing with an accuracy of 0.7" (Zampieri et al. [252], Chapter 3). The astrometric calibration of the optical and *Chandra* images was checked using the very accurate radio position of SN 1978K (Ryder et al. [208], Zampieri et al. [252], Chapter 3). Our *Chandra* position of NGC 1313 X-2 is shown in Figure C.2, together with the *ROSAT* HRI [211] and *XMM* EPIC [149] error boxes, overlaid on our ESO image. All measurements are consistent within 1-σ. Object C ($R \sim 23$) is inside the Chandra error box and its position coincides within 1-σ with that of NGC 1313 X-2, making it a likely counterpart and ruling out the previous proposed counterpart, object A. From the maximum absorbed X-ray flux of NGC 1313 X-2 ($f_X \sim 2 \times 10^{-12}$ erg cm^{-2} s^{-1}) and optical magnitude of object C, we estimate $f_X/f_{opt} \gtrsim 1000$.

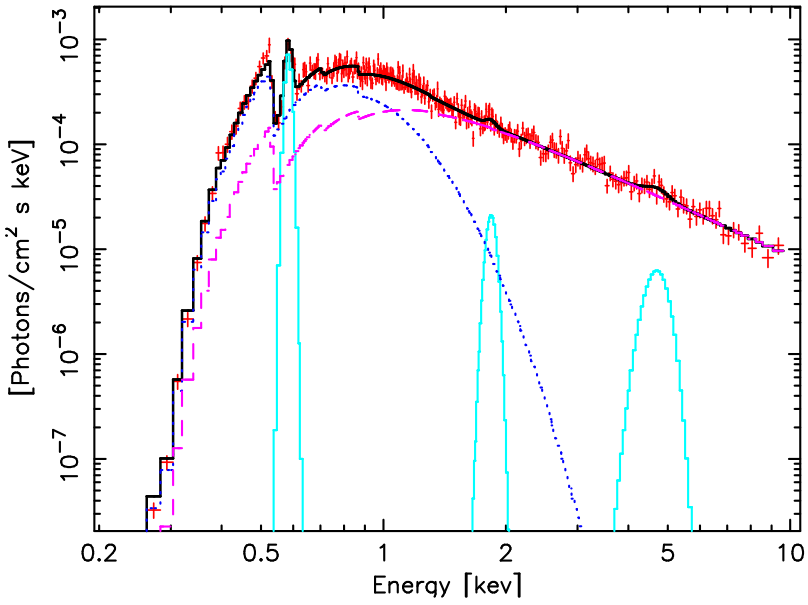

Figure C.1 *XMM* EPIC-pn spectrum of NGC 1313 X-1: absorbed MCD (dotted line)+PL (dashed line) model with three gaussian components (thin solid lines) at energies 0.59, 1.8 and 4.7 keV.

C.4 Discussion

The X-ray spectral parameters, in particular the temperature of the MCD fit (T_{MCD}), can be used to estimate the BH mass. From the effective temperature of a standard accretion disk, under the assumption that T_{MCD} represents an estimate of the maximum disk temperature, Zampieri et al. ([252] , Chapter 3) infer $M_{BH}/M_{\odot} = (\dot{M}c^2/L_{Edd})f^4(\alpha T_{MCD}/1.5 \times 10^7\,\mathrm{K})^{-4}$ (where $f \sim 1.5$ is a color correction factor). The temperature obtained from the two-components fit to the *XMM* spectrum (Table C.1) implies $M_{BH} \approx (130/90)f^4\,M_{\odot}$ for NGC 1313 X-1/X-2 (assuming $\alpha \simeq 2$ and Eddington limited accretion).

Up to now evidence of emission lines in ULXs has been reported in M82 X-1 [219], NGC 4559 X-10 [53] and M101 ULX-1 [127]. The presence of an Oxygen line in the EPIC-pn spectrum of NGC 1313 X-1 appears to be significant at above $3.5\,\sigma$ while the statistical evidence of other features is at most marginal ($< 2\,\sigma$). The simplest interpretation is that we are observing typical emission features of intermediate mass elements left over after the explosion of one or more supernovae belonging to the stellar association of massive stars where the two ULXs are probably embedded.

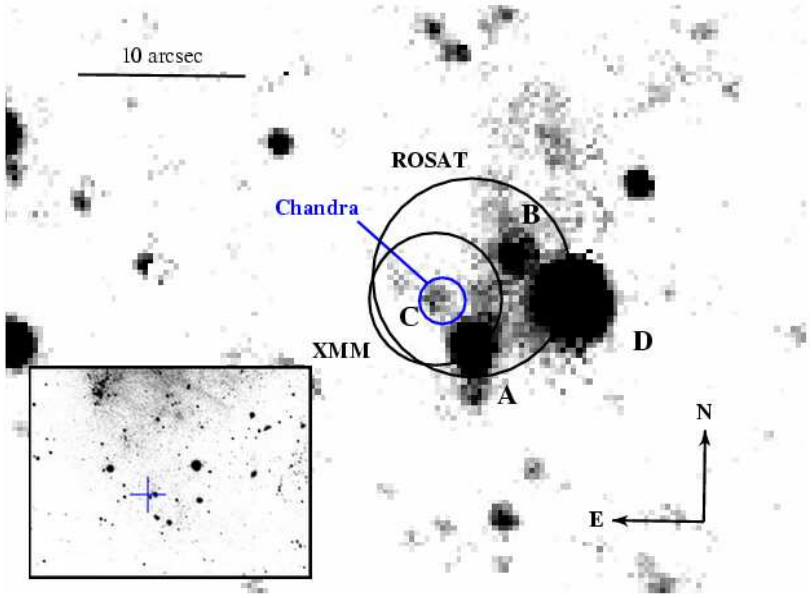

Figure C.2 ESO 3.6m R-band image of the field of NGC 1313 X-2. The circles show the *ROSAT* HRI, *XMM* EPIC and *Chandra* ACIS-S positions. The estimated 90% confidence radii are $6''$, $4''$ and $1.4''$ respectively. Labels A and C mark the old and new proposed optical counterparts. The insert at the bottom-left shows a larger portion of the image with the position of the X-ray source (cross).

Concerning NGC 1313 X-2, the luminosity inferred from the apparent magnitude of object C is consistent with a $\approx 20 M_{\odot}$ main sequence star or a $\sim 15 - 20 M_{\odot}$ evolved OB supergiant making NGC 1313 X-2 a High-Mass X-ray Binary. This picture seems to be confirmed also by the study of the environment of NGC 1313 X-2 (see Zampieri et al. [252]; Chapter 3) and by the association of both ULXs with extended optical emission nebulae (Pakull & Mirioni [178]).

Bibliography

[1] Adelman-McCarthy, J., Agueros, M. A., Allam, S. S., et al., 2006, ApJS 162, 38

[2] Afonso, C., Albert, J. N., Alard, C., et al., 2003, A&A 404, 145

[3] Agol, E. & Kamionkowski, M., 2002, MNRAS 334, 553

[4] Agol, E., Kamionkowski, M., Koopmans, L. V. E. & Blandford, R. D., 2002, ApJ 576, L131

[5] Agüeros, M. A., Anderson, S. F., Margon, B., et al., 2006, AJ 131, 1740

[6] Ahumada, J. & Lapasset, E., 1995, Astron. Astrophys. Suppl. 109, 375

[7] Alcock, C., Allsman R.A., Alves D. R., et al., 1995, ApJ **454**, L125

[8] Alcock, C., Allsman R.A., Alves D. R., et al., 1997, ApJ 479, 119

[9] Alcock, C., Allsman R.A., Alves D. R., et al., 2000, ApJ 541, 734

[10] Baldi, A., Molendi, S., Comastri, A., et al., 2002, ApJ 564, 190

[11] Bartelmann, M. & Loeb, A., 1998, ApJ 503, 48

[12] Barbuy, B., Bica, E. & Ortolani, S., 1998, A&A 333, 117

[13] Barger, A. J., Cowie, L. L., Capak, P., et al., 2003, ApJ 126, 632

[14] Beichman, C. A. Neugebauer, G., Habing, H. J., et al., 1988, Infrared Astronomical Satellite (IRAS) Catalog and Atlases, vol. 1, Explanatory Supplement, NASA RP-1190 (Washington, DC:GPO).

[15] Bennett, D. P., Becker, A. C., Quinn, J. L., et al., 2002, ApJ 579, 639

[16] Bennett, D. P., Becker, A. C., Calitz, J. J., et al., 2006, astro-ph/0207006

[17] Bica, E., Ortolani, S. & Barbuy, B., 1994, A&A 283, 67

[18] Bignami, G. F. & Caraveo, P. A., 1996, ARA&A 34, 331

[19] Bignami, G. F., Caraveo, P .A., De Luca, A. & Mereghetti, S., 2004, Nature 423, 725

[20] Binney, J., Bissantz, N. & Gerhard, O., 2000, ApJ 537, L99

[21] Bissantz, N., Englmaier, P., Binney, J., & Gerhard, O., 1997, MNRAS 289, 651

[22] Bissantz, N., & Gerhard, O., 2002, MNRAS 330, 591

[23] Bissantz, N., Debattista, V. P. & Gerhard, O., 2004, ApJ 601, L155

[24] Blaes O. & Madau P., 1993, ApJ 403, 690

[25] Bock, D. C. -J., Large, M. I. & Sadler, E. M., 1999, AJ 117, 1578

[26] Bohlin, R. C., Savage, B. D. & Drake, J. F., 1978, ApJ 224, 132

[27] Bond, I. A., Udalski, A., Jaroszyński, M., et al., 2004, ApJ 606, L155

[28] Bowers, R. L. & Deeming, T. 1984, Astrophysics: Volume 1 – Stars (Jones and Bartlett Publishers, Inc.)

[29] Bozza, V., Jetzer, P., Mancini, L., & Scarpetta, G. 2002, A&A, 382, 6

[30] Brandt, W. N. & Hasinger, G., 2005, ARA&A 43, 827

[31] Browne, I. W. A., Wilkinson, P. N., Jackson, N. J. F., et al., 2003, MNRAS 341, 13

[32] Brusa, M., Comastri, A., Daddi, E., et al., 2002, ApJ 581, L89

[33] Burwitz, V., Haberl, F., Neuhäuser, R., et al. 2003, A&A 399, 1109

[34] Cagnoni, I., Elvis, M., Kim, D. W., et al., 2001, ApJ 560, 86

[35] Cagnoni, I., Elvis, M., Kim, D. W., et al., 2002, ApJ 579, 148

[36] Cagnoni, I., Turolla, R., Treves, A., et al. 2003, ApJ, 582, 654

[37] Calzetti, D., Armus, L., Bohlin, R. C., et al., 2000, ApJ 533, 682

[38] Camilo, F., Kaspi, V. M., Lyne, A. G., et al., 2000, ApJ 541, 367

[39] Campana, S., Lazzati, D., Panzera, M. R., et al., 1999, ApJ 524, 423

[40] Campana, S., Moretti, A., Lazzati, D. & Tagliaferri, G., 2001, ApJ 560, L19

[41] Carraro, G., Méndez, R. A., May, J. & Mardones, D., 2005, AJ 130, 635

[42] Chang, K. & Refsdal, S., 1979, Nature 282, 561

[43] Chiang, E. & Rappaport, S. 1996, ApJ 469, 255

[44] Chieregato, M., Campana, S., Treves, A., Moretti, A., Mignani, R. P. & Tagliaferri, G., 2005, A&A 444, 69

[45] Chwolson, O., 1924, Astr. Nachr. 221, 329

[46] Clénet, Y., Kasper, M., Gendron E. et al. 2006, in Proc. SPIE Vol. 6272, Advances in Adaptive Optics II, eds., Brent L. Ellerbroek, & Domenico Bonaccini Calia, 62723T

[47] Colbert, E. J. M., Petre, R., Schlegel, E. M. & Ryder, S. D., 1995, ApJ 446, 177

[48] Colbert, E. J. M. & Mushotzky, R. F., 1999, ApJ 519, 89

[49] Colbert, E. J. M. & Ptak, A. F., 2002, ApJS 143, 25

[50] Comastri, A., Setti, G., Zamorani, G.& Hasinger, G., 1995, A&A 296, 1

[51] Condon, J. J., Cotton, W. D., Greisen, E. W. et al., 1998, AJ 115, 1693

[52] Cropper, M., Zane, S., Ramsay, G., et al., 2001, A&A 365, L302

[53] Cropper, M., Soria, R., Mushotzky, R. F., et al., 2004, MNRAS 349, 39

[54] Cropper, M., Haberl, F., Zane, S. & Zavlin, V. E., 2004, MNRAS 351, 1099

[55] David, L. P., Harnden, F. R., Kearns K. L., et al., 1998, The ROSAT High Resolution Imager(HRI) Calibration Report, U.S. ROSAT Science Data Center (SAO)

[56] de Jong, J.A., van Paradijs, J. & Augusteijn, T. 1996, A&A 314, 484

[57] De Rújula, A., Jetzer, P. & Massó, E., 1991, MNRAS 250, 348

[58] de Vries, C. P., Vink, J., Mndez, M. & Verbunt, F., 2004, A&A 415, L31

[59] Dias, W. S., Alessi, B. S., Moitinho, A. & Lépine, J. R. D., 2002, A&A 389, 871

[60] Dickey, J. & Lockman, F., 1990, ARA&A 28, 215

[61] Di Stefano, R., Paerels, F. & Rappaport, S., 1995, ApJ 450, 705

[62] Drake, J. J., Marshall, H. L., Dreizler, S., et al., 2002, ApJ 572, 996

[63] Einstein, A., 1936, Science 84, 506

[64] Evans, N. W. & Belokurov, V. 2002, ApJ 567, L119

[65] Fabbiano, G. & Trinchieri, G., 1987, ApJ 315, 46

[66] Fabbiano, G., 1989, ARA&A, 27, 87

[67] Fabbiano, G., Zezas, A., King, A. R., et al., 2003, ApJ 584, L5

[68] Fabbiano, G. & White, N. E., 2003, in Compact Stellar X-ray Sources, eds., W. Lewin & M. van der Klis, Cambridge University Press

[69] Falomo, R., Kotilainen, J.K., Scarpa, R. & Treves, A., 2005, A&A 434, 469

[70] Fiorucci, M. & Munari, U., 2003, A&A 401, 781

[71] Flesch, E. & Hardcastle, M.J., 2004, A&A 427, 387

[72] Foschini, L., Di Cocco, G., Ho, L. C., et al., 2002, A&A 392, 817

[73] Foschini, L., Ho, L. C. Masetti, N., et al., 2002, A&A 396, 787

[74] Fossati, G., Maraschi, L., Celotti, A., et al., 1998, MNRAS 299, 433

[75] Frank, J., King, A.R. & Raine, D.J. 2002, Accretion Power in Astrophysics (Cambridge University Press)

[76] Gavriil, F., Kaspi, V. M. & Woods, P., 2003, Nature 419, 142

[77] Ghisellini, G., Celotti, A., Fossati, G., et al., 1998, MNRAS 301, 451

[78] Giacconi, R., Zirm, A., Wang, J. Xi., et al., 2002, ApJS 139, 369

[79] Gioia, I. M., Maccacaro, T., Schild, R. E., et al.,. 1990, ApJS 72, 567

[80] Glicenstein, J. F. 2004, Talk at the Hawaiian Gravitational Microlensing Workdhop

[81] Goad, M.R., Roberts, T.P., Knigge, C. & Lira, P., 2002, MNRAS 335, L67

[82] Gould, A., 2000, ApJ 542, 785

[83] Green, P. J., Silverman, J. D., Cameron, R. A, et al., 2003, ApJS 150, 43

[84] Grenacher, L., Jetzer, P., Strässle, M. & de Paolis, F. 1999, A&A 351, 775

[85] Griest, K., 1991, ApJ 366, 412

[86] Griest, K., Alcock, C., Axelrod, T. S., et al., 1991, ApJ 372, L79

[87] Griest, K. & Thomas, C.L., 2005, MNRAS 359, 464

[88] Haberl, F., 2004, Adv. Sp. Res. 33, 638

[89] Haberl, F., 2004, MmSAI 75, 454

[90] Haberl, F., 2005, in 5 years of Science with XMM-Newton, MPE Report 288, 39, eds. U. G. Briel, S. Sembay & A. Read

[91] Haberl, F., Pietsch, W. & Motch, C., 1999, A&A 351, L53

[92] Haberl, F., Schwope, A. D., Hambaryan, V., et al., 2003, A&A 403, L19

[93] Haberl, F., Motch, C., Zavlin, V. E., et al. 2004, A&A 424, 635

[94] Haberl, F., Zavlin, V. E., Trümper, J.& Burwitz, V., 2004, A&A 419, 1077

[95] Hailey, C. J. & Mori, K., 2002, ApJ 573, L133

[96] Hamadache, C., Le Guillou, L., Tisserand, P., et al., 2006, A&A 454, 185

[97] Hambly, N. C., Irwin, M. J. & MacGillivray, H. T., 2001, MNRAS 326, 1295

[98] Han, C. & Gould, A., 2003, ApJ 592, 172

[99] Harrison, F. A., Eckart, M. E., Mao, P. H., et al., 2003, ApJ 596, 944

[100] Hasinger, G., Burg, R., Giacconi, R., et al., 1993, A&A 275, 1

[101] Hasinger, G., Burg, R., Giacconi, R., et al., 1998, A&A 329, 482

[102] Hayes, D. S., 1985, IAU Symp. 111: Calibration of Fundamental Stellar Quantities, 111, 225

[103] Ho, W. C. G., Lai, D., Potekhin A. Y. & Chabrier, G., 2003, APJ 599, 1293

[104] Ho, W. C. G. & Lai, D., 2004, APJ 607, 420

[105] Huchra, J., Gorenstein M., Kent, S., et al., 1985, AJ 90, 691

[106] Iovino, A., Clowes, R. & Shaver, P., 1996, A&AS 119, 265

[107] Israel, G., Mereghetti, S. & Stella, L. 2002, MmSAI 73, 465

[108] Iwamoto, K., Mazzali, P. A., Nomoto, K., et al., 1998, Nature 395, 672

[109] Jackson, N., de Bruyn, A.G., Myers, S., et al., 1995, MNRAS 274, L25

[110] Jetzer, P., Strässle, M. & Wandeler, U., 1998, A&A 336, 411

[111] Jetzer, P., 2002, *Gravitational lensing*, in: *Modern cosmology*, 378, S. Bonometto, V. Gorini and U. Moschella, eds. (Institute of Physics Publishing: Bristol)

[112] Kaaret, P., Prestwich, A. H., Zezas, A., et al., 2001, MNRAS 321, L29

[113] Kaaret, P., Corbel, S., Prestwich, A. H., & Zezas, A., 2003, Science 299, 365

[114] Kaplan, D. L., van Kerkwijk, M. H. & Anderson, J., 2002, ApJ 571, 447

[115] Kaplan, D. L., van Kerkwijk, M. H., Marshall, H. L., et al., 2002, ApJ 570, L79

[116] Kaplan, D.L., Kulkarni, S.R. & van Kerkwijk, M.H., 2003, ApJ 588, L33

[117] Kassiola, A. & Kovner, U., 1993, ApJ 417, 450

[118] Keeton, C. R., 2006, ApJ submitted, astro-ph/0102340

[119] Keeton, C. R. & Kochanek, C. S., 1998, ApJ 495, 157

[120] Keeton, C. R., Kuhlen, M. & Haiman, Z., 2005, ApJ 621, 559

[121] Kharchenko, N. V., Piskunov, A. E., Röser, S., et al. 2005, A&A 438, 1163

[122] King, A. R., Davies, M. B., Ward, M. J., et al., 2001, ApJ 552, L109

[123] Kiraga, M. & Paczyński, B., 1994, ApJ 430, L101

[124] Kleinmann, S. G., Lysaght, M. G., Pughe, W. L., et al., 1994, Ap&SS 217, 11

[125] Kochanek, C. S., Schneider, P. & Wambsganss, J., 2005, *Gravitational Lensing: Strong, Weak & Micro*, Proceedings of the 33rd Saas-Fee Advanced Course, G. Meylan, P. Jetzer & P. North, eds. (Springer-Verlag: Berlin)

[126] Koekemoer, A. M., Alexander, D. M., Bauer, F. E., et al., 2004, ApJ 600, L123

[127] Kong, A. K. H., Rupen, M. P., Sjouwerman, L. O., & Di Stefano, R., 2005, presented at the XXII Texas Symposium on Relativistic Astrophysics, Stanford University, Dec. 13-17, 2004, astro-ph/0503465.

[128] Kormann, R., Schneider, P. & Bartelmann, M., 1994, A&A 284, 285

[129] Lazzati, D., Campana, S., Rosati, P., et al., 1999, ApJ 524, 423

[130] Le Brun, V., Smette, A., Surdej, J. & Claeskens, J.-F., 2000, A&A 363, L837

[131] Liebes S., 1964, Phys. Rev. 133, 835

[132] Loktin, A. V., Matkin, N. V., & Gerasimenko, T. P., 1994, Astron. & Astrophys. Trans. 4, 153

[133] Maccacaro T., Gioia, I. M., Wolter, A., et al. 1988, ApJ 326, 680

[134] Mainieri, V., Bergeron, J., Hasinger, J., et al., 2002, A&A 393, 425

[135] Makishima, K., Kubota, A., Mizuno, T., et al., 2000, ApJ 535, 632

[136] Mapelli M., Ferrara A.& Rea N., 2006, MNRAS 368, 1340

[137] Mao, S., Smith, M. C., Woźniak, P., et al., 2002, MNRAS 329, 349

[138] Masetti, N., 1997, PhD Thesis, unpublished
(http://www.bo.iasf.cnr.it/m̃asetti/phdth.hml)

[139] Matonick, D. M. & Fesen, R. A., 1997, ApJS 112, 49

[140] McLaughlin, M. A., Stairs, I. H. Kaspi, V. M., et al., 2003, ApJ 591, L135

[141] McLaughlin, M. A., Lyne, A. G., Lorimer, V. M,, et al., 2006, Nature 439, 817

[142] McLean, B. J., Greene, G. R., Lattanzi, M. G. & Pirenne, B., 2000, ADASS 216, 145.

[143] McLean, B. J., et al. 2006, in preparation

[144] McMahon, R. G., Irwin, M. J., & Maddox, S. J. 2000, VizieR Online Data Catalog 1267, 0

[145] McMahon, R. G., White, R. L., Helfand, D. J. & Becker, R. H., 2002, ApJS 143, 1

[146] Mereghetti, S., De Luca, A., Caraveo, P. A., et al., 2002, ApJ 581, 1280

[147] Mereghetti, S., Chiarlone, L., Israel, G. L. & Stella, L., 2002, in Proceedings of the 270. WE-Heraeus Seminar on Neutron Stars, Pulsars, and Supernova Remnants. MPE Report 278. Edited by W. Becker, H. Lesch and J. Trümper. Garching bei Mnchen: Max-Plank-Institut für extraterrestrische Physik, 2002, p.29

[148] Mereghetti, S., Tiengo, A., Stella, L., et al., 2004, ApJ 608, 472

[149] Miller, J. M., Fabbiano, G., Miller, M. C., & Fabian, A. C., 2003, ApJ 585, L37

[150] Miller, J. M., Fabian, A. C. & Miller, M. C., 2004, ApJ 607, 931

[151] Miller, M. C. & Colbert, E.J.M., 2004, Int. Jour. of Modern Physics D, 13, 1

[152] Miller, S., Schlegel, E. M., Petre, R. & Colbert, E., 1998, AJ 116, 1657

[153] Mollerach, S. & Roulet, E., 1997, ApJ 479, 147

[154] Monet, D. G., Levine, S. E., Casian, B., et al., 2003, AJ 125, 984

[155] Moretti, A., Campana, S., Lazzati, D. & Tagliaferri, G., 2002, ApJ 570, 502

[156] Moretti, A., Campana, S., Lazzati, D. & Tagliaferri, G., 2003, ApJ 588, 696

[157] Moretti, A., Guzzo L., Campana S., et al., 2004, A&A 428, 21

[158] Mori, K., Chonko, J. C. & Hailey, C. J., 2005, ApJ 631, 1082

[159] Moro, D. & Munari, U., 2000, A&AS 147,361

[160] Morris, D. J., Hobbs, G., Lyne, A. G., et al., 2002, MNRAS 335, 275

[161] Moshir, M., Kopan, G., Conrow, T., et al., 1990, BAAS 22, 1325

[162] Motch C., Guillout, P., Haberl, F., et al., 1998, A&AS 132, 341

[163] Motch, C., Zavlin, V. E. & Haberl, F., 2003, A& 408, 323

[164] Motch, C., Sekiguchi, K., Haberl, F., et al., 2005, A&A 429, 257

[165] Mucciarelli, P. et al., 2006, in preparation

[166] Mushotzky, R. F., Cowie, L. L., Barger, A. J. & Arnaud, K. A., 2000, Nature 404, 459

[167] Musso C., Mignani, R. P., Becker, W., et al., 1998, AdSpR 21, 255

[168] Myers, S.T., Jackson, N.J., Browne, I.W.A., et al., 2003, MNRAS 341, 1

[169] Nair, V. & Miralda-Escudé, J., 1999, ApJ 515, 206

[170] Narayan, R. & Bartelmann, M., 1999, *Gravitational lensing*, in: *Formation of Structure in the Universe*, Proceedings of 1995 Jerusalem Winter School ,360, A. Dekel & J. P. Ostriker, eds. (Cambridge University Press: Cambridge)

[171] Narayan, R., & Schneider, P., 1990, MNRAS 243, 192

[172] Neuhäuser R. & Trümper J.E., 1999, A&A 343, 151

[173] Norman, C., Hasinger, G., Giacconi, R., et al., 2002, ApJ 571, 218

[174] Otrupcek R. E., Hartley M.& Wang J. -S., 2000, PASA 17, 92

[175] Paczyński, B., 1971, ARA&A 9, 183

[176] Paczyński, B., 1986, ApJ. 301, 503

[177] Paczyński, B., 1991, ApJ 371, L63

[178] Pakull, M. W. & Mirioni, L., 2002, in Proc. ESA Symp., New Visions of the X-ray Universe in the *XMM-Newton* and *Chandra* Era, eds. F. Jansen, et al. (ESA SP-488)

[179] Panzera, M. R., Campana, S., Covino, S., et al., 2003, A&A 399, 351

[180] Patnaik, A. R., Browne, I. W. A., King, L. J., et al., 1993, MNRAS 261, 435

[181] Paturel, G., Fouque, P., Bottinelli, L., & Gouguenheim, L., 1989, A&AS 80, 299

[182] Pavlov, G. G., Shibanov, I. A.& Zavlin, V. E., 1991, MNRAS 253, 193

[183] Peng, C. Y., Ho, L. C., Impey, C. D. & Rix, H.-W. 2002, AJ 124, 266

[184] Perlman, E. S., Stocke, J. T., Schachter, J. F., et al., 1996, ApJS 104, 251

[185] Perna, R., Loeb, A., & Bartelmann, M., 1997, ApJ 488, 550

[186] Perna, R., Narayan, R., Rybicki, G., et al., 2003, ApJ 594, 936

[187] Petre, R., Okada, K., Mihara, T., et al., 1994, PASJ 46, L115

[188] Pian, E., Vacanti, G., Tagliaferri, G., et al., 1998, ApJ 492, L17

[189] Pickles, A. J., 1998, PASP 110, 863

[190] Pierini, D. & Tuffs, R. J. 1999, A&A 343, 751

[191] Popov, S. B., Colpi, M., Prokhorov, M. E. et al., ApJ 544, L53

[192] Popov, S. B., Colpi, M., Prokhorov, M. E., et al., 2003, A&A 406, 111

[193] Popov S. B., Turolla R., Prokhorov, M. E., et al., 2005, Ap&SS 299, 117

[194] Popowski, P., 2006, MNRAS submitted, astro-ph/0205044

[195] Popowski, P., Griest, K., Thomas, C. L., et al., 2005, ApJ 631, 879

[196] Pramesh Rao, A. & Subrahmanyan, R., 1988, MNRAS 231, 229

[197] Protassov, R., van Dyk, D. A., Connors, A., et al., 2002, ApJ 571, 545

[198] Rajagopal, M. & Romani, R. W., 1996, ApJ 461, 327

[199] Rajagopal, M., Romani, R. W. & Miller, M. C., 1997, ApJ 479, 347

[200] Refsdal, S., 1964, MNRAS 128, 295

[201] Refsdal, S., 1966, MNRAS 132, 101

[202] Reid, I. N., Brewer, C., Brucato, R. J., et al., 1991, PASP 103, 661

[203] Rengelink, R. B., Tang, Y., de Bruyn, A. G., et al., 1997, A&AS 124, 259

[204] Renn, J., Sauer, T. & Stackel, J., 1997, Science 275, 184.

[205] Roberts, T. P., Goad, M. R., Ward, M. J., et al., 2001, MNRAS 325, L7

[206] Romano, P., Campana, S., Mignani R. P., et al., 2006, A&A submitted

[207] Rutledge, R. E., Fox, D.W., Bogosavljevic, M., et al., 2003, ApJ 598, 458

[208] Ryder, S., Staveley-Smith, L., Dopita, M., et al. 1993, ApJ 416, 167

[209] Saha, P., & Williams, L. L. R., 2003, AJ 125, 2769

[210] Sanwal, D., Pavlov, G. G., Zavlin, V. E. & Teter, M. A., 2002, ApJ 574, L61

[211] Schlegel, E. M., Petre, R., Colbert, E. J. M., & Miller, S., 2000, AJ 120, 2373

[212] Schneider, P., Ehlers, J. & Falco E. E., 1992, *Gravitational Lenses*(Springer-Verlag: Berlin)

[213] Schramm, T., 1990, A&A 231, 19

[214] Schwarz, D.J. & Seidel, D., 2002, A&A 388, 483

[215] Shimura, T. & Takahara, F., 1995, ApJ 445, 780

[216] Smith, M. C., Mao, S., Woźniak, P. et al. 2002, MNRAS 336, 670

[217] Stern, D., Moran, E. C., Coil, A. L., et al., 2002, ApJ 568, 71

[218] Stocke, J. T., Wang, Q. D., Perlman, E. S., et al., 1995, AJ 109, 1199

[219] Strohmayer, T. E., & Mushotzky, R. F., 2003, ApJ 586, L61

[220] Sumi, T., Abe, F., Bond, I. A., et al., 2003, ApJ 591, 204

[221] Sumi, T., Woźniak, P. R., Udalski, A., et al., 2006, ApJ 636, 240

[222] Swartz, D. A., Ghosh, K. K., McCollough, M. L., et al., 2003, ApJS 144, 213.

[223] Szokoly, G. P., Bergeron, J., Hasinger, J., et al., 2004, ApJS 155, 271

[224] Thomas, C. L., Griest, K., Popowski, P., et al., 2005, ApJ 631

[225] Treves A. & Colpi M. 1991, A&A 241, 107

[226] Treves, A., Turolla, R., Zane, S.& Colpi, M., 2000, PASP 112, 297

[227] Treves, A., Campana, S., Chieregato, M., Moretti, A., Nelson, T. & Orio, M., 2006, to appear in Ap&SS, in the proceedings of "Isolated Neutron Stars: from the Interior to the Surface", edited by D. Page, R. Turolla and S. Zane, astro-ph/0609194

[228] Tully, R. B., 1988, Nearby Galaxies Catalog (Cambridge: Cambridge University Press)

[229] Turolla, R., Mucciarelli, P., Zampieri, L., Falomo, R., Chieregato, M., & Treves, A., 2006, to be published in AdSpR, astro-ph/0506341

[230] Udalski, A., Szymański, M., Kaluzny, J. et al., 1993, Acta Astronomica 43, 289

[231] Udalski, A., Szymański, M., Stanek, K. Z., et al., 1994, Acta Astronomica 44, 165

[232] Udalski, A., Żebruń, K., Szymański, M., et al., 2000, Acta Astronomica 50, 1

[233] Ueda, Y., Ishisaki, Y., Takahashi, T., et al., 2001, ApJS 133, 1

[234] Urry, C. M. & Padovani, P., 1995, PASP 107, 803

[235] van der Marel, R. P., 2004, Carnegie Observatories Astrophysics Series, Vol. 1: Coevolution of Black Holes and Galaxies, ed. L. C. Ho (Cambridge: Cambridge Univ. Press), astro-ph/0302101

[236] Van Kerkwjik, M. H., Kaplan, D. L. Durant, M., et al. 2004, ApJ 608, 432

[237] Véron-Cetty, M. P., & Véron, P., 2001, A&A 374, 92

[238] Vink, J., de Vries, C. P., Mndez, M. & Verbunt, F., 2004, ApJ 609, L75

[239] Voges, W., Aschenbach, B., Boller, T., et al., 1996, IAU Circ., 6420

[240] Walter, F. M.& Lattimer, J. M., 2002, ApJ 576, 145

[241] White, N. E., Giommi, P. & Angelini, L., 1994, IAU Circ., 6100 http://wgacat.gsfc.nasa.gov

[242] White, R. L., Becker, R. H., Helfand, D. J., et al., 1997, ApJ 475, 479

[243] Wilms, J., Allen, A. & McCray, R., 2000, ApJ 542, 914

[244] Winn, J. N., Hall, P. B., & Schechter, P. L., 2003, ApJ 597, 672

[245] Woods, P., Kaspi, V. M., Thompson, C., et al., 2004, ApJ 605, 378

[246] Woźniak, P. R., Udalski, A., Szymański, M., et al., 2001, Acta Astronomica 51, 175

[247] Wu, H., Xue, S. J., Xia, X.Y., et al., 2002, ApJ 576, 738

[248] Yakovlev, D. G., Gnedin, O. Y., Kaminker, A. D., et al. 2004, Proceedings of the 34th COSPAR Scientific Assembly, Adv. Sp. Res. 33, 523-530

[249] York, D. G., Adelman, J., Anderson, J. E., Jr., et al., 2000, AJ 120, 1579

[250] Zampieri, L., Turolla, R., & Szuszkiewicz, E. 2001, MNRAS 325, 1266

[251] Zampieri, L., Campana, S., Turolla, R., Chieregato, M., Falomo, R., Fugazza, D., Moretti, A.& Treves, A., 2001, A&A 378, L5

[252] Zampieri, L., Mucciarelli, P., Falomo, R., Kaaret, P., Di Stefano, R., Turolla, R., Chieregato, M. & Treves, A., 2004, ApJ 603, 523

[253] Zampieri, L., Mucciarelli, P., Falomo, R., Kaaret, P., Di Stefano, R., Turolla, R., Chieregato, M. & Treves, A., 2004, NuPhS 132, 387

[254] Zane, S., Haberl, F., Cropper, M., et al., 2002, MNRAS 334, 345

[255] Zane, S., Cropper, M., Turolla, R., Zampieri, L., Chieregato, M., Drake, J. J. & Treves, A., 2005, ApJ 627, 397

[256] Zaritsky, D., Kennicutt, R. C. & Huchra, J.P., 1994, ApJ 420, 87

[257] Zavlin, V. E., Pavlov, G. G., & Shibanov, Y. A., 1996, A&A 315, 141

[258] Zavlin, V. E., & Pavlov, 2001, Proceedings of the 270. WE-Heraeus Seminar on "Neutron Stars, Pulsars and Supernova Remnants". MPE Report 278. Edited by Becker, W., Lesch, H., and Trümper, J.. Garching bei München: Max-Plank-Institut für extraterrestrische Physik, 2002, pag. 263-272

[259] Zavlin, V. E., Pavlov, G. G. & Sanwal, D., 2004, ApJ 606, 444

[260] Zhao, H., Spergel, D. N. & Rich, R. M., 1995, ApJ 440, L13

[261] Zhao, H. & Mao, S., 1996, MNRAS 283, 1197

[262] Zickgraf, F. -J., Engels, D., Hagen, H. -J., et al., 2003, A&A 406, 535

[263] Zimmermann, H. -U. 1994, IAU Circ. 6102

[264] Zwicky, F., 1937, Phys. Rev. 51, 290

[265] Zwicky, F., 1937, Phys. Rev. 51, 679

Publications list

Refereed Publications

Chieregato, M., Campana, S., Treves, A., Moretti, A., Mignani, R. P. & Tagliaferri, G.: "Blank Field Sources in the ROSAT HRI Brera Multiscale Wavelet catalog" 2005, A&A 444, 69

Zane, S., Cropper, M., Turolla, R., Zampieri, L., **Chieregato, M.**, Drake, J. J. & Treves, A.: "Detection of pulsations and a spectral feature in the X-ray emission of the isolated neutron star 1RXS J214303.7+065419/RBS 1774", 2005, ApJ 627, 397

Zampieri, L., Mucciarelli, P., Falomo, R., Kaaret, P., Di Stefano, R., Turolla, R., **Chieregato, M.** & Treves, A.: "Optical Counterpart of The Ultraluminous X-ray Source NGC 1313 X-2" 2004, NuPhS 132, 387

Zampieri, L., Mucciarelli, P., Falomo, R., Kaaret, P., Di Stefano, R., Turolla, R., **Chieregato, M.** & Treves, A.: "The Ultraluminous X-ray Source NGC 1313 X-2 (MS 0317.7-6647) and its Environment", 2004, ApJ 603, 523

Zampieri, L., Campana, S., Turolla, R., **Chieregato, M.**, Falomo, R., Fugazza, D., Moretti, A.& Treves, A.: "1RXS J214303.7+065419/RBS 1774: A New Isolated Neutron Star Candidate", 2001, A&A 378, L5

Conference proceedings

Treves, A., Campana, S., **Chieregato, M.**, Moretti, A., Nelson, T. & Orio, M.: "Persistent and Transient Blank Field Sources" 2006, to appear in Ap&SS, in the proceedings of "Isolated Neutron Stars: from the Interior to the Surface", edited by D. Page, R. Turolla and S. Zane, astro-ph/0609194

Turolla, R., Mucciarelli, P., Zampieri, L., Falomo, R., **Chieregato, M.,** & Treves, A.: "The Ultraluminous X-ray Sources NGC 1313 X-1 and X-2", 2006, to be published in AdSpR, astro-ph/0506341

Abstracts

Chieregato, M., Zampieri, L., Campana, S., Turolla, R., Falomo, R., Fugazza, D., Moretti, A. & Treves, A. : "RBS 1774: A New Isolated Neutron Star Candidate", 2001, The Second National Conference on Astrophysics of Compact Objects, 6

Submitted publications

Chieregato, M., Miranda M. & Jetzer, P. : "Q0045-3337: a candidate for strong lensing by a spiral galaxy", 2006, A&A submitted

Acknowledgements

Many people helped me in many ways during these years. I will cite:

Aldo Treves, my supervisor in Como, for his teaching, his example, his enthusiasm, and for being always present when I needed his help.

Philippe Jetzer, my supervisor in Zürich, that took a student completely new to the gravitational lensing topic and brought him to a PhD level, and that always left me free to choose what to do.

My other coauthors:

For the BFS (Chapter 1 and 2 and appendices A and B), Alberto Moretti, Roberto Mignani, Gianpiero Tagliaferri, Marina Orio and Thomas Nelson; and especially Sergio Campana, who was somehow a bonus supervisor, and who did the first author's job when I was incapacitated.

For NGC 1313 X-2 (Chapter 3 and appendix C), Luca Zampieri, Paola Mucciarelli, Renato Falomo, Philip Kaaret, Rosanne Di Stefano, and Roberto Turolla.

For RBS 1774 (Chapter 4), Silvia Zane, Mark Cropper, Roberto Turolla, Luca Zampieri and Jeremy Drake.

An additional mention is needed for the Padova Group (Roberto Turolla, Luca Zampieri and Silvia Zane) that encouraged me to take my first steps in astrophysics.

For Q0045-3337 (Chapter 7), Marco Miranda.

... besides, obviously, Aldo Treves and Philippe Jetzer...

Other people contributed to the various part of the thesis. In particular, Ilaria Cagnoni authored the parent project of BFS and, having the misfortune of being an office mate at the beginning of my PhD., was compelled to answer an huge quantity of questions.

Victor DeBattista kindly furnished his Milky Way model and pointed up the anomaly of MACHO field 104. Sonia Hirt had the idea to blame NGC 6540 for the anomaly.

Renato Falomo gave us access to the NaCo data on Q0045-3337, explained me the peculiarity of adaptive optics and had extensive discussions on the possible instrumental origin of the stretching of Q0045-3337.

Many others contributed with software help, seminars revision, sharp questions, criticism or simply with scientific discussions. In particular, the astrophysicists of Como, and present and past members of the astrophysics group of Zürich.

Additional help with the German Zusammenfassung was provided by Joachim

Naef and Linda Roberts.

For a different kind of help, I would like to thank my father, my mother, my brother, and the rest of my family. My flatmates in Zürich. My friends in Padova, in Badia Polesine, in Como, in Zürich... and in other parts of the world.

I will remember all the people that faced my illness making me receive somehow their solidariety.

Barbara has been always with me in the darkest of the shadows as in the glow of pink-fingered auroras.